Chem Soc Rev

REVIEW ARTICLE

View Article Online
View Journal | View Issue

Cite this: *Chem. Soc. Rev.*, 2021, **50**, 7587

Organic thermally activated delayed fluorescence (TADF) compounds used in photocatalysis

Megan Amy Bryden and Eli Zysman-Colman *

Received 22nd February 2021

DOI: 10.1039/d1cs00198a

rsc.li/chem-soc-rev

Organic compounds that show Thermally Activated Delayed Fluorescence (TADF) have become wildly popular as next-generation emitters in organic light emitting diodes (OLEDs). Since 2016, a subset of these have found increasing use as photocatalysts. This review comprehensively highlights their potential by documenting the diversity of the reactions where an organic TADF photocatalyst can be used in lieu of a noble metal complex photocatalyst. Beyond the small number of TADF photocatalysts that have been used to date, the analysis conducted within this review reveals the wider potential of organic donor–acceptor TADF compounds as photocatalysts. A discussion of the benefits of compounds showing TADF for photocatalysis is presented, which paints a picture of a very promising future for organic photocatalyst development.

1. Introduction

In the most basic definition, photocatalysis involves using light as an energy input in concert with a light-absorbing material to increase reaction rates. Since 2007, there has been a resurgence of activity in the domain of photocatalysis following the pioneering demonstrations by the likes of MacMillan, Yoon and Stephenson, who showed that photoactive organometallic complexes can mediate useful organic reaction transformations.[1–3] The prospect of the widescale development of greener, more economical reactions that proceed under mild reaction conditions has propelled photocatalysis from a niche concept to a widely accepted and highly useful synthetic strategy. Photocatalysis presents a significant advantage over traditional synthetic methodologies in that it can allow for generation of products which are inaccessible thermally. Moreover, the reactive intermediates are generated under mild conditions, which opens the door to new transformations and to reaction conversions at higher efficiencies.

Upon absorption of light, the photocatalyst (PC) accesses its excited state, PC*. From here, photoinduced energy transfer (PEnT) and/or photoinduced electron transfer (PET) can occur between the PC* and the substrate, with the latter requiring an additional single electron transfer (SET) step to close the

Organic Semiconductor Centre, EaStCHEM School of Chemistry, University of St Andrews, St Andrews, KY16 9ST, UK. E-mail: eli.zysman-colman@st-andrews.ac.uk; Web: http://www.zysman-colman.com/

Megan Amy Bryden

Megan Amy Bryden obtained her MChem from the University of Durham in 2018, with her master's project being undertaken at the Université Grenoble Alpes focusing on luminescent lanthanide redox probes. She is now completing her PhD project at the University of St Andrews and is interested in exploring new photocatalytic reactions with TADF compounds as the photocatalyst.

Eli Zysman-Colman

Eli Zysman-Colman obtained his PhD in Chemistry from McGill University in 2003 with Prof. David N. Harpp. He then completed two postdoctoral fellowships, one in supramolecular chemistry with Prof. Jay Siegel at the University of Zurich and the other in inorganic materials with Prof. Stefan Bernhard at Princeton University. He joined the Université de Sherbrooke as an assistant professor in 2007. In 2013, he moved to the University of St Andrews where he is presently Professor of Optoelectronic Materials, Fellow of the RSC and is the holder of a Royal Society Leverhulme Trust Senior Research Fellowship.

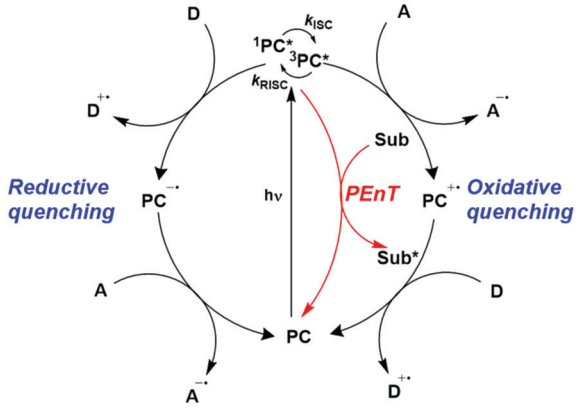

Fig. 1 Energy transfer, oxidative quenching and reductive quenching photocatalytic cycles of a generic TADF PC with donor (D) and acceptor (A) substrates (Sub).

photocatalytic cycle, reflected in Fig. 1. When PET is in operation, this is termed photoredox catalysis.

Regardless of the mechanism in operation, it is important to use a PC that can be photoexcited selectively in the presence of the organic substrate or the product formed. Thus, PCs with absorption bands in the visible (or just within the UV) spectrum are desirable as the absorption spectra of many organic compounds are transparent in this regime. As the energy used to photoexcite the photocatalyst increases, direct homolytic cleavage of bonds within both the PC and the organic substrates becomes more prevalent, resulting in undesired side reactions and, thus, limiting the usefulness of the process.

The yield of the formation of the excited state should be as high as possible, which relates to both the quantum yield of its formation, as well as the absorption cross section of the PC (as measured by the concentration and the molar extinction coefficient, ε).[4] Ideally, the quantum yield, $\Phi(\lambda)$, for a photocatalytic reaction, as defined in eqn (1), should be as close to 1 as possible, for reactions not proceeding *via* a radical chain mechanism.

$$\Phi = \frac{\text{mol of product formed}}{\text{mol of photons absorbed}} \quad (1)$$

The intensity of the excitation source, the molar extinction coefficient of the PC at the excitation wavelength and the optical path length each affect the reaction rate.[5] Additionally, the excited state of the PC must be sufficiently long-lived, on the order of at least a few nanoseconds, in order to overcome diffusion processes that are required to generate an encounter complex in these bimolecular reactions.[6–10] The diffusion rates to generate the required encounter complex define a rate-limiting step in photocatalysis.

Traditionally, visible light PCs have been based around 4d- and 5d-transition metal complexes that possess low-lying charge transfer excited states. The most popular PCs remain those based on iridium(III) and ruthenium(II) complexes (*cf.* Fig. 9 and 10).[11] These phosphorescent complexes possess long-lived excited states. For instance, $[Ru(bpy)_3]^{2+}$ (bpy = 2,2′-bipyridine) has a lifetime, τ_{PL}, of 1100 ns in acetonitrile[12] while *fac*-Ir(ppy)$_3$ (ppyH = 2-phenylpyridine) has a τ_{PL} of 1322 ns in acetonitrile (Table 1).[13,14] However, despite their inherently attractive photophysical and electrochemical properties, the scarcity of the metals in these commonly used PCs, their expensive cost (1287 GBP/Oz and 215 GBP/Oz for iridium and ruthenium, respectively),[15] and the unfavourable toxicity profiles are all detracting features that present barriers to wider and larger scale adoption of photocatalysis.[16–18]

To address these problems, PCs based on either Earth-abundant metal complexes, previously reviewed by us and others,[19,20] or organic fluorescent compounds[6] have been developed. Organic PCs are generally inexpensive, possess lower toxicity profiles than transition metal complexes and are widely available.[21] A broad range of organic PCs have now been studied. Notable examples

Table 1 Redox potentials and selected photophysical properties of 4CzIPN and common visible light photocatalysts[a]

Photocatalyst	λ_{abs}/nm	λ_{PL}/nm	$E_{0,0}$/eV (kJ mol^{-1})	E_{ox}/V	E_{red}/V	E_{ox}*/V	E_{red}*/V	τ/ns	Ref.
4CzIPN	435	535	2.67 (258)	1.52	−1.21	−1.04	1.35	18.7 τ_{pf} 1390 τ_{df}	60, 114 and 119–121
fac-Ir(ppy)$_3$	375	518	2.75[f] (265)	0.77	−2.19	−1.73	0.31	1322	14, 122 and 126
$[Ir(ppy)_2(dtbbpy)]PF_6$	410	581		1.21	−1.51	−0.96	0.66	557	122, 123, 127 and 128
$[Ir(dF(CF_3)ppy)_2(bpy)]PF_6$	405	473	2.20[f] (212)	1.69	−1.37	−1.00	1.32	2280	11 and 122
$[Ir(dF(CF_3)ppy)_2(dtbbpy)]PF_6$	380	470	2.77[f] (267)	1.69	−1.37	−0.89	1.21	2300	11 and 122–124
$[Ir(dF(Me)ppy)_2(dtbbpy)]PF_6$	360	512	2.97[f] (287)	1.49	−1.44	−0.97	0.92	1187	123 and 128
$[Ir(F(Me)ppy)_2(dtbbpy)]PF_6$		543	2.44[f] (235)	1.33	−1.50	−0.77	0.94	1100	123
$[Ru(bpy)_3](PF_6)_2$	452	615	2.10[f] (203)	1.29	−1.33	−0.81	0.77	1100	12 and 53
[Acr-Mes]ClO$_4$	430	570	2.65 (256)		−0.57		2.08	6.4 τ_S 30 000 τ_T	23, 107 and 129
Eosin Y	520[c]	537[d]	2.31[c] (223)	0.78[b]	−1.06[b]	−1.11[b]	0.83[b]	2.10[c] τ_S 160 000[d] τ_T	118 and 130–134
Rose Bengal	558	576	2.17[c] (209)	0.84[c]	−0.99[c]	−0.96[c]	0.81[c]	2.38 τ_S 2400[e] τ_T	132 and 135–137

[a] All potentials are given in V *versus* SCE. $E_{ox}^* = E_{ox} - E_{0,0}$ and $E_{red}^* = E_{red} + E_{0,0}$. 1 eV = $(1.602 \times 10^{-22}$ kJ$) \times N_A$ where N_A = Avogadro's constant. λ_{abs} refers to the absorption maximum of the lowest energy absorption band. λ_{PL} refers to the photoluminescence maximum. $E_{0,0}$ values given correspond to the optical gap to the S_1 state unless otherwise noted. τ_{pf}, τ_{df}, τ_S and τ_T are the prompt fluorescence lifetime, the delayed fluorescence lifetime, the singlet excited state lifetime and the triplet excited state lifetime, respectively. Data reported in MeCN at room temperature unless otherwise noted. [b] Determined in CH_3CN:H_2O (1 : 1). [c] Determined in methanol. [d] Determined in H_2O. [e] Determined in 10^{-4} M NaOH in an air saturated sample. [f] Corresponds to the optical gap to the T_1 state.

include acridinium salts[22,23] and organic dyes such as eosin Y,[24,25] fluorescein[26,27] and rose bengal[28,29] (*cf.* Fig. 9 and 10), which all have moderate redox windows making them suitable in photoredox catalysis (Table 1).[28] In multiple cases, these organic PCs have been shown to outperform their transition metal-based counterparts,[30–34] although their limitations must still be considered. Lengthy and often complex syntheses may be required to produce the PC, which can reduce its desirability to industry. Moreover, there have also been reported problems with separation and low recyclability when using organic PCs.[35] One of the main disadvantages with organic PCs is the limited flexibility in terms of tuning their redox potentials in comparison to transition metal complexes, whereby modification of the ligands generally permits a wide tuning of the redox properties.

Although these phosphorescent and fluorescent compounds have been well documented in the literature as PCs, beyond their ground and excited state redox potentials, their intrinsic photophysical properties have often been neglected when gauging their effectiveness as PCs. These compounds differ greatly in terms of available excited states, and thus their ability as PCs is quite different. Thus, a fundamental understanding of their photophysics must first be considered.

General photophysics of luminescent compounds

In photocatalysis, the first fundamental step involves formation of the excited PC, whereby a photoinduced transition from the ground state to an excited state must occur. The rate and feasibility of radiative transitions are dependent on the spin, vibrational and electronic wavefunctions of the initial and finial electronic states. The probability of transitions to/from these states are reflected in the oscillator strength, f, which takes into account orbital, vibrational and spin configuration factors and varies between 0 and 1.[36]

For spin considerations, only transitions between states of equivalent spin are formally allowed (spin selection rule), although this can be relaxed through spin orbit coupling (SOC).

The dependence of the vibrational wavefunctions is in accordance with the Frank–Condon factor, F, defined in eqn (2), where $\Psi_{\mathrm{vib,f}}$ and $\Psi_{\mathrm{vib,i}}$ are the final and initial vibrational wavefunctions, respectively. This gives the transition probability, which for absorption reflects the transition from the zeroth vibrational level of the ground state to the mth vibrational level of the excited state. A greater overlap of the vibrational wavefunctions will lead to a greater probability that the transition occurs.

$$F = \left|\langle \Psi_{\mathrm{vib,f}} | \Psi_{\mathrm{vib,i}} \rangle\right|^2 \quad (2)$$

The electronic factor dictates the overall intensity of the transition and is proportional to the overlap of the initial and final state wavefunctions, as well as the transition dipole moment.

Therefore, to maximize the probability of a transition, the spin must be conserved, the vibrational and electronic wavefunctions of the initial and final states should each overlap strongly and a change in symmetry must occur. The more probable an absorption transition, the greater the associated molar absorptivity, ε, a beneficial factor to the efficiency of a photocatalytic process.

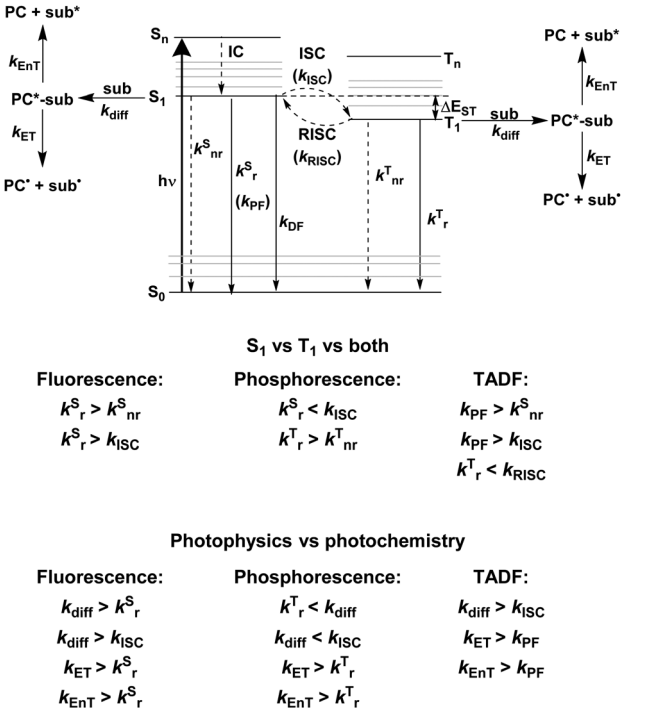

Fig. 2 Jablonski diagram for luminescent compounds alongside possible photochemistry routes of the excited states. The prototypical rate constants for defining the dominant photoactive excited state for fluorescent, phosphorescent and organic TADF compounds are given alongside the required rate constants for productive photocatalysis, where k_{EnT} and k_{ET} are the rate constants for energy and electron transfer, respectively, k_{diff} is the rate constant for diffusion, k^S_{nr} and k^S_r are the rate constants for non-radiative and radiative decay, respectively, from the singlet state, k^T_{nr} and k^T_r are the non-radiative and radiative decay, respectively, from the triplet state and k_{PF} and k_{DF} are the rate constants for prompt and delayed fluorescence, respectively.

Fig. 2 shows a Jablonski diagram outlining many of the different photophysical and photochemical processes available to the excited PC. The probable pathways for each of fluorescent, phosphorescent and TADF PCs depend on the relative magnitudes of the rate constants for each class of PC. The photophysical processes shown in Fig. 2 are mononuclear; however, the photocatalysis implicates bimolecular reactions. Promotion of an electron from the closed shell singlet ground state, S_0, to a higher-level singlet excited state, S_n, occurs upon photoexcitation, with the initially accessed excited state based on the energy of the excitation source. Rapid vibrational relaxation and internal conversion (IC) occur typically within picoseconds, causing the excited electron to populate the lowest vibrational level within the lowest singlet electronic excited state, S_1, in accordance with Kasha's rule.[37] Radiative decay, in the form of fluorescence, or non-radiative decay can ensue from S_1 to regenerate the ground state, which are both spin-allowed processes, hence the lifetime of molecules in the S_1 state is short, on the order of a few nanoseconds. Intersystem crossing (ISC) can also occur from S_1 to the triplet manifold, although this a formally spin-forbidden process (see below for a detailed discussion of ISC rates). Subsequent IC results in population of

the lowest triplet excited state, T_1, which can decay radiatively (*via* phosphorescence), or non-radiatively to the ground state, both of which are spin-forbidden processes. On account of the formally spin-forbidden nature of these decay process from the T_1 state, the triplet excited state is typically much longer-lived, with a lifetime on the order of microseconds.

These are the available photophysical processes of all compounds, with the dominating processes depending upon the intrinsic properties and structure of the molecule in question and will be discussed in detail in the following sections. The rate constant for diffusion, k_{diff}, to form an encounter complex, corresponds to the first step in a photochemical reaction, and as previously mentioned, is a bimolecular process on the order of 10^9 M^{-1} s^{-1}.[38] An encounter complex can be formed between the substrate and either $^1PC^*$ or $^3PC^*$. Which encounter complex is most likely, is dependent upon the magnitude of the inter-system crossing rate constant, k_{ISC}. When $k_{ISC} < k_{diff}$, this implies the singlet excited state of the PC is involved in encounter complex formation, while when $k_{ISC} > k_{diff}$, the triplet excited state of the PC participates. It is also possible that $k_{ISC} \sim k_{diff}$, in which case both $^1PC^*$ or $^3PC^*$ are available to participate in the photochemistry. Upon formation of the encounter complex, subsequent electron and energy transfer can occur, with relative rate constants of k_{ET} and k_{EnT}, respectively. These must occur sufficiently fast to outcompete alternative radiative and non-radiative decay pathways from the excited PC.

To ensure that photochemistry occurs (PET and/or PEnT), the associated rates for these processes must outcompete those of alternative photophysical pathways. To simplify the analysis of competing pathways, it can be helpful to use a PC with a high photoluminescence quantum yield, Φ_{PL}, (eqn (3)), where in this limiting case only the radiative decay rate constant, k_r^S or k_r^T, need be considered as a competing pathway as either will outcompete k_{nr}. This simplifies the analysis as the only competitive pathway for PET and PEnT that must be considered is radiative decay, which can be experimentally determined through emission lifetime measurements. The rate of radiative decay must still be slow compared to k_{ET} and k_{EnT}. However, a high PLQY is not a necessity for a compound to be a useful PC. Ultimately, as long as k_{ET} and k_{EnT} are faster than all other mononuclear decay processes, radiative or non-radiative, then photocatalysis is kinetically feasible.

$$\Phi_{PL} = \frac{\text{photons emitted}}{\text{photons absorbed}} \tag{3}$$

The rate constant k_{ISC} is key to determining whether $^1PC^*$ or $^3PC^*$ is involved in the subsequent photocatalysis, the importance of these states will be discussed in the photocatalysis mechanism section. As ISC is a formally spin-forbidden process, it is important to understand the factors that moderate the kinetics of this pathway.

Spin-forbidden transitions are only possible when state mixing occurs. This transpires with the aid of spin orbit coupling (SOC), which is a relativistic effect.[39] SOC occurs through coupling of the total spin angular momentum, $\vec{S}$, and total orbital angular momentum, $\vec{L}$, to yield a total angular momentum, $\vec{J}$, defined by the vector sum in eqn (4).[40] Since the total angular momentum must be conserved during a transition, a change in $\vec{S}$ can be compensated for through a corresponding change in $\vec{L}$, to allow for $\vec{J}$ to remain constant. This allows for the spin flip of an electron, required for processes such as ISC, RISC or phosphorescence to be feasible. Hence, a formally spin-forbidden process becomes possible through the perturbation of singlet and triplet state wavefunctions, which is made possible by SOC.

$$\vec{J} = \vec{S} + \vec{L} \tag{4}$$

The importance of SOC is manifested in terms of El Sayed's rule,[41] which imposes a symmetry change between the S_n and T_n state in order to facilitate spin-forbidden ISC. This rule was initially developed to describe ISC in carbonyl compounds and states that there must be a change in orbital angular momentum in concert with the change in spin. This implies that rates of spin-forbidden processes, such as ISC, become faster when there is a greater difference in orbital symmetry of the excited states. For example, $^1(\pi\text{–}\pi^*) \rightarrow {}^3(n\text{–}\pi^*)$ is fast while $^1(\pi\text{–}\pi^*) \rightarrow {}^3(\pi\text{–}\pi^*)$ is formally forbidden. However, it should be noted that this rule assumes the involvement of pure electronic states in a static nuclear configuration.

Within the El Sayed framework, there is the intrinsic spin–orbit coupling constant associated with each atom involved in the transition. As the mass of the atom increases, so does the magnitude of the SOC; this is known as the heavy atom effect. The degree of state mixing is also dependent on the energy difference between the two states, as shown in eqn (5). The first order mixing coefficient between the S_1 and T_1 states, λ, is proportional to both the direct spin–orbit coupling (H_{SO}) (which is itself proportional to the fourth power of the atomic number (Z) of atoms involved in the S_1 and T_1 transitions divided by the third power of the principal quantum number (n)), and on the aforementioned difference in orbital symmetry between the two states, and inversely proportional to the energy gap between the S_1 and T_1 states, ΔE_{ST}.

$$\lambda \propto \frac{H_{SO}}{\Delta E_{ST}} \propto \frac{Z^4}{n^3} \tag{5}$$

This description of state mixing is suitable for static nuclear configurations. When vibrational motion is taken into account, both spin-vibronic coupling and SOC must be considered. This can be done using second-order perturbation theory, which involves both spin–orbit and non-adiabatic coupling, with additional intermediate state(s) mediating the coupling.[42,43] This provides a route for El Sayed-forbidden ISC to occur between S_1 and T_1. These factors play a role, to varying degrees, to explain the importance of ISC as a potentially competing pathway in Fig. 2 for fluorescent, phosphorescent and thermally activated delayed fluorescence (TADF) compounds.

An additional consideration to be made is the nature of the excited state. For organic compounds, there are two predominant types of excited states: locally excited (LE) or charge transfer (CT). In the former, the electron density distribution is retained in the same area of the molecule during the transition, which usually

involves the promotion of an electron from a π-orbital to a π*-orbital in a symmetry-allowed transition. In the latter, the electron density distribution is displaced from one part of the molecule, the donor moiety, to another, the acceptor moiety. Here, the overlap of the orbitals involved in the symmetry-allowed transition is smaller and so the probability of the transition is lower, reflected in the smaller molar absorptivity values observed in the absorption spectrum of the compound.

Transitions to/from LE states usually occur with a higher oscillator strength in comparison to the CT state, since transitions to/from LE states exhibit a greater amount of orbital overlap. Accordingly, LE absorptions will have a greater ε, and from this, may seem like the preferential state to access in terms of photocatalysis. However, these LE states are typically shorter-lived than CT states owing to their larger radiative rate constants, k_r, according to Fermi's golden rule.[44,45]

There are of course some exceptions to the relative behaviour of LE and CT states typically observed, which presuppose that both transitions are symmetry-allowed. Pyrene is a notable example where transitions to/from the LE state (a $S_0 \rightarrow S_1$ transition) of this rigid organic molecule are weak despite strong spatial overlap of the relevant orbitals. This is due to the similar symmetries of the HOMO and LUMO wavefunctions, which results in a symmetry-forbidden transition that is reflective of the low oscillator strength ($f = 0.0016$ in *n*-heptane).[46] Consequently, a weak fluorescence is observed with a much longer radiative decay rate ($k_r \approx 10^6\ s^{-1}$).[47] A long-lived excited state is preferable in terms of photocatalysis, as if the LE (or CT) state decays quicker than the rate at which an encounter complex can form, productive photocatalysis cannot occur. Therefore, although generally the longer-lived CT states would be more advantageous than the shorter-lived LE states for photocatalysis, the example of pyrene illustrates that LE states are not always short-lived. Thus, emission lifetimes should be explicitly determined to assess whether the excited state of the compound is sufficiently long-lived for it to act as a photocatalyst.

Further, the energy of the CT state (but not the LE state) can be significantly influenced by the polarity of the medium. The size of the Stokes shift in a particular solvent, and hence the available energy to initiate the photocatalysis, becomes dependent on whether the excited state is LE or CT in nature. For most of the PCs discussed, the CT excited states have a larger associated transition dipole moment (TDM) in comparison to the permanent dipole moment associated with the ground state. In these cases, increasing polarity of the medium is associated with a more stabilized CT excited state, reflected in a red-shifted emission (positive solvatochromism).[48] The energy of LE states is relatively independent of medium as there is no large TDM, hence the Stokes shift will be small. In the context of photocatalysis, a smaller Stokes shift would be preferred as this indicates that most of the energy absorbed is available for the photochemistry.

This behaviour is present in not only organic compounds, but also organometallic complexes with excited states with CT character, such as metal to ligand charge transfer (MLCT) or a ligand to metal charge transfer (LMCT) states.

Consideration of these fundamental photophysical concepts is important when discussing the pros and cons of each sub-category of compounds used in the literature as PCs.

Fluorescent compounds as photocatalysts

The vast majority of fluorescent compounds are organic molecules, with photophysical processes occurring as described by Fig. 2. Fluorescence, in almost all cases, occurs from the S_1 state (adhering to Kasha's rule), hence, is independent of the excitation wavelength. For fluorescence to be detected, the non-radiative decay rate originating from S_1 must not be more than three orders of magnitude greater than k_r; with k_{nr} two orders of magnitude faster than k_r, emission will appear very faint.[49]

The rate constants that typically define a successful fluorescent PC are shown in Fig. 2. Fluorescent compounds possess slow k_{ISC} and so there is little to no population of the T_1 state. This is a generalised statement, typically organic fluorescent compounds have k_{ISC} in the region of $10^6\ s^{-1}$.[50–52] Assuming the rate constant for fluorescence is faster than k_{ISC}, fluorescence is the only radiative decay process possible.

For productive photocatalysis, diffusion of the excited PC to form the encounter complex must ensue and be faster than k_r^S (and k_{ISC} and k_{nr}^S) to allow for bimolecular reactions to compete with monomolecular photophysical decay pathways of the excited state. Typically, if the lifetime of the singlet excited state is less than 1 ns, the compound will not be useful as a PC as the compound will fluoresce before diffusion to the substrate can occur.[6] Upon formation of the encounter complex, k_{ET} and k_{EnT} must then be sufficiently fast to occur prior to dissociation of the encounter complex and to outcompete alternative decay pathways for the excited PC in terms of radiative and non-radiative decay.

Phosphorescent compounds as photocatalysts

Phosphorescent compounds are typically transition metal complexes. The presence of the central metal allows for these compounds to readily access the triplet excited state on account of the heavy atom effect. This increases the magnitude of the SOC, in accordance with eqn (5), and relaxes the spin-forbidden nature of the ISC. As a result, rapid population of the T_1 state occurs, which is long-lived with τ_{PL} typically on the order of microseconds.

In most low oxidation state transition metal complexes surrounded by π-accepting ligands, absorption of a photon typically results in promotion of an electron from a metal d-orbital to a ligand π* orbital,[53,54] which describes a MLCT transition and is symmetry-allowed. Rapid ISC from the singlet to the triplet MLCT state requires these states to have different symmetry for a direct transition to be allowed, for example when the π* orbital is the same, but the d-orbital is different.[55] When the two MLCT states have the same symmetry, an intermediate state of different symmetry must instead mediate the ISC. Typically, ISC occurs from the S_1 state with $^1d\pi^*$ character, to a higher lying triplet state, T_n, as S_1 and T_1 have analogous electronic transitions, hence the ISC is symmetry-forbidden.[55] Since ISC is usually very fast, ($\sim 10^{10}$–$10^{12}\ s^{-1}$ regime for complexes with strong MLCT character in the excited state),[55,56] k_{ISC} therefore outcompetes k_r^S by several orders of magnitude.

The presence of the heavy metal contributes to near unity intersystem crossing quantum yield, Φ_{ISC}, being frequently observed.[57] Thus, the rapidly generated, long-lived ^{3}MLCT state is the only accessible excited state when considering the subsequent photochemistry. This implies that $k_{ISC} > k_{diff}$; however, k_{diff} must be faster than k_r^T and k_{nr}^T to allow for formation of the encounter complex. As these latter two rate constants are typically much slower, this is not an issue. Subsequent k_{ET} and k_{EnT} must also be fast processes with respect to other decay pathways of the excited PC.

TADF compounds as photocatalysts

A third class of homogeneous PCs that can be used are TADF compounds. Although examples of organic, organometallic and inorganic TADF compounds have each demonstrated photocatalytic behaviour,[58,59] this review focuses solely on the use of the organic analogues.

The S_1 state is rapidly populated upon photoexcitation. Radiative decay can then occur by direct fluorescence, known as prompt fluorescence (PF), with a lifetime of τ_{pf} on the order of nanoseconds, analogous to that observed for normal fluorescent compounds. Alternative competing pathways include non-radiative decay back to the ground state or ISC to the triplet manifold followed by IC such that the electron populates the lowest triplet excited state, T_1. Phosphorescence from this state remains a spin-forbidden process and so is typically not observed at ambient temperatures in these molecules (due to large $\Delta E_{S_0T_1}$, *cf.* eqn (5)); however, reverse intersystem crossing (RISC) from T_1 back to S_1 is possible at ambient temperatures due to the small singlet–triplet energy gap, ΔE_{ST}, between the lowest lying singlet and triplet excited states that can be overcome thermally, resulting in delayed fluorescence (DF), which occurs on a time scale of similar order to phosphorescent complexes, typically in the microsecond regime.[60] RISC can also be mediated by spin-vibronic coupling, as discussed earlier (Fig. 3). As shown in Fig. 2, the rate constant for prompt fluorescence, k_{PF}, is greater than k_{ISC} (and k_{nr}^S), which explains why prompt fluorescence is observed. Delayed fluorescence occurs as k_{RISC} is faster than both k_r^T and k_{nr}^T.

For organic TADF compounds k_{ISC} is typically $<10^7$ s^{-1},[56] although this value can vary widely depending on the individual compound. For this class of compounds $k_{ISC} < k_{diff}$, hence PET and PEnT are most likely to occur from the S_1 state. For TADF compounds in which faster k_{ISC} rates are observed, this opens the availability of the triplet manifold to participate in photocatalysis. When this is the case, the relative populations of the singlet and triplet excited states, which are dependent on the quantum yields of prompt, Φ_{PF}, and delayed fluorescence, Φ_{DF}, respectively, become significant in identifying the probablity of PET and PEnT from each state.

The excited state from which the photocatalysis occurs is directly dependent on both k_{ISC} and k_{RISC} in TADF PCs. The rates associated with ISC/RISC are, to a first approximation, understood through the relation disclosed in eqn (5), where the rate constants are dependent upon both H_{SO} and ΔE_{ST}.

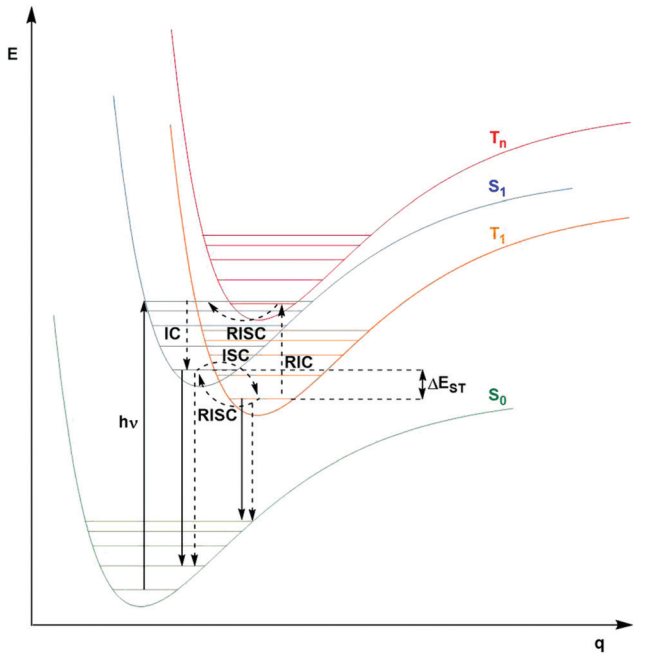

Fig. 3 Modified Jablonski type diagram with Morse potentials, showing the photophysical processes of TADF molecules including photon absorption, radiative (solid arrow) and non-radiative (dashed arrow) decay, internal and reverse internal conversion (IC and RIC, respectively), intersystem and reverse intersystem crossing (ISC and RISC, respectively) along nuclear coordinate, q.

Organic TADF compounds distinguish themselves by possessing a small ΔE_{ST}, typically less than 0.3 eV,[61] which is the primary factor that governs the degree of the mixing of states.[62] The ΔE_{ST} itself is proportional to the exchange integral, J, between the excited singlet and triplet states, according to eqn (6).[61,63] The exchange integral is dependent on the orbital overlap of the frontier molecular orbitals involved in the transitions to S_1/T_1 (eqn (7)), where Φ and Ψ are typically the highest occupied molecular orbital (HOMO) and lowest unoccupied molecular orbital (LUMO) wavefunctions, respectively, as these are involved in the S_0–S_1 and S_0–T_1 transitions, and e is the electron charge.

$$\Delta E_{ST} = E_S - E_T = 2J \quad (6)$$

$$J = \iint \Phi(r_1)\Psi(r_2)\left(\frac{e^2}{r_1 - r_2}\right)\Phi(r_2)\Psi(r_1)\mathrm{d}r_1\mathrm{d}r_2 \quad (7)$$

From eqn (7), it becomes clear that by minimising the overlap of the electron density distribution between the HOMO and LUMO, a reduction in J will be observed and hence a small ΔE_{ST} will be obtained.[61] Spatially separated and electronically decoupled donor–acceptor compounds in which there are large torsions between the donor and acceptor groups are thus the most commonly employed molecular design strategies invoked in TADF emitters, in which the HOMO and LUMO are localised on the donor and acceptor units, respectively.[64]

Since the excited singlet state of TADF compounds is CT in nature, positive solvatochromism will be exhibited. Therefore, solvent choice should be considered when utilising these

compounds as PCs, as it will affect not only the excited state redox potentials, but also the relative competition between k_{ISC}/k_{RISC} and therefore from which state the PET or PEnT originates.

Photocatalysis mechanism

All three subcategories of luminescent compounds previously discussed; fluorescent, phosphorescent and TADF, have been successfully applied as photocatalysts in both PEnT and PET reactions. An understanding of their intrinsic photophysical properties is required in order to correlate the performance of the photocatalysts to their structure and to distinguish under which mechanism the photocatalysis takes place, a point which is all too often not adequately discussed in the photocatalysis literature.

PEnT photocatalysis

In the photoinduced energy transfer (PEnT) mechanism, the excited PC sensitises the substrate by direct energy transfer (Fig. 1). Upon acceptance of the embedded energy, the substrate is in an electronically excited state, allowing for the subsequent reaction to occur.[65] This energy transfer process can proceed *via* Förster or Dexter quenching mechanisms, which are both non-radiative decay processes.[66] The former involves dipole–dipole coupling interactions mediated through space, whereby the transition dipole moment on the donor (the excited PC) and the acceptor (the substrate) couple non-radiatively, generating the required electronic transition through relaxation of the donor and simultaneous excitation of the acceptor.[67] Since this mechanism is dipolar in nature, orbital overlap of the two species is not required, allowing for Förster resonance energy transfer (FRET) to occur over long distances (1–10 nm).[68] Spectral overlap of the emission of the donor and absorption of the acceptor species is instead crucial for this mechanism, as quantified in the overlap integral, J^F, in eqn (8), where f_D is the normalised donor emission spectrum, [($f_D(\sigma)$ is the photon exitance of the donor at wavenumber σ], $\varepsilon_A(\sigma)$ is the molar extinction coefficient of the acceptor at wavenumber σ, and σ is the wavenumber.[69,70]

$$J^F = \int_0^\infty \frac{f_D(\sigma)\varepsilon_A(\sigma)}{\sigma^4} d\sigma \quad (8)$$

The distance dependence associated with FRET in indicated in eqn (9), which shows the dependence of the rate constant of FRET, k_{FRET}, on both the spectral overlap integral and the donor–acceptor distance, R_{DA}.[67] The $(R_{DA})^{-6}$ distance dependence of FRET allows for this energy transfer to still be possible at longer distances. In eqn (9), κ^2 is the orientation parameter, n is the refractive index of the medium, N_A is Avogadro's constant and $\tau_r^0(D)$ is the lifetime of the donor in the absence of the acceptor.

$$k_{FRET} = \frac{9000\ln(10)\kappa^2}{128\pi^5 n^4 N_A \tau_r^0(D)(R_{DA})^6} J^F \quad (9)$$

By contrast, the Dexter energy transfer (DET) mechanism typically involves simultaneous intermolecular electron exchange between the excited state of the donor, the excited PC, and the ground state of the acceptor, the substrate.[71] The DET mechanism is electric-dipole forbidden on account of the change in the local spin state of the excited donor and acceptor, which disables the FRET mechanism.[72]

For DET, orbital overlap is essential, which is achieved through collisional interaction for bimolecular PEnT mechanisms. To aid this orbital overlap, easily accessible spin density on the excited PC is beneficial, which is linked to the shape of the PC. Spectral overlap of the emission of the donor (phosphorescence) and absorption of the acceptor (singlet to triplet absorption) is likewise important, which is calculated according to eqn (10) for DET, where f_D is the normalised donor emission spectrum and ε_A is the normalised acceptor absorption spectrum.[66,70] Unlike Förster PEnT, which requires spectral overlap of spin-allowed transitions, for Dexter PEnT the spectral overlap required is for spin-forbidden transitions and so the overlap integral is inherently smaller in this case.

$$J^D = \int_0^\infty f_D(\sigma)\varepsilon_A(\sigma) d\sigma \quad (10)$$

The absence of information on spin-forbidden transitions for many organic substrates means that assessing whether spectral overlap occurs becomes challenging. In light of this, the energy of the triplet state, E_T, of the donor (the photocatalyst) relative to the acceptor (the substrate) is instead used to provide an estimation of the thermodynamic feasibility of the energy transfer mechanism.[66] The criterion for an exergonic energy transfer thus is E_T (D) > E_T (A). In this instance, it is assumed that J^D is large, which correlates to a faster rate of DET according to eqn (11), where R_{DA} is the donor–acceptor distance, K is the parameter for specific donor and acceptor orbital interactions and L is the sum of the van der Waals radii of the donor and acceptor.[71]

If, however, E_T (D) < E_T (A), then energy transfer from donor to acceptor is only possible if the donor, in its vibrationally/rotationally excited state of its electronically excited state, is higher in energy than the acceptor in its electronic excited state. Spectral overlap between the emission of the donor and the absorption of the acceptor remains a criterion for energy transfer.

The main drawback of the Dexter mechanism is that it is limited to shorter distances of typically no more than 10 Å due to the exponential dependence of the energy transfer rate with donor–acceptor distance, eqn (11).[73] Comparing the two energy transfer mechanisms, both FRET and DET require spectral overlap for the energy transfer to occur; however, the latter also requires orbital overlap as it is a double electron exchange mechanism. For bimolecular mechanisms, since DET requires collisional interactions, higher reactant concentrations are beneficial for this mechanism, while FRET can operate efficiently at lower concentrations.[69] At all but the shortest donor–acceptor distances, FRET will be faster than DET, due to the $R_{DA}{}^{-6}$ distance dependence of FRET (eqn (9)) in comparison to the exponential distance dependence of DET (eqn (11)).

$$k_{DET} = KJ^D e^{\frac{-2R_{DA}}{L}} \quad (11)$$

At larger distances, FRET occurs at a faster rate and is consequently the dominant PET mechanism while DET only

becomes the dominant pathway when FRET is not allowed. Regardless of which PEnT mechanism is in operation, a sufficiently fast rate of energy transfer is required in order to outcompete other radiative and non-radiative decay pathways available to the excited PC. Similarly, for exergonic energy transfer, both mechanisms require the excited state energy of the donor to be greater than that of the acceptor.

The nature of the FRET and DET mechanisms mean compounds with a predominately photoactive singlet state, namely fluorescent compounds, undergo energy transfer through a FRET mechanism while phosphorescent compounds, whose photophysics relies on triplet excited states, undergo DET, since the FRET mechanism would result in breaking of the spin conservation rule of Wigner.[66,74]

Some energy transfer photochemistry proceeds *via* the singlet excited state of the substrate while other photochemistry requires accessing the triplet excited state of the substrate, and the precise nature of the photochemical reaction must be considered when designing a PC that can participate in PEnT photocatalysis. For example, in the Paternò–Buchi [2+2] cycloaddition reaction of 2,3-dihydrofuran with different aromatic carbonyls (Fig. 4), the nature of the excited state of the carbonyl impacts upon the diastereoselectivity of the reaction. Naphthaldehydes react through excited singlet states while benzaldehydes (such as mesitylaldehyde), react through excited triplet states.[75]

Another example of the importance of singlet state photochemistry is the Norrish–Yang photocyclization.[76] When using an alanine derivative, and in the presence of a triplet quencher, the cyclization proceeds through a helically chiral singlet biradical, conveying a "memory of chirality" effect to the product.[77] If the reaction proceeds in the absence of a triplet quencher, the longer-lived triplet biradical forms and this leads to racemization, destroying the enantioconservation.

Triplet state sensitisation occurs through the DET mechanism, typically forming triplet biradical intermediates. These tend to have lifetimes of the order of nanoseconds to microseconds, which is enough time to allow for single bond rotations to occur.[78] By contrast, singlet biradical intermediates, formed through a FRET mechanism, are much more short lived,[79] hence the configuration found in the starting material is retained in the product. High enantioconservation is thus typically observed with singlet photochemistry.[80–82] This is also possible with triplet biradical intermediates which only slowly interconvert.[83,84]

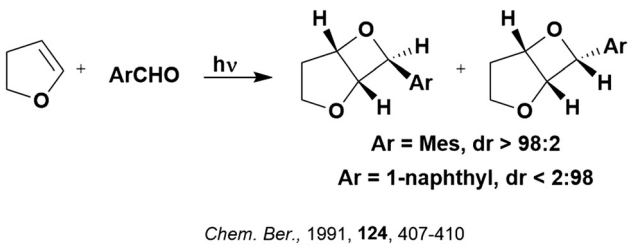

Chem. Ber., 1991, **124**, 407-410

Fig. 4 Reaction scheme for the Paternò–Buchi [2+2] cycloaddition reaction of 2,3-dihydrofuran with different aromatic aldehydes.

The benefit of TADF compounds is that they have the potential to access both FRET and DET pathways. However, since k_{ISC} is typically slower than k_{diff}, DET from the triplet state is inefficient for organic TADF compounds, much more so than for phosphorescent complexes. The capacity for organic TADF compounds to participate in triplet DET is dependent on the intersystem crossing quantum yield, Φ_{ICS}, which describes the population of PCs in their triplet excited states.[85] Under the constant irradiation conditions employed in photocatalysis and given the long delayed lifetimes of most organic TADF PCs, there is sufficient population of triplet excitons to permit triplet sensitization reactions by organic TADF PCs. Additionally, it should be noted that DET is not limited to PEnT from triplet states, and can indeed occur from the singlet excited state.[86] Since TADF compounds have singlet excited states that are accessible for subsequent photochemistry, this opens the pathway for DET energy transfer to occur from this state.

Undoubtedly, TADF compounds can access the FRET pathway, a mechanism exploited in the sensitization of fluorophores by TADF compounds, coined Hyperfluorescence™, that has been exploited in OLED developement.[87] Accessing the FRET mechanism is beneficial in photocatalysis as it allows the reaction to occur over much longer distances, implicating lower required concentrations. However, as stated above, this relies on the singlet radical intermediate formed being productive in forming the required product.

PET photocatalysis

Photoredox catalysis involves in nearly all cases single electron transfer (SET) processes. Photocatalysis proceeding by PET is more prevalent than by PEnT and the majority of the examples in this review proceed *via* photoredox catalysis. It is important to first understand both the thermodynamic and kinetic factors at play when discussing PET.

Upon absorption of light, the excited PC becomes both a stronger oxidising and reducing agent than in the ground state. It can then either be oxidatively or reductively quenched *via* SET (Fig. 1), depending on the relative energies of the molecular orbitals of the substrate compared to the PC. The PC, in its oxidized or reduced form, respectively, can then participate in a second SET that will close the photocatalytic cycle and regenerate the ground state of the photocatalyst. Typically, a sacrificial oxidant or reductant is employed to complete or initiate the photocatalytic cycle; however, if none is required then the process is considered redox neutral. Photoredox catalysis typically produces radical ion intermediates as a result of the SET, which are usually difficult to access using conventional chemical synthetic procedures.[88]

The redox properties of a PC define its oxidising and reducing power. The ground state reduction and oxidation potentials are defined as $E_{red} = (PC/PC^{\bullet -})$ and $E_{ox} = E(PC^{\bullet +}/PC)$, respectively, while the excited state reduction and oxidation potentials are given by $E_{red}{}^{*}(PC^{*}/PC^{\bullet -}) = E_{red}(PC/PC^{\bullet -}) + E_{0,0}$ and $E_{ox}{}^{*}(PC^{\bullet +}/PC^{*}) = E_{ox}(PC^{\bullet +}/PC) - E_{0,0}$,[6,9,89,90] where $E_{0,0}$ is the lowest energy electronic transition between the lowest vibrational states of the ground and first excited state, otherwise known as the

optical gap. In fluorescent compounds, this is defined as the intersection point between the normalized absorption and emission spectra of the PC, and typically involves a transition between the S_0 and S_1 states.[69] By contrast, in phosphorescent compounds, the $E_{0,0}$ is correlated with the triplet state energy, E_T, and is estimated from the onset of the phosphorescence spectrum.

According to Marcus theory, the redox potentials of the PC must be sufficiently oxidising or reducing to allow the required SET to occur. To permit the maximum reactivity it is therefore desirable that the PC have a wide redox window, both in the ground and the excited states. When proceeding *via* a reductive quenching cycle, the PC is described as a photooxidant. To ensure that oxidation of the substrate is thermodynamically feasible, ν must be more positive than E_{ox} of the substrate. By contrast, for an oxidative quenching cycle, the PC behaves as a photoreductant. In this case, E_{ox}^* must be more negative than E_{red} of the substrate for the reduction to take place.[6,9,19,89]

These criteria are encapsulated within the Gibbs energy of photoinduced energy transfer (eqn (12)),[9,89,91] which relates the change in the Gibbs free energy, ΔG^0, and hence the thermodynamically feasibility of the reaction, with the ground state redox potentials and the optical gap. In eqn (12), e is the electronic charge, $E^0(D^{\bullet+}/D)$ is the oxidation potential of the donor, $E^0(A/A^{\bullet-})$ is the reduction potential of the acceptor, ε_0 is the vacuum permittivity, ε is the dielectric constant of the solvent, r is the electron donor–acceptor distance and $E_{0,0}$ is the optical gap of the photoexcited species.

$$\Delta G^0 = e[E^0(D^{+\bullet}/D) - E^0(A/A^{-\bullet})] - \frac{e^2}{4\pi\varepsilon_0\varepsilon r} - E_{0,0} \qquad (12)$$

For the electron transfer to be thermodynamically allowed, ΔG^0 must be negative. Since the excited triplet state is lower in energy than the excited singlet state, the absolute ΔG^0 value for electron transfer from the triplet state is smaller than that from the singlet state. Taking this into consideration, this information can be applied to the kinetics of electron transfer, which is explained using the Marcus equation (eqn (13)).[10,92] Here, the rate of electron transfer, k_{ET}, is linked to the electronic coupling between the initial and final states, H_{if}, the reorganisation energy, λ, and ΔG^0.

$$k_{ET} = \frac{2\pi}{\hbar}|H_{if}|^2 \frac{1}{\sqrt{4\pi\lambda k_B T}} \exp\left\{-\frac{\left(+\Delta G^0 + \lambda\right)^2}{4\lambda k_B T}\right\} \qquad (13)$$

When ΔG^0 is equal to λ, this represents a situation in which the activation energy, $\Delta G^{\ddagger}$, is equal to zero and represents the maximum rate of the electron transfer. In the normal Marcus region, increasing the absolute value of ΔG^0 causes a decrease in $\Delta G^{\ddagger}$ and an increase in k_{ET}. However, in the inverted Marcus region, the opposite relationship is observed, whereby increasing the thermodynamic driving force, ΔG^0, actually causes a decrease in k_{ET} (and an increase in $\Delta G^{\ddagger}$). In PET from an excited compound to another reactant, namely the forward electron transfer, the normal Marcus region is in operation;[9,89] however, in back electron transfer the inverted Marcus region has been observed.[93–102] In the forward PET regime, in the highly exergonic region, the absence of the inverted region is thought to be related to λ, which increases in value on going from a contact radical ion pair to a solvent separated radical ion pair since the latter involves a greater distance between the radical ions.[103]

Considering only forward electron transfer first, since the absolute value of ΔG^0 is smaller when electron transfer occurs from the triplet state, the rate of electron transfer, according to eqn (13), is slower when arising from the triplet state rather than the singlet.[104,105] Recall that k_{ET} must be sufficiently fast to outpace unproductive decay pathways, both radiative and non-radiative. With these thermodynamic and kinetic factors in mind, the nuances in PET mechanisms of fluorescent, phosphorescent and TADF compounds can be understood. Since fluorescent compounds are usually dominated by singlet excited states, PET occurs from this state. For phosphorescent compounds, the triplet excited state is the assumed state from which electron transfer can occur. Despite k_{ET} being slower from triplet excited states, this does not present much of a problem in phosphorescent compounds since the T_1 states are so long-lived, reflecting slower radiative and non-radiative rates.

For TADF compounds, the situation is less clearly ascertained. Since TADF compounds are characterised by small ΔE_{ST}, ΔG^0 and consequently k_{ET} will be similar from both the singlet and triplet states, suggesting that there is negligible difference in electron transfer rates from these states when using TADF compounds as PCs.

Since k_{ET} is rate-limited by k_{diff}, it is therefore less than or equal to 10^9 s^{-1}. As this is faster than the typical k_{ISC} observed for organic TADF compounds ($<10^7$ s^{-1} [56]), the excited state involved in SET is likely to be the S_1 state. If k_{ISC} and k_{RISC} are fast in comparison to k_{ET}, then a steady-state approximation may be assumed, and the relative populations of singlet and triplet excited states will be governed by a Boltzmann distribution. The majority of excitons will thus exist in the triplet state, on account of its lower energy.[106] The exact populations of these states are determined by the respective quantum yields of the prompt and delayed fluorescence. SET under this scenario is thus more likely to occur from the $^3PC^*$.

Therefore, on account of the small ΔE_{ST} of TADF compounds, the reactivity and kinetics of PET from both singlet and triplet excited states are similar, hence from this point of view, both states would be equally productive in photoredox catalysis.

Back electron transfer (BET) can be a detrimental path in photocatalysis. As previously mentioned, BET has been shown to occur through the inverted Marcus region, whereby the rate of electron transfer increases with decreasing thermodynamic driving force. This is exemplified in the selective oxygenation of *p*-xylene to *p*-tolualdehyde, using 10-methyl-9-phenylacridinium perchlorate ([AcrPh]ClO_4), as the PC (Fig. 5).[107] The proposed mechanism involves PET from *p*-xylene to the singlet excited state of the PC, as supported by previous work from the same group.[108] Deprotonation of the resultant *p*-xylene radical cation occurs in competition with BET. When the former outcompetes the latter, a *p*-xylenyl radical is formed, which is trapped by oxygen, reduced by the reduced PC and decomposed to yield *p*-tolualdehyde selectively.

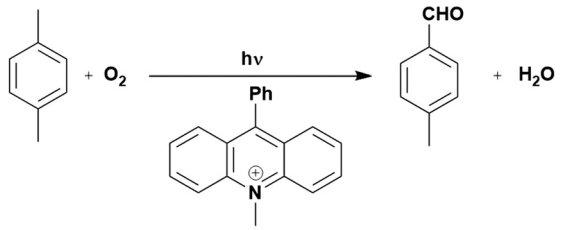

Org. Lett., 2000, **2**, 3647-3650

Fig. 5 Reaction scheme for the oxygenation of *p*-xylene to *p*-tolualdehyde.

In changing the solvent for this reaction from MeCN to chloroform, the yield of product increases despite a slower Stern–Volmer quenching rate constant observed (k_q = 8.6 × 10^9 M^{-1} s^{-1} and 4.2 × 10^9 M^{-1} s^{-1} for MeCN and chloroform, respectively). Since the reorganization energies (0.34 eV and 0.27 eV for MeCN and chloroform, respectively) are much smaller than the driving force of the back electron transfer (ΔG^0 = −2.36 eV when using [AcrH]ClO_4 as the PC), the back electron transfer falls within the Marcus inverted region. With decreasing solvent polarity, a slower back electron transfer rate is observed, and thus an increase in final product yield. This example highlights the impact of solvent selection on reaction yield when conducting photocatalytic reactions. Of course, the choice of PC is also important, if using [AcrPh]ClO_4 instead of [AcrH]ClO_4, the thermodynamic driving force increases (2.48 eV and 2.34 eV, respectively), resulting in slower BET and consequently higher yields.

Whether PET occurs from the S_1 or T_1 state may also have an impact on whether BET becomes an important non-productive pathway (Fig. 6). Upon SET transfer from a donor (D) to the excited PC in a reductive quenching mechanism, a radical ion pair (RIP) is formed (Fig. 6a). For successful photocatalysis, this RIP will then dissociate to form the free ions/radicals, which can then react productively to complete the reaction. An alternative unproductive mechanism for this RIP involves BET from the $PC^{\bullet-}$ back to the $D^{\bullet+}$, regenerating the ground state PC and the donor. A spin flip must occur for the electron during BET from the $PC^{\bullet-}$ to the $D^{\bullet+}$ when the PC has a triplet excited state, whereas this is not the case if the PC were in the singlet excited state. As a spin-forbidden process is required for BET when involving the ^{3}PC*, this makes the BET a much slower process, therefore making dissociation to the free ions the more favourable pathway.[109,110] For ^{1}PC*, the BET is a spin-allowed process, hence is much faster, and can provide significant competition to the productive dissociation pathway. Therefore, BET is likely to be least competitive when PET occurs from the triplet excited state of the PC. Moreover, PET from ^{3}PC* does not have to overcome the associated pairing energy penalty present when the PC is in the singlet excited state. A similar situation is shown in Fig. 6b, where an oxidative quenching mechanism is in operation. Assuming the rate determining BET occurs as shown in Fig. 6, then this signifies that BET becomes more problematic when the PC is in its singlet excited state rather; however, it should be noted that k_{BET} may not be a significant competing pathway to productive photocatalysis.

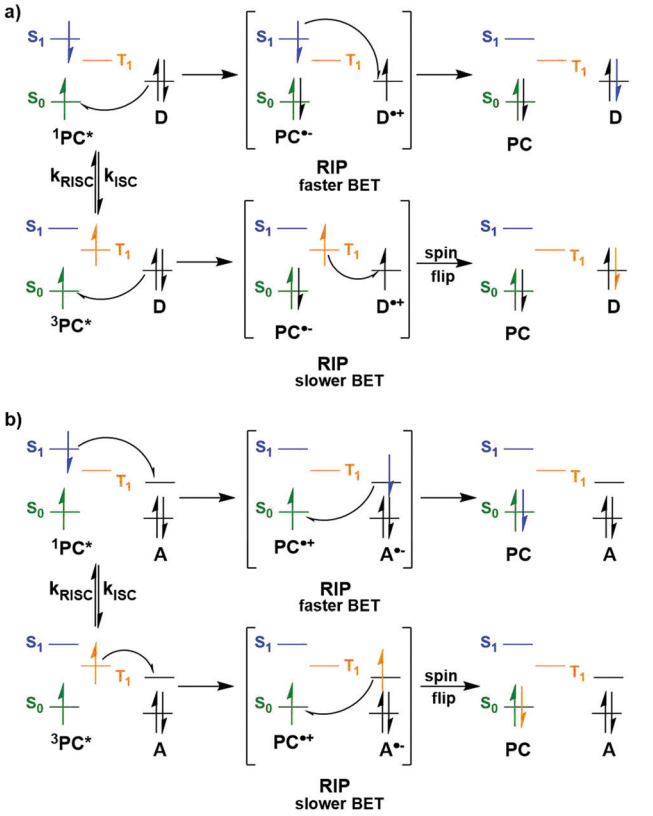

Fig. 6 Back electron transfer mechanisms for a) reductive quenching and b) oxidative quenching of the PC with donor (D) and acceptor (A) substrates.

Thus, both the energetics of the states and the nature of the excited state are important determinants for k_{BET}.

In diffusion-controlled photocatalysis processes, the triplet states are perhaps more attractive owing to their longer-lived excited states in comparison to singlet states. However, when assessing the potential thermodynamic driving force of a PC, the energy loss from the initial photon through processes such as IC and ISC within the PC must be considered. For example, for compounds with fast and efficient ISC, such as Ir(III) photocatalysts, an energy loss equivalent to ΔE_{ST} occurs to solvent (0.65–1.08 eV, 63–105 kJ mol^{-1}), resulting in a less potent PC.[111] Since the singlet state retains a larger component of the initial photon energy in comparison to the triplet state, it is *a priori* more desirable to access this state for photoredox catalysis. A recent study by Lupton *et al.* concluded that when the photocatalysis mechanism involves pre-association of the PC and the substrate, the long excited state lifetime of the PC no longer becomes an important feature since diffusion is not a limiting factor.[112] In this case, the authors propose electron transfer from the singlet state to be much more beneficial as a result of the lower available energy in triplet states in comparison to singlets.

A combination of all the aforementioned factors must be taken into consideration when evaluating whether electron transfer from the singlet or triplet excited states is preferable. Electron transfer from the singlet state is more exergonic according to

the Gibbs free energy and therefore will have faster electron transfer rates. However, utilisation of the triplet excited state means slower BET as well as having the advantage of a longer excited state lifetime, making electron transfer a more competitive pathway to radiative decay as k_r will be slower. Quantifying the relative rates of ISC and electron transfer is crucial to understanding which state is predominantly active in the SET. Notably, measurements of these kinetic parameters are rarely reported in photocatalysis investigations.

In-depth mechanistic consideration of the photoactive state of organic photocatalysts has seldom been reported, with this being non-existent for TADF PCs. A study from Kwon *et al.* focused on using TADF compounds as PCs in polymerisation reactions (see Section 7), implicating the triplet state as responsible for electron transfer,[113] although no evidence was provided to support this conjecture. As TADF compounds have accessible singlet and triplet excited states, SET from each is viable. At this point, it is unclear whether the nature of TADF compounds is particularly beneficial for facilitating photoredox reaction. Typically, the success of TADF (and indeed most) PCs are rationalised using only thermodynamic considerations by acknowledging their promising redox potentials in comparison to alternative photocatalysts.[114] Recently, the success of these compounds as PCs has been linked to their accessible CT states which, as previously mentioned, are significant in photoredox catalysis. This is seen in the hypothesis of Diebel *et al.* who suggested the presence of chlorine in **3CzClIPN** increases the charge transfer character of the excited states in comparison to **4CzIPN**, which may contribute to the former outperforming the latter in a recently demonstrated oxidation reaction.[115] While this observation may be true, there is no explanation provided as to how an increase in the CT character can translate into improved thermodynamics or kinetics for aiding the photocatalysis process.

Although the specific impact the TADF character of the PC has on its photocatalytic potential is unclear at present, what is evident is that TADF compounds have long excited state lifetimes, comparable to those of iridium and ruthenium PCs. Redox potentials of TADF compounds in both the ground and excited state are of comparable magnitude to those of heavy metal PCs, and the organic compounds have been shown to have in many cases enhanced molar absorptivity for the CT band compared to transition metal complexes. All of these are contributing factors to their success as PCs.

The significance of 4CzIPN in photocatalysis

The first TADF compound to be tested as a PC was eosin Y,[116] an organic dye that was one of the first organic compounds identified as showing TADF.[117] In fact, for many years TADF was known as E-type fluorescence, acknowledging eosin Y's historic link to this radiative decay process. The moderate redox potentials (E_{ox} = 0.78 V, E_{red} = −1.06 V, E_{ox}* = −1.11 V and E_{red}* = 0.83 V in MeCN:H_2O 1 : 1) as well as absorption in the visible region (λ_{abs} = 520 nm in MeOH), have contributed to the popularity of this commercially available and inexpensive dye being widely used as a PC.[25] However, to the best of our knowledge, no mention of its TADF character has ever been discussed in the context of its use in photocatalysis. Interestingly, it has been widely accepted that SET occurs from the triplet state of eosin Y,[6] owing to its large Φ_{ISC} as well as its extremely short singlet excited state lifetime (2 ns in MeOH),[118] which reduces the probability of interaction of the PC in this excited state with the substrate. The ability of eosin Y to act as a PC has been well documented previously and so will not be included within this review.

Of the articles published using TADF compounds as PCs, one TADF material, 2,4,5,6-tetra(carbazol-9-yl)benzene-1,3-dicarbonitrile, **4CzIPN**, first reported by Adachi *et al.* in 2012,[60] has been predominant (Fig. 7a). **4CzIPN** is composed of four carbazole electron-donor moieties and an isophthalonitrile that acts as the electron-acceptor component. The torsions of the carbazolyl groups from the plane of the dicyanobenzene are large due to steric interactions between adjacent carbazoles. This twisted conformation results in the HOMO and LUMO being localised on the donor and acceptor moieties, respectively, thus reducing the exchange integral between the two and ensures a sufficiently small ΔE_{ST} of 0.08 eV in toluene,[60] allowing for the necessary RISC to occur to make this compound TADF.

In polar solvents such as MeCN, the Φ_{ISC} is extremely low at 0.041, with k_{ISC} being 2.2 × 10^6 s^{-1}.[119] These data indicate minimal formation of triplet excitons and implies that the singlet excited state is the state from which subsequent photochemistry is likely to occur in this solvent. In apolar solvents like toluene, the value of Φ_{ISC} increases dramatically to 0.73. This clear difference in intersystem crossing quantum yields upon changes in medium highlights the significant role that solvent can play in modulating the photophysical and potentially the photochemical properties of a PC.

The photophysical and electrochemical properties of **4CzIPN**, summarised in Table 1, mimic quite closely those of the commonly used iridium complex [Ir(dF(CF_3)ppy)$_2$(dtbbpy)]PF_6 (Fig. 7b) [(dF(CF_3)ppy) = 2-(2,4-difluorophenyl)-5-trifluoromethylpyridinato and dtbbpy = 4,4′-di-*tert*-butyl-2,2′-bipyridine], as can be seen clearly in Fig. 8, and, as will become evident below, can serve as a useful replacement for the latter. Both compounds exhibit CT excited states. In **4CzIPN** this is manifested in a radical cation delocalised over the donor component and a radical anion associated with the isophthalonitrile acceptor unit. Similarly, in the mixed metal-to-ligand/ligand-to-ligand charge transfer excited

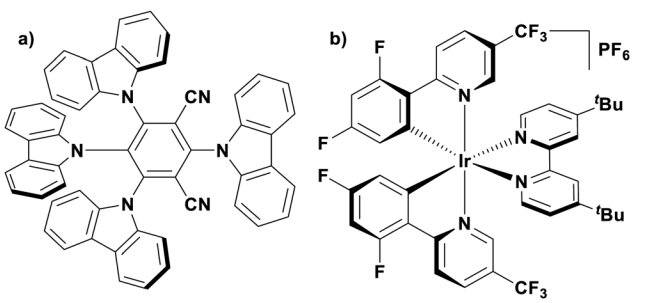

Fig. 7 Structures of (a) **4CzIPN** and (b) [Ir(dF(CF_3)ppy)$_2$(dtbbpy)]PF_6.

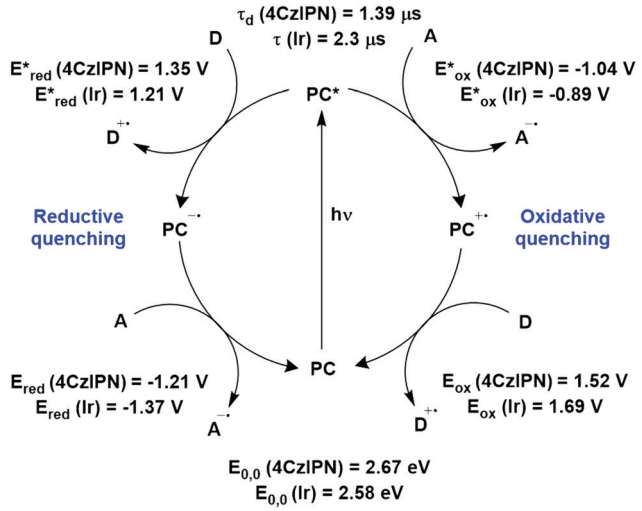

Fig. 8 Photocatalytic cyclic comparing selected photophysical and redox properties of 4CzIPN and $[Ir(dF(CF_3)ppy)_2(dtbbpy)]PF_6$ in MeCN.[11,60,114,119–124]

state of the iridium complex, the radical cation has $d\pi_{(dF(CF3)ppy)}$ character and the central metal can be considered to be oxidised to Ir(IV), while the dtbbpy ligand is reduced to its radical anion.

The excited-state redox properties of **4CzIPN** are particularly significant, making it a very strongly photooxidising and photoreducing photocatalyst in comparison to other commonly used visible light photocatalysts, as shown in Fig. 9 and 10.

One of the primary advantages of **4CzIPN** is its relatively low synthesis cost. The one-pot synthesis of **4CzIPN** from the corresponding dicyanotetrafluorobenzene *via* an S_NAr reaction translates to an approximate cost of \$5 per mmol for **4CzIPN** in comparison to \$935 per mmol for $[Ir(dF(CF_3)ppy)_2(dtbbpy)]PF_6$ (prices are in US\$ in 2020).[125] These values come from Wendlandt *et al.* in 2020,[125] who determined this cost based on the price of the reagents, solvent and energy as well as the product yield. Cost considerations, in addition to the lower toxicity profile, wide redox potentials, appreciable visible-light absorption ($\varepsilon = 6.2 \times 10^3$ M^{-1} cm^{-1} at 380 nm for $[Ir(dF(CF_3)ppy)(dtbbpy)]PF_6$ in

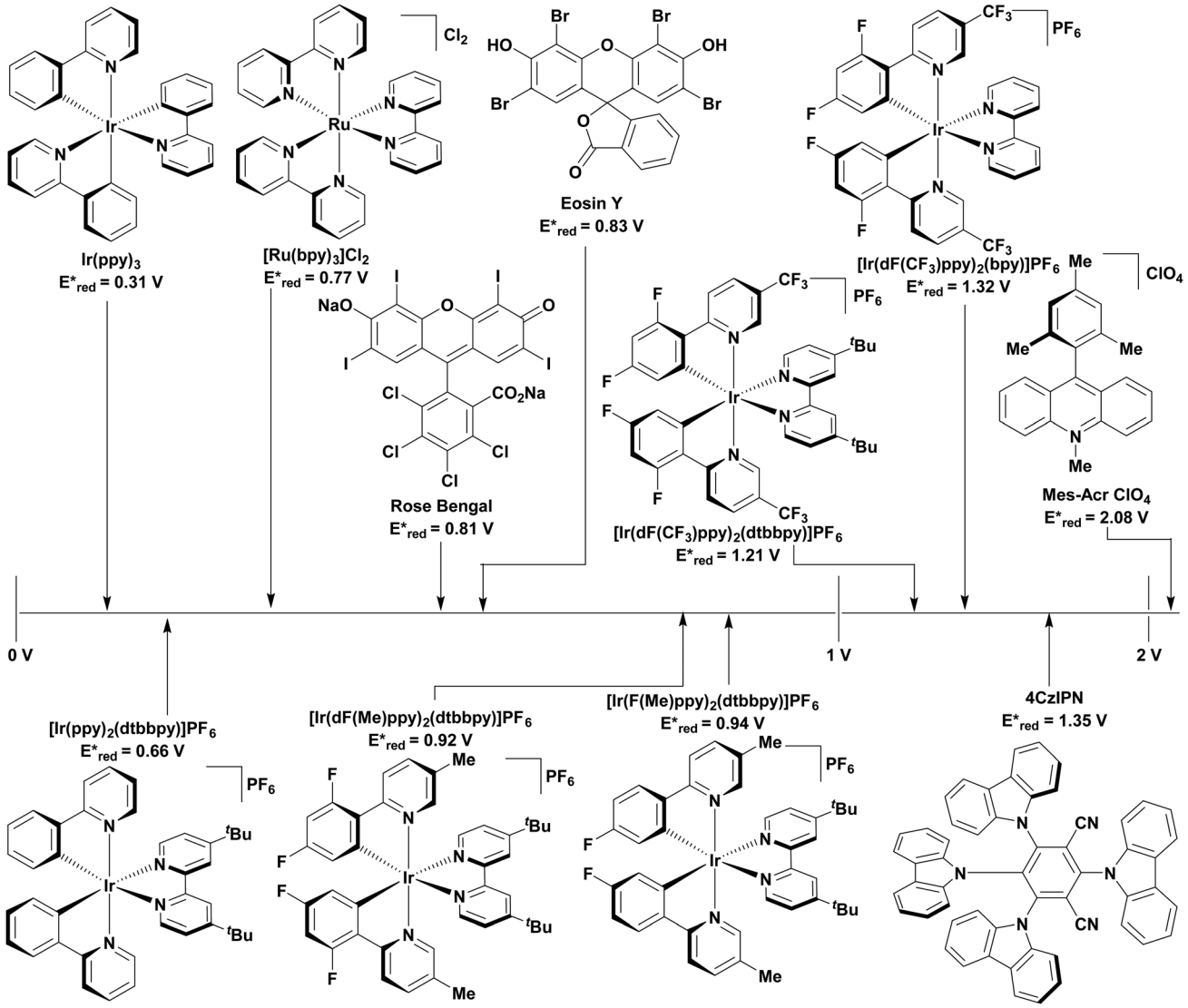

Fig. 9 Excited state reduction potentials of common, visible light PCs.

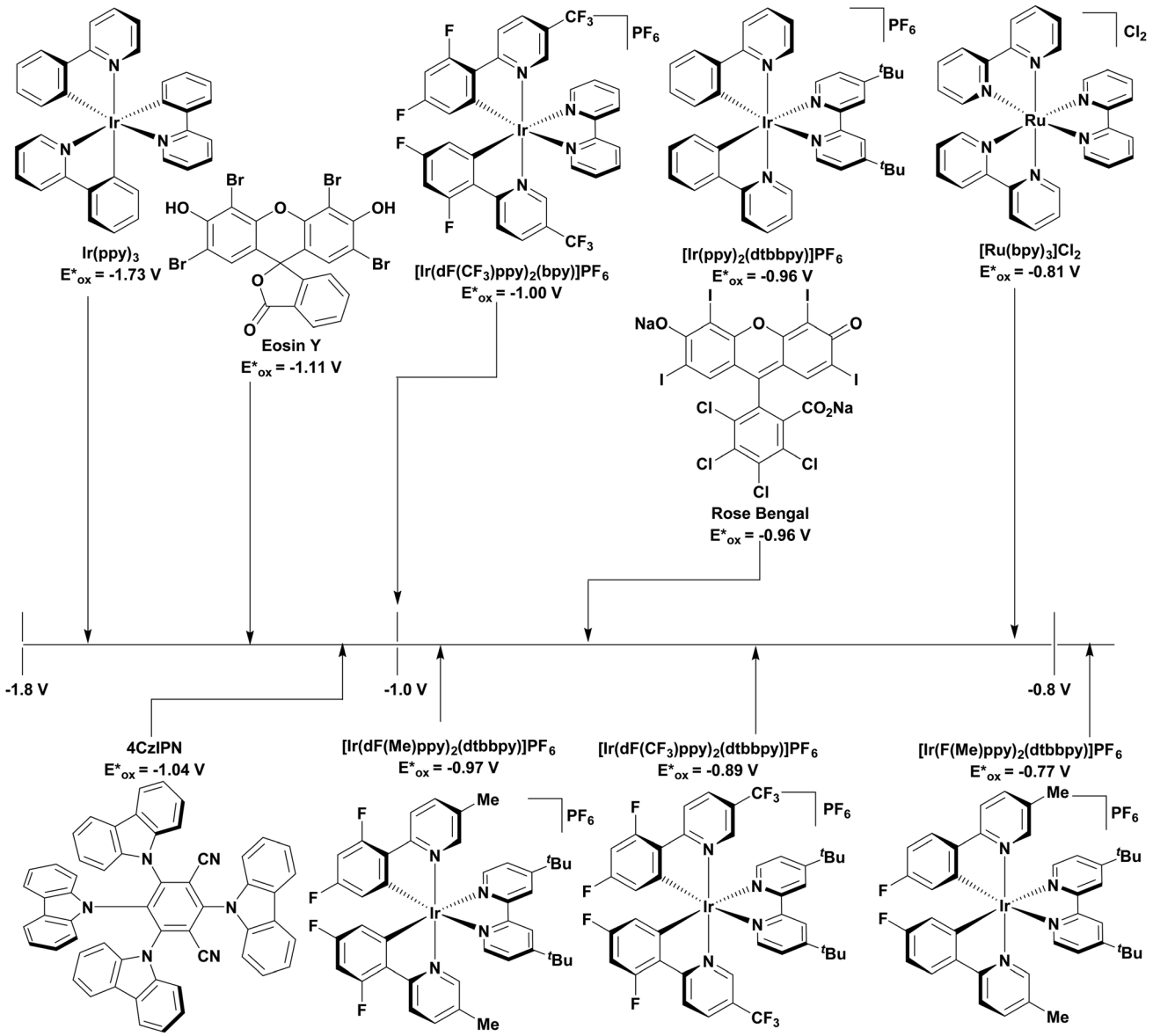

Fig. 10 Excited state oxidation potentials of common, visible light PCs.

MeCN[123] and $\sim 1.7 \times 10^5$ M^{-1} cm^{-1} at 377 nm for **4CzIPN**[60]) and long excited-state lifetime (τ_{pf} = 18.7 ns and τ_{df} = 1390 ns in MeCN)[119] are all important factors that contribute to the popularity of **4CzIPN** as a PC.

Throughout this review, we will highlight the comparative performance of TADF photocatalysts with alternative PCs. However, there are some caveats to these comparisons and caution must be taken when drawing conclusions as to performance. Firstly, in almost all articles referenced, a photocatalyst is considered the best when it provides the highest yield of product. It is not always the case that the reaction has been identified as going to full conversion and so differences in yield may reflect a combination of differences in reaction kinetics and differences in reactivity. As such, we define a threshold for yield comparison whereby a variation of less than 5% between reaction yields obtained using different photocatalysts will be classed as not statistically significantly different. Further, product yields are sometimes based on isolated yields where there is a greater chance for variance between experiments, NMR yields by contrast, provide more accurate quantification of product formation. For photocatalysts, a more quantitative method is the quantum yield of reaction, $\Phi(\lambda)$, (eqn (1)); however, these are seldom reported.[138] A maximum quantum yield of one is obtained for situations in which one mol of photons absorbed produces one mol of product. Typically, quantum yields are only reported as mechanistic evidence for a radical chain mechanism or a lack thereof, whereby one mol of photons forms n mols of product, producing a quantum yield >1. Usually, a quantum yield less than one signifies that a radical chain mechanism is not operational; however, this is a largely oversimplified interpretation of the reaction quantum yield. It is possible that the reaction proceeds through a radical

chain mechanism even with a quantum yield less than 1, but with a highly inefficient initiation step. Estimations of the chain length are possible if the quenching fraction is taken into consideration,[139] although such an analysis is rarely undertaken in much of the photocatalysis literature. As such, we are largely limited to reporting the quantum yield determined by the authors and the conclusions that have been drawn from such a value.

Cross-comparison of multiple studies becomes fraught when the excitation source changes, affecting both the photon flux and the excitation wavelength used to photoexcited the PC.[138,140] Throughout the development of photocatalysis, a wide variety of excitation sources have been employed from simple household compact fluorescent lightbulbs (CFLs) with moderate light intensity and a broad excitation spectrum to high-powered light emitting diode (LED) lamps, which have controllable intensity and narrow excitation spectra.[141] Further, photoreactors that are capable of capturing and reflecting all of the photons emanating from the excitation source and directing them into the reaction vessel will lead to more efficient reaction transformations.

Furthermore, throughout this review mechanisms are shown for each reaction mentioned; however, it should be noted that for the most part, these are putative with frequently little evidence provided to corroborate the proposed mechanism. Typically, only a comparison of the thermodynamic parameters of the PCs and the substrates is used to support the mechanistic proposals. This type of comparison and its correlation to reaction yields provides a very crude assessment of PC potency and ignores the reaction kinetics. For example, a study by Wolf *et al.* investigated the impact of the lifetime of the photoexcited state of the PC on the product yield in the trifluoromethylation of quinoline.[142] It was found that a longer excited-state lifetime resulted in faster SET involving the excited PC; however, there was no significant impact on the yield, indicating the rate determining step is not the initial SET for this reaction; indeed, further investigations suggested the second SET was the rate limiting step. The importance of reaction kinetics was highlighted also in the work of Scaiano *et al.*[143] It was concluded that while appropriate redox potentials are necessary for the PC to initiate the required SET, the kinetics of the process may be the deciding factor as to how successful the photocatalyst is. Unfortunately, kinetics studies like these are rarely completed.

Despite of these lacunes, this review aims to summarize the reactivity and document the potential of TADF compounds, such as **4CzIPN**, as photocatalysts.

2. 4CzIPN as an independent photocatalyst

Thus far, **4CzIPN** is the most widely studied TADF-based photocatalyst. The majority of examples in this section proceed *via* PET and are therefore photoredox catalysis reactions although a very small handful to be discussed occur *via* PEnT. Where applicable, the relative success of **4CzIPN** is compared with other photocatalysts.

Photoinduced decarboxylation of carboxylic acids in the formation of C–C and C–X bonds in a reductive quenching mechanism

Many examples employing **4CzIPN** as a photocatalyst involve decarboxylation of the substrate, whereby a reductive quenching mechanism is typically in operation. Utilisation of carboxylic acids to form C(sp^3) radicals *via* photoinduced oxidative decarboxylation has opened a variety of new synthetic pathways for the formation of C–C or C–X bonds.[144] The carboxylic acid or carboxylic acid derivative is activated through SET to the excited photocatalyst, forming an alkyl or haloalkyl radical. This requires the photocatalyst to be a relatively strong photooxidant in order to oxidise the carboxylate (E_{ox} of carboxylates typically ranges from 1.2–1.5 V).[145] Through either a radical addition or radical coupling mechanism, a C–C or C–X bond (where X = O or N) is formed. This step is usually facilitated through a SET reduction from the reduced photocatalyst, concomitantly closing the photocatalytic cycle and regenerating the photocatalyst. A generic mechanism for this process, involving a radical addition mechanism can be seen in Fig. 11.

Reactions that have exploited this decarboxylation mechanism in combination with a radical addition include the formation of: formyl radical equivalents (from 2,2-diethoxyacetic acid)[146] which can be used in hydroformylation reactions (Fig. 12a), alkyl radicals which can subsequently react with nitrosoarenes to synthesise hydroxylamines (Fig. 12b),[147] α-amino radicals which can be added to vinyl boronic esters producing γ-amino boronic esters (Fig. 12c),[148] amidyl radicals which can be added to alkenes (Fig. 12d),[149] alkyl radicals, which can be added to C=C bonds of amino acids or peptides (Fig. 12e)[150] and silyl radicals, which can be added to alkenes (Fig. 12f).[151]

These reactions all proceed *via* a photoinduced decarboxylation followed by a radical addition mechanism (Fig. 11). For the hydroformylation reaction (Fig. 12a), **4CzIPN** is the most efficient photocatalyst, obtaining 70% yield of product, as well as 100% conversion, in the batch reaction while all other organic

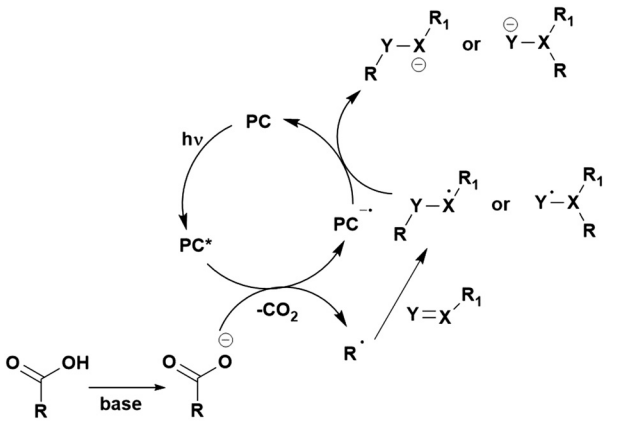

Fig. 11 Photoinduced oxidative decarboxylation catalytic cycle using a radical addition mechanism where X = C or N, and Y = C or O.

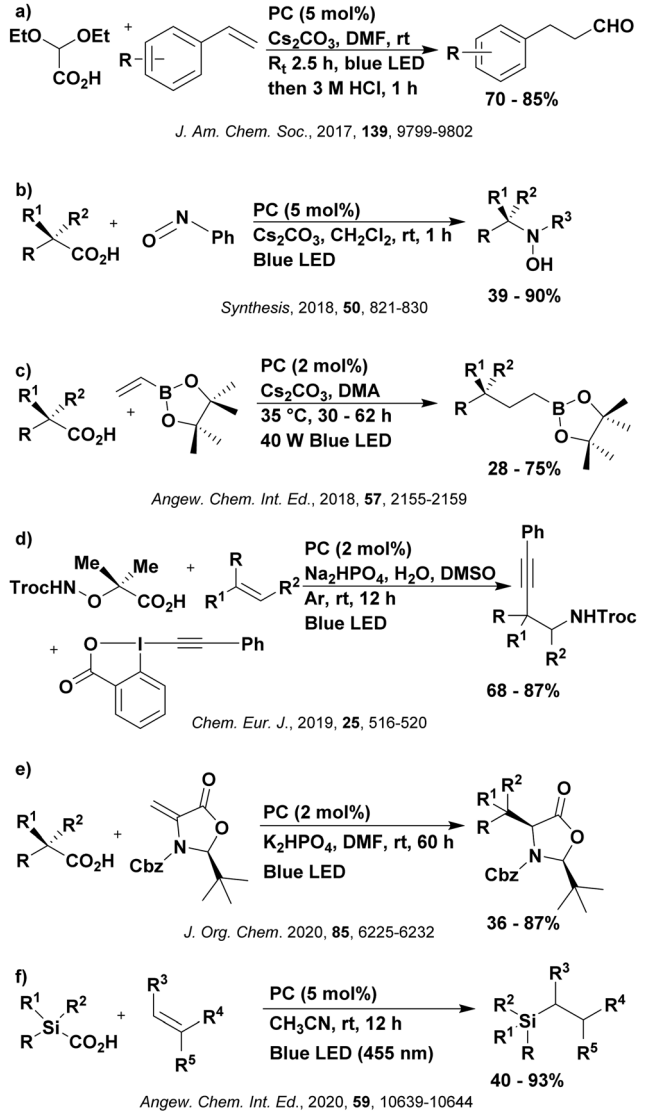

Fig. 12 Reaction schemes involving photocatalytic decarboxylation; (a) hydroformylation of aromatic vinyl substrates, (b) synthesis of hydroxylamines, (c) synthesis of γ-amino boronic esters, (d) 1,2-amidoalkynylation of alkenes, (e) derivatisation of amino acids and (f) hydrosilylation of alkenes. R_t = residence time in the flow reactor.

photocatalysts tested, including eosin Y and [Mes-Acr]ClO_4, obtained no product.[146] Similarly, in the 1,2-amindoalkynlation of alkenes (Fig. 12d), **4CzIPN** produced a 77% yield of product when using 2-methylpent-1-ene as the alkene, while other organic photocatalysts yielded between 7–33% of product, with eosin Y being the next best photocatalyst at 33% yield.[149] These differences in yield correlate with the ground state reduction potential of the photocatalysts (E_{red} = −1.21 V, −1.06 V and −0.57 V for **4CzIPN**, eosin Y and [Mes-Acr]ClO_4, respectively), suggesting this thermodynamic parameter may have crucial impact on the success of the photocatalyst. In the hydrosilylation of alkenes (Fig. 12f),[151] **4CzIPN** considerably outcompeted the iridium and ruthenium complexes, yielding 82% while the next best PC, [Ir(dF(CF_3)ppy)$_2$(dtbbpy)]PF_6, could manage only 45%. This is likely on account of the superior photooxidising ability of **4CzIPN** (E_{red}* = 1.35 V and 1.21 V for **4CzIPN** and [Ir(dF(Me)ppy)$_2$(dtbbpy)]PF_6, respectively), which is implicated in the oxidation of the silacarboxylate ($E_{ox}(Ph_2MeSiCO_2^{\bullet}/Ph2MeSiCO_2^{-})$ = 1.32 V *vs.* SCE). For the derivatisation of amino acids (Fig. 12e),[150] **4CzIPN** and [Ir(dF(Me)ppy)$_2$(dtbbpy)]PF_6 provided the same yields (90% and 89%, respectively), with **4CzIPN** being selected as the PC for the subsequent substrate scope.

Unfortunately, **4CzIPN** proved unsuccessful in synthesising the hydroxylamine product (Fig. 12b), as did the iridium photocatalyst tested, [Ir(dF(CF_3)ppy)$_2$(dtbbpy)]PF_6.[147] Both [Mes-Acr]ClO_4 and [Mes-Acr]BF_4 worked as photocatalysts for this reaction, which is likely due to their far superior oxidising capability in the excited state (E_{red}* = 2.06 V for Mes-Acr$^+$ compared to 1.35 V for **4CzIPN** and 1.21 V for [Ir(dF(CF_3)ppy)$_2$(dtbbpy)]PF_6). For γ-amino boronic ester synthesis (Fig. 12c), four photocatalysts were considered: [Ir(ppy)$_2$(dtbbpy)]PF_6, [Ir(dF(CF_3)ppy)$_2$(dtbbpy)]PF_6, [Ru(phen)$_3$]Cl_2 and **4CzIPN**. [Ir(ppy)$_2$(dtbbpy)]PF_6 was the most efficient photocatalyst with the substrate Boc-Pro-OH, giving a final product yield of 88% in the presence of the additive Cs_2CO_3, although **4CzIPN** also provided a moderate yield of 66% in the absence of this additive. No yield was given for the use of **4CzIPN** with the additive Cs_2CO_3, making a direct comparison somewhat challenging. Nevertheless, a possible reason for [Ir(ppy)$_2$(dtbbpy)]PF_6 outperforming **4CzIPN** is their relative ground state reduction potentials (E_{red} = −1.51 V and −1.21 V, respectively). The more negative E_{red} value for the iridium photocatalyst facilitates the SET between the reduced photocatalyst and the intermediate α-boryl radical and thus the turnover of the photocatalytic cycle.

A mechanistically related example can be seen in the remote functionalisation of amides and amines using electrophilic nitrogen radicals (Fig. 13).[152] This reaction proceeds *via* decarboxylation of the carboxylic acid derivatives to generate an electrophilic amidyl radical, which can then undergo a 1,5-hydrogen atom transfer (HAT) to form a distal alkyl radical (Fig. 14). Homolytic atom/group transfer with a polarised SOMOphile (SOMO = singly occupied molecular orbital) affords amines or amides that are remotely substituted. An extensive SOMOphile substrate scope study was undertaken, in the comparison of **4CzIPN** and [Ir(dF(CF_3)ppy)$_2$(dtbbpy)]PF_6, **4CzIPN** gave a higher product yield in γ-chlorination (76% *vs.* 64%), thioetherification (71% *vs.* 59%), cyanation (64% *vs.* 21%) and alkynylation (80% for **4CzIPN**, iridium PC not tested). Unusually, for γ-fluorination, **4CzIPN** was not tested, so in this case [Ir(dF(CF_3)ppy)$_2$(dtbbpy)]PF_6 was the best photocatalyst. Quantum yields were obtained for the reactions involving the five SOMOphile substrates with their respective superior photocatalyst and varied

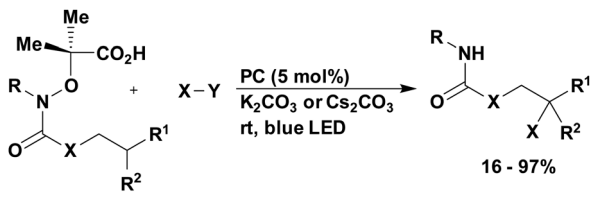

Angew. Chemie. Int. Ed., 2018, 57, 12945-12949

Fig. 13 Reaction scheme for the remote functionalisation of amides and amines using electrophilic nitrogen radicals.

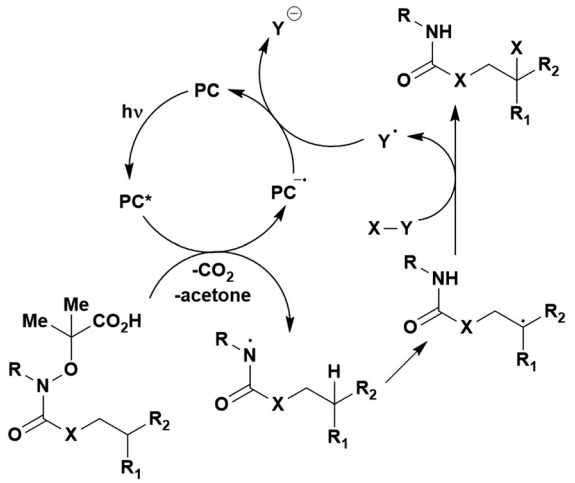

Fig. 14 Proposed photocatalytic cycle for decarboxylation and group transfer in C–H functionalisation.[152]

from 0.02–0.08. Unfortunately, quantum yields were not obtained across the PCs tested and so a direct comparison of the photocatalysts is not possible using this metric.

Carboxylic acids may be used as radical precursors in C(sp^3)–C(sp) type coupling reactions, for example the acetalation of alkynyl bromides (Fig. 15).[153] Decarboxylation occurs to generate an acetal radical, which then adds to alkynyl bromide, forming a bromoalkenyl radical (Fig. 16). Elimination of a bromyl radical, which is reduced by the reduced photocatalyst, results in the formation of product. Radical trapping experiments confirmed the presence of the acetal radical while radical inhibition experiments provided further confirmation this is a radical-based process. Only **4CzIPN** and $[Ir(dF(CF_3)ppy)_2(dtbbpy)]PF_6$ provided any product (36% and 5% yield, respectively), with photocatalysts such as $[Ru(bpy)_3](PF_6)_2$ and eosin Y giving no product. Wang *et al.* postulated that this is a result of the photooxidising capability of the PC. The caesium salt of 2,2-diethoxyacetic acid has an oxidation potential of E_{ox} = 0.95 V,[21] hence the excited state reduction potential of the photocatalyst must be more positive than this for the transformation to be thermodynamically feasible. Both **4CzIPN** and $[Ir(dF(CF_3)ppy)_2(dtbbpy)]PF_6$, are sufficiently photooxidizing (E_{red}* = 1.35 V and 1.21 V, respectively) and their relative strength as photooxidants may explain why the former outperforms the latter. For $[Ru(bpy)_3](PF_6)_2$ and eosin Y, however, this SET is not thermodynamically possible (E_{red}* = 0.77 V and 0.83 V, respectively).

Cyclisation reactions following an oxidative decarboxylation have also been reported. This can be observed in the synthesis of functionalised cyclopropanes (Fig. 17a),[154] intramolecular arene alkylation (Fig. 17b)[155] and the synthesis of 2-substituted piperazines (Fig. 17c).[156] The former involves a radical addition-polar cyclisation cascade mechanism, generating functionalised cyclopropanes through a polar 3-*exo*-tet cyclisation (Fig. 18a).[154] This mechanism was supported by quantum yield measurements for the reaction between Boc-Pro-OH and (4-chlorobut-1-en-2-yl)-boronic acid pinacol ester, giving a quantum yield of 0.65.

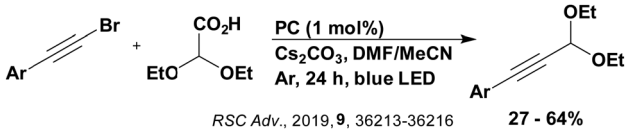

Fig. 15 Reaction scheme for the acetalation of alkynyl bromides.

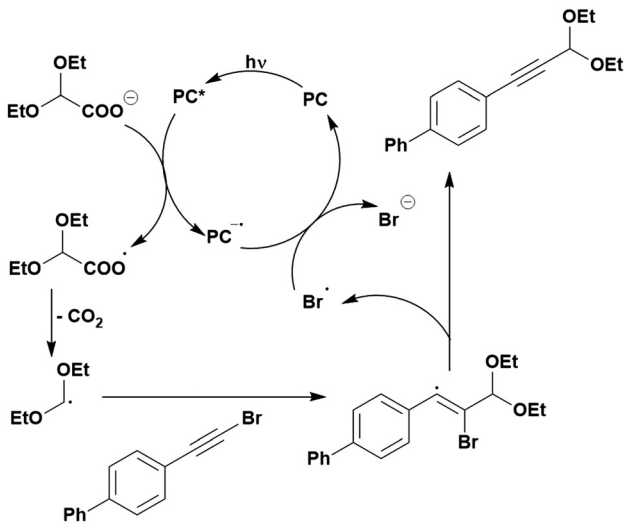

Fig. 16 Putative mechanism for the photocatalytic acetalation of alkynyl bromides.[153]

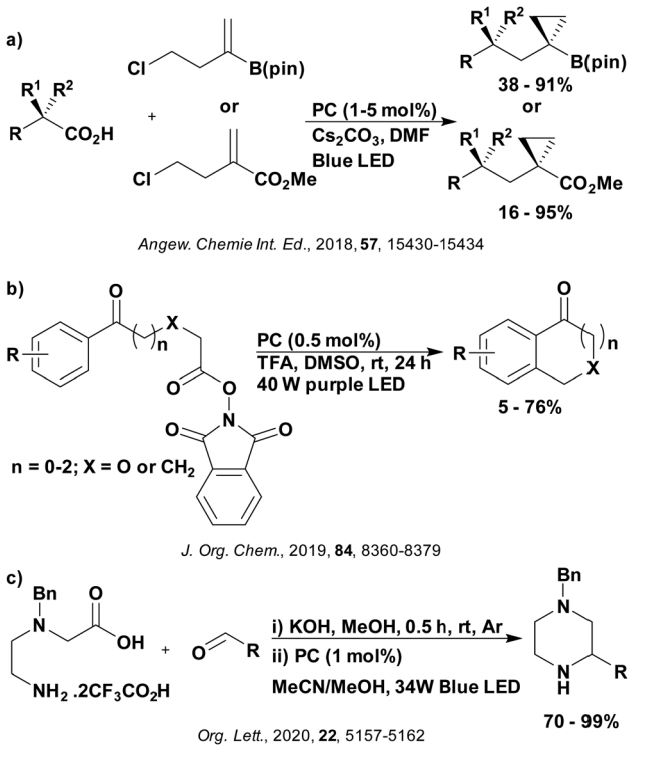

Fig. 17 Reaction schemes for cyclisation reactions involving a photoinduced decarboxylation mechanism for the formation of (a) functionalised cyclopropanes, (b) intramolecularly alkylated arenes and (c) 2-substituted piperazines.

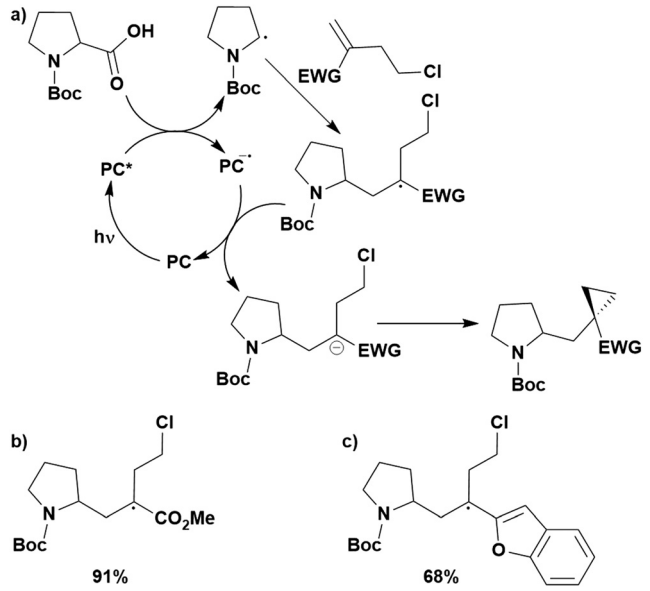

Fig. 18 (a) Proposed mechanism for the photoinduced cyclopropanation using carboxylic acids as radical precursors (EWG = electron withdrawing group), (b) carboxylate radical intermediate and (c) electron rich benzylic radical intermediate.

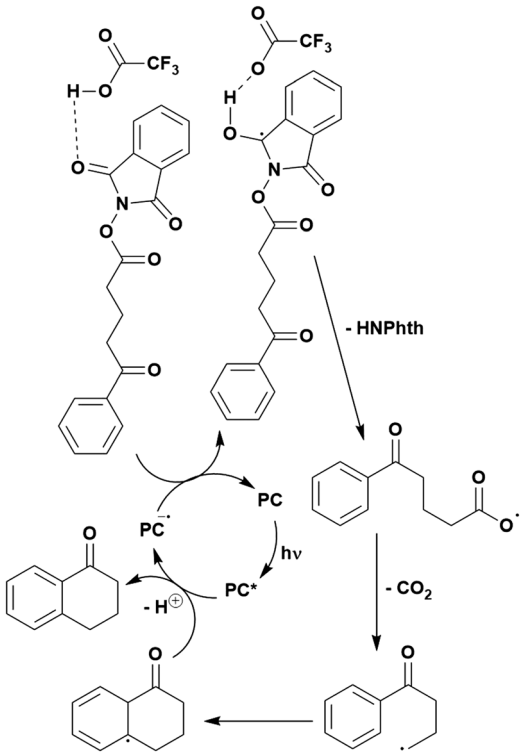

Fig. 19 Possible mechanism for the photoinduced intramolecular arene alkylation of *N*-(acyloxy)phthalimides (NAPs).

Since the quantum yield is below 1, this helps to support the proposal of the closed photocatalytic mechanism, rather than any alternative radical chain mechanisms. Under the optimised conditions, **4CzIPN** was highlighted as the best photocatalyst, providing a 99% yield of product with a slightly lower yield of 90% obtained with $[Ir(ppy)_2(dtbbpy)]PF_6$ under the same reaction conditions. The wide ground state redox window of **4CzIPN** allows the substrate scope to go beyond just homoallyl chlorides bearing electron-withdrawing substituents. For example, **4CzIPN** ($E_{red} = -1.21$ V) could undergo SET with α-carboxylate ester radicals (Fig. 18b) ($E_{red}(R^{\bullet}/R^{-}) \approx -0.6$ V)[157] as well as electron-rich benzylic radicals (Fig. 18c) ($E_{red}(R^{\bullet}/R^{-}) < -1.4$ V).[158]

The intramolecular arene alkylation reaction (Fig. 17b) also involves a radical addition mechanism in combination with decarboxylation (Fig. 19).[155] Stern–Volmer quenching experiments were conducted in order to support the proposed mechanism as well as quantum yield determination (0.022 for 1,3-dioxoisoindolin-2-yl 5-oxo-5-phenylpentanoate). For this reaction, 23 photocatalysts were screened initially with **4CzIPN** and iridium photocatalysts $[Ir(ppy)_2(dtbbpy)]PF_6$, $[Ir(dF(CF_3)ppy)_2(bpy)]PF_6$, $[Ir(dF(CF_3)ppy)_2(dtbbpy)]PF_6$, $[Ir(dF(Me)ppy)_2(dtbbpy)]PF_6$, $Ir(dFppy)_3$, $Ir(dF(^tBu)ppy)_3$ providing the highest yields (70–75%). Since **4CzIPN** provided high yields at a lower cost, it was chosen as the PC for the scope study.

The synthesis of 2-substituted piperazines (Fig. 17c)[156] proceeds through condensation of the aldehyde and amine to generate an imine prior to irradiation. Oxidative decarboxylation of the imine by the excited PC leads to the α-amino radical, which intramolecularly adds to the imine. Closure of the photocatalytic cycle is proposed to occur through either reduction of the resultant *N*-centred radical, which after protonation yields the final piperazine product, or the *N*-centred radical abstracts a proton from the solvent, MeCN, to afford the piperazine directly, and the cyanomethyl radical is reduced by the reduced PC. Both **4CzIPN** and $[Ir(ppy)_2(dtbbpy)](PF_6)$ provided essentially the same yields under the same conditions (70% and 75%, respectively), with $[Ru(bpy)_3](PF_6)_2$ and $[Ir(dF(CF_3)ppy)_2(dtbbpy)]PF_6$ both managing only 33%. There seems to be no obvious link between the thermodynamic parameters of these PCs and the yields obtained.

Additionally, the $C(sp^3)$ radical produced from oxidative decarboxylation of carboxylic acids or their derivatives can be used to generate new C–C or C–O bonds *via* a radical coupling mechanism. In the reductive quenching photocatalytic reaction conditions, two different radical species from two different substrates may be formed that can then couple together. For example, a benzylic radical and an α-amino radical anion were demonstrated to couple together to produce β-arylethylamines (Fig. 20a)[159] The proposed mechanism (Fig. 21) was supported by Stern–Volmer quenching studies that indicated that the excited photocatalyst is not quenched by the imine, but rather by the carboxylic acid in the presence of K_2HPO_4. For PC optimisation, both **4CzIPN** and $[Ir(dF(CF_3)ppy)_2(bpy)]PF_6$ yielded a comparable amount of product (45% and 50%, respectively). Perhaps the stronger ground state reduction capacity of the iridium PC ($E_{red} = -1.21$ V and -1.37 V for **4CzIPN** and $[Ir(dF(CF_3)ppy)_2(bpy)]PF_6$, respectively) is the reason it performs slightly better, especially since imines can have challenging reduction potentials (up to $E_{red} = -2$ V).[160,161]

An additional example involves an alkyl radical and (2,2,6,6-tetramethylpiperidin1-yl)oxyl (TEMPO), which couples to form

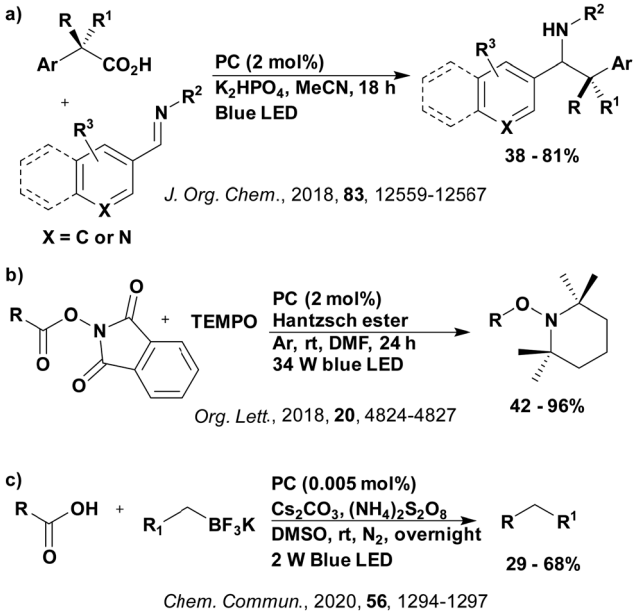

Fig. 20 Reaction schemes for (a) benzylation of imines, (b) oxygenation of aliphatic carboxylic acids and (c) coupling of aliphatic acids with trifluoroborate salts.

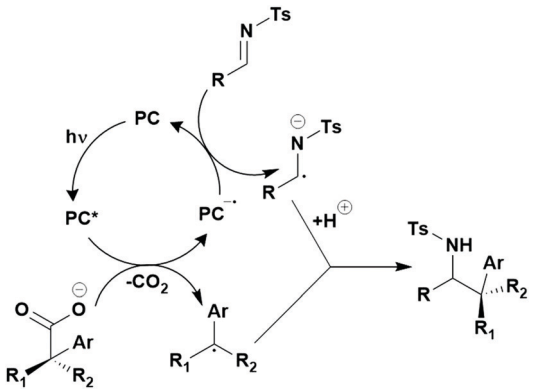

Fig. 21 Photoinduced oxidative decarboxylation catalytic cycle used for a radical–radical coupling mechanism.[159]

an alkoxyamine (Fig. 20b).[162] In this case, **4CzIPN** is outperformed as a PC by $[Ru(bpy)_3]Cl_2.6H_2O$ (yields of 80% and 95%, respectively), which again could be related to the regeneration of the PC. The PC needs to be moderately reducing in the ground state in order to reduce the *N*-(acyloxy)phthalimides, which have a reduction potential of $E_{red} = -1.26$ to -1.37 V.[162] Since the ruthenium PC is more reducing in the ground state ($E_{red} = -1.33$ V), this may explain the difference in yields. A quantum yield of 6.7 was obtained with the ruthenium(II) photocatalyst. It is unlikely that a radical chain process is involved since the TEMPO trapping of the alkyl radical is a termination process, hence Chen *et al.* propose an energy transfer process is likely to be occurring simultaneously to rationalize the high quantum yield, although no further investigations were undertaken to substantiate this claim.

Similarly, radical–radical coupling can be seen in the cross-coupling of aliphatic acids with trifluoroborates salts (Fig. 20c).[163] In this case, the excited PC is reductively quenched by both the carboxylic acid and the trifluoroborate salt to generate two alkyl radicals, suggesting two photocatalytic cycles are in operation. These alkyl radicals can then couple together to form the product. The photocatalyst is regenerated in both cycles by oxidation from persulfate. This proposed mechanism is supported by the observation that both carboxylic acids and trifluoroborate salts quench the photocatalyst emission, while persulfate did not; radical trapping experiments are corroborative. Only **4CzIPN** and $[Ir(dF(Me)ppy)_2(dtbbpy)]PF_6$ were considered as photocatalysts, with both providing similar yields (50% and 44%, respectively). The slightly higher yield obtained by **4CzIPN** is likely related to its superior photooxidising behaviour (E_{red}^* = 1.35 V and 0.92 V for **4CzIPN** and $[Ir(dF(Me)ppy)_2(dtbbpy)]PF_6$, respectively) which is needed for the oxidation of both carboxylic acids and trifluoroborate salts.

Photoinduced decarboxylation of carboxylic acids in the formation of C–C and C–X bonds in an oxidative quenching mechanism

Carboxylic acids have also been used as carbon-centred radical precursors in C–C or C–X bond forming reactions when then photocatalyst is operating in an oxidative quenching mechanism, for example in formation of urethanes and ureas (Fig. 22a).[164] Reduction of oxamic acids by the excited photocatalyst precipitates a decarboxylation to generate a carbamoyl radical. When this reaction was first developed, the carbamoyl radical was oxidised to form an isocyanate, regenerating the photocatalyst (Fig. 23). Radical trapping experiments with TEMPO were conducted to corroborate the mechanism proposed. **4CzIPN** was chosen as the photocatalyst, despite slower reaction kinetics, requiring 24 hours to reach a 91% product yield in comparison to $[Ru(bpy)_3]Cl_2$, which gave a 94% product yield in 15 hours. This is due to the authors' aim of identifying a "green" route to the synthesis of urethanes and ureas, which **4CzIPN** provides in comparison to transition metal photocatalysts. A follow-up study demonstrated that the carbamoyl radical could be reacted with heteroarenes (Fig. 22b).[165] Of the photocatalysts screened, **4CzIPN** gave the highest yield of 95%, with $[Mes\text{-}Acr]ClO_4$ managing 70%, eosin Y obtaining only a trace of product and rose bengal being completely unreactive. This is likely to be related the superior ground state oxidation potential of **4CzIPN** (E_{ox} = 1.52 V for **4CzIPN** compared with 0.78 V for eosin Y and 0.84 V for rose bengal).[28]

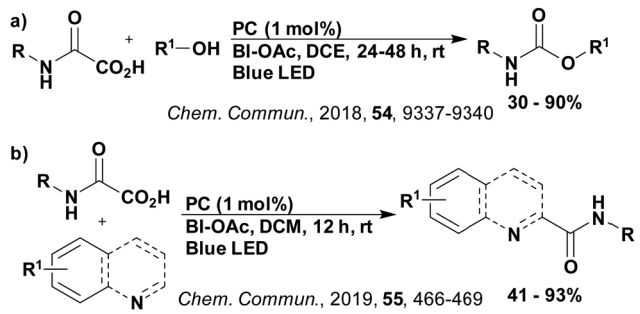

Fig. 22 Reaction scheme for oxidative decarboxylation of oxamic acids with (a) alcohols and (b) heteroarenes.

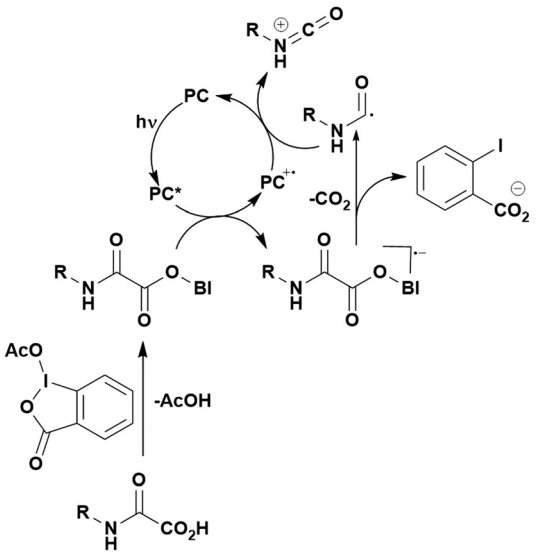

Fig. 23 Possible mechanism for the oxidative decarboxylation of oxamic acids using a photocatalyst.[164]

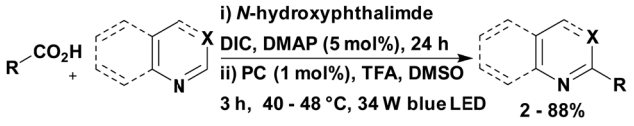

J. Org. Chem., 2018, **83**, 3000-3012

Fig. 24 Reaction scheme for a Minisci reactions using carboxylic acids *via* *N*-acyloxyphthalimides.

Analogously, oxidative quenching of the excited photocatalyst by *N*-(acyloxy)phthalimides (NAPs) generates an alkyl radical,[166] which can then undergo radical addition to a heteroarene to afford the functionalised product (Fig. 24). Three photocatalysts achieved comparable yields: **4CzIPN**, $[Ir(dF(CF_3)ppy_2)(dtbbpy)]PF_6$ and *fac*-$Ir(ppy)_3$; however, **4CzIPN** was chosen as the photocatalyst since the authors sought an organocatalysed reaction to prevent elemental impurity toxicity concerns presented by iridium photocatalysts.

A similar mechanism is involved in the formation of C–F bonds using *N*-hydroxyphthalimide esters as the radical precursor (Fig. 25).[167] The excited PC is proposed to be oxidatively quenched by this redox-active ester, forming an alkyl radical (Fig. 26). Rather than this radical adding to a double bond or coupling with another radical, as has been the case so far, the alkyl radical is oxidised by the oxidised PC to form a carbocation, closing the photocatalytic cycle. The carbocation is trapped by the fluoride ion to yield the alkyl fluoride. This proposed mechanism

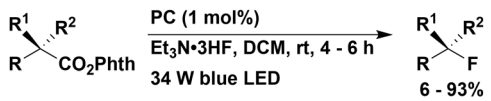

J. Am. Chem. Soc., 2020, **142**, 20, 9493–9500

Fig. 25 Reaction scheme for the nucleophilic fluorination of redox active esters.

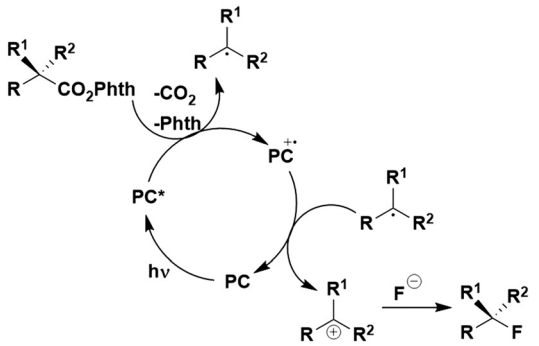

Fig. 26 Suggested mechanism for the nucleophilic fluorination of redox active esters.

is consistent with the measured quantum yield of 0.37, suggesting this is not a chain mechanism. Moreover, Stern–Volmer quenching experiments revealed that the excited PC is indeed quenched efficiently by the phthalimide ester. Addition of TEMPO inhibits formation of the desired product, instead favouring a TEMPO adduct, which confirms the formation of the alkyl radical. The presence of the alkyl radical is also demonstrated by addition of other radical trapping reagents, including methyl acrylate and styrene. Finally, the formation of the carbocation was corroborated through trapping experiments with a range of nucleophiles, including alcohols and 1,3,5-trimethoxybenzene. **4CzIPN** was the only organic PC considered for this reaction, with the desired product formed in 91% yield, which is comparable to the yields obtained using $Ir(dFppy)_3$ (99%), *fac*-$Ir(ppy)_3$ (96%) and $[Ir(dF(CF_3)ppy)_2(dtbbpy)]PF_6$ (94%).

Thus far, the excited photocatalyst has been oxidatively quenched by the carboxylic acid derivative to generate the required alkyl radical; however, it is possible for the oxidised photocatalyst to be responsible for generation of the alkyl radical. This can be observed in the photocatalytic synthesis of aldehydes and ketones from arylacetic acids (Fig. 27a),[168] a δ-C–H mono and dihalogentation reaction (Fig. 27b),[169] the intermolecular hydroalkylative dearomatization of electron-deficient indole derivatives (Fig. 27c),[170] the intermolecular dearomatization of naphthalene derivatives by 1,2-hydroalkylation (Fig. 27d)[171] and the decarboxylative radical addition bifunctionalization cascade for the production of 1,4-amino alcohols (Fig. 27e).[172]

In the former, radical coupling of the alkyl radical with a superoxide radical (generated by SET from the excited PC), followed by protonation and dehydration yields the final product (Fig. 28). Stern–Volmer quenching experiments indicated that significant PC luminescence quenching was only observed with oxygen. Moreover, when 4-benzoquinone was added to the reaction, which acts as a superoxide radical scavenger, the yield decreased markedly from 91% to 18%, suggesting that the superoxide radical does play an active role in the mechanism. Electron paramagnetic spectroscopy (EPR) provided further evidence of the presence of the superoxide radical. Addition of TEMPO arrested the reaction, providing further evidence that this reaction involves radical processes. Only organic photocatalysts were considered, with **4CzIPN** giving an impressive yield of 91%

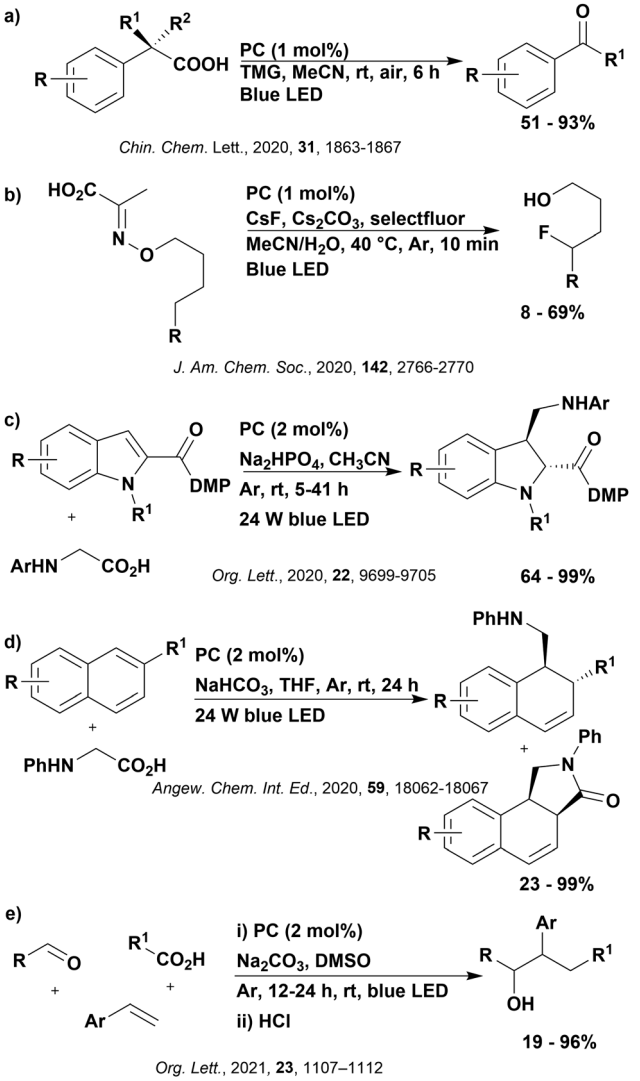

Fig. 27 Reaction scheme for the (a) photocatalytic generation of aldehydes and ketones from carboxylic acids, (b) δ-fluorination using carboxylic acid derivatives, (c) intermolecular hydroalkylative dearomatization of electron deficient indole derivatives, (d) intermolecular dearomatization of naphthalene derivatives by 1,2-hydroalkylation and (e) decarboxylative radical addition bifunctionalization cascade to produce 1,4-amino alcohols.

while others, such as eosin Y or rose bengal provided only a trace amount of product. This is likely related to the ground state oxidation potential of the photocatalyst, with eosin Y and rose bengal (E_{ox} = 0.78 V and 0.84 V, respectively) not capable of oxidising the carboxylate (E_{ox} = 1 to 1.25 V),[173] while **4CzIPN** is more than capable of doing this transformation (E_{ox} = 1.52 V). Decreasing the photocatalyst loading from 5 mol% to 1 mol% resulted in a slightly higher product yield (91% to 98%, respectively).

In the δ-C–H mono and dihalogentation reaction (Fig. 27b),[169] the oxidised photocatalyst is used to oxidise the carboxylic acid derivative, which loses CO_2 and MeCN, and undergoes 1,5-HAT to yield an alkoxy radical (Fig. 29). This radical then abstracts a F atom from selectfluor to generate the fluorinated product, with the selectfluor radical cation being reduced by the excited PC. This mechanism was supported by Stern–Volmer quenching experiments. A very short reaction time of 10 mins was needed to accomplish the fluorination reaction (with 1 mol% of PC) while for chlorination, a reaction time of 18 h was necessary (with 3 mol% of PC), hence quantum yield measurements were undertaken to confirm suspicion of a radical chain mechanism for the fluorination reaction. However, quantum yields of 0.070 and 0.016 were obtained for the fluorination and chlorination, respectively, suggesting radical chain mechanisms are not in operation. This result instead seemed to indicate that the fluorination reaction is more efficient, even with lower photocatalyst loading. Indeed, the rate of quenching of the alkoxy radical was found to be 53 times higher in the fluorination than chlorination reaction through radical clock experiments. Only **4CzIPN** and $[Ir(dF(CF_3)ppy)_2(dtbbpy)]PF_6$ were considered as photocatalysts, providing the same yields (67% isolated yield with **4CzIPN** and 71% LCMS yield with $[Ir(dF(CF_3)ppy)_2(dtbbpy)]PF_6$) with the former being chosen as the photocatalyst of choice.

For the reaction involving intermolecular hydroalkylative dearomatization of electron-deficient indole derivatives (Fig. 27c),[170] a similar mechanism is invoked. The excited PC is oxidatively quenched by the indole to generate a radical species, which after protonation, couples with the α-amino radical formed from

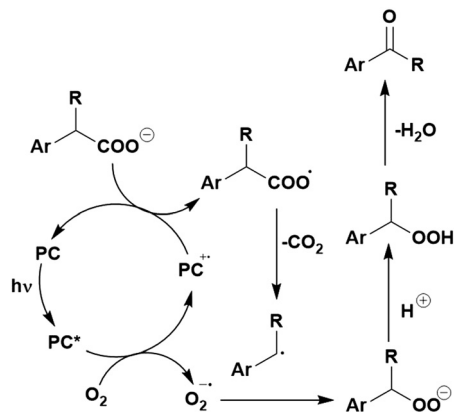

Fig. 28 Plausible reaction mechanism for the photocatalytic generation of aldehydes and ketones from carboxylic acids.

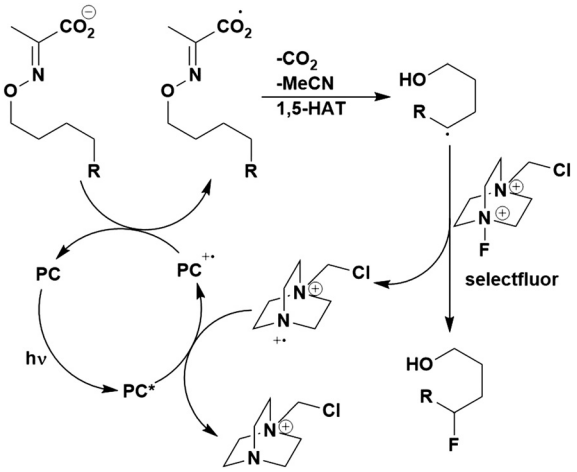

Fig. 29 Proposed mechanism for the fluorination of carboxylic acid derivatives.[169]

the oxidative decarboxylation of the carboxylic acid derivative (induced by the oxidised PC), to yield the final product. The proposed mechanism is supported by Stern–Volmer quenching experiments, which indicated that the excited PC is quenched by the indole much faster than by glycine (Stern–Volmer constant, K_{SV} = 1460 and 173, respectively). Moreover, addition of a radical trapping agent proved the presence of the indole-based radical. **4CzIPN** provided an essentially quantitative yield of 99%, while high yields were obtained by the transition metal PCs $[Ir(ppy)_2(dtbbpy)]PF_6$ (84%), *fac*-$Ir(ppy)_3$ (73%) and $[Ru(bpy)_3]Cl_2$ (56%). The relative yields correlate generally with the photoreducing ability of the PC (E_{ox}^* = −1.04 V, −0.96 V and −0.81 V for **4CzIPN**, $[Ir(ppy)_2(dtbbpy)]PF_6$ and $[Ru(bpy)_3]Cl_2$, respectively); however, the data do not align for *fac*-$Ir(ppy)_3$ (E_{ox}^* = −1.73 V). Instead, the lower yields obtained for *fac*-$Ir(ppy)_3$ may be related to its less positive ground state oxidation potential (E_{ox} = 1.52 V and 0.77 V for **4CzIPN** and *fac*-$Ir(ppy)_3$, respectively).

Penultimately, the intermolecular dearomatization of naphthalene derivatives by 1,2-hydroalkylation (Fig. 27d)[171] occurs analogously to the previous example. Stern–Volmer experiments indicated the naphthalene derivative oxidatively quenches the excited PC at a significantly faster rate than the carboxylic acid (Stern–Volmer constant, K_{SV}, = 3870 and 253, respectively, in MeCN and 3068 and 232, respectively, in THF). **4CzIPN** performed considerably better in this reaction than alternative PCs, yielding 90% of the product (2 : 1 ratio of uncyclized and cyclised product), while the next best competitor, $[Ir(ppy)_2(dtbbpy)]PF_6$ managed only 60% (3.7 : 1 ratio of products). It is unclear why this difference in yield was obtained, especially given that thermodynamically, neither should be capable of reducing the naphthalene derivative (E_{red} = −1.45 V *vs.* SCE for (3,5-dimethyl-1*H*-pyrazol-1-yl)-2-naphthalenylmethanone) and E_{ox}^* = −1.04 V and −0.96 V for **4CzIPN** and $[Ir(ppy)_2(dtbbpy)]PF_6$, respectively).

Finally, in the decarboxylative radical addition bifunctionalization cascade for the production of 1,4-amino alcohols (Fig. 27e)[172] the excited PC is oxidatively quenched by the aldehyde to form a ketyl radical. The oxidised PC generates the alkyl radical from the carboxylate analogously to the previous two examples. The alkyl radical adds to the olefin, with the resultant radical coupling with the ketyl radical. Subsequent protonation yields the final product. Addition of a radical scavenger TEMPO and deuterium labelling experiments substantiated the proposed mechanism. Of the eight PCs screened, only **4CzIPN** and $[Ir(dF(CF_3)ppy)_2(dtbbpy)]PF_6$ yielded any product (90% and 42%, respectively). This may be on account of their photoreducing ability (E_{ox}^* = −1.04 V and −0.89 V, respectively, compared to −0.81 V for $[Ru(bpy)_3]Cl_2$ which obtained no product). Alternatively, the authors imply a reductive quenching mechanism may also be in operation, the lack of mechanistic clarity makes it difficult to ascertain why **4CzIPN** performed so excellently in comparison to the other PCs.

Alternative radical precursors in forming C–C or C–X bonds

In lieu of carboxylic acids, a number of other precursors have been used to generate carbon-centred radicals *via* a reductive quenching pathway. These include alkyltrifluoroborates,[174,175] alkyl bis(catecholato)silicates (or other alkyl silicates),[161,175–180]

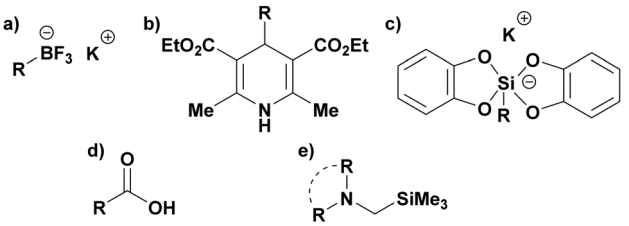

Fig. 30 Radical precursors which are used in photoredox reactions: (a) trifluoroborate salts, (b) 4-alkyl-1,4-dihydropyridine derivatives (DHPs), (c) silicates, (d) carboxylic acids and (e) α-trimethylsilylamines.

4-alkyl-1,4-dihydropyridine derivatives (DHPs)[177,181] and α-trimethylsilylamines[175] (Fig. 30), all of which are oxidised *via* SET by the excited PC. These subsequent radicals were then reported to react with a structurally diverse number of substrates such as alkenes (Fig. 31a),[175] heteroarenes (Fig. 31b, 31c and 31i),[174,177,180] imines (Fig. 31d),[161] CO (Fig. 31e and 31h),[176,179] SO_2 (Fig. 31f)[181] and *N*-acylhydrazones (Fig. 31g).[178]

For the alkylation of imines (Fig. 31d),[161] the carbonylation of alkenes (Fig. 31e),[176] hydrosulfonylation of alkenes (Fig. 31f)[181] and synthesis of aliphatic amides (Fig. 31h),[179] **4CzIPN** was demonstrated to be the best photocatalyst as it provided the highest product yields. In the alkylation of *N*-acylhydrazones (Fig. 31g), **4CzIPN** was the only photocatalyst considered, reaching very high yields of 88% during the optimisation experiments.[178]

However, in the alkylation of heteroarenes (Fig. 31b, c and i), the identification of the superior photocatalyst is far more substrate dependent. For example, primary alkyltrifluoroborates have a significantly higher oxidation potential (E_{ox} = 1.90 V *vs.* SCE)[182] than their secondary and tertiary counterparts, hence require a much stronger photooxidant. Since [Mes-Acr]* has a considerably greater excited state oxidising capacity compared with **4CzIPN** (E_{red}^* = 2.06 V and 1.35 V, respectively), it is not surprising that it performed better; **4CzIPN**, however, was a promising alternative for tertiary alkylation, outperforming $[Mes\text{-}Acr]^+$ (96% yield for **4CzIPN** and 57% for the acridinium salt).[174] For the heteroarene alkylation shown in Fig. 31i, **4CzIPN** was again outcompeted by $[Mes\text{-}Acr]^+$ (73% and 87%, respectively).[180] **4CzIPN** was shown to give high product yields when DHPs ($E_{ox} \approx$ 1.05 V *vs.* SCE)[183] were used as the radical precursor (although no other photocatalysts were tested), but unfortunately gave low yields when silicates were used ($E_{ox} \approx$ 0.75 V *vs.* SCE),[177,184] achieving only 14% of product in comparison to 78% obtained with $[Ru(bpy)_3](PF_6)_2$. The inferiority of **4CzIPN** to $[Ru(bpy)_3](PF_6)_2$ was also evident in the defluorinative alkylation protocol (Fig. 31a), whereby the ruthenium photocatalyst resulted in a 0.28 ratio of product:internal standard, while **4CzIPN** managed only 0.23.[175] Perhaps this is related to the regeneration of the photocatalyst, since **4CzIPN** is less reducing in the ground state (E_{red} = −1.21 V for **4CzIPN** compared to −1.33 V for $[Ru(bpy)_3](PF_6)_2$).

Another important class of radical precursor is amines, which undergo SET to the excited PC, generating α-amino radicals after a subsequent deprotonation. This reactivity is seen in the dicarbofunctionalization of styrenes with amines

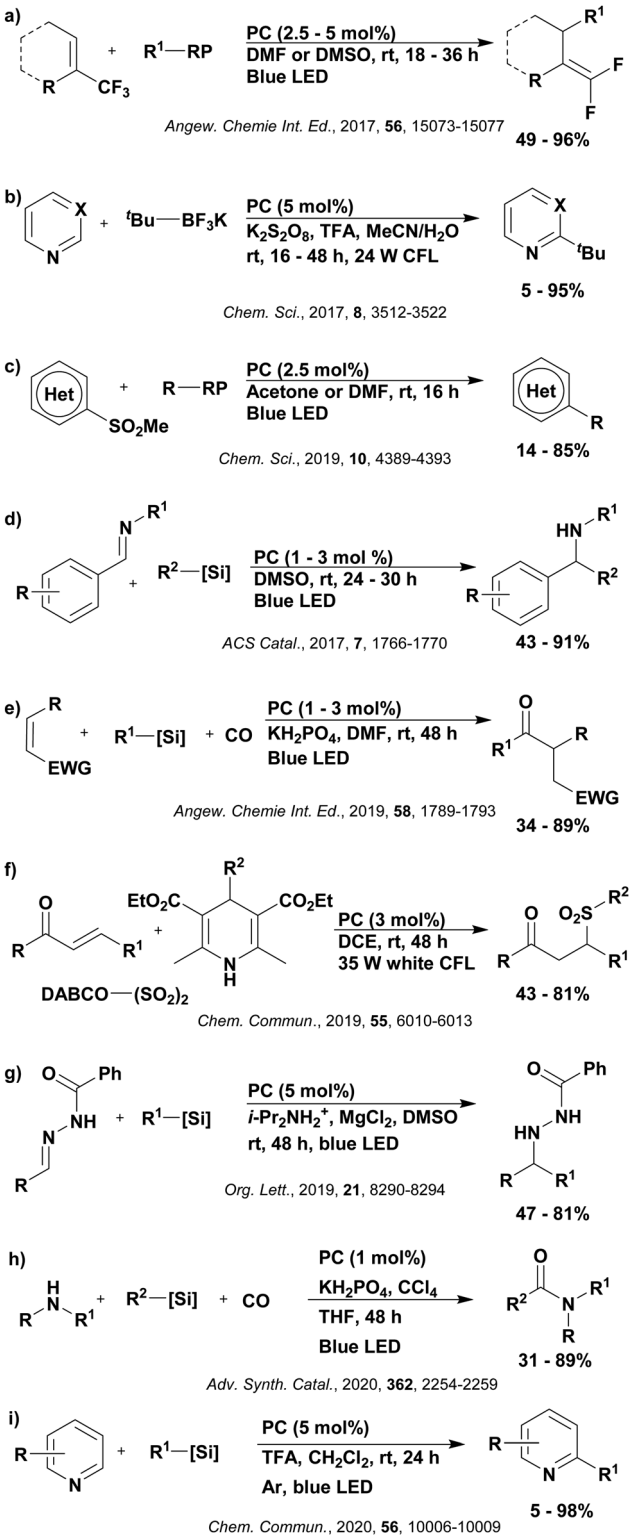

Fig. 31 Reaction schemes for the use of common radical precursors other than carboxylic acid derivatives in C–C and C–X bond forming reactions.

and CO_2 to generate γ-amino acids (Fig. 32).[185] The α-amino radical adds to the styrene derivative, with the resultant γ-amino benzylic radical being reduced by the reduced PC to

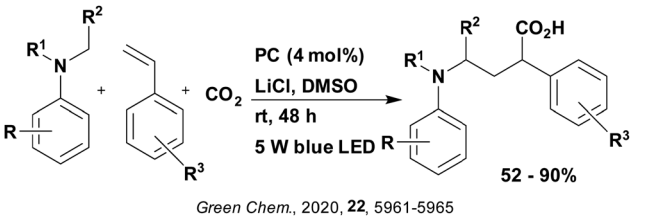

Fig. 32 Reaction scheme for the dicarbofunctionalization of styrenes with amines and CO_2 to generate γ-amino acids.

form a carbanion. Nucleophilic addition of this carbanion to CO_2, followed by protonation, yields the final product. The quantum yield of the reaction was determined to be 0.04, implying a radical chain mechanism is unlikely; radical scavengers such as TEMPO inhibited product formation, confirming that the reaction is a radical process. Deuterium labelling studies implicated the presence of the γ-amino benzylic anion as an intermediate.

4CzIPN performed excellently, yielding 95% of product. Cationic iridium and ruthenium complexes also performed very well ($[Ir(dF(CF_3)ppy)_2(dtbbpy)]PF_6$, $[Ir(ppy)_2(dtbbpy)]PF_6$ and $[Ru(bpy)_3](PF_6)_2$ obtained 76%, 84% and 83%, respectively). *fac*-$Ir(ppy)_3$ was the only PC in the study that performed poorly, yielding only 12% of product. The success of **4CzIPN** may be on account of its stronger photooxidising ability (E_{red}^* = 1.35 V, 1.21 V, 0.66 V, 0.77 V and 0.31 V for **4CzIPN**, ($[Ir(dF(CF_3)ppy)_2$-$(dtbbpy)]PF_6$, $[Ir(ppy)_2(dtbbpy)]PF_6$, $[Ru(bpy)_3](PF_6)_2$ and *fac*-$Ir(ppy)_3$, respectively).

Interestingly, the α-amino radicals formed may not necessarily be present in the final product, but may instead be used as a halogen atom transfer (XAT) agents in the alkylation (Fig. 33a) and allylation (Fig. 33b) of alkyl and aryl halides.[186] A proposed mechanism is shown in Fig. 34 for the alkylation reaction, with a similar mechanism being suggested also for the allylation. A quantum yield of less than 1 for both reactions is suggestive that this is not a radical chain process. Only **4CzIPN** was utilised as a PC in both reactions; however, in the study, Leonori *et al.* do justify this choice by conducting a PC optimisation for the dehalogenation reaction involving a HAT catalyst, finding **4CzIPN** to be the highest yielding and employing this PC in the subsequent reactions. For further information on this study and the PC optimisation, refer to the HAT dual catalysis Section 3.

Alkylboranes may be used as the radical precursors, which themselves are obtained from functionalised 1,2-bis(boronic esters) (Fig. 35).[187] A boronate complex is first formed through

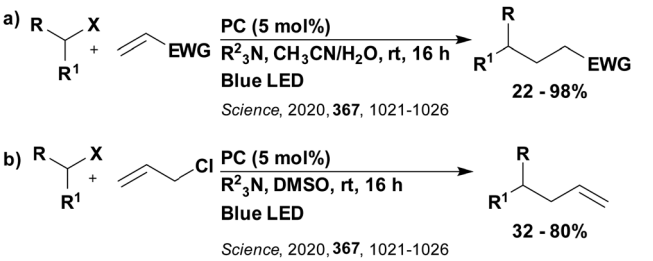

Fig. 33 Reaction scheme for the (a) alkylation and (b) allylation of alkyl and aryl halides.

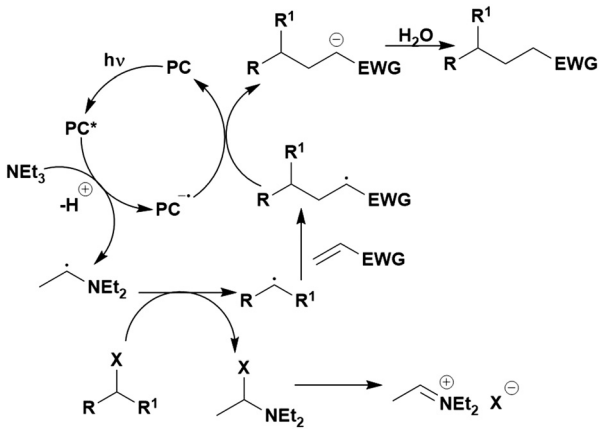

Fig. 34 Proposed mechanism for the alkylation of alkyl halides.

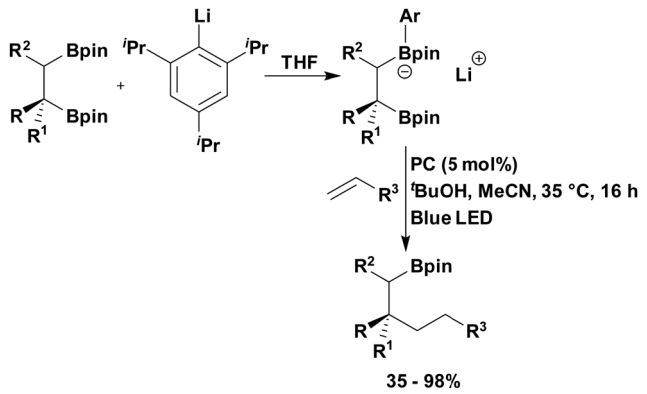

J. Am. Chem. Soc., 2019, **141**, 14104-14109

Fig. 35 Reaction scheme for the functionalisation of 1,2-bis(boronic esters).

reaction of the 1,2-bis(boronic esters) with an aryl lithium species, which is oxidised by the excited PC, generating a primary radical (Fig. 36). A 1,2-boron shift results in the more thermodynamically favourable secondary radical, which undergoes radical addition to an alkene. Reduction of this species by the reduced photocatalyst closes the photocatalytic cycle and allows for the formation for the final functionalised product. This mechanism, particularly the 1,2-boron shift, was supported by mechanistic studies, DFT modelling and boron isotope labelling. Only **4CzIPN** and fluorescein were considered as PCs in this study, with **4CzIPN** vastly outperforming the latter (100% and 11% yield, respectively). These results were expected based on their relative excited state reduction potentials (E_{red}^* = 1.35 V and 0.77 V, respectively).

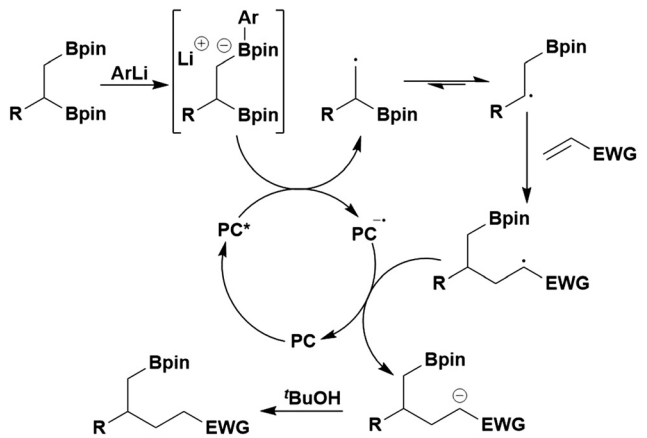

Fig. 36 Proposed mechanism for the functionalisation of 1,2-bis(boronic esters).

Borylation of aryl groups is additionally possible in a sp^3-sp^2 type coupling to form C-B bonds (Fig. 37).[188] All six PCs considered in this study performed well, ranging between 68–95%, with **4CzIPN** performing the best. Since the mechanism is unknown as of yet, it is difficult to ascertain why **4CzIPN** yielded the largest amount of product.

Carbotrifluoromethylation *via* photocatalytic decomposition of reagents such as CF_3SO_2Na to generate CF_3 radicals has been reported to proceed by a reductive quenching pathway.[189–192] This electrophilic trifluoromethyl radical can then add to electron-rich substrates such as alkenes in an anti-Markovonikov fashion to afford trifluoromethylated products. When the substrate is an α,α-diaryl allylic alcohol, β-trifluoromethyl-α-aryl ketones are obtained (Fig. 38a), proceeding *via* a radical 1,2-aryl migration.[189] When the substrate is an *N*-aryl acrylamide, an oxindole is generated (Fig. 38b),[190] proceeding *via* a radical cyclisation (Fig. 39) while if the additional reactants involve quinoxalin-2(1*H*)-ones and alkenes, 3-trifluoroalkylated quinoxalin-2(1*H*)-ones are formed (Fig. 38c).[191] Finally, in the combination of styrene and carbonyls, β-trifluoromethyl-α-substituted alcohols are obtained (Fig. 38d).[192]

The proposed mechanism for carbotrifluoromethylation involving *N*-aryl acrylamides was supported by radical trapping experiments and the results from control reactions. A quantum yield of 3.33 was obtained for the cyclisation reaction of *N*-methyl-*N*-(*p*-tolyl)-methacrylamide using **4CzIPN**, suggesting strongly that a radical chain process is involved.[190]

In the reactions shown in Fig. 38a and b, **4CzIPN** gave the highest product yields, with $[Ir(ppy)_2(dtbbpy)]PF_6$ and $[Ir(dF(CF_3)ppy)_2(dtbbpy)]PF_6$ being the closest competitors (86%, 45% and 68% yields, respectively in the reaction shown in Fig. 38a, 83%, 64% and 71% yield, respectively in the reaction in Fig. 38b). For the reaction shown in Fig. 38d, only **4CzIPN** and $[Ir(dF(CF_3)ppy)_2(bpy)]PF_6$ provided any product (82% and 48%, respectively). The superiority of **4CzIPN** could be corelated to its excited state

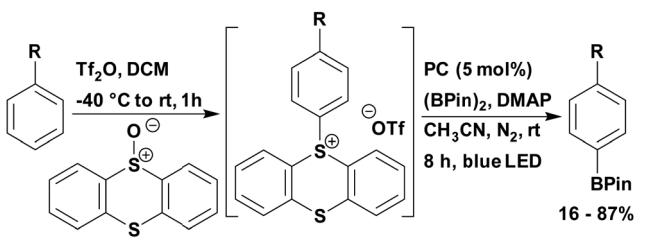

Sci. China Chem., 2020, **63**, 336-340

Fig. 37 Reaction scheme for the borylation of aryl groups. R = alkyl, aryl, F, OR or NR_2.

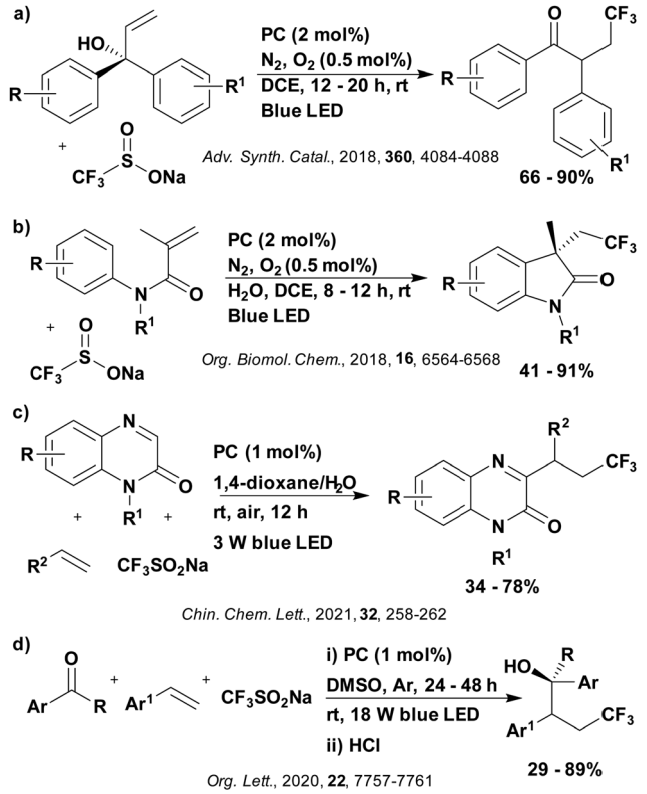

Fig. 38 Reaction scheme showing carbotrifluoromethylation of (a) allylic alcohols, (b) *N*-aryl acrylamides, Nc) quinoxalin-2(1*H*)-ones and alkenes and (d) styrenes and carbonyls.

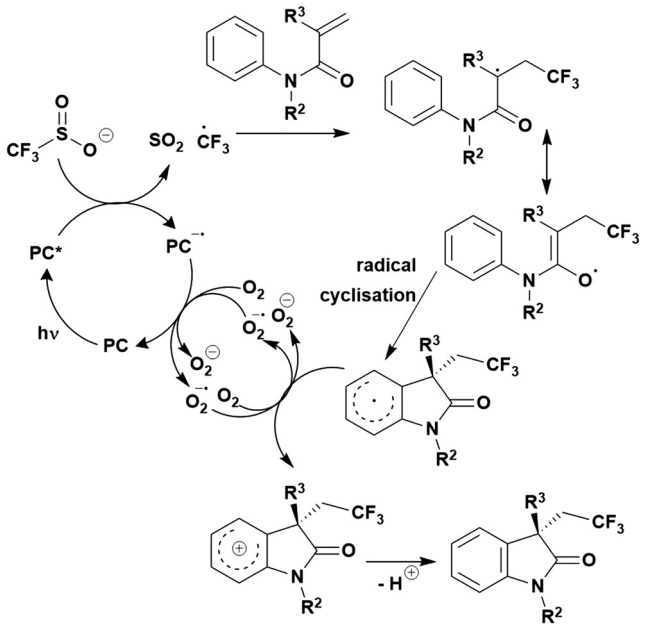

Fig. 39 Proposed mechanism for the photocatalytic carbotrifluoromethylation of *N*-aryl acrylamides.

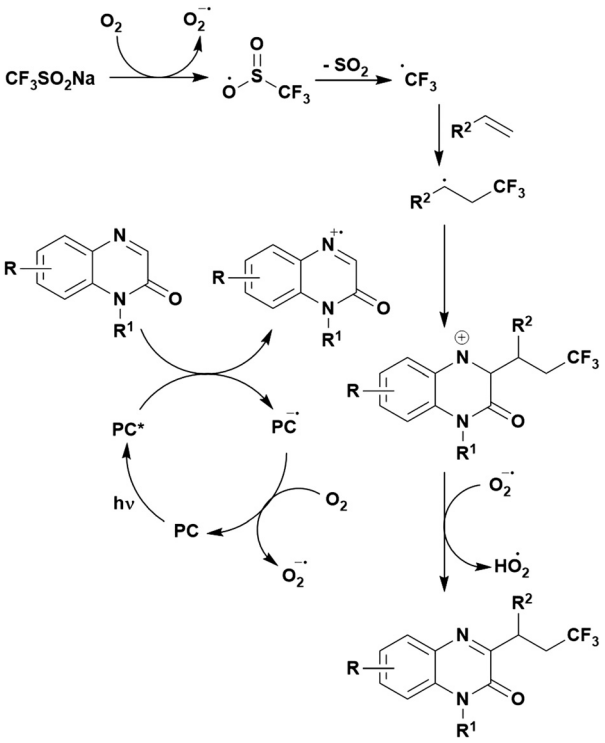

Fig. 40 Putative mechanism for the synthesis of 3-trifluoroalkylated quinoxalin-2(1*H*)-ones.

reduction potential (E_{red}^* = 1.35 V), which is considerably more positive than those of the other PCs considered (E_{red}^* = 0.66 V, 1.21 V and 1.32 V for $[Ir(ppy)_2(dtbbpy)]PF_6$, $[Ir(dF(CF_3)ppy_2(dtbbpy)]PF_6$ and $[Ir(dF(CF_3)ppy)_2(bpy)]PF_6$, respectively). Given the oxidation potential of CF_3SO_2Na (E_{ox} = 1.05 V),[193] there is a greater thermodynamic driving force for the generation of the CF_3 with **4CzIPN**, which may be why it attains the highest yield.

Meanwhile, in the synthesis of 3-trifluoroalkylated quinoxalin-2(1*H*)-ones (Fig. 38c), the mechanism differs, as shown in Fig. 40.[191] In this case, the excited PC is reductively quenching by the qunoxalin-2(1*H*)one, affording a nitrogen centred radical cation. The CF_3 radical, generated by oxidation and fragmentation of CF_3SO_2Na using molecular oxygen, then adds to the alkene. The carbon-centred radical intermediate couples with the aforementioned nitrogen-centred radical cation, which after deprotonation, yields the final product. The photocatalytic cycle is closed by oxidation of the reduced PC induced by molecular oxygen. Addition of the radical scavenger TEMPO inhibited the reaction, forming instead an adduct with CF_3, confirming the presence of the CF_3 radical and that this is a radical process. Stern–Volmer quenching experiments conducted by Wei *et al.* indicated that only quinoxaline-2(1*H*)-one could quench the excited PC while CF_3SO_2Na did not, which contradicts the mechanism shown in Fig. 39, as proposed by Huang, Cai and Liang.[189,190,192] Only organic PCs were considered for this reaction, with **4CzIPN** outperforming its competitors, obtaining 56% yield while the next best PC, rose bengal, afforded only 30%. This is likely due to the superior photooxidising ability of **4CzIPN** (E_{red}^* = 1.35 V and 0.81 V for **4CzIPN** and rose bengal, respectively).

Carbotrifluoromethylation can also proceed *via* an oxidative quenching cycle using CF_3SO_2Cl or Togni's reagent [1,3-dihydro-

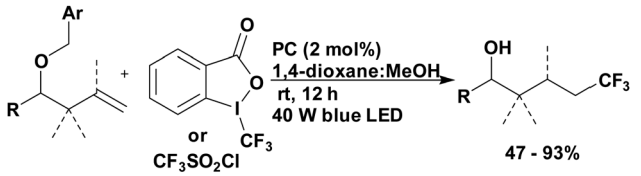

Org. Lett., 2019, **21**, 5116-5120

Fig. 41 Carbotrifluoromethylation reaction scheme for the synthesis of δ-fluoromethylated alcohols.

3,3-dimethyl-1-(trifluoromethyl)-1,2-benziodoxole] as the trifluoromethylating agent (Fig. 41).[193] The CF_3 radical, generated through reduction by the excited PC, can undergo radical addition to benzyl-protected homoallylic alcohol and amine derivatives, which upon 1,5-HAT, produce a radical that is oxidized by the oxidized PC, closing the photocatalytic cycle (Fig. 42); the corresponding benzylic carbocation is quenched by the alcohol solvent to form an acetal, with an aqueous work-up resulting in the formation of the final product. Of the PCs investigated, eosin Y produced only trace amounts of the desired product while $[Ir(ppy)_2(dtbbpy)]PF_6$ yielded 57% and 4CzIPN 69%. The more positive oxidation potential for 4CzIPN than the other PCs (E_{ox} = 1.52 V compared with 0.78 V for eosin Y and 1.21 V for the iridium PC), may account for its improved performance. Replacement of the CF_3 source, in this case Togni's reagent or CF_3SO_2Cl, with CF_3SO_2Na altered the mechanism, favouring a reductive quenching cycle instead, as had been demonstrated by Huang *et al.*[189]

Coupling of a CRF_2 group is likewise possible using photocatalysis (Fig. 43). The excited photocatalyst is first reductively quenched by an *in situ* formed hydrazone, resulting in a radical intermediate (Fig. 44). The reduced photocatalyst then generates the difluoroalkyl radical from $BrCF_2R$ by SET, closing the photocatalytic cycle. The two radical intermediates subsequently couple together to form α,α-difluoroketone hydrazones.[194] Only **4CzIPN** was considered for this reaction and investigation into the catalyst

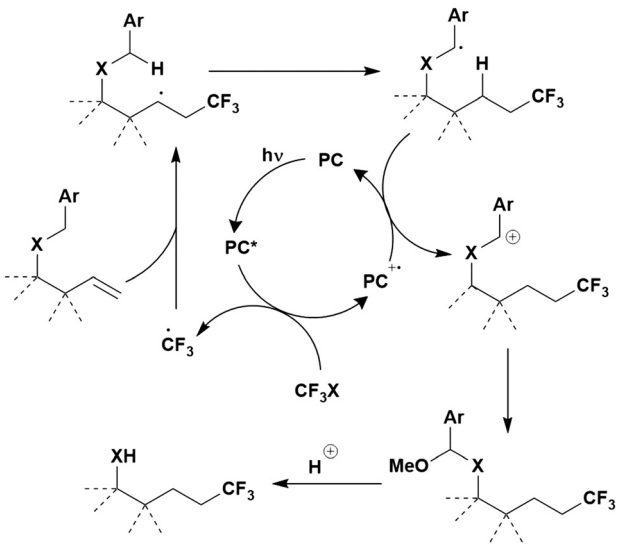

Fig. 42 Proposed mechanism for organic photoredox catalysed synthesis of δ-trifluoromethylated alcohols and amines where X = O or NAr.

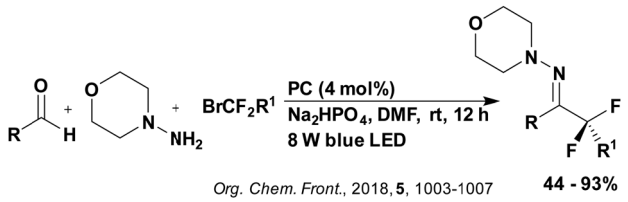

Org. Chem. Front., 2018, **5**, 1003-1007

Fig. 43 Reaction scheme for the coupling of aldehydes with hydrazines and bromodifluorinated reagents.

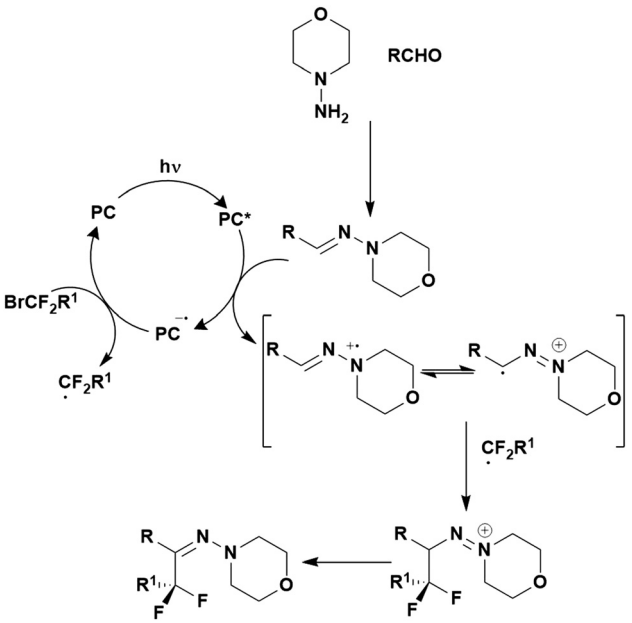

Fig. 44 Potential mechanism for the formation of α,α-difluoroketone hydrazones using photocatalysis.

loading revealed that increasing the loading from 2 to 4 mol% did little to impact the product yield (increasing from 72 to 75%). The suggested mechanism (Fig. 44) was supported by radical trapping experiments with TEMPO as well as Stern–Volmer quenching studies.

A similar example involves the fluoroalkylation of arylidene and alkylidene amidrazones (Fig. 45).[195] The putative mechanism involves first the reductive quenching of the excited PC by DABCO. The reduced PC is then proposed to reduce the fluorinated iodide reagent to yield the fluorinated radical. This radical then adds to the amidrazone and after oxidation (from oxidized DABCO) and deprotonation, the final product is formed. No evidence is provided to support this mechanism. **4CzIPN** performed very well in

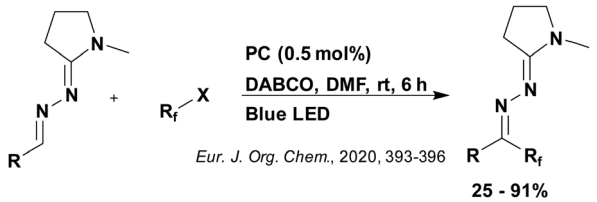

Eur. J. Org. Chem., 2020, 393-396

Fig. 45 Reaction scheme for the fluoroalkylation of arylidene and alkylidene amidrazones.

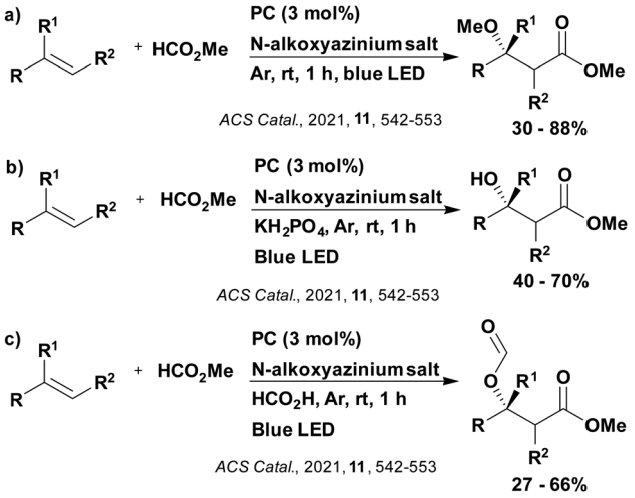

Fig. 46 Reaction schemes for the difunctionalisation of alkenes.

this reaction (89% yield), closely followed by $[Ru(bpy)_3](PF_6)_2$ (78% yield), while $[Ir(ppy)_2(dtbbpy)]PF_6$ and eosin Y acted poorly (38% and 10%, respectively). The trends in reaction yield may be linked to the photooxidising ability of the PC (E_{red}^* = 1.35 V, 0.77 V, 0.66 V and 0.83 V for **4CzIPN**, $[Ru(bpy)_3](PF_6)_2$, $[Ir(ppy)_2(dtbbpy)]PF_6$ and eosin Y, respectively), which is linked to the capacity to oxidise DABCO (E_{ox} = 0.69 V *vs.* SCE).

Alkyl formates have been utilised as precursors for alkoxycarbonyl radicals, which can then react with alkenes to form a variety of substituted alkanoates, depending on the conditions employed (Fig. 46).[196] The proposed mechanism involves oxidative quenching of the excited PC by the *N*-alkyoxyazinium salt (Fig. 47) to yield an isopropoxy radical, which first abstracts a hydrogen atom from methyl formate and then adds to the alkene. The resultant radical is oxidised by the oxidised PC. From here, products can form depending on the reaction conditions, as shown in Fig. 47. For example, when excess formic acid is present, this acts as a nucleophile and a β-formyloxy ester is produced (Fig. 46c) while when MeOH is present as the nucleophile, a β-methoxy ester is formed (Fig. 46a). Support for this mechanism was provided in the form of Stern–Volmer quenching experiments, which revealed that the *N*-alkyoxyazinium salt was responsible for quenching the excited PC. Complementary mechanistic studies involved isotope labelling, addition of radical scavengers and control experiments to investigate the role of the additives used. The 1,2-methoxy methoxycarbonylation of α-methyl styrene was investigated as the model reaction in order to determine the optimal reaction conditions. Only 3 PCs were tested, **4CzIPN** (80%), $[Ru(bpy)_3]Cl_2$ (72%) and $[Ir(dF(CF_3)ppy)_2(dtbbpy)](PF_6)$ (62%). This difference in yield seems to be a reflection of the photoreducing ability of the PC (E_{ox}^* = −1.04 V, −0.89 V and −0.81 V). Consequently, **4CzIPN** was chosen for the substrate scope.

All radical precursors shown thus far can be used to generate the corresponding radical species relatively easily through SET to or from the excited or ground state PC; however, the situation becomes more complex when the reagents used are

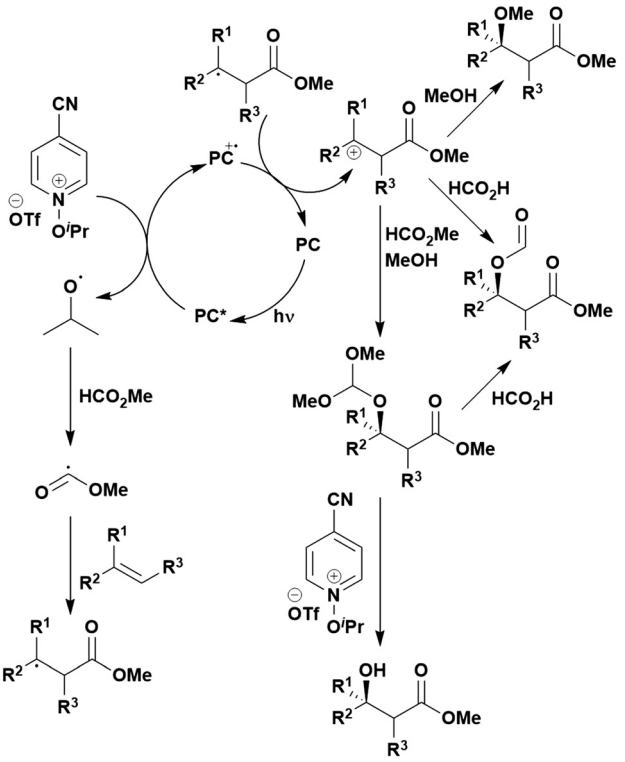

Fig. 47 Proposed mechanism for the dinfunctionalisation of alkenes using alkyl formates.

difficult to oxidise or reduce directly. This is exemplified through the use of aldehydes as radical precursors. Oxygen is required as an additive to allow for the formyl radical to be accessed, which upon dicarbonylation form alkyl radicals that can be added to heteroarenes (Fig. 48).[197] In this case, the excited PC is oxidatively quenched by oxygen, generating a superoxide radical anion, which can abstract a proton from the aldehyde, forming the acyl radical. Decarbonylation of this acyl radical followed by addition to the heteroarene and deprotonation, results in a tertiary radical species that is then oxidised by the oxidised PC (Fig. 49). This mechanism is supported by radical trapping experiments using TEMPO, whereby an adduct was formed between TEMPO and the acyl radical of the aldehyde reagent. Stern–Volmer quenching experiments identified oxygen as the only significant quencher involved in the reaction. Both **4CzIPN** and $[Ir(dF(CF_3)ppy)_2(dtbbpy)]PF_6$ provided the same yields (70% and 66%, respectively). These high yields are likely due to the strong ground state oxidation potential of these PCs (E_{ox} = 1.52 V and 1.69 V for **4CzIPN** and $[Ir(dF(CF_3)ppy)_2(dtbbpy)]PF_6$, respectively) in comparison to that of eosin Y (E_{ox} = 0.78 V), which afforded only 33% of product.

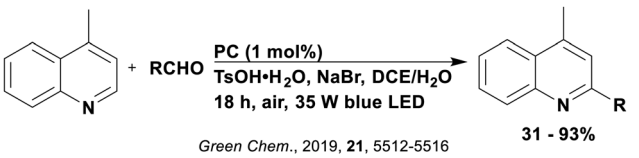

Fig. 48 Reaction scheme for the alkylation of heteroarenes using aldehydes.

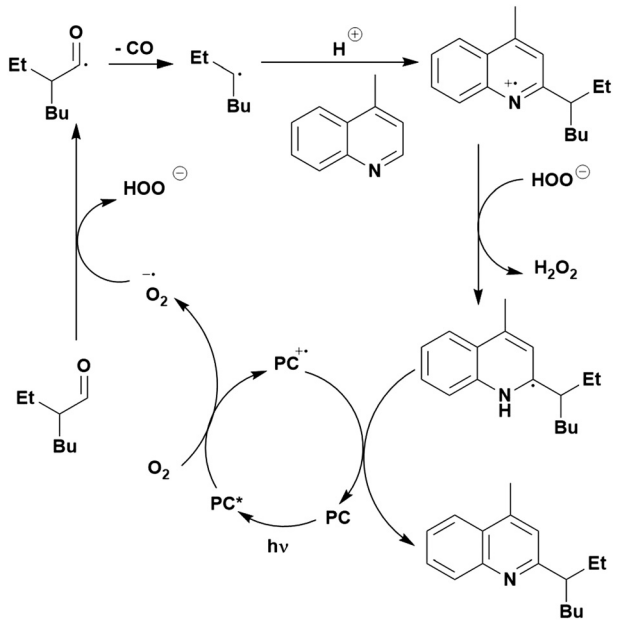

Fig. 49 Possible mechanism for the photocatalytic alkylation of heteroarenes using aldehydes.

Alternatively, LiBr has been used as an additive for accessing a formyl radical species from aldehydes as shown in the hydroxyalkylation of quinolines with aryl aldehydes (Fig. 50a)[198] and alkyl aldehydes (Fig. 50b).[199] A reductive quench of the PC is proposed to occur by the bromide anion, forming a bromyl radical, which abstracts a proton from the aldehyde *via* a deprotonated electron transfer (DPET) step (Fig. 51). The resultant acyl radical can add to the quinolines, yielding the hydroalkyl radical after subsequent deprotonation and a spin-centre shift. This radical is reduced by the reduced PC to form the product and close the photocatalytic cycle. Control deuterium labelling experiments indicated that a ketyl radical pathway was not occurring and formation of the acyl radical was likely the dominant pathway. This was further confirmed by the trapping of an acyl adduct with TEMPO, with product formation inhibited. Stern–Volmer

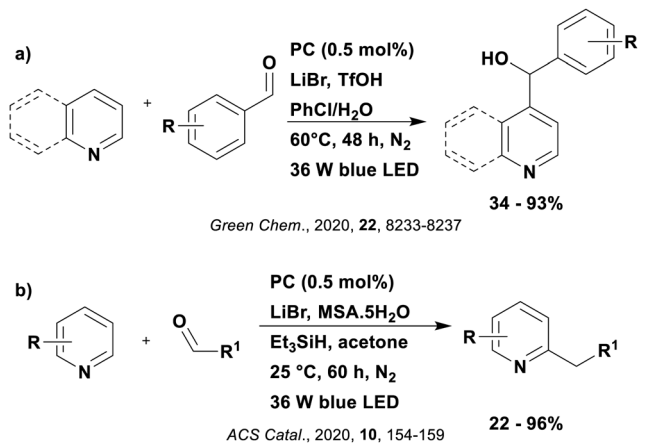

Fig. 50 Reaction scheme for the hydroxyalkylation of quinolines with (a) aryl aldehydes and (b) alkyl aldehydes.

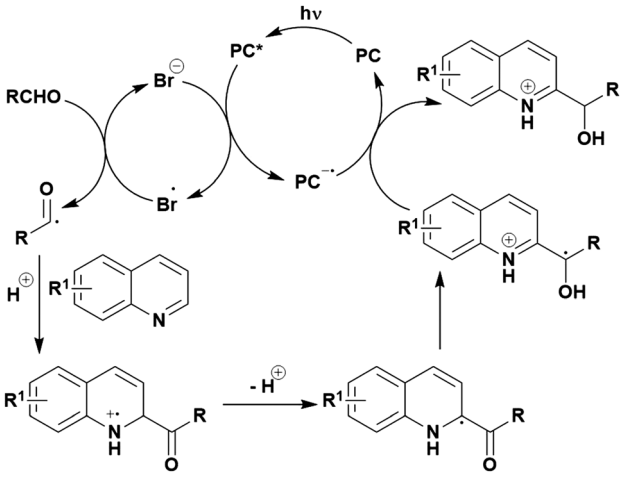

Fig. 51 Putative mechanism for the hydroxyalkylation of quinolines with aldehydes.

quenching experiments showed that only the bromide ion acted to significantly quench the luminescence of the PC.

In the coupling with alkyl aldehydes, an additional additive Et_3SiH was included, which was proposed to cause the mechanism to differ. The putative mechanism still involves the reductive quenching of the excited PC by the bromide ion, but the resultant bromyl radical then undergoes HAT with Et_3SiH. The silyl radical adds to the aldehyde to form a nucleophilic silylether radical, which then adds to the protonated heteroarene. The mechanism then follows similarly to that shown in Fig. 51, where deprotonation followed by spin-centre shift (and elimination of triethylsilanol) forms a carbon-centred radical that is then reduced by the reduced PC to yield the final product.

Only **4CzIPN** and $[Ir(dF(CF_3)ppy)_2(dtbbpy)]PF_6$ were investigated as PCs in the coupling with aryl aldehdyes,[198] providing yields of 77% and 66%, respectively. The relative yields correlate with the photooxidising ability of the PC (E_{red}^* = 1.35 V and 1.21 V for **4CzIPN** and $[Ir(dF(CF_3)ppy)_2(dtbbpy)]PF_6$, respectively), which must be capable of oxidising the bromide anion. Since single electron oxidation of halides cannot accurately be determined by cyclic voltammetry, recent estimations from Marcus theory suggest the single electron oxidation of bromide in MeCN is E_{ox} = 1.11 V *vs.* SCE.[200] The greater thermodynamic driving force for **4CzIPN** for the oxidation of bromide may explain the higher product yield for this PC.

In the follow up study with alkyl aldehydes, $[Ir(dF(CF_3)ppy)_2(dtbbpy)]PF_6$ shown to be superior to **4CzIPN** (60% and 41%, respectively), while the other PCs employed, such as eosin Y or $[Ru(bpy)_3](PF_6)_2$, could not complete the transformation.[199] These other PCs are likely to have failed on account of their poor photooxidising ability (E_{red}^* = 0.83 V and 0.77 V for eosin Y and $[Ru(bpy)_3](PF_6)_2$, respectively). It is unclear why the iridium PC outperformed **4CzIPN** in this case.

The use of bromide ions to facilitate the formation of radical species can also be seen in the coupling of alkyl bromides and heteroarenes using silyl-mediated visible light photocatalysis (Fig. 52).[201] The excited PC oxidises the bromide ion, generating

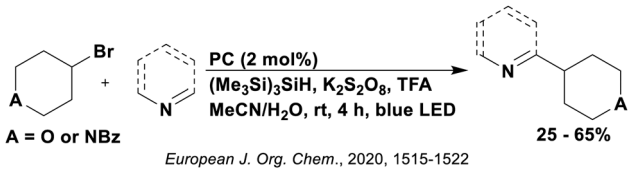

Fig. 52 Reaction scheme for the coupling of alkyl bromides and heteroarenes, where A = O or NBz.

an electrophilic bromyl radical (Fig. 53). This radical then abstracts a hydrogen atom from $(Me_3Si)_3SiH$, producing a silyl radical species, which in turn abstracts the halogen atom from the alkyl bromide. The resultant alkyl radical then undergoes a radical addition mechanism with the protonated heteroarene, forming the alkylated product. The photocatalytic cycle is closed in the presence of a sacrificial perfsulfate oxidant. Both **4CzIPN** and $[Ir(dF(CF_3)ppy)_2(dtbbpy)]PF_6$ were evaluated as the photocatalyst for this reaction, with **4CzIPN** providing slightly superior yields (81% and 70%, respectively), which may be linked to its greater photooxidizing power (E_{red}^* = 1.35 V for **4CzIPN** *vs.* 1.21 V for the iridium photocatalyst).

The aid of the hypervalent iodine oxidant trifluoroacetoxyiodobenzene (PIFA), which is reduced in the presence of the excited photocatalyst, helps to promote the formation of radicals that may be difficult to generate through direct oxidation/reduction from the PC. The resultant iodanyl radical is then used to generate the alkyl radical *via* H-atom abstraction from the substrate. Three mechanistically related examples involving PIFA have been reported: the oxidative alkylation of unactivated alkenes with DMSO (Fig. 54a),[202] of *N*-aryl/benzoyl acrylamides with acetonitrile (Fig. 54b)[203] and of alkenes with carbonyl compounds (Fig. 54c).[204] In the former, α-sulfinyl radicals are generated from DMSO, which then add to a α,α-diaryl allylic alcohol,

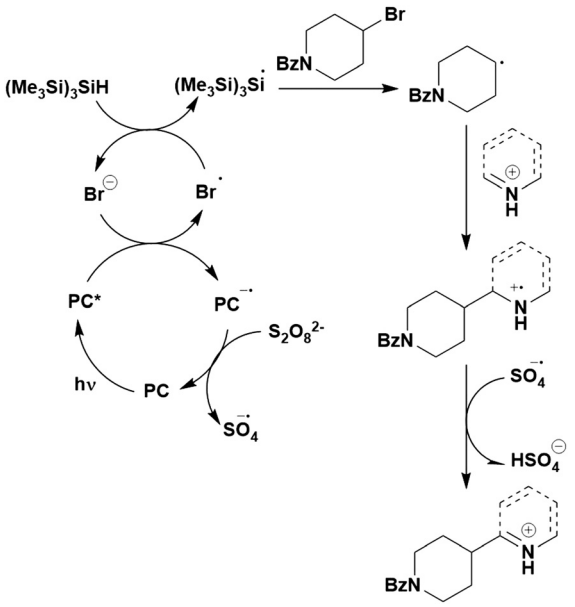

Fig. 53 Proposed mechanism for the coupling of unactivated alkyl bromides with heterocycles.

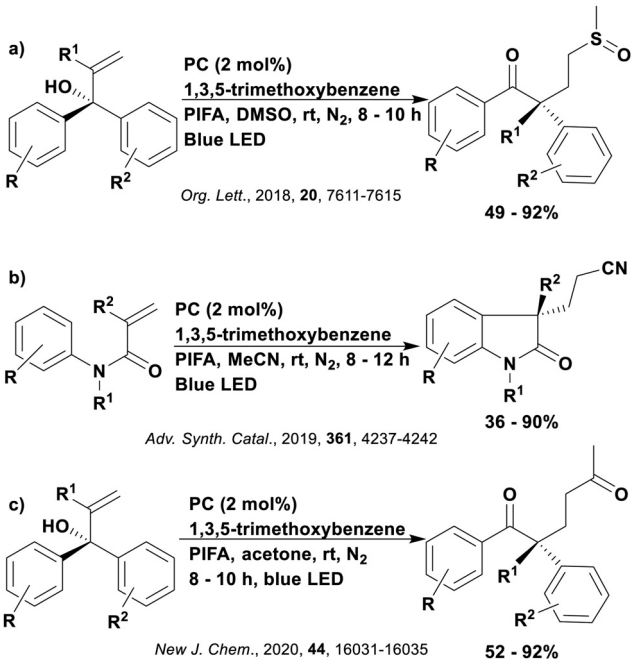

Fig. 54 Reaction schemes for (a) oxidative alkylation of unactivated alkenes with DMSO, (b) oxidative alkylarylation of *N*-aryl/benzoyl acrylamides and (c) oxidative alkylation of alkenes with carbonyl compounds.

producing α-aryl-γ-methylsulfinyl ketones (Fig. 54a).[202] Stern-Vomer quenching experiments support the proposed mechanism (Fig. 55) since quenching of the PC is only observed with the hypervalent iodide compound, not the alcohol. Of the PCs tested, **4CzIPN** provided a considerably greater yield of 89% in comparison to $[Ru(bpy)_3](PF_6)_2$ (23%) and $[Ir(dF(CF_3)ppy)_2(dtbbpy)]PF_6$ (47%). The higher yield is likely due to the greater reducing power of **4CzIPN** in the excited state (E_{ox}^* = −1.04 V for **4CzIPN**, −0.81 V for $[Ru(bpy)_3](PF_6)_2$ and −0.89 V for $[Ir(dF(CF_3)ppy)(dtbbpy)]PF_6$.

A similar mechanism was invoked for the oxidative alkylarylation of *N*-aryl/benzoyl acrylamides (Fig. 54b), whereby the iodanyl radical was used to abstract a H atom from acetonitrile, generating the key alkyl radical, which in turn adds to the *N*-aryl acrylamide.[203] Subsequent cyclisation, oxidation and deprotonation results in the required product. This mechanism was supported by radical trapping experiments with TEMPO, as well as Stern–Volmer quenching studies. Kinetic isotope effect studies (K_H/K_D = 3.2) implied that the C–H bond cleavage is likely to be the rate-determining step. **4CzIPN** performed similarly to both $[Ru(bpy)_3]Cl_2$ and $[Ir(dF(CF_3)ppy)_2(dtbbpy)]PF_6$, (82%, 76% and 79% product yields, respectively), and was chosen as the PC for the remainder of the study.

Fig. 54c documents the oxidative alkylation of alkenes with carbonyl compounds.[204] In this case, the iodanyl radical abstracts a H atom from acetone to generate the α-carbonyl alkyl radical, which then adds to the alkene. Addition of TEMPO inhibits the reaction and a kinetic isotope effect of K_H/K_D = 5.6 again implies that the C–H bond cleavage constitutes the rate determining step. In the PC screen, **4CzIPN** yielded 78% of product, similar to that of $[Ir(dF(CF_3)ppy)_2(dtbbpy)]PF_6$ at 72%. This modest statistically

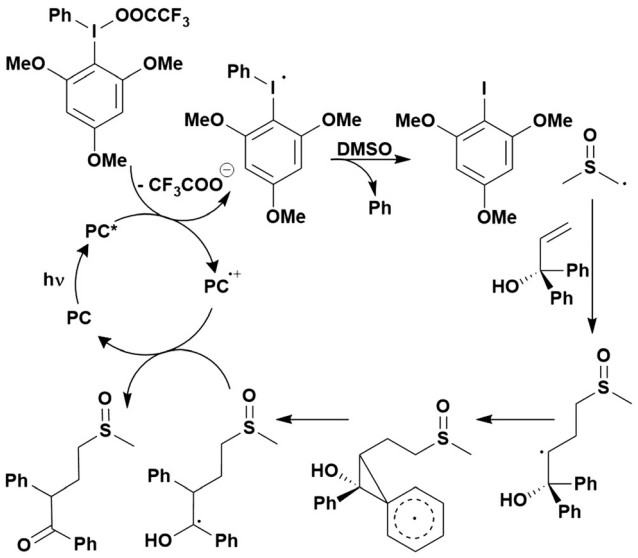

Fig. 55 Suggested mechanism for the oxidative alkylation of alkenes using DMSO.

different yield may relate to the slightly stronger photoreducing ability of **4CzIPN**.

As previously discussed, alkyl or haloalkyl radicals generated from radical precursors can then add to alkenes to form alkylated products. An alternative reaction pathway can involve reduction of the radical intermediate to the anion, which then can undergo a cyclisation reaction (Fig. 56a–c) in the presence of a remote leaving group. For example, cyclopropanation can occur through anionic 3-*exo-tet* ring closure (Fig. 56a with the mechanism shown in Fig. 57).[205,206] Additionally, 4-*exo-tet* cyclisation can be observed to form functionalised cyclobutanes (Fig. 56b), and further functionalised cycloalkanes can also be synthesised depending on the length of the alkyl chain linking the halide leaving group to the alkene.[207] The proposed mechanism was

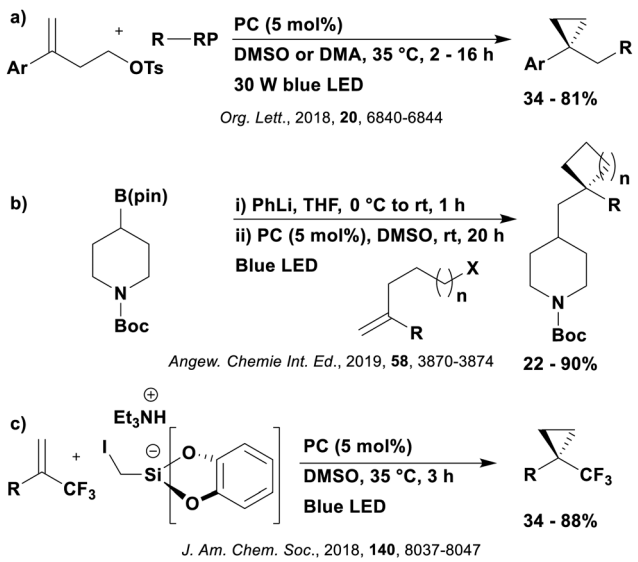

Fig. 56 Reaction schemes for using radical precursors (RP) in cyclisation reactions; (a and c) cyclopropanes and (b) cyclobutanes.

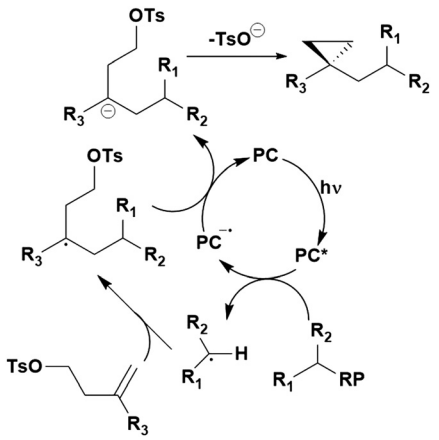

Fig. 57 Viable mechanism for photocatalysed cyclopropanation where RP is radical precursor.

supported by Stern–Volmer quenching studies, and a quantum yield value of 0.066 indicates the likely absence of a radical chain process.[206]

$[Ir(dF(CF_3)ppy)_2(bpy)]PF_6$, $[Ru(bpy)_3](PF_6)_2$ and **4CzIPN** all performed similarly in the cyclopropanation reaction involving styrene and a silicate radical precursor (Fig. 56a, 94%, 88% and 87%, respectively);[205] **4CzIPN** was chosen as the PC due to cost considerations. Interestingly, in the cyclopropanation with trifluoromethyl-substituted alkenes (Fig. 56c), **4CzIPN** and $[Ir(dF(CF_3)ppy)_2(dtbbpy)]PF_6$ afforded the same high product yield (94% and 92%, respectively) while $[Ru(bpy)_3](PF_6)_2$ and *fac*-$Ir(ppy)_3$ provided lower yields (71% and 74%, respectively).[206] The low oxidation potential of silicates (E_{ox} = 0.4–0.7 V) should allow the SET to be thermodynamically feasible for most of PCs studied (E_{red}^* = 1.32 V, 1.21 V and 1.35 V for $[Ir(dF(CF_3)ppy)_2(bpy)]PF_6$, $[Ir(dF(CF_3)ppy)_2(dtbbpy)]PF_6$ and **4CzIPN**, respectively) but this step may be more challenging for the less photooxidising PCs (E_{red}^* = 0.77 V and 0.31 V for $[Ru(bpy)_3](PF_6)_2$ and *fac*-$Ir(ppy)_3$, respectively). For the cyclobutanation reaction (Fig. 56b), **4CzIPN** significantly outperformed alternative PCs (70% yield for **4CzIPN**, but only 46% for $[Ir(dF(CF_3)ppy)_2(bpy)]PF_6$).[207] This difference in yield is a result of the iridium PC producing a Giese-type side product in addition to the cyclised product (Fig. 58). The Giese-type side product is only observed with **4CzIPN** if the reaction is conducted in the presence of water.

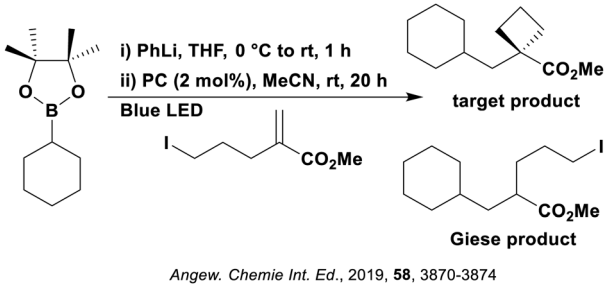

Fig. 58 Reaction scheme for the cyclobutanation reaction showing the different products than can be obtained.

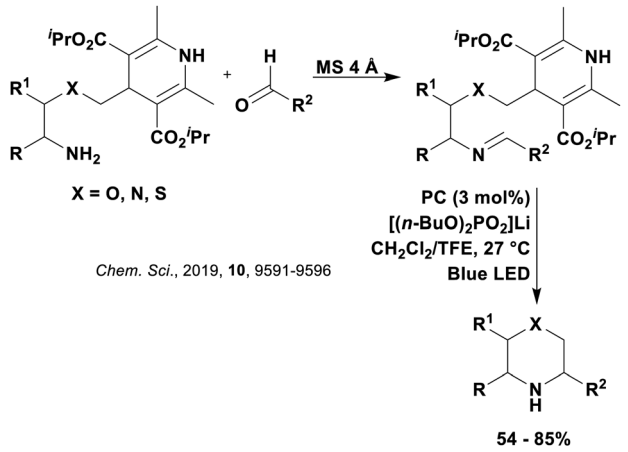

Chem. Sci., 2019, **10**, 9591-9596

Fig. 59 Reaction scheme for the photocatalytic cyclisation of imino tethered DHPs to form N-containing heterocycles.

Photocatalytic cyclisation reactions can be applied to the formation nitrogen heterocycles from imino-tethered DHPs (Fig. 59).[208] This reaction proceeds *via* a proton coupled electron transfer (PCET) mechanism, as shown in Fig. 60, with the excited PC being reductively quenched by the imino-DHP, facilitated by the presence of the Brønsted-basic phosphate anion. The α-heteroatom-stabilised radical that eventually forms, undergoes a 6-*endo-trig* cyclisation to produce the cyclised product containing a nitrogen-centred radical. This radical intermediate can then be reduced by the reduced PC, closing the photocatalytic cycle, and generating the final product. Since the imino-DHPs have oxidation potentials ranging from E_{ox} = 1.01 V to 1.23 V, the PC should have a moderate to strong photooxidising power. **4CzIPN** was considered alongside iridium and ruthenium PCs. Only $[Ir(dF(CF_3)ppy)_2(bpy)]PF_6$ and $[Ir(dF(CF_3)ppy)_2(dtbbpy)]PF_6$ were shown to provide comparable yields as **4CzIPN** (33%, 25% and 20% yields, respectively); the poor yield of 9% from $[Ru(bpy)_3](PF_6)_2$ is likely related to its poor photooxidising ability (E_{red}^* = 0.77 V compared to 1.35 V for **4CzIPN**).

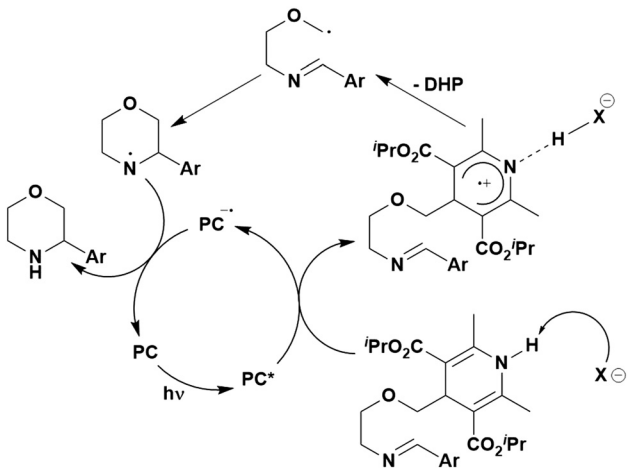

Fig. 60 Suggested mechanism for the photocatalytic cyclisation of imino-tethered DHPs to form heterocycles.

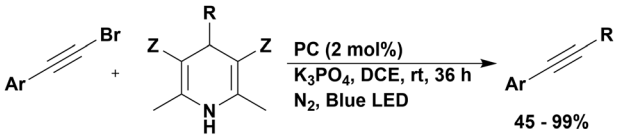

Org. Biomol. Chem., 2019, **17**, 181-185

Fig. 61 Reaction scheme for the coupling of alkynyl bromides and Hantzsch esters to synthesise internal alkynes where Z = CO_2Et or CN.

The preceding examples involve a C(sp^3)–C(sp^2) type coupling, but C(sp^3)–C(sp) coupling reactions have also been reported using **4CzIPN** as the photocatalyst. Ye *et al.* reported the coupling of alkynyl bromides with Hantzsch esters to produce internal alkynes (Fig. 61).[209] In an analogous fashion to the work of Molander *et al.* with heteroaryl sulfones,[177] a Hantzsch ester was used as the alkyl radical precursor under reductive quenching conditions. The nucleophilic alkyl radical then adds to the electrophilic alkynyl carbon, producing a vinylic radical intermediate (Fig. 62). This collapses to give a bromyl radical and alkylated alkyne. The photocatalytic cycle is closed by reduction of the bromyl radical. Similar yields were obtained for $[Ru(bpy)_3]Cl_2$, *fac*-$Ir(ppy)_3$ and **4CzIPN** (76%, 71% and 70%, respectively), with **4CzIPN** being chosen as the optimal PC as it was considered to be more environmentally benign.

Photocatalytic C–C and C–X bond formation can occur *via* an energy transfer mechanism, rather than *via* an electron transfer as has been the case for the aforementioned examples. A first example of PEnT involves the cross-dehydrogenative coupling of C(sp^3)–H-containing compounds with *N*-heteroarenes (Fig. 63).[210]

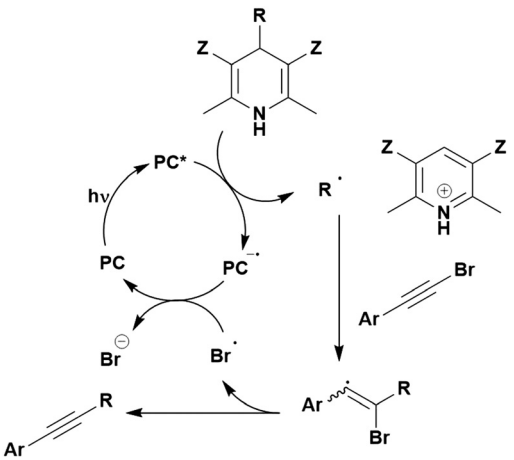

Fig. 62 Potential mechanism for the coupling of alkynyl bromides with Hantzsch esters using visible light mediated photocatalysis, where Z = CO_2Et or CN.

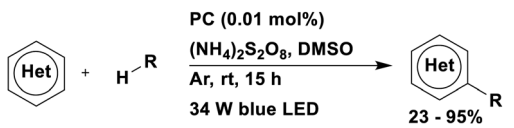

Org. Lett., 2020, **22**, 7709-7715

Fig. 63 Reaction scheme for the dehydrogenative cross-coupling of C(sp^3)–H with *N*-heteroarenes.

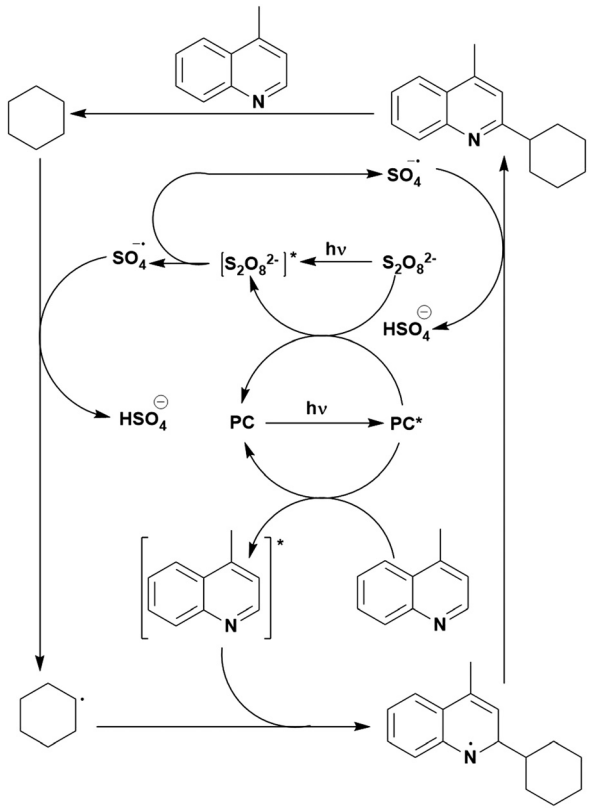

Fig. 64 Viable mechanism for the dehydrogenative cross-coupling of cyclohexane with lepidine.

Two energy transfer pathways are proposed to be operational (Fig. 64). The minor pathway involves PEnT from the excited PC to $(NH_4)_2S_2O_8$, resulting in homolysis and the formation of two sulfate radicals. Hydrogen atom transfer occurs between the sulfate radical and cyclohexane, the C(sp^3)–H source in this example, to form a cyclohexyl radical. In the dominant PEnT pathway, the excited PC transfers energy to the heteroarene, lepidine, which can then react with the cyclohexyl radical. The sulfate radical then abstracts a hydrogen from this adduct to yield the final product.

Support for the dual PEnT mechanism is provided in Stern–Volmer quenching experiments, whereby both $(NH_4)_2S_2O_8$ and lepidine can quench the excited PC, although the latter does so at a significantly faster rate (K_{SV} = 0.038 and 0.28, respectively). Kinetic isotope effect studies suggest that the C–H activation is the rate determining step. The process was confirmed to involve radicals as the addition of TEMPO inhibited the reaction and the presence of diphenylethene resulted in the formation of a cyclohexyl-containing adduct. EPR spectroscopy confirmed the presence of the sulfate radicals and that irradiation was necessary for their formation. No additional radical signals were observed when adding PC to the peroxydisulfate under irradiation, suggesting that the reaction proceeds *via* PEnT rather than PET.

Both 4CzIPN and $[Ir(dF(CF_3)ppy)_2(dtbbpy)]PF_6$ afforded the same yields (82% and 77%, respectively), which is likely due to their similar triplet state energies [E_T = 2.58 eV (249 kJ mol^{-1}) and 2.61 eV (251 kJ mol^{-1}), respectively]. Other PCs tested

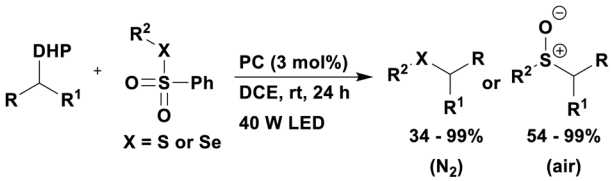

Org. Lett., 2020, **22**, 4908-4913

Fig. 65 Reaction scheme for the cross-coupling of DHPs with thiosulfonates or selenium sulfonates.

provided much low yields (6–22%), which is likely due to their lower triplet state energies [1.77 eV (171 kJ mol^{-1}) – 2.51 eV (242 kJ mol^{-1} for eosin Y and *fac*-Ir(ppy)$_3$, respectively].

Photoinduced energy transfer is also proposed to be involved in the cross-coupling of DHPs with thiosulfonates or selenium sulfonates (Fig. 65); however, in this case, the PEnT proceeds in tandem with photoinduced electron transfer.[211] In the putative mechanism, reductive quenching of the excited PC by the DHP radical precursor to release the alkyl radical first occurs (Fig. 66). This alkyl radical reacts with the thiosulfonate, forming the functionalised product and a sulfone radical intermediate. Reduction of this intermediate by the reduced PC followed by protonation yields a benzosulfinic acid. When conducted under nitrogen, the reaction stops here; however, in the presence of air, the authors suggest the excited PC can also undergo energy transfer to form singlet oxygen, which is then responsible for oxidizing the sulfide to the corresponding sulfoxide. To probe the reaction mechanism, TEMPO was added, which resulted in inhibition of product formation, confirming this is a radical process. When the thiosulfonate was replaced with PhSSPh no product was formed, implying that PhSSPh is not an intermediate in this process. However, no mechanistic support was provided to substantiate the energy transfer portion of this proposed mechanism. The same yields

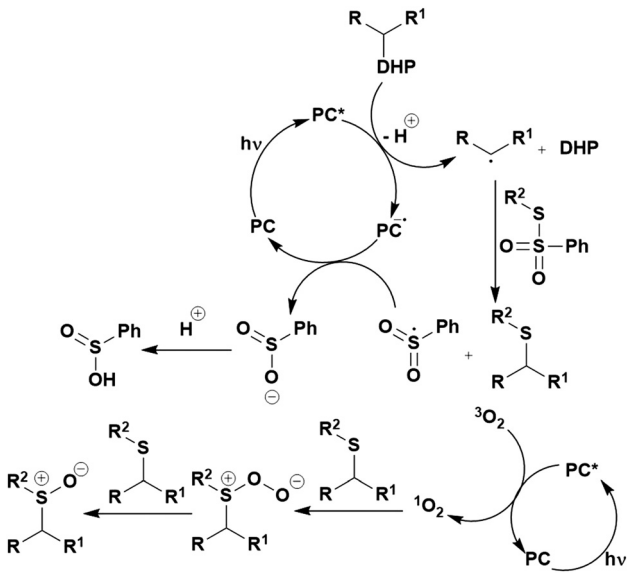

Fig. 66 Putative mechanism for the cross-coupling of DHPs with thiosulfonates.

were obtained using *fac*-Ir(ppy)$_3$, **4CzIPN** and eosin Y as PCs under N_2 (77%, 81% and 76%, respectively) while the use $[Ir(ppy)_2(dtbbpy)]PF_6$ proved to be slightly less successful (64%). There is no obvious correlation between the redox potentials and the yields obtained.

Oxidation and reduction reactions

Photoredox catalysis also has broad applications in oxidation and reduction reactions. For instance, photocatalytic reduction of enamides to form α-amino carbanions can be reacted with CO_2 in order to generate α,α-disubstituted α-amino acids (Fig. 67a).[212] This reaction is hypothesized to proceed *via* a reductive quenching cycle of the photocatalyst, although a complete mechanism is not proposed. From Stern–Volmer quenching studies, it was surmised that the excited PC undergoes SET from DIPEA to generate the reduced photocatalyst, which then reduces the enamide to form an α-amino carbanion, which is then trapped by CO_2 synthesising the conjugate base of the α,α-disubstituted α-amino acid. **4CzIPN** gave the highest yield of all photocatalysts tested at 85% compared with 65% for $[Ir(ppy)_2(dtbbpy)]PF_6$, 62% for $[Ir(dF(CF_3)ppy)_2(dtbbpy)]PF_6$ and 17% for *fac*-Ir(ppy)$_3$. The higher yield obtained by **4CzIPN** may be related to its photooxidising strength compared to the other PCs (E_{red}^* = 1.35 V for **4CzIPN** compared to 0.66 V for $[Ir(ppy)_2(dtbbpy)]PF_6$, 1.21 V for $[Ir(dF(CF_3)ppy)_2(dtbbpy)]PF_6$ and 0.31 V for *fac*-Ir(ppy)$_3$), especially given the oxidation potential of DIPEA is E_{ox} = 0.81 V.[35]

Direct reductive amination is also possible using photocatalysis whereby aromatic aldehydes may be converted to tertiary amines (Fig. 67b).[213] This is possible though oxidation of an *in situ* formed aminal intermediate by the excited photocatalyst, forming the α-amino radical (Fig. 68), which then undergoes fragmentation, reduction by the photocatalyst and protonation, affording the desired product. For photocatalyst screening, 2 mol% of $[Ir(dF(CF_3)ppy)_2(bpy)]PF_6$ produced superior yields of 78% while when 5 mol% of **4CzIPN** was used, only 53% of product was isolated. This difference in PC loading makes a direct comparison of the photocatalysts challenging.

An example of the use of **4CzIPN** as a PC in a rather different context is directed towards the heterogeneous photocatalytic degradation of lignin. The degradation of lignin, which is typically treated as a waste product, to obtain small molecules or value-added energy fuels has received significant attention.[214,215]

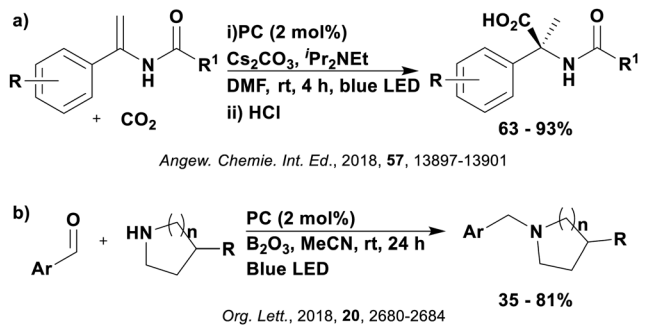

Fig. 67 Reaction scheme for (a) reduction of enamides and (b) reductive amination.

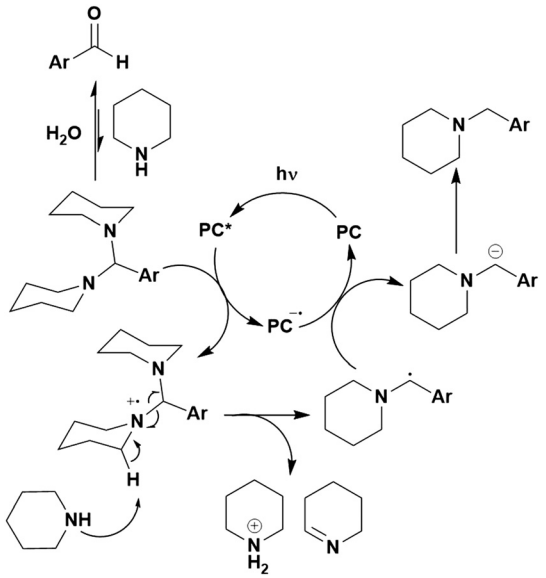

Fig. 68 Plausible mechanism for photoredox catalysed reductive amination.

The popular two-step approach to degrade lignin involves both oxidation and reduction steps; selective oxidation of the benzylic β-O-4 alcohol to benzylic β-O-4 ketone followed by a reduction to cleave the C–O bond (Fig. 69a).[216] Porous organic frameworks (POFs) have been considered as photocatalysts for this process[217] and the following is an example of their use. Zhang *et al.* synthesised copolymers of 1,4-bis(9*H*-carbazol-9-yl)benzene (DCB) (Fig. 69b) and **4CzIPN** to form carbazolic copolymers (CzCPs).[35] In these polymers, DCB acts as the electron donor component to allow for the reduction of the lignin models while **4CzIPN** is the electron acceptor moiety responsible for the oxidation step. Varying the ratio of DCB and **4CzIPN** results in CzCPs with tuneable redox properties. Nine of these copolymers were synthesised with D:A ratios varying from 100 : 0 (CzCP0) and 0 : 100 (CzCP100). Increasing the ratio of the **4CzIPN** acceptor component results in a stabilisation of the LUMO energy level, making the photocatalyst increasingly oxidising in the ground state.

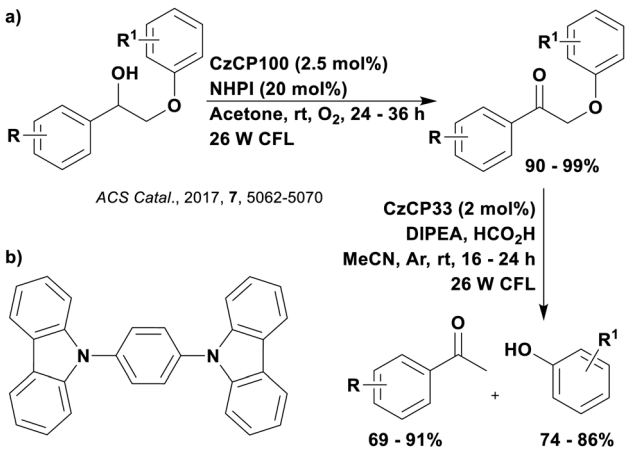

Fig. 69 a) Reaction scheme for the degradation of lignin models and b) the structure of the donor molecule used in the POFs of CzCPs.

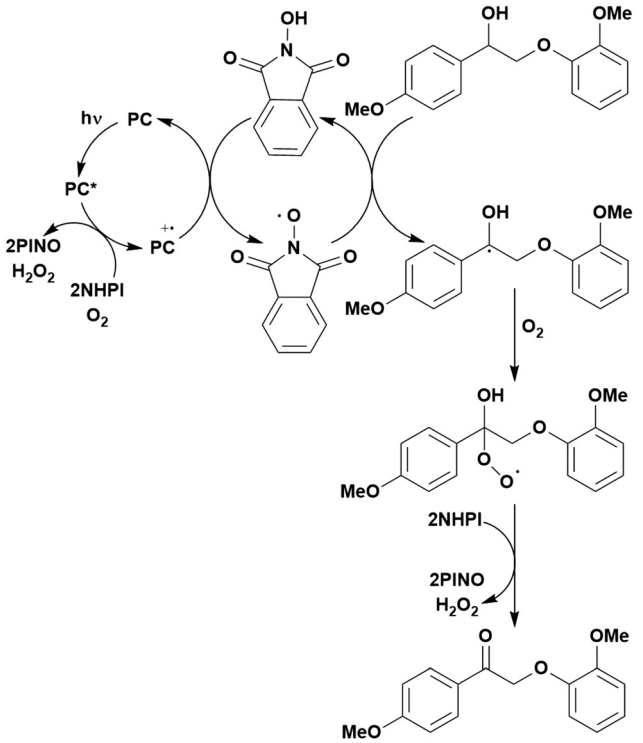

Fig. 70 Photocatalytic oxidation of β-O-4 lignin alcohols.

To evaluate the effectiveness of the CzCPs towards lignin degradation, the initial oxidation step of β-O-4 lignin alcohols was first considered, for which an oxidative quenching mechanism of the photocatalyst is observed (Fig. 70). The photocatalyst CzCP100 (0 DCB: 100 **4CzIPN**) proved most successful, obtaining 100% conversion and 99% yield. As the ratio of **4CzIPN** in the copolymer decreases, the conversion and yield also decreased accordingly; for example, CzCP0 (100 DCB: 0 **4CzIPN**) resulted in 55% conversion and 52% yield. These results are reflective of the stronger ground state oxidising capacity of CzCP100 (E_{ox} = 1.83 V) compared to CzCP0 (E_{ox} = 1.23 V), facilitating the required SET. For comparison, $[Ru(bpz)_3]^{2+}$ provides a comparable yield as CzCP100 (15% and 11% yield of product, respectively, as *N*-hydroxyphthalimide (NHPI) was not used), likely owing to its similar E_{ox} = 1.86 V. Alternative catalytic systems used for the degradation of lignin, such as *tert*-butyl nitrate/DDQ[218] and 1,4-benzoquinone[219] were also tested with the former producing a yield of 99% and the latter a 59% yield in comparison to the 99% yield from the CzCP100/NHPI/O_2 system.

The reduction step involving C–O bond cleavage of β-O-4 ketones was next investigated, whereby the ground state reduction potential of the PC was identified as the key parameter (Fig. 71). Since a higher ratio of the donor component results in a more reducing ground state reduction potential (E_{red} = −2.09 V and −0.99 V for Cz:CP33 and CzCP100, respectively), it was predicted that the polymers with a greater amount of the donor would prove better in this reaction. In reality, the copolymer Cz:CP33 obtained the highest yield of 89%, with Cz:CP0 only yielding 30% of product. Ground and excited state reduction potentials have not been defined for the

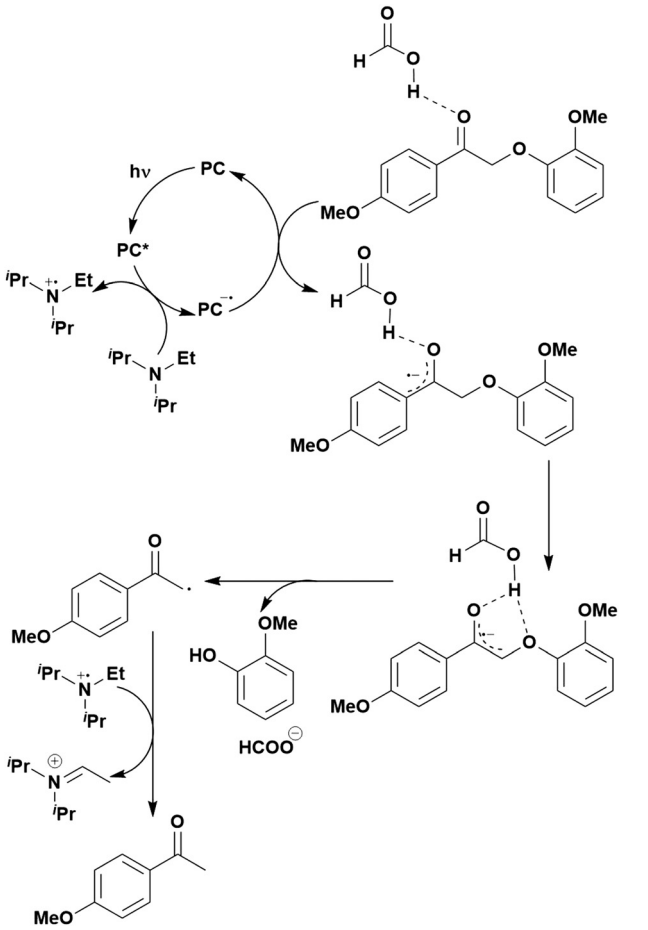

Fig. 71 Photocatalytic reduction of lignin β -O-4 ketones.

CzCP0 copolymer. Unfortunately, comparison with reference photocatalysts used for lignin degradation were not provided.

Cyclisation reactions

A phosphorus radical-mediated cascade cyclisation of 1,6-diynes (Fig. 72a) that proceeds *via* an oxidative quench of the photocatalyst (Fig. 73) has been reported.[220] This mechanism was supported by Stern–Volmer quenching studies alongside radical trapping experiments. In this study, Xu *et al.* developed a family of highly photoreducing, substituted 5,12-dihydroquinoxalino[2,3-b]quinoxaline organic PCs (Fig. 72b) with E_{ox}^* = −1.79 to −2.31 V. These gave higher product yields (51–80%) than **4CzIPN** (E_{ox}^* = −1.04 V, 40% product yield), although this can be rationalised by their stronger reducing capacity in the excited state, which is required to reduce the pyridinium oxidant.

Cyclisation reactions are also possible through a reductive quenching mechanism, for example in the preparation of heterocycles *via* the selenation of olefins (Fig. 74a),[221] the synthesis of 2-phosphorylated thioflavones (Fig. 74b),[222] the synthesis of 3-phosphorylated benzothiphenes (Fig. 74c),[223] the formation of polysubstituted γ-lactones (Fig. 74d)[224] and the dearomative arylcarboxylation of indoles (Fig. 74e).[225] The first involves aerobic dehydrogenative cyclisation of alkenes with diaryl diselenides.[221] The diselenide undergoes SET to the excited PC, with the resultant

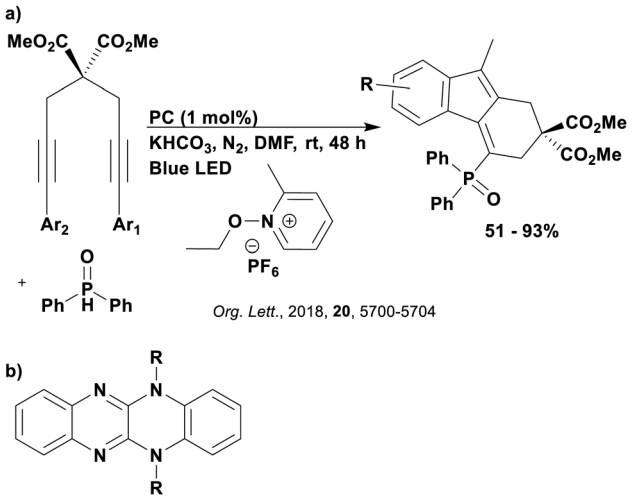

Fig. 72 (a) Reaction scheme for the cyclisation of 1,6-diynes and (b) generic structure of the organic photocatalyst developed for the cyclisation of 1,6-diynes where R = H, Et, Ph, *p*-$OMeC_6H_5$ or *p*-$CF_3C_6H_5$.

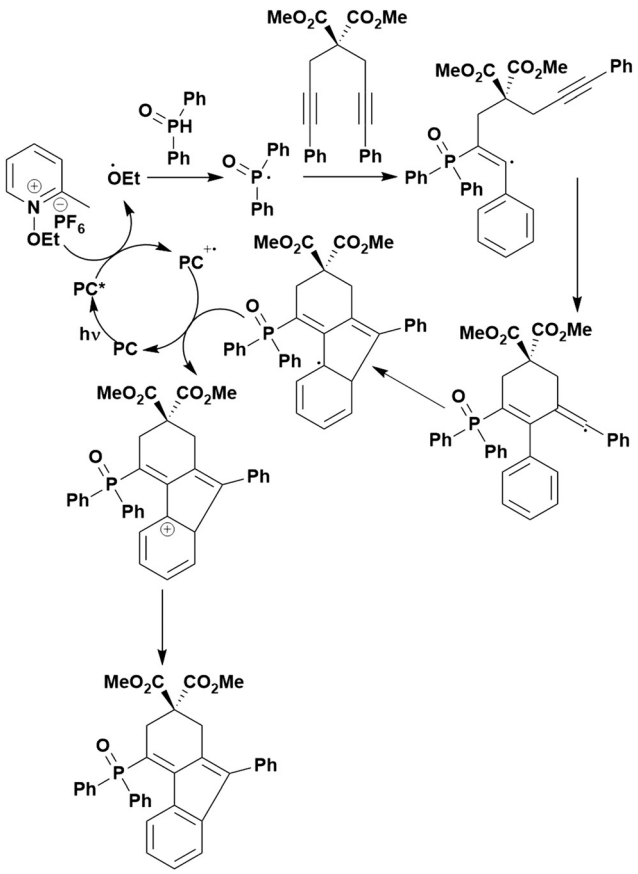

Fig. 73 Proposed mechanism for the phosphorus radical-mediated cascade cyclisation of 1,6-diynes using photoredox catalysis.

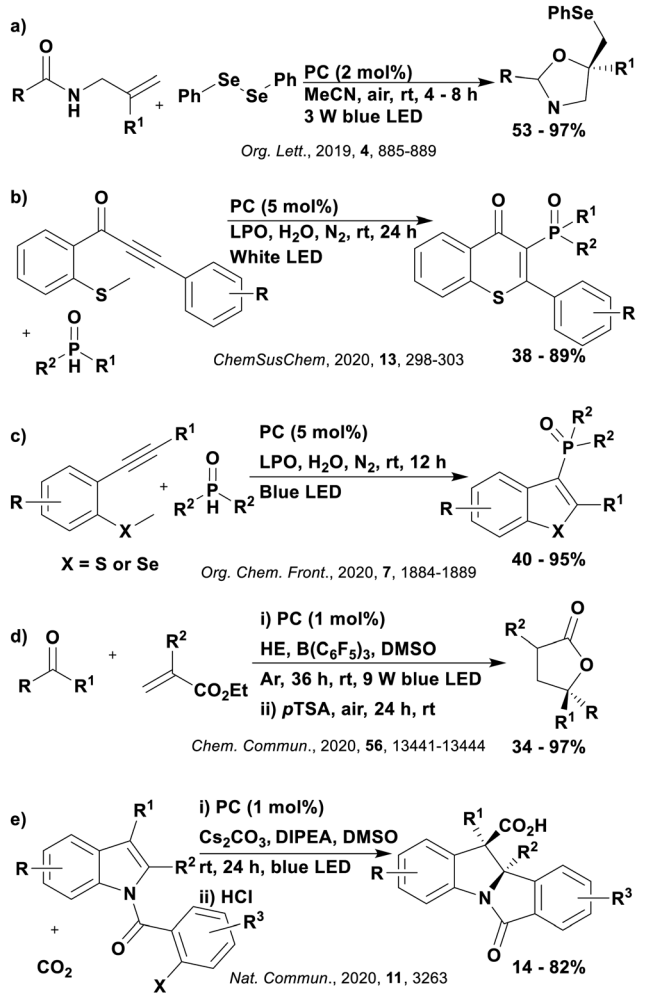

Fig. 74 Reaction scheme for cyclisation reactions that proceed *via* a reductive quenching cycle: (a) preparation of heterocycles, (b) synthesis of 2-phosphorylated thioflavones, (c) synthesis of 3-phosphorylated benzothiophenes, (d) polysubstituted γ-lactone formation and (e) the dearomative arylcarboxylation of indoles.

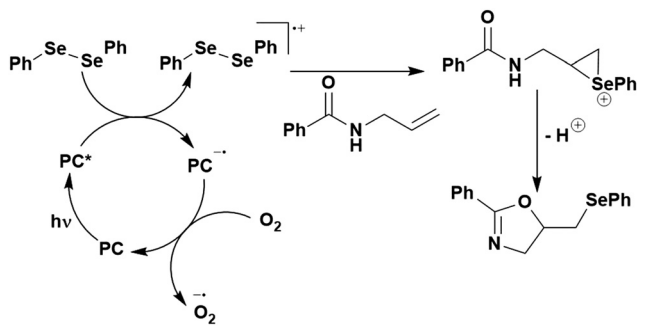

Fig. 75 Possible mechanism for photocatalytic heterocycle formation.

radical cationic diselenide intermediate activated towards attack by pendant alkenes. This forms a reactive cationic phenylselenium species, which rearranges to the selenophane-decorated oxazoline (Fig. 75). Molecular oxygen is used as a sacrificial oxidant to close the photocatalytic cycle. Only organic PCs were screened for this reaction, of which **4CzIPN** produced the highest product yield (94% obtained after 4 hours), which was matched by $[Mes\text{-}Acr]^+$ (90% after 2 hours). Since the oxidation potential of diphenyl selenide is E_{ox} = 1.35 V, photocatalysts with a more positive E_{red}^* should be thermodynamically capable of completing the SET

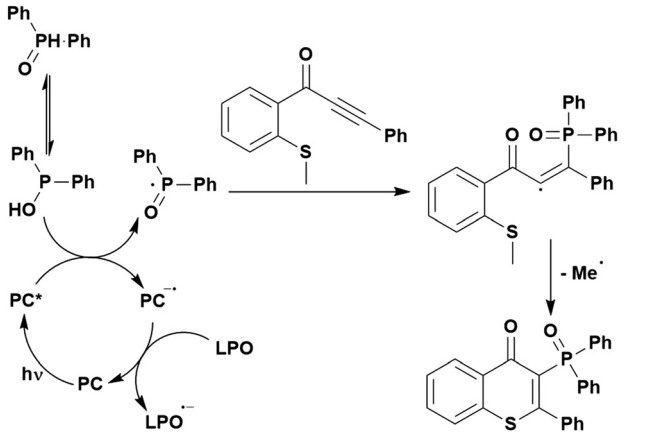

Fig. 76 Proposed mechanism for the synthesis of 2-phosphorylated thioflavones.

(E_{red}* = 2.06 V and 1.35 V for $[Mes\text{-}Acr]^+$ and **4CzIPN**, respectively), which contributes to the success of both PCs in this reaction.

In the synthesis of 2-phosphorylated thioflavones (Fig. 74b), the excited PC is reductively quenched by the diphenylphosphine oxide, resulting in a phosphoryl radical, which adds to the alkyne of the methylthiolated phenylpropynone (Fig. 76).[222] Intramolecular cyclisation affords the final product. The photocatalyst is regenerated by SET to dilauroyl peroxide (LPO). Evidence for this mechanism was obtained by experiments that showed the suppression of the reaction upon addition of TEMPO, suggesting a radical process, while a quantum yield of 0.24 indicates a radical chain mechanism is unlikely. By contrast, in the proposed mechanism for the synthesis of 3-phosphorylated benzothiophenes (Fig. 74c),[223] the excited photocatalyst is quenched by the methylthiolated alkyne. The resulting radical couples with the phosphoryl radical generated from irradiation of diphenylphosphine oxide in the presence of LPO. Consistent with the proposed mechanism in Fig. 76, the reduced photocatalyst reduces LPO to close the photocatalytic cycle. Stern–Volmer quenching studies support the putative mechanism as the alkyne was observed to quench the luminescence of the PC. The addition of a radical scavenger inhibited the reaction, confirming that the reaction involves radical processes. These conflicting mechanistic proposals for two extraordinarily similar reactions highlight the uncertainty that typically surrounds photocatalysis mechanism elucidation.

A range of organic photocatalysts were trialled in both phosphorylation reactions, with **4CzIPN** proving the best in both instances. When forming 2-phosphorylated thioflavones, **4CzIPN** yielded 45% while organic dyes such as eosin Y (24%) and rose bengal (19%) proved themselves to be poorer options. These results are most likely related to the photooxidising ability of the PC, which, according to the proposed mechanism, must be capable of oxidising the diphenylphosphine oxide ($E_{ox} \approx 1.0$ V).[226] The relative yields may be correlated to **4CzIPN**'s more positive E_{red}* (E_{red}* = 1.35 V) compared to those of eosin Y or rose bengal (E_{red}* = 0.83 V and 0.81 V, respectively). For the synthesis of 3-phosphorylated benzothiophenes, only **4CzIPN** provided any detectable yield (90%) while the other organic PCs, such as eosin Y or rose bengal, proved ineffective. Again, this is likely related to the greater photooxidising ability of **4CzIPN**.

In the formation of polysubstituted γ-lactones (Fig. 74d), the putative mechanism involves reductive quenching of the excited PC by the Hantzsch ester followed by the reduction of the aldehyde by the reduced PC in a PCET step facilitated by one of the Lewis acid or the oxidised Hantzsch ester[224] The ketyl radical adds to the α,β-unsaturated ester and this resultant radical is reduced by the Hantzsch ester radical. Protonation and acid-catalysed intramolecular transesterification yields the final product. Addition of TEMPO to the reaction inhibits product formation, implicating a radical process. Deuterium labelling of the Hantzsch ester and the absence of deuterium incorporation in the final product imply that a HAT process is unlikely to be in operation. Stern–Volmer quenching experiments indicated that the Hantzsch ester was the only species capable of significantly quenching the luminescence of the PC. In the PC screen for the reaction involving ketones as the carbonyl reagent, **4CzIPN** fared slightly more poorly than $[Ir(dF(CF_3)ppy)_2(dtbbpy)]PF_6$ (32% and 42%, respectively), while when aldehydes were used as substrates, the opposite trend in reactivity was observed (97% and 59% for **4CzIPN** and $[Ir(dF(CF_3)ppy)_2(dtbbpy)]PF_6$, respectively). The authors proposed that since the aromatic ketones are more difficult to reduce, the stronger ground state reducing ability of the Ir PC provides the greater driving force for turning over the photocatalytic cycle (E_{red}= −1.37 V and −1.21 V, respectively), while for aldehydes, **4CzIPN** is sufficient reducing and the reaction proceeds without the need for the Lewis acid additive.

For the dearomative arylcarboxylation of indoles with CO_2 (Fig. 74e),[225] the mechanism differs from the previous examples of photoinduced cyclisation in that two photocatalytic cycles are invoked, implying a two photon process. In both cycles, the excited PC is reductively quenched by DIPEA (Fig. 77). The reduced PC is then suggested to reduce the aryl halide, which after fragmentation to release the halide anion, produces an aryl radical. This species undergoes fast intramolecular radical addition to C=C double bond of the indole to form a benzylic radical. Reduction of this species by the reduced PC, closing the second photocatalytic cycle, forms a carbanion, which undergoes nucleophilic addition to CO_2, followed by protonation to yield the final product. The radical nature of this process was confirmed by the addition of TEMPO, which reduced the yield of the final product as an adduct with the benzylic radical was formed. Deuterium labelling studies eliminated the possibility of an HAT mechanism and provided support for the formation of the benzylic carbanion intermediate. Stern–Volmer experiments demonstrated that DIPEA was the predominant species responsible for the luminescence quenching of the PC. Only three PCs were considered for this reaction: **4CzIPN**, $[Ir(dF(Me)ppy)_2(dtbbpy)]PF_6$ and $[Ru(bpy)_3](PF_6)_2$. These provided yields of 88%, 78% and 52%, respectively, which correlate with the photooxidisng ability of the PC (E_{red}* = 1.35 V, 0.92 V and 0.77 V, respectively).

Distinct from the previous examples, Yu *et al.* report an example of cyclisation that is proposed to proceed through an

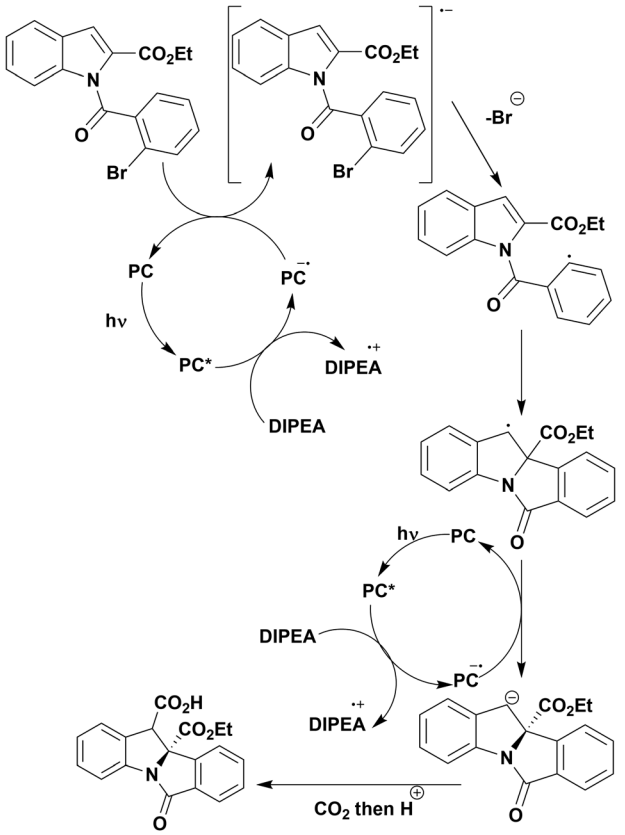

Fig. 77 Viable mechanism for the dearomative arylcarboxylation of indoles.

energy transfer mechanism. In this example, cyclisation of *N*-arylpropiolamides to 3-phosphorylated, trifluoromethylated or thiocyanated azaspiro[4.5]trienones occurs (Fig. 78a and 78b).[227] Energy transfer from the excited PC to the *N*-arylpropiolamide is suggested, with the excited *N*-arylpropiolamide undergoing SET to LPO (Fig. 79). Another SET event occurs from the

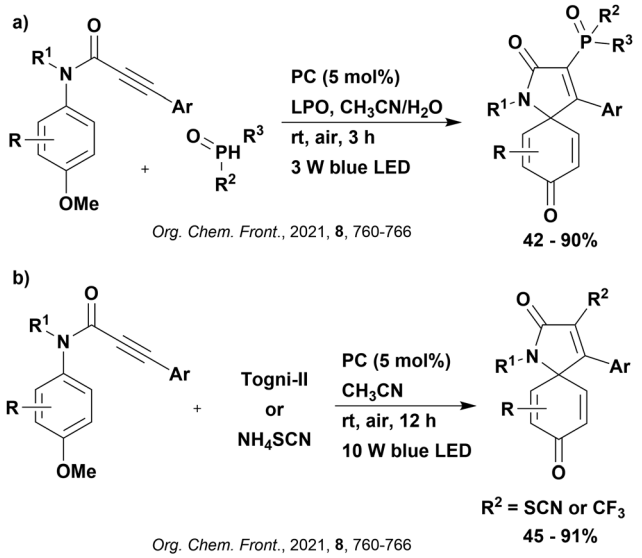

Fig. 78 Reaction scheme for the cyclisation of *N*-arylpropiolamides.

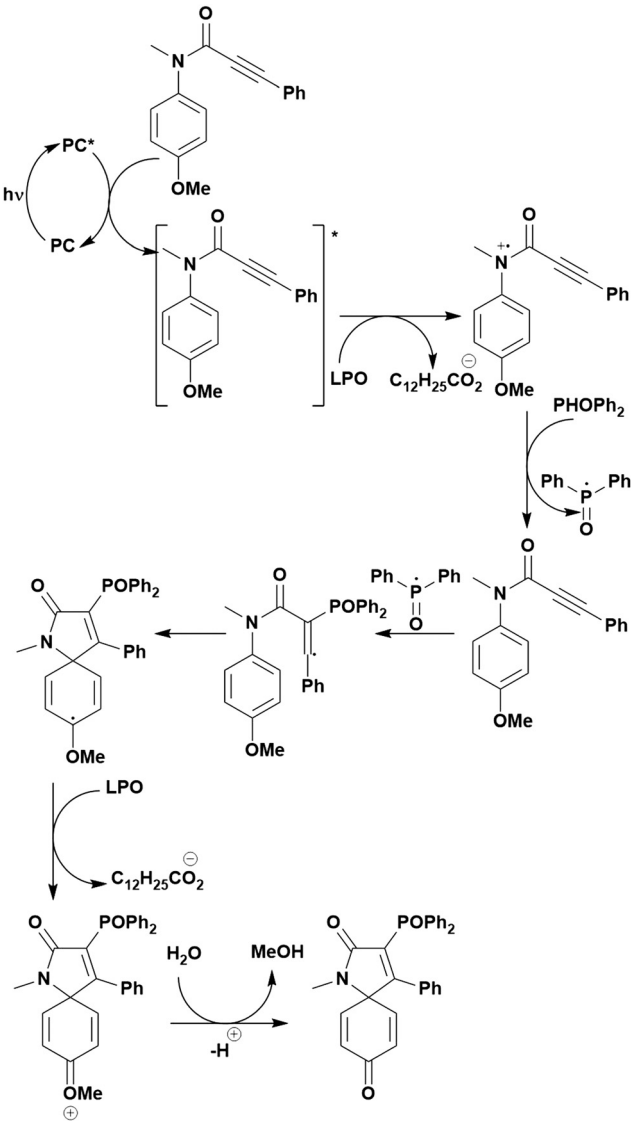

Fig. 79 Possible mechanism for the cyclisation of *N*-arylpropiolamides.

diphenylphosphine to the nitrogen centred radical cation, regenerating the initial *N*-arylpropiolamide. The phosphoryl radical then adds to the alkyne, generating an alkenyl radical intermediate, which undergoes intramolecular cyclisation to give an azaspiro radical. Oxidation of this species by LPO, followed by a cascade sequence of steps, including addition of H_2O, methanol elimination and deprotonation, yields the final product.

Stern–Volmer experiments revealed that *N*-arylpropiolamide quenches the luminescence of the PC. A PET mechanism was ruled out based on an analysis of the redox potentials; the *N*-arylpropiolamide (E_{ox} = 1.58 V *vs.* SCE) is thermodynamically incapable of being oxidised by the excited PC (E_{red}* = 1.35 V for 4CzIPN). Control experiments with radical scavengers TEMPO and BHT suppressed the reaction, confirming that radical intermediates exist in the reaction. **4CzIPN** far outcompeted the other organic PCs considered in this reaction, such as eosin Y and rose bengal, with respective yields of 83%, 15% and trace.

Since an energy transfer process is proposed, there should be a correlation between the triplet energies of the PCs and the reaction yields; however, as the triplet energy of the *N*-arylpropiolamide was not provided, it is not possible to infer this link.

Polymerisation reactions

4CzIPN also functions as a suitable photocatalyst for polymerisation reactions, including atom transfer radical polymerisation (ATRP) and reversible addition–fragmentation transfer (RAFT) polymerisation reactions. Methyl methacrylate (MMA) can be polymerised using an ATRP mechanism using **4CzIPN** at photocatalyst loading of parts per million (ppm) and ethyl α-bromophenyl-acetate (EBPA) as the initiator (Fig. 80a).[228] The photocatalyst activates the initiator in an oxidative quenching cycle to generate the propagating radical species (Fig. 81). The PC is then regenerated by SET from the propagating chain to the oxidised photocatalyst, thus terminating the polymerisation. Comparison of yields with other photocatalysts under the same conditions was not conducted; however, polymers of similar dispersity have been reported with other organic dyes, although under very different reaction conditions.[229] For example, Zhu *et al.* reported 90% conversion of the monomer to poly(methyl methacrylate) (PMMA) with M_w/M_n = 1.50 (where M_w = weight average molecular weight and M_n = number average molecular weight) after 3 hours using 0.0015 mol% of **4CzIPN** as the photocatalyst.[228] By comparison, Theriot *et al.*, when using perylene as a photocatalyst (0.11 mol %) and α-bromophenyl-acetate (BPA) as the initiator, obtained PMMA with M_w/M_n = 1.49.[229] This similarity confirms the success of **4CzIPN** as a PC in polymerisation reactions, especially since it can be used at such low loadings.

4CzIPN has been shown to act as a radical initiator in the RAFT polymerisation of acrylonitrile when used in combination with the chain transfer agent 2-cyanoprop-2-yl-1-dithionaphthalate (CPDN) (Fig. 80b).[230] The results indicated that **4CzIPN** provided molecular weight control of the resulting polymer of a similar level to commonly used ultra-violet photoinitiators such as diphenyl-(2,4,6-trimethylbenzoyl) phosphine oxide (TPO) and 2,2′-azobis(2-methylpropionitrile) (AIBN).

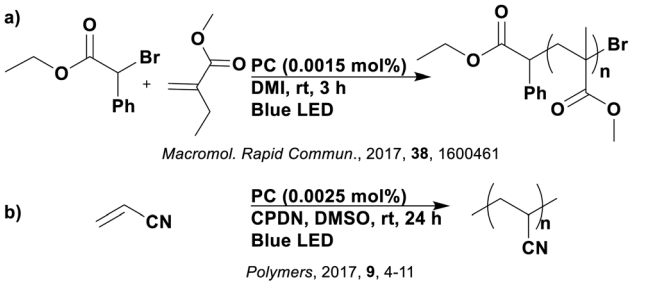

Fig. 80 Reaction schemes for photocatalytic polymerisations of (a) methyl methacrylate and (b) acrylonitrile.

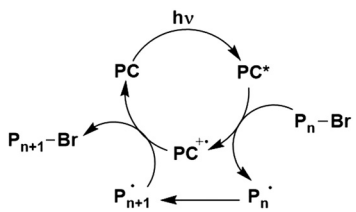

Fig. 81 Photocatalyzed ATRP mechanism.

Halogenation

Visible light promoted chlorination of electron-rich arenes has also been demonstrated using **4CzIPN** as the photocatalyst (Fig. 82).[231] An *in situ* bromination of the arene is first implicated before a halogen exchange occurs, generating the corresponding chlorinated product (Fig. 83). Here, the photoexcited catalyst is used to oxidise both bromide and chloride ions to their respective radical counterparts. Oxygen, acting as a sacrificial oxidant, is then used to regenerate the photocatalyst, closing the photocatalytic cycle. Other organic PCs were tested but all gave very poor yields in comparison with **4CzIPN**. For example, using 2 mol% of **4CzIPN** yielded 63% of the chloroanisole product while the second highest yield was obtained from eosin Y (5 mol%) at 16%. This large difference in yield is likely to be correlated with the much greater excited state oxidising capacity of **4CzIPN** in comparison to eosin Y (E_{rex}^* = 1.35 V and 0.83 V for **4CzIPN** and eosin Y, respectively). However, $[Mes\text{-}Acr]^+$ (E_{red}^* = 2.06 V) also only gave a 16% yield of product using 5 mol% catalyst loading. Since the oxidation potential of anisole is E_{ox} = 1.75 V, it is possible that the excited $[Mes\text{-}Acr]^+$ could be also oxidising anisole, potentially leading to a non-productive side product formation that may explain the low product yield in this case.

3. 4CzIPN in dual catalysis

Diverse in its applications, **4CzIPN** has also been used as a photocatalyst in dual catalytic reactions for example, with transition

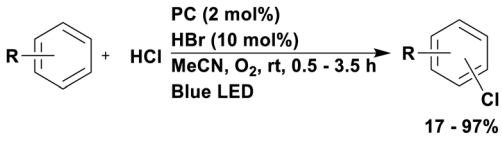

Fig. 82 Photochlorination reaction scheme.

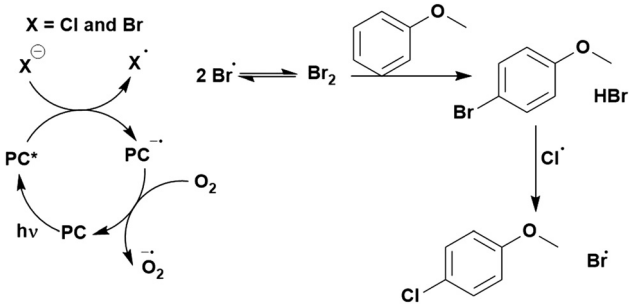

Fig. 83 Proposed mechanism for the photochlorination of arenes.

metals and hydrogen atom transfer (HAT) co-catalysts. In this section, we highlight examples of **4CzIPN** in synergistic catalysis.

Photoredox/nickel cross-coupling reactions

Visible light photocatalysis working in combination with transition metal catalysis, unsurprisingly termed metallaphotocatalysis, has become an alluring and fruitful strategy to access new bond-forming reactions.[232,233] There are multiple examples where **4CzIPN** is used in combination with a nickel co-catalyst to promote cross-coupling reactions. These reactions typically involve the cross coupling of C(sp^3) nucleophiles with electrophiles under mild conditions, typically through a Ni(I)/Ni(III) catalytic cycle.[234] Radical precursors, generated photocatalytically *via* a reductive quenching cycle, add to the Ni(0) catalyst to generate a transient Ni(I) complex. Oxidative addition with an aryl halide to generate an intermediate Ni(III) complex followed by reductive elimination generates the coupled product. Alternatively, oxidative addition of the aryl halide to Ni(0) occurs first, generating a Ni(II) species, followed by addition of the C(sp^3) radical to form the Ni(III) complex, which can then undergo reductive elimination. Regardless, the resultant Ni(I) complex is reduced by the reduced PC, closing both the catalytic and photocatalytic cycles (Fig. 84). The photocatalyst must have a wide redox window to accomplish both the alkyl radical formation and the nickel complex reduction.

The most common photoredox/nickel cross-coupling reaction involves C(sp^3)–C(sp^2) coupling, using a nickel catalyst formed from one of NiX_2.dme or $Ni(COD)_2$ (COD = 1,5-cyclooctadiene) in the presence of a diine ligand that is typically 4,4′-di-*tert*-butyl-2,2′bipyridine (dtbbpy). A variety of radical precursors have been reported, including alkyl or aryl trifluoroborate salts,[235–237] trifluoroboratochromanones,[238] 4-alkyl-1,4-dihydropyridine derivatives (DHPs),[183,234,239] carboxylic acids,[21,240–242] alkyl bis(catecholato)silicates,[243] aliphatic amines[244] or aziridines[245] and cycloalkanols.[246] Upon undergoing SET to the excited photocatalyst, these C(sp^3) radicals can then be cross-coupled with alkyl, aryl or hetero aryl halides,[21,183,234–236,238,240–246] aryl triflates,[21] vinyl halides,[21,243] carboxylic acids[239] or anhydrides (Fig. 85 and 86).[237]

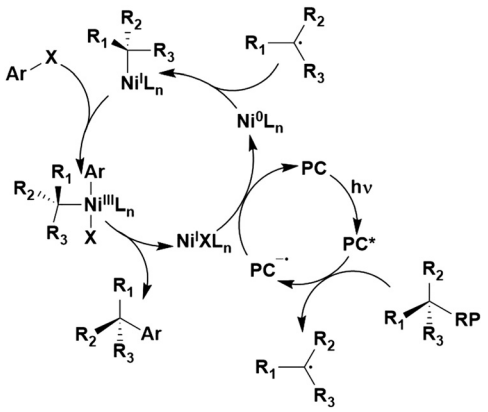

Fig. 84 Generic mechanism applicable to photoredox-nickel catalysed cross coupling reactions for C(sp^3)–C(sp^2) bond formation going through a Ni(I)/Ni(III) catalytic cycle where RP signifies radical precursor.

For this subset of reactions, **4CzIPN** was shown to be the most efficient PC in terms of final product yield for the formylation of aryl halides and triflates (Fig. 85a),[21] alkylation of aryl and hetero aryl halides (Fig. 85b),[183] synthesis of arylated C-saccharides (Fig. 85c),[234] cross coupling of aryl halides with trifluoroborate salts in flow (Fig. 85d),[235] synthesis of non-anomeric C-acyl glycosides (Fig. 85e),[239] enantioselective desymmetrization of cyclic meso-anhydrides (Fig. 85f),[237] α-arylation/heteroarylation of 2-trifluoroboratochromanones (Fig. 85g),[238] synthesis of aryl/heteroaryl-C-nucleosides (Fig. 85h),[241] synthesis of complex alkyl boronic esters (Fig. 85i)[242] and the synthesis of β-phenethyl-amines (Fig. 85j).[245]

Although **4CzIPN** has been shown to be highly successful in most of these dual catalytic C(sp^3)–C(sp^2) cross coupling reactions, the two commonly used iridium complexes, $[Ir(dF(CF_3)ppy)_2(bpy)]PF_6$ and $[Ir(dF(CF_3)ppy)_2(dtbbpy)]PF_6$, can outperform **4CzIPN** in terms of yield in examples including the synthesis of secondary benzylic alcohols (Fig. 86a), decarboxylative arylation reaction (Fig. 86b), alkylation of aryl halides or alkenes (Fig. 86c), deaminative reductive arylation (Fig. 86d) and site specific arylation of ketones (Fig. 86e).[236,240,243,244,246] This could be as a result of their more reducing ground state reduction potentials (E_{red} = −1.37 V for both iridium photocatalysts *vs.* −1.21 V for **4CzIPN**), since reduction of these Ni(I) species is typically around $E_{red} \approx -1.1$ V.[247] However, factors other than final product yield must be considered when evaluating which photocatalyst to employ in these types of reactions. For example, **4CzIPN** produced the highest *E*/*Z* isomeric ratio despite a lower yield in the stereoselective alkenyl-alkyl cross-coupling reaction (Fig. 86c).[243] For the decarboxylative arylation cross-coupling reaction (Fig. 86b),[240] higher product yields were reached much faster with **4CzIPN** than with $[Ir(dF(CF_3)ppy)_2(dtbbpy)]PF_6$; although, conversion plateaued and a lower overall yield was observed than with the iridium photocatalyst. Finally, in many cases the differences in product yields in examples with **4CzIPN** and iridium-based photocatalysts argue based on cost considerations for the choice of the former.[244] For the remote site specific arylation of ketones using tertiary alcohols (Fig. 86e),[246] only highly photooxidising PCs were capable of oxidation of the cycloalkanol (E_{ox} = 1.57 V for 1-(4-methoxyphenyl)cyclohexan-1-ol), rendering **4CzIPN** (E_{red}* = 1.35 V, 0% yield) incapable whereas $[Mes\text{-}Acr]ClO_4$ flourished (E_{red}* = 2.06 V, 86% yield).

Although C(sp^3)–C(sp^2) dual catalytic cross-coupling tends to follow the mechanism shown in Fig. 84, the excited PC could instead be reductively quenched by a sacrificial electron donor and the reduced PC be used to reduce the radical precursor as well as the Ni(I) species. The nickel catalytic cycle generally follows the process shown in Fig. 84 but in this case, two photocatalytic cycles are proposed, suggesting this is a two-photon process. Examples where this alternative mechanism may be in operation are the coupling of α-chloro esters with aryl iodides (Fig. 87a)[248] and the site-selective 1,2-dicarbofunctionalization of vinyl boronates (Fig. 87b).[249] In the former reaction, however, it should be noted that the pathway for the formation of the α-carbonyl radical has not been conclusively proven, it may instead be formed by reduction from a Ni(I) or Ni(0) species

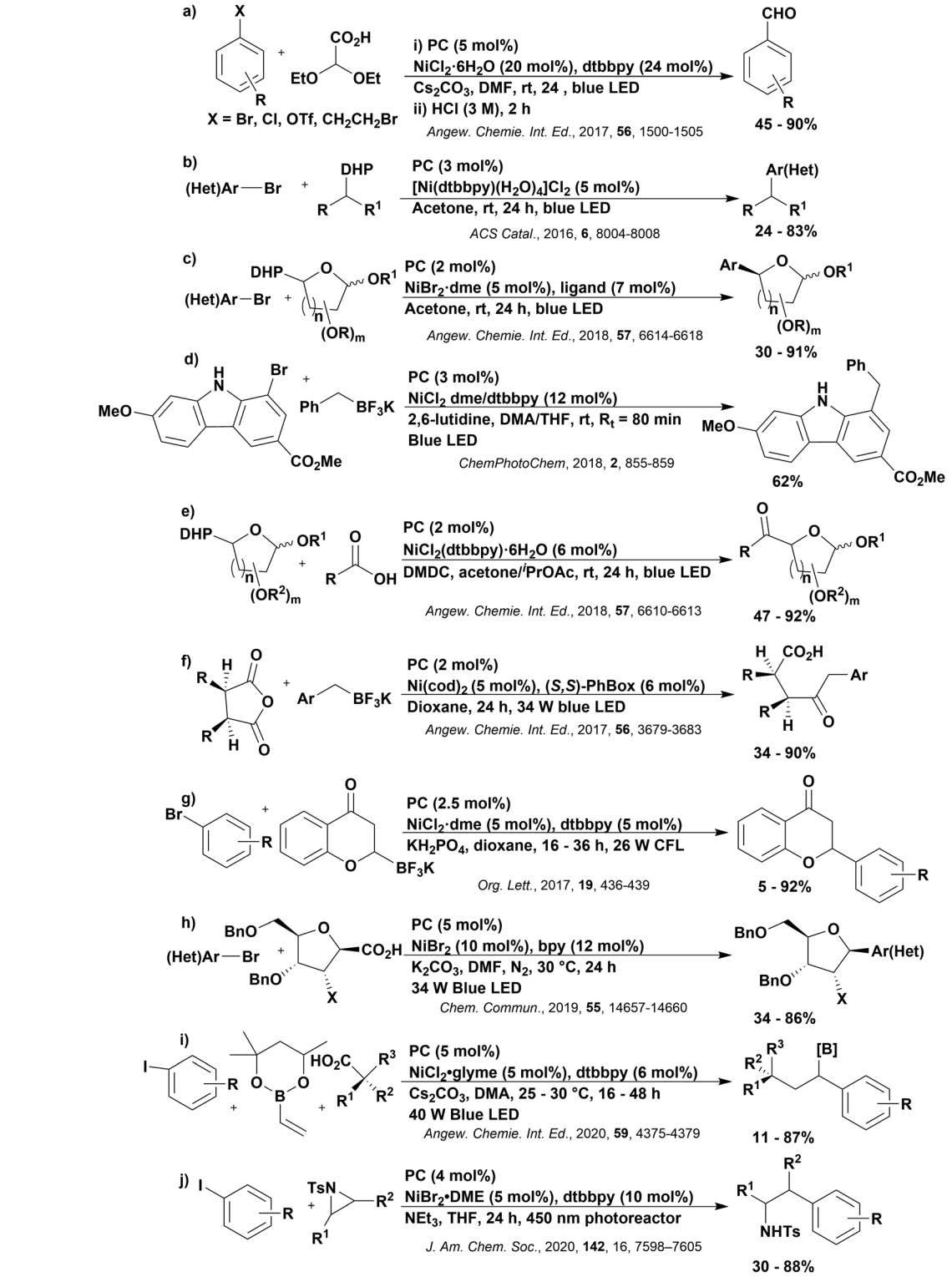

Fig. 85 Reaction schemes for the dual catalytic $C(sp^3)$–$C(sp^2)$ cross-coupling reactions with Ni where 4CzIPN has proven to be the best photocatalyst.

rather than from the reduced PC. $[Ir(ppy)_2(dtbbpy)]PF_6$ and **4CzIPN** were considered in the coupling of α-chloro esters with aryl iodides; however, direct comparison is difficult since neither were tested under the exact same reaction conditions. The former gave 25% yield using Cy_2NMe as the sole reductant while the latter gave 95% when using a Hantzsch ester, HEH, as the reductant.

In the 1,2-dicarbofunctionalization of vinyl borates (Fig. 87b)[249] the excited PC is proposed to be reductively quenched by TMEDA in both photocatalytic cycles with the regeneration of the PC

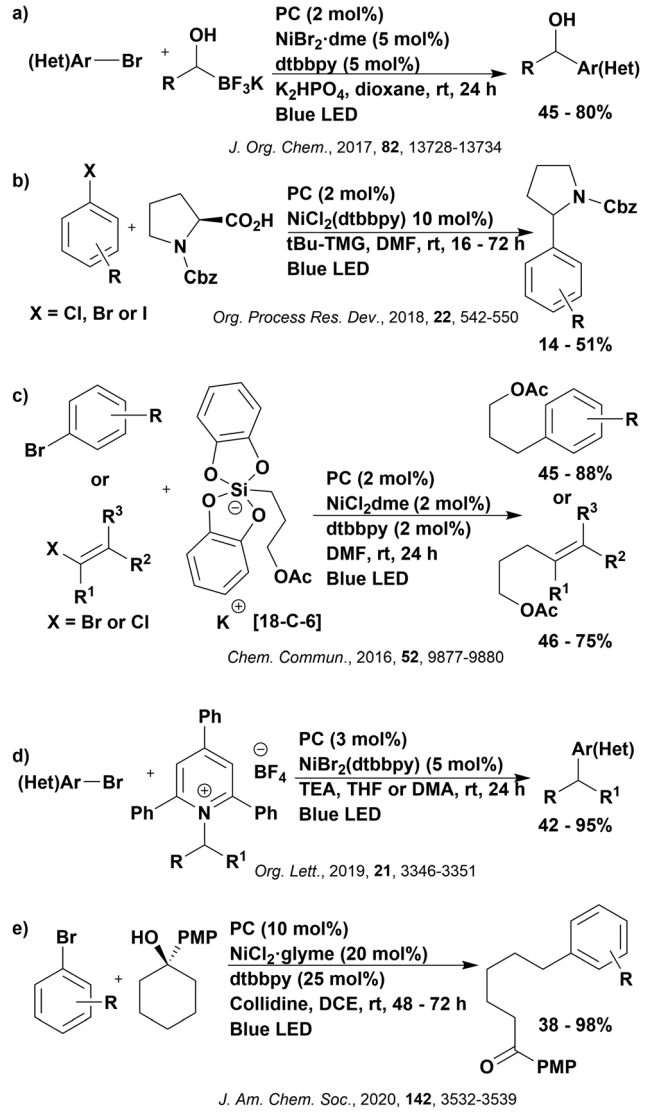

Fig. 86 Reaction schemes for the metallaphotocatalysis involving Ni for $C(sp^3)$–$C(sp^2)$ cross coupling where 4CzIPN does not give the highest final product yield.

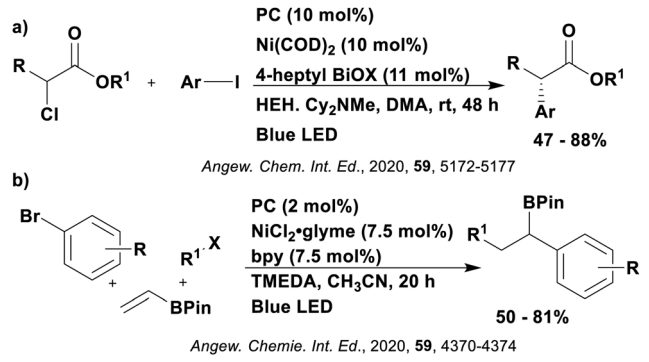

Fig. 87 Reaction scheme for the $C(sp^3)$–$C(sp^2)$ cross coupling involving (a) α-chloro esters with aryl iodides and (b) 1,2-dicarbofunctionalization of vinyl borates.

occurring through either SET to the Ni(I) species (as in Fig. 84) and SET to the tertiary alkyl halide to generate an alkyl radical.

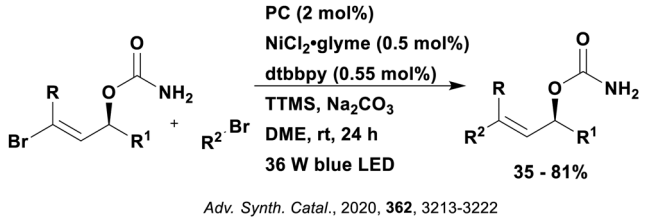

Fig. 88 Reaction scheme for the coupling of alkyl bromides with vinyl bromides. TTMS = tris(trimethylsilyl)silane.

Addition of the alkyl radical to the vinyl borate forms another carbon-centred radical, which is captured by the Ni catalyst; at this point the nickel catalytic cycle proceeds as normal. Stern–Volmer quenching studies reveal that TMEDA is responsible for quenching the luminescence of the excited PC. The presence of the alkyl radical was confirmed by EPR spectroscopy and corroborated by radical trapping experiments with additives such as TEMPO. Only three PCs were considered in this reaction: **4CzIPN**, $[Ir(ppy)_2(dtbbpy)]PF_6$ and $[Ir(ppy)_2(bpy)]PF_6$, providing yields of 86%, 53% and 62%, respectively. Notably, the organic PC was present in 5 mol% while the iridium PCs were used at 2 mol%. When the catalyst loading of **4CzIPN** was decreased to 3 mol% the yield decreases to 55%, comparable with the iridium PCs.

A different mechanism is proposed for the $C(sp^3)$–$C(sp^2)$ cross coupling of alkyl bromides with vinyl bromides (Fig. 88).[250] Reductive quenching of the excited PC by a bromide ion yields a bromyl radical, which can abstract a hydrogen atom from $(TMS)_3SiH$ (as shown in Fig. 53). The silyl radical formed can then abstract a bromine from the alkyl bromide, generating the alkyl radical. The nickel catalytic cycle occurs as usual (shown in Fig. 84), with closure of the photocatalytic cycle occurring in tandem with the reduction of the Ni(I) species. However, no mechanistic evidence is provided. In the PC screen, 2 mol% of organic PCs were compared against 1 mol% of organometallic PCs, making direct comparison between these results difficult. For example, **4CzIPN** obtained the highest yield of 81% while $[Ir(dF(CF_3)ppy)_2(dtbbpy)]PF_6$ performed the next best, giving 72% of product. However, it is clear that **4CzIPN** could photocatalyse this reaction while eosin Y and rose bengal could not. This may be due to the stronger photooxidising ability of **4CzIPN** (E_{red}^* = 1.35 V, 0.83 V and 0.81 V for **4CzIPN**, eosin Y and rose bengal, respectively).

The $C(sp^3)$–$C(sp^2)$ dual catalytic cross coupling can also be observed in the remote arylation of nitriles using aryl halides (Fig. 89a).[251] Utilisation of alkynes instead allows for vinylation of nitriles (Fig. 89b) while alkyl bromides can be used to alkylate the nitrile *via* a $C(sp^3)$–$C(sp^3)$ cross coupling (Fig. 89c). The proposed mechanism involves reductive quenching of the excited PC by the oxime radical precursor, subsequently generating an iminyl radical (Fig. 90), which undergoes rapid ring opening, forming a distal nitrile radical. This radical is trapped by the Ni(II) species, forming a Ni(III) complex, which upon reductive elimination, allows for release of the arylated product. The proposed mechanism was based on similar work from Leonori *et al.*[252] A quantum yield of 0.19 provides further support that this reaction is not a

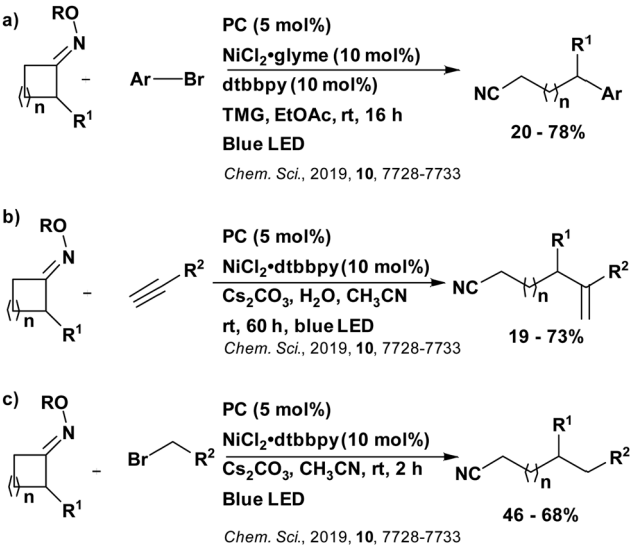

Fig. 89 Reaction scheme for the (a) arylation, (b) vinylation and (c) alkylation of nitriles.

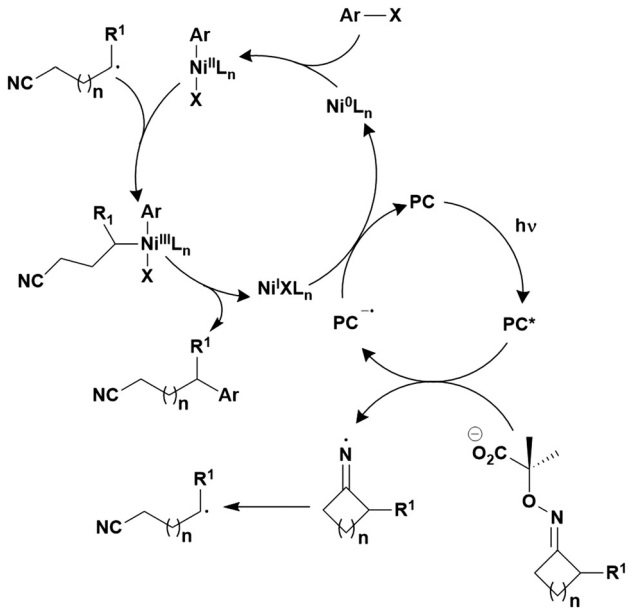

Fig. 90 Suggested mechanism for the dual catalytic arylation of nitriles.

radical chain process. For the arylation reaction (Fig. 89a), **4CzIPN** was identified as the second best photocatalyst, obtaining a yield of 24% in comparison to the superior 41% yield attained with $[Ir(ppy)_2(dtbbpy)]PF_6$. This is likely related to the superior ground state reducing capacity of the iridium photocatalyst (E_{red} = −1.51 V for $[Ir(ppy)_2(dtbbpy)]PF_6$ and E_{red} = −1.21 V for **4CzIPN**), which is needed to reduce the Ni(I) species (E_{red} = −1.20 V in DMF).[253]

Interestingly, in the reaction of the oxime with an alkyne (Fig. 89b), **4CzIPN** was identified as the optimal photocatalyst, yielding 41% of product while $[Ir(ppy)_2(dtbbpy)]PF_6$ managed only 33%. When using alkyl bromides as the coupling partner (Fig. 89c), the most successful catalyst was shown to be $[Ir(dF(CF_3)ppy)_2(dtbbpy)]PF_6$, which gave 5% yield of product. Both **4CzIPN** and $[Ir(ppy)_2(dtbbpy)]PF_6$ yielded no product in this case.

Although less common, $C(sp^3)$–$C(sp^3)$ cross-coupling has also been reported using this form of dual catalysis. Cross coupling of alkyl halides with silicate radical precursors (Fig. 91a)[254] or with ethers (Fig. 91b),[255] allylic alcohols with DHP radical precursors (Fig. 91c)[256] or oxabenzonorbornadiene with alkylamines (Fig. 91d)[257] have been investigated. In the former, $Ni(COD)_2$ with bpy acting as the ancillary ligand, was utilised to generate the coupled poduct.[254] Only three PCs were tested, with both **4CzIPN** and $[Ru(bpy)_3](PF_6)_2$ giving 22% yield of the desired product and $[Ir(dF(CF_3)ppy)_2(bpy)_2]PF_6$ performing slightly better, yielding 34% of the coupled product. Undesired homocoupling between the alkyl halides prevented higher yields from being achieved under these conditions; follow on mechanistic studies are currently underway by Fensterbank *et al.*

In the coupling of alkyl bromides with ethers (Fig. 91b), a proposed mechanism is shown in Fig. 92.[255] Oxidative addition of the alkyl bromide to the Ni(0) species produces a Ni(II) alkyl halide complex, which reductively quenches the excited PC. Photoelimination of the Ni(III) species releases an electrophilic bromyl radical, which undergoes HAT with the ether. The as formed carbon-centred radical is then captured by the Ni(II) species. Reductive elimination from the resultant Ni(III) complex releases the product. Both catalytic cycles close following a SET

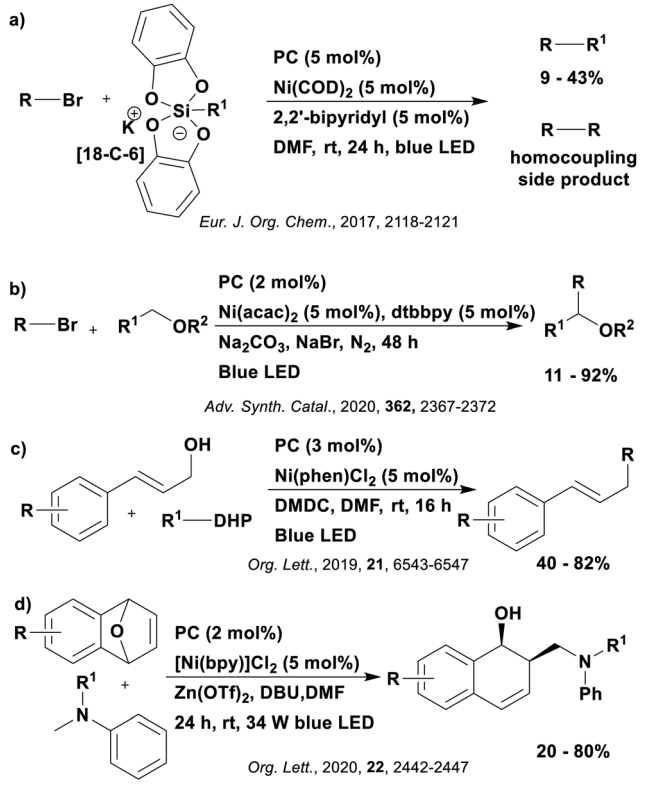

Fig. 91 Reaction scheme for the $C(sp^3)$–$C(sp^3)$ metallaphotoredox cross coupling involving a) alkyl halides and silicates, b) alkyl halides and ethers, c) allylic alcohols with DHP radical precursors and d) oxabenzonorbornadiene and alkylamines. DMDC = dimethyl carbonate.

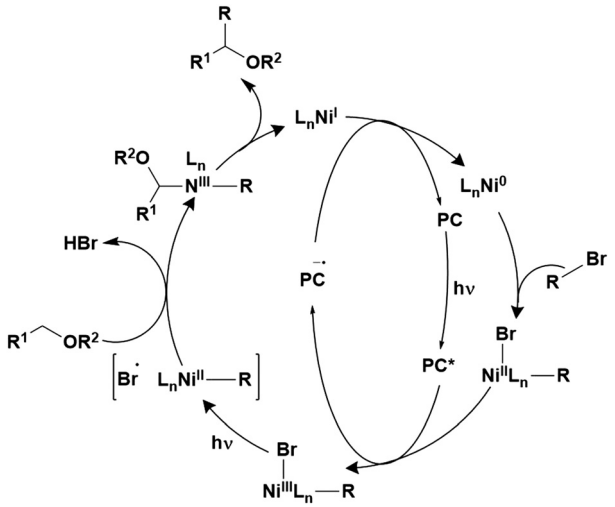

Fig. 92 Viable mechanism for the C(sp^3)–C(sp^3) cross coupling of alkyl halides and ethers.

from the reduced PC to the Ni(I) species. Alkyl iodides or triflates proved unsuccessful as substrates in this reaction because they cannot promote the HAT step. The reaction yield was dependent on the power of the LED source, supporting a proposed two-photon mechanism. In the PC screen, only [Ir(dF(CF_3)ppy)$_2$(dtbbpy)]PF_6 and **4CzIPN** provided any product, 82% and 65%, at 2 mol% and 5 mol%, respectively. The higher yields with the iridium PC may be due to its stronger reduction potential in the ground state (E_{red} = −1.37 V and −1.21 V, respectively).

Molander *et al.* demonstrated the photocatalyzed C(sp^3)–C(sp^3) Tsuji–Trost cross coupling reaction (Fig. 91c).[256] The proposed mechanism (Fig. 93) involves formation of the alkyl radical from DHP radical precursors through SET to the excited PC. This radical is trapped by the Ni(0) complex, followed by oxidative addition of the *in situ*-generated allyl methyl carbonate. Reductive elimination releases the final product and the resultant Ni(I) is reduced by the reduced PC, simultaneously closing both catalytic cycles. Stern–Volmer quenching studies were conducted to support this proposed mechanism, which indicated that neither the nickel catalyst nor the allyl methyl carbonate could quench the excited PC. A secondary kinetic isotope effect (k_H/k_D = 1.15) was observed, supporting the hypothesis that oxidative addition of the allyl methyl carbonate onto the Ni(I) species is the rate-determining step. High throughput screening was conducted to identify the optimum conditions, with only **4CzIPN** and [Ir(dF(CF_3)ppy)$_2$(bpy)]PF_6 considered as PCs, and both providing comparable yields.

Aminomethylation/ring opening of oxabenzonorbornadienes (Fig. 91d) also provides a route for the formation of C(sp^3)–C(sp^3) bonds *via* dual photoredox/Ni catalysis.[257] Operating in a similar mechanism to that illustrated in Fig. 93, the excited PC is reductively quenched by the alkylamine, furnishing an α-aminoalkyl radical after deprotonation. Simultaneously, oxidative addition of Ni(0) into the C–O bond of the oxabenzonorbornadiene, facilitated by Zn(OTf)$_2$, forms a *σ*-allyl intermediate, which then rearranges to a π-allyl Ni(II) species. Addition of the α-aminoalkyl reagent to the Ni(II) species forms a Ni(III) complex. Reductive elimination affords the final product. SET from the reduced PC to the Ni(I) species closes both catalytic cycles. The addition of TEMPO quenches the reaction, confirming this to be a radical process. The most efficient quenching of the excited PC, as confirmed by Stern–Volmer experiments, was by the alkylamine, while DBU only moderately quenched the luminescence. No photocatalyst screen was conducted in this study, only **4CzIPN** was employed and provided yields of 20–80%. However, for five alkylamine substrates, **4CzIPN** gave 0% yield and instead, [Ir(dF(CF_3)ppy)$_2$(dtbbpy)]PF_6 was used as the PC, providing yields between 45–80% for these substates. The authors propose no reasoning for this and acknowledge that both PCs should be capable, thermodynamically, of photooxidising all the alkylamines utilised in the substrate scope.

A further example of C(sp^3)–C(sp^3) cross-coupling, although proceeding slightly differently mechanistically, involves the coupling of aliphatic alcohol derivatives with alkyl halides (Fig. 94a). The same protocol can also be applied to C(sp^2)–C(sp^3) cross-coupling when used with aryl halides (Fig. 94b).[258] The putative mechanism is shown in Fig. 95 and reflects the general mechanism shown in Fig. 84, except the formation of the alkyl radical differs. In this instance, β-scission of the aliphatic alcohol derivative generates an alkyl radical. The excited PC is reductively quenched instead by a Hantzsch ester. An association constant of 2.9 M^{-1} between the Hantzsch ester

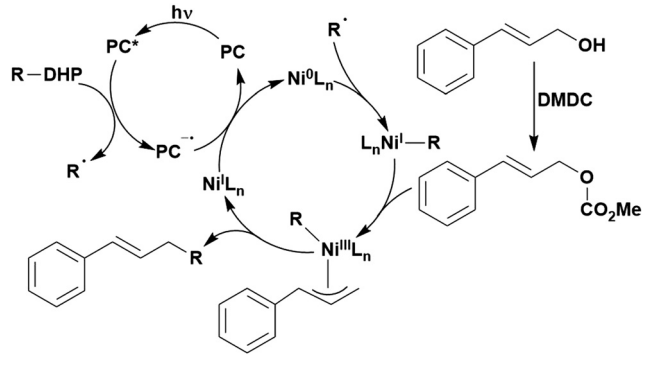

Fig. 93 Proposed mechanism for the metallaphotoredox cross coupling of allylic alcohols with DHP radical precursors.

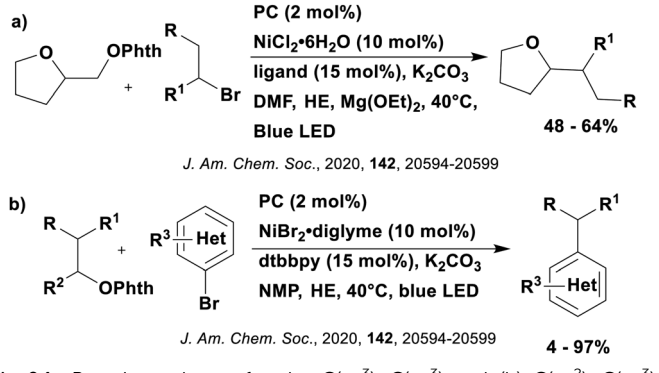

Fig. 94 Reaction scheme for the C(sp^3)–C(sp^3) and (b) C(sp^2)–C(sp^3) cross coupling of aliphatic alcohol derivatives with a) alkyl and (b) aryl halides. HE = Hantzsch ester.

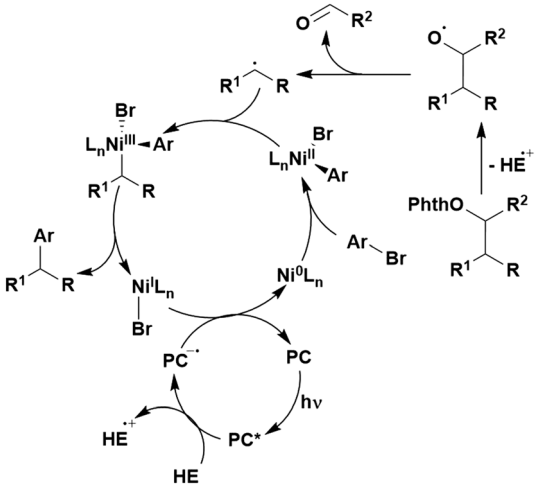

Fig. 95 Putative mechanism for the C(sp^2)–C(sp^3) cross-coupling of aryl halides with aliphatic alcohol derivatives.

and the alcohol derivate implies an electron donor–acceptor (EDA) complex is formed between the two prior to homolytic cleavage. Both **4CzIPN** and [Ir(ppy)$_2$(dtbbpy)]PF$_6$ afforded the same amount of product (84% and 87%, respectively), while [Mes-Acr]ClO$_4$ and [Ru(bpy)$_3$]Cl$_2$ provided similar yields (54% and 51%, respectively). These results correlate generally to the ground state reduction potential of the PC (E_{red} = −1.51 V, −1.21 V and −0.57 V for **4CzIPN**, [Ir(ppy)$_2$(dtbbpy)]PF$_6$ and [Mes-Acr]ClO$_4$, respectively). For [Ru(bpy)$_3$]Cl$_2$, however, the low photooxidising ability of this PC may be responsible for its lower yield (E_{red}* = 0.77 V and 1.35 V for [Ru(bpy)$_3$]Cl$_2$ and **4CzIPN**, respectively).

Photoredox/nickel cross-coupling reactions have been developed to promote the carboxylation of aliphatic and aromatic bromides and triflates (Fig. 96)[259] which may be classified as C(sp^2)–C(sp) cross-coupling. In this case, the nickel catalyst is NiBr$_2$.glyme in combination with neocuproine. The initial Ni(II) catalyst is first thought to be reduced to a Ni(0) species, before undergoing oxidative addition with the aryl halide. Reductive quenching of the photocatalyst by a Hantzsch ester is observed before the reduced photocatalyst is used to reduce the Ni(II) species. The putative mechanism involves carboxylation of the *in situ* formed Ni(I) complex, followed by product dissociation and regeneration of the Ni(II) catalyst (Fig. 97). In the carboxylation of bromobenzene, [Ir(dF(CF$_3$)ppy)$_2$(dtbbpy)]PF$_6$, **4CzIPN** and [Ir(dF(CF$_3$)ppy)$_2$(bpy)]PF$_6$ all yielded essentially the same product yield (46%, 45% and 40%, respectively). Other PCs considered were considerably worse,

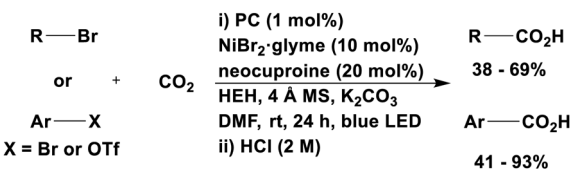

Angew. Chemie. Int. Ed., 2017, **56**, 13426-13430

Fig. 96 Reaction schemes for the metallaphotocatalysis mediated carboxylation of alkyl or aryl halides or triflates.

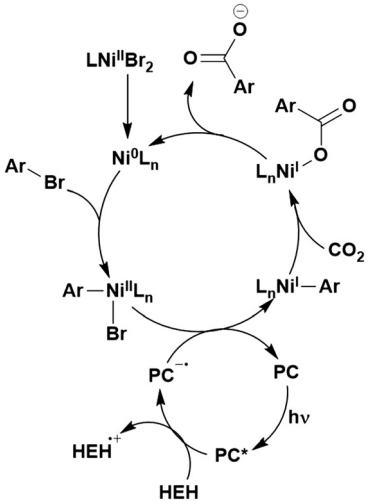

Fig. 97 Viable mechanism for the carboxylation aryl bromides using combined photo and nickel catalysis (where L = neocuproine and HEH = Hantzsch ester).

including [Ru(bpy)$_3$](PF$_6$)$_2$ (3%) and *fac*-Ir(ppy)$_3$ (5%). The excited photocatalyst must first be capable of oxidising the Hantzsch ester (E_{ox} = 0.887 V),[260] which explains why low yields were obtained for [Ru(bpy)$_3$](PF$_6$)$_2$ (E_{red}* = 0.77 V) and *fac*-Ir(ppy)$_3$ (E_{red}* = 0.31 V). Secondly, the ground state reduction potential of the photocatalyst must be sufficiently negative in order to reduce the Ni(II) species (E_{red} ≈ −1.2 V),[261] which is easily achieved by [Ir(dF(CF$_3$)ppy)$_2$(dtbbpy)]PF$_6$, [Ir(dF(CF$_3$)-ppy)$_2$(bpy)]PF$_6$ and **4CzIPN**. It should also be noted that the NiBr$_2$.glyme (E_{red} = −1.70 V *vs.* Fc/Fc$^+$) was shown by Stern–Volmer quenching studies to be capable of oxidatively quenching **4CzIPN**, as does the *in situ* generated LNiBr$_2$ (E_{red} = −1.27 V *vs.* Fc/Fc$^+$), despite this not being a thermodynamically favourable process (E_{ox}* = −1.04 V for **4CzIPN**). Both of these processes occur at a slower rate than the quenching from the Hantzsch ester (K_{SV} = 0.18 M^{-1}, 0.20 M^{-1} and 0.61 M^{-1} for NiBr$_2$, LNiBr$_2$ and Hantzsch ester, respectively).

The combination of photocatalysis with nickel catalysis for cross-coupling reactions has also been extended to C(sp)-S bond formation to form alkynyl sulfides in flow (Fig. 98).[262] The proposed mechanism invokes a two photon process, whereby the excited PC is first reductively quenched by the thiol, which after deprotonation, results in a thiyl radical. The reduced PC is then proposed to reduce the nickel catalyst, NiCl$_2$.dme (in the presence of pyridine acting as the ancillary ligand), to generate the active Ni(I) species. This Ni(I) complex traps the thiyl radical, generating a Ni(II) complex, which is subsequently reduced by the reduced photocatalyst. Oxidative addition to the resultant

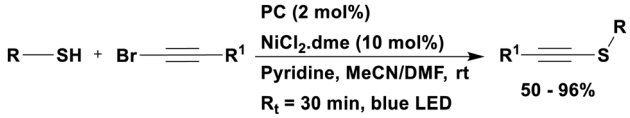

Angew. Chemie. Int. Ed., 2017, **56**, 12255-12259

Fig. 98 Reaction scheme for the formation ok alkynyl sulfides.

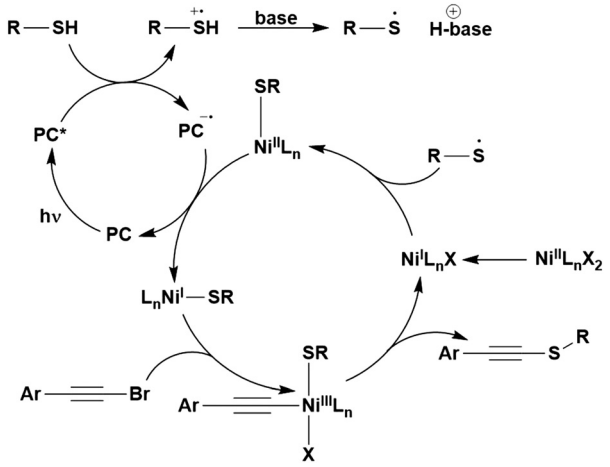

Fig. 99 Plausible mechanism for the photo/nickel catalysed formation of alkynyl sulfides.

Ni(I) complex followed by reductive elimination closes the nickel catalytic cycle as well as generating the required alkynyl sulfide (Fig. 99). Although two reduction steps involving the PC are proposed, no mechanistic support of this is provided. This reaction has been shown to work in both the presence and absence of the nickel catalyst (96% and 28%, respectively), although a much higher product yield is obtained when the dual catalysis is in operation. In choice of PC, **4CzIPN** proved far superior in comparison to the other PCs, obtaining 96% yield of product while the second-best PC, $[Ir(dF(CF_3)ppy)_2(bpy)]PF_6$, resulted in only 46% yield and the third best, $[Ir(dF(CF_3)ppy)_2(dtbbpy)]PF_6$ formed 24%. There seems to be a correlation between the decreasing excited state oxidation potential and the decreasing yield (E_{red}* = 1.35 V, 1.32 V and 1.21 V, respectively).

Finally, photoredox/nickel cross coupling can be applied to a cascade coupling reaction, generating three new bonds in one synthetic step when using a combination of a diene, a substituted sulfinates and an aryl(hetero) halide (Fig. 100).[263] The sulfinate reductively quenches the excited PC, generating the sulfonyl radical, which then undergoes a radical cascade cyclisation with the diene, yielding a C-centred radical (Fig. 101). This radical is then captured by the Ni(0) catalyst followed by oxidative addition of the aryl halide. The resultant Ni(III) complex undergoes reductive elimination to release the product, with the Ni(I) being reduced by the reduced photocatalyst, concomitantly closing both catalytic cycles. This proposed mechanism has been supported by

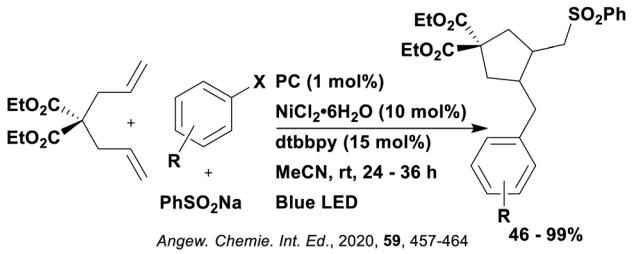

Fig. 100 Reaction scheme for the dual catalytic cascade coupling reaction of dienes, sulfinates and aryl halides.

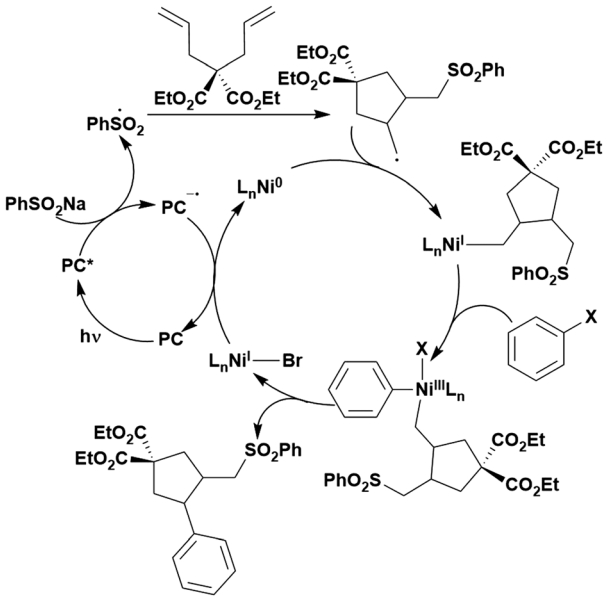

Fig. 101 Proposed mechanism for the dual catalytic radical cascade coupling involving dienes, sulfinates and aryl halides.

Stern–Volmer quenching experiments, showing the sulfinate to be responsible for the PC quenching. Radical inhibition experiments with TEMPO also confirmed the presence of radicals in this process, while stoichiometric studies with a Ni(II)–ArCl complex resulted in none of the desired product, suggesting a Ni(II)–aryl species is not present in the catalytic cycle. Photocatalysts **4CzIPN**, $[Ir(ppy)_2(dtbbpy)]PF_6$ and $[Ir(dF(CF_3)ppy)_2(dtbbpy)]PF_6$ all provided comparably high yields (89%, 91% and 88%, respectively) although **4CzIPN** was used with 2.5 mol% loading while the iridium photocatalysts were used at 1 mol%. Ruthenium photocatalysts tested, including $[Ru(bpy)_3](PF_6)_2$, proved far inferior, managing only 20% yield of product. Rueping *et al.* suggested this difference in yield is due to the lower photooxidising capacity of the ruthenium photocatalyst in comparison to the others (E_{red}* = 0.77 V for $[Ru(bpy)_3](PF_6)_2$ in comparison to E_{red}* = 1.35 V and 1.21 V for **4CzIPN** and $[Ir(dF(CF_3)ppy)_2(dtbbpy)]PF_6$, respectively), making the oxidation of $PhSO_2Na$ (E_{ox} = 0.5 V)[264] more challenging. However, this explanation does not account for the success of $[Ir(ppy)_2(dtbbpy)]PF_6$, which is an even worse photooxidant (E_{red}* = 0.66 V), which suggests something other than these thermodynamic parameters is significant here.

Photoredox/palladium cross-coupling reactions

Several reports exist merging photocatalysis with palladium-catalysed cross-coupling, for example decarboxylative formylation of aryl halides (Fig. 102a), acetoxylation of oximes (Fig. 102b), hydroxylation of arenes (Fig. 102c and d), and decarboxylative alkenylation of aliphatic carboxylic acids (Fig. 102e). In the former reaction, photoinduced decarboxylation of glyoxylic acid under a reductive quenching cycle, results in the formation of a formyl radical.[265] This then coordinates to a palladium(II) species generating transiently a Pd(III) complex that is reduced to a Pd(II) complex by the reduced PC, closing the photocatalytic cycle.

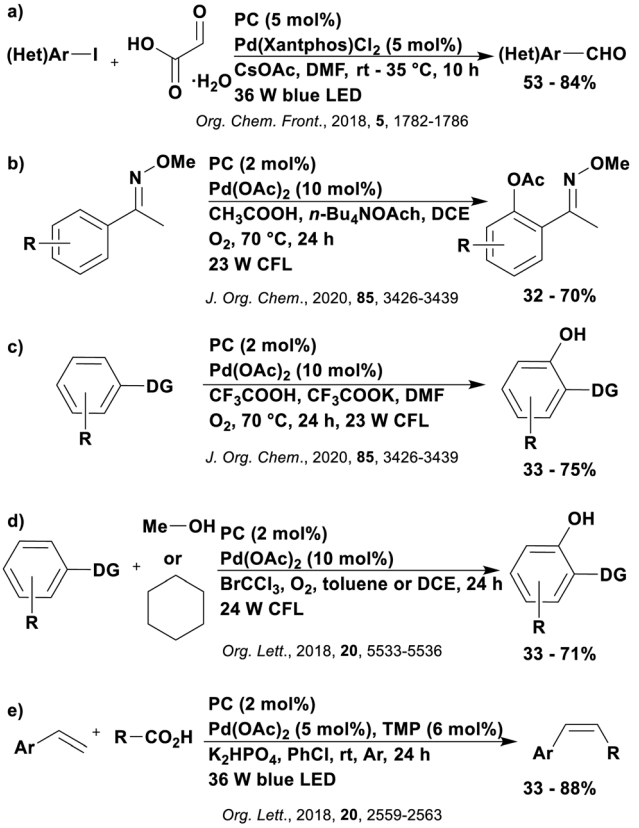

Fig. 102 Reactions scheme for metallaphotocatalysis involving palladium where (a) decarboxylative formylation of aryl halides, (b) acetoxylation of oximes, (c and d) hydroxylation of arenes (DG = donor group) and (e) decarboxylative alkenylation of aliphatic carboxylic acids with vinyl arenes.

This Pd(II) complex then undergoes reductive elimination, ejecting the formylated product, regenerating the Pd(0) catalyst, which is then free to undergo another oxidative addition with the aryl halide (Fig. 103). **4CzIPN** gave higher product yields in comparison to $[Ir(dF(CF_3)ppy)_2(dtbbpy)]PF_6$ (78% and 51%, respectively), although both achieved 100% reaction conversion. This suggests that the iridium photocatalyst allowed for a greater formation of the hydrodeiodination by-product, which was observed in only ≈ 10% yield for **4CzIPN**. This reaction can be considered a $C(sp^2)$–$C(sp^2)$ coupling and proceeds in a very similar manner to the photoredox/Ni dual catalysis described previously. Although none of the Ni examples given involved $C(sp^2)$–$C(sp^2)$ coupling, a study by Wang *et al.* also involved the formylation of aryl halides; however, in this particular case the carboxylic acid was used to generate the $C(sp^3)$ radicals.[21] In the formylation of 4-bromobenzonitrile, Wang *et al.* obtained a 75% yield using Ni as the co-catalyst, while Fu *et al.* obtained 68% with a Pd co-catalyst, demonstrating that both procedures are similarly successful for the formylation of arenes.

More commonly, **4CzIPN** has been reported to work in tandem with the palladium catalyst $Pd(OAc)_2$ under an oxidative quenching mechanism. Examples include the acetoxylation of oximes (Fig. 102b)[266] or the hydroxylation of arenes (Fig. 102c and 102d).[266,267] The proposed mechanism for these reactions is

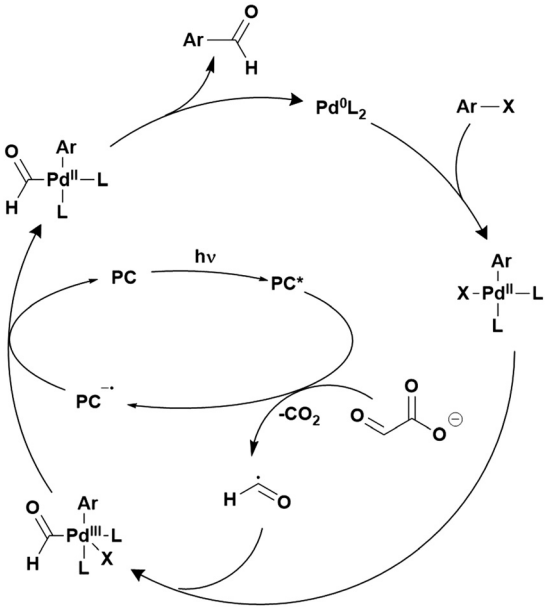

Fig. 103 Working mechanism for the photoredox/Pd catalysed formylation of aryl halides.

shown in Fig. 104.[266] Oxidative quenching of the excited PC by oxygen generates the superoxide radical anion as well as the oxidised PC. Cyclopalladation of the oxime or arene generates the Pd(II) complex, which is oxidised by both the oxidised PC and the superoxide radical, resulting in a Pd(IV) species. Reductive elimination of the acetoxylated product closes the Pd-based catalytic cycle. A hydrolysis step then ensues for the hydroxylation reaction. The presence of the superoxide radicals was confirmed by EPR spectroscopy and an observed kinetic isotope effect suggested C–H bond cleavage may be the rate-determining step. Optimisation of the photocatalyst was considered for the acetoxylation reaction, with **4CzIPN** proving superior to eosin Y, rose bengal and $[Ru(bpy)_3]Cl_2$ (69%, 21%, 17% and 57%).

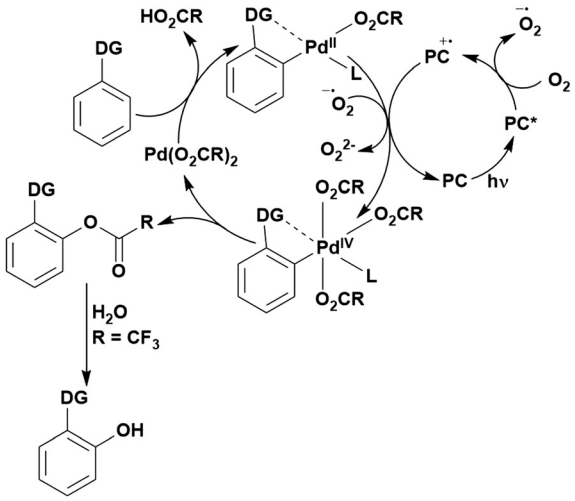

Fig. 104 Proposed mechanism for the acetoxylation of oximes and hydroxylation of arenes. DG = oxime for acetoxylation reaction and donor group for hydroxlation reaction.

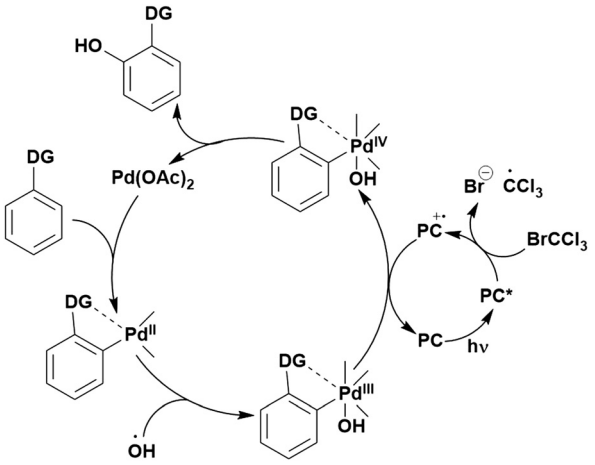

Fig. 105 Proposed mechanism for the hydroxylation of arenes using photoredox and palladium dual catalysis where DG is pyridine or benzothiazole.

The photocatalyst is required to oxidise the Pd(II) complex, which has an oxidation potential of E_{ox} = 0.83 V,[268] which explains the lower yields of the other organic photocatalysts in comparison to **4CzIPN** (E_{ox} = 0.78 V, 0.84 V and 1.52 V for eosin Y, rose bengal and **4CzIPN**, respectively). For $[Ru(bpy)_3]Cl_2$ the lower yield can be explained by the excited state oxidation potential, which must be sufficiently negative to reduce oxygen to the superoxide radical anion (E_{red} = −0.86 V);[269] hence, this process is more thermodynamically challenging for the ruthenium photocatalyst in comparison to **4CzIPN** (E_{ox}* = −0.81 V and −1.04 V for $[Ru(bpy)_3]Cl_2$ and **4CzIPN**, respectively).

In the case of hydroxylation of arenes (Fig. 102d), the excited PC is used to reduce the hydrogen abstractor $BrCCl_3$ (Fig. 105) and then also to promote the oxidation of a transient Pd(III) species to Pd(IV), closing the photocatalytic cycle, prior to reductive elimination of product in the Pd-based catalytic cycle.[267] Only organic photocatalysts were considered in this study of which **4CzIPN** provided the highest yield of 67% in comparison to eosin Y at 45%, which was the next best PC. Analogously to the previous example, this is likely due to the greater ground state oxidising capacity of **4CzIPN** (E_{ox} = 1.52 V and 0.78 V for **4CzIPN** and eosin Y).

Despite having compatible redox potentials, **4CzIPN** was an unsuitable photocatalyst for the *cis*-selective decarboxylative alkenylation of aliphatic carboxylic acids (Fig. 102e), giving 0% yield.[270] This is hypothesized to be due to its incompatibility with the palladium catalyst under the required reaction conditions, although no further investigation was undertaken. Instead, $[Ir(dF(CF_3)ppy)(dtbbpy)]PF_6$ was found to be the best photocatalyst, giving an 80% yield.

Photoredox/cobalt dual catalysis

A third example of metallaphotocatalysis employs a cobalt co-catalyst, examples of which are the cross-dimerization of two alkynes to form 1,3-enynes (Fig. 106a),[271] the isomerisation of alkenes (Fig. 106b)[272] the olefination of alkyl halides (Fig. 106c),[186] the allylic alkylation (Fig. 106d),[273] the desulfonylative allylic substitution (Fig. 106e)[274] and the decarboxylation of

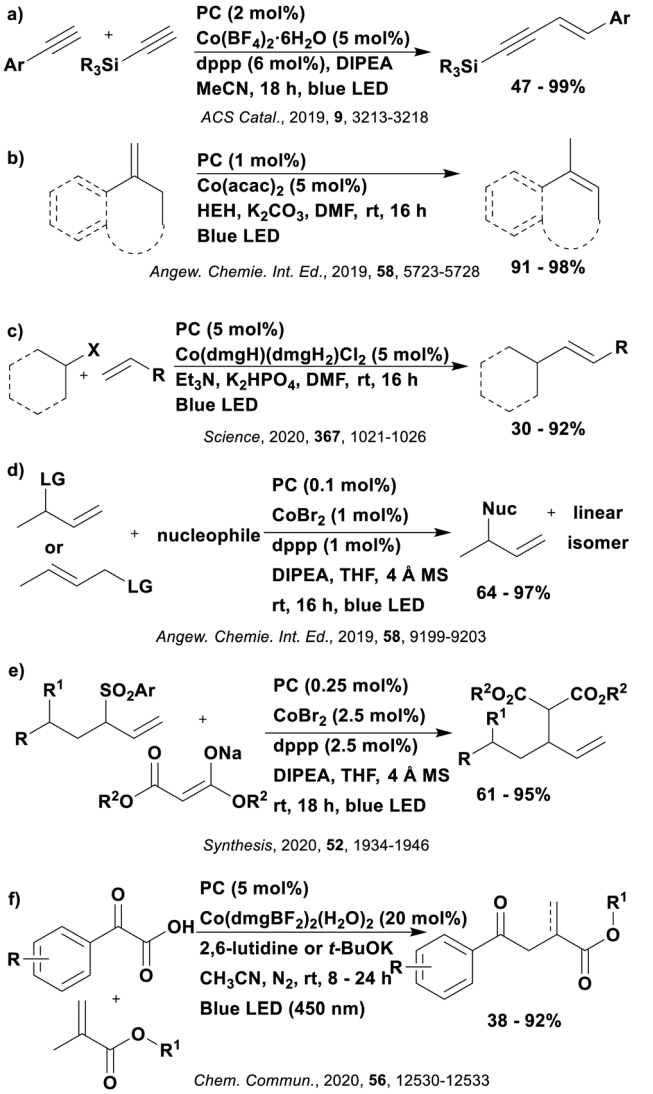

Fig. 106 Reaction schemes for the Co/PC dual catalysis of (a) cross-dimerisation of two alkynes (b) isomerisation of alkenes, (c) olefination of alkyl halides, (d) allylic alkylation, (e) desulfonylative allylic substitution and (f) decarboxylation of α-ketoacids to allylic ketones.

α-ketoacids to allylic ketones (Fig. 106f).[275] The optimized conditions identified for the former reaction used a combination of $Co(BF_4)_2{\cdot}6H_2O$ with 1,3-bis(diphenylphosphino)propane (dppp) as an ancillary ligand and **4CzIPN** as the photocatalyst. An oxidative quenching mechanism is proposed (Fig. 107) whereby two equivalents of the excited photocatalyst reduces the cobalt(II) catalyst to a Co(0) species, with DIPEA (*N*,*N*-Diisopropylethylamine) added as a putative sacrificial electron donor to regenerate the photocatalyst. A third equivalent of photocatalyst is then invoked by the authors to access a Co(I)/Co(III) catalytic cycle. Deuterium labelling experiments conducted indicated the likelihood of the oxidative addition and migratory insertion steps in the cobalt catalytic cycle. Only **4CzIPN** and $[Ir(dF(CF_3)ppy)_2(dtbbpy)]PF_6$ were considered as photocatalysts, with respective yields of 71% and 28%. The difference in yields is possibly linked to the greater reducing capacity of the excited state for **4CzIPN** (E_{ox}* = −1.04 V and

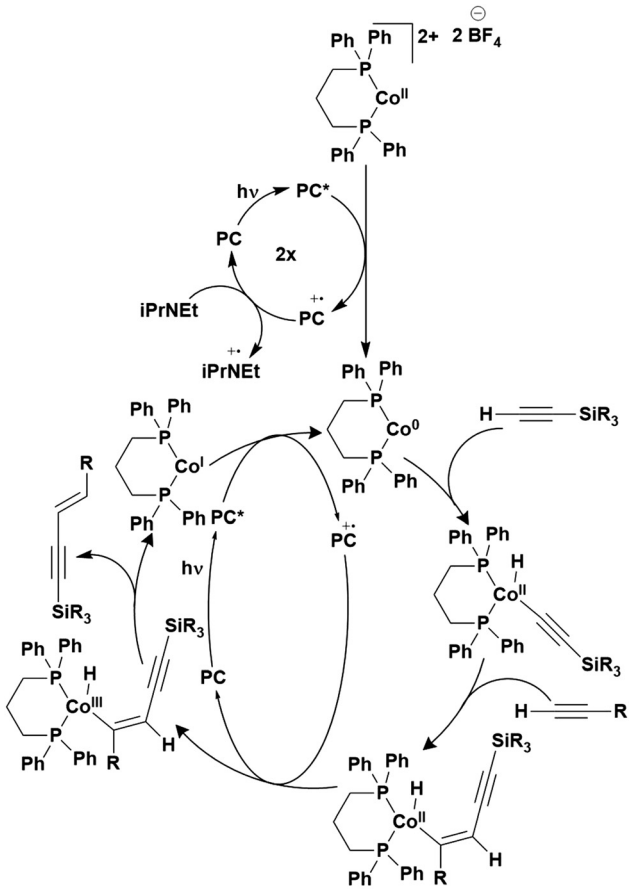

Fig. 107 Proposed mechanism for the metallaphotocatalysis reaction involving a cobalt catalyst in the cross-dimerization of two alkynes.

−0.89 V for **4CzIPN** and the iridium PC, respectively), making the reduction of the Co(II) complex more facile, particularly since an analogous Co complex Co(dppp)Br_2 exhibited a reduction potential of $E_{red} \approx -0.6$ V.[276]

Dual catalysis involving **4CzIPN** and Co(acac)$_2$ has been reported for the isomerisation of alkenes (Fig. 106b). The presence of 4,5-bis(diphenylphosphino)-9,9-dimethylxanthene (Xantphos) or (oxydi-2,1-phenylene)bis(diphenylphosphine) (DPEphos) as a ligand is used to control the regio- and stereoselectivity of the reaction.[272] A Hantzsch ester is employed as a sacrificial reductant of the excited PC, and the resulting reduced PC then catalyses the reduction of the Co(II) catalyst to a Co(I) species (Fig. 108). The reaction was shown to proceed in the absence of **4CzIPN**, indicating direct reduction of Co(II) by the photoexcited Hantzsch ester is likely to occur as an alternative pathway. Photocatalysts other than **4CzIPN** were not considered in this reaction; noteworthy is that **4CzIPN** provided very high yields of 91–98% yield in the five substrates tested.

The combination of a PC with Co(dmgH)(dmgH$_2$)Cl$_2$ (dmg = dimethylglyoximate) has been shown to promote the olefination of alkyl halides through the creative use of amino radicals as halogen atom transfer (XAT) agents. (Fig. 106c).[186] The excited PC is reductively quenched by triethylamine (TEA), forming the amino radical cation, which abstracts a halogen from the alkyl

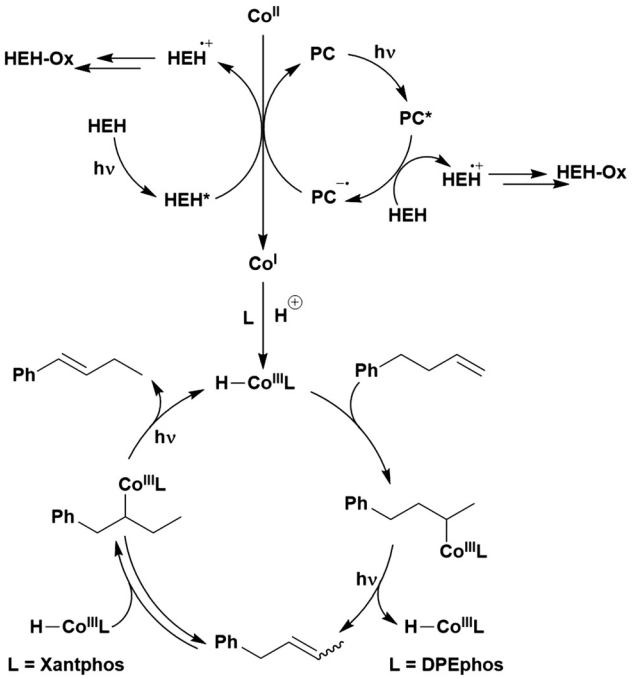

Fig. 108 Plausible mechanism for the dual catalytic isomerisation of alkenes.

halide (Fig. 109). Closure of the photocatalytic cycle involves the reduced photocatalyst reducing a Co(III) species. A quantum yield of 0.01 suggests this is not a radical chain process. Leonari *et al.* have utilised this technique of XAT agents in combination with hydrogen atom transfer (HAT) catalysts for deuteration, alkylation and allylation of aryl and alkyl halides; however, in the olefination of alkyl halides, a Co complex is also used as the

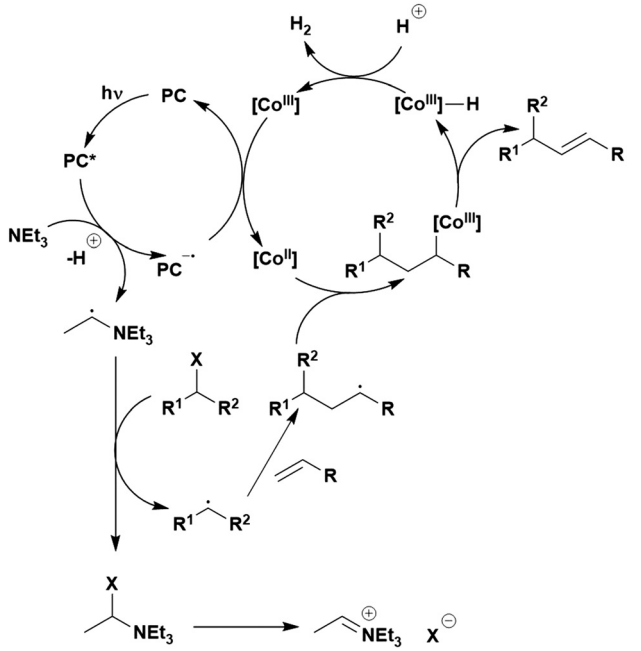

Fig. 109 Suggested mechanism for the olefination of alky halides using dual PC and Co catalysis with amino radicals as XAT agents.

second catalyst. Photocatalyst screening was conducted in the alkylation reaction and applied throughout the study; hence, only **4CzIPN** was considered as the photocatalyst for this olefination reaction. For more information about the study, refer to section on dual catalysis with HAT catalysts.

In the allylic substitution reactions (Fig. 106d and e), $CoBr_2$ in the presence of the ancillary ligand dppp is used in combination with **4CzIPN**.[273,274] As the desulfonylative substitution (Fig. 106e) is a subsequent study by the same group as the allylic alkylation reaction (Fig. 106d), the same optimized conditions and mechanistic suggestions proposed in the initial study were used. Thus, only in the allylic alkylation from Fig. 106d will be discussed. The basic mechanistic proposal involves reductive quenching of the excited PC by the additive, DIPEA, with the reduced PC then serving to reduce the Co(II) species to the catalytically active Co(I) complex. Oxidative addition of the allylic electrophile forms a π-allyl Co(III) intermediate, which upon attack from the nucleophile, releases the final product and regenerates the Co(I) species. A quantum yield of 0.13 was obtained, suggesting that this reaction does not proceed *via* a radical chain process.

$[Ir(dF(CF_3)ppy)_2(dtbbpy)]PF_6$, eosin Y and **4CzIPN** were tested in the PC screen, providing yields of 41%, 59% and 64%, respectively, hence **4CzIPN** was selected for further optimization. As the most photooxidising PC, this may be why **4CzIPN** performed the best (E_{red}* = 1.35 V, 0.83 V and 1.21 V for **4CzIPN**, eosin Y and $[Ir(dF(CF_3)ppy)_2(dtbbpy)]PF_6$, respectively); however, the trends in E_{red}* do not explain the relative product yields. Eosin Y has the lowest E_{red}* but provided comparable yields to **4CzIPN** and outperformed the Ir PC.

Finally, for the decarboxylation of α-ketoacids to allylic ketones (Fig. 106f),[275] the proposed mechanism is similar to that shown in Fig. 109. Reductive quenching of the excited PC by the α-ketoacid carboxylate yields a benzoyl radical after decarboxylation. This radical then adds to the methacrylate derivative with the formed alkyl radical trapped by the Co(II) catalyst. Cleavage of Co-C bonds and β-H elimination allows release of the final product. Closure of both catalytic cycles occurs as in Fig. 109. Stern–Volmer quenching experiments indicated that the α-ketoacid could only quench the luminescence of the PC in the presence of base. Using TEMPO inhibited product formation and an adduct with the benzoyl radical was detected, providing evidence of the presence of this radical species. Of the PCs tested, only **4CzIPN** yielded any product (85%) while the use of $[Ru(bpy)_3](PF_6)_2$ and $[Mes\text{-}Acr]ClO_4$ yielded no product. Oxidation of phenylglyoxylic carboxylate is moderately challenging (E_{ox} = 0.98 V *vs.* SCE), which may explain why the ruthenium PC was unsuccessful in this reaction (E_{red}* = 0.77 V and 1.35 V for $[Ru(bpy)_3](PF_6)_2$ and **4CzIPN**, respectively). Despite $[Mes\text{-}Acr]ClO_4$ being capable of this SET (E_{red}* = 2.06 V), the limited reducing ability in the ground state may act as a barrier to it being effective in this reaction (E_{red} = −0.57 V and −1.21 V for $[Mes\text{-}Acr]ClO_4$ and **4CzIPN**, respectively).

Photoredox/titanium dual catalysis

The fourth example of metallaphotocatalysis involves the use of a titanium complex as the additional catalyst. This can be applied to the spirocyclisation of epoxides (Fig. 110a),[277] the

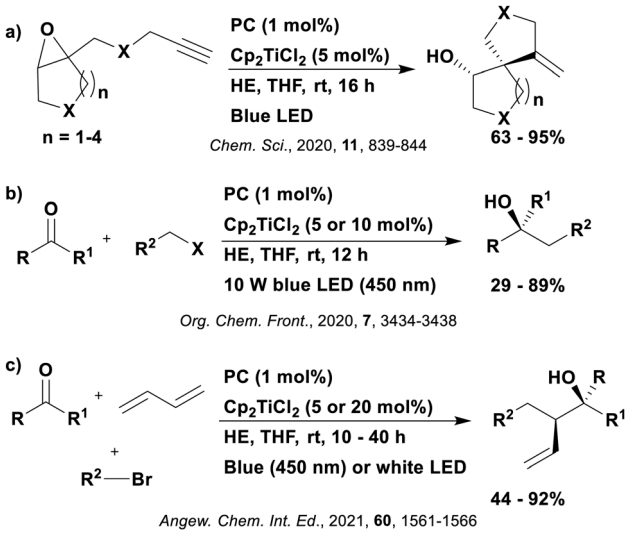

Fig. 110 Reaction scheme for the (a) spirocyclisation of epoxides, (b) Barbier allylation of aldehydes and ketones and (c) the allylation of carbonyls with 1,3-butadiene.

Barbier allylation of aldehydes and ketones (Fig. 110b)[278] and the allylation of carbonyls with 1,3-butadiene (Fig. 110c)[279] all of which use Cp_2TiCl_2 as the titanium catalyst of choice. In all reactions, the plausible mechanism involves reduction of the Cp_2TiCl_2 catalyst to a Ti(III) species by the excited photocatalyst. Closing of the photocatalytic cycle is obtained by oxidation of a Hantzsch ester (HE) by the oxidised photocatalyst. For the spirocyclisation of epoxides, the proposed mechanism is depicted in Fig. 111. Reductive opening of the epoxide is stimulated by the Ti(III) complex, generating the Ti(IV) complex, whereby the carbon

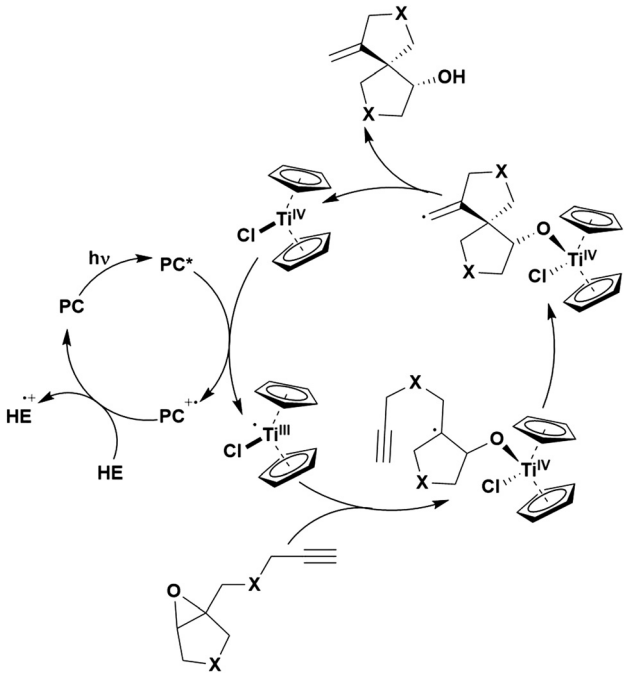

Fig. 111 Possible mechanism for the spirocyclisation of epoxides using metallaphotocatalysis, where HE is the Hanztsch ester.

centred radical adds intramolecularly to the alkyne functionality, producing the spirocyclic structure. The resultant vinyl radical abstracts a proton from the oxidised HE and the product is released from the Ti(IV) complex, completing the titanium catalytic cycle.

Stern–Volmer experiments conducted in all cases indicated that both the titanium catalyst and the HE can quench the emission of the excited photocatalyst, suggesting the possibility of both an oxidative and reductive quenching mechanism, although Shi *et al.* proposed the oxidative quenching mechanism showing in Fig. 111 since quenching with the titanium catalyst occurs faster ($k_q = 3.9 \times 10^9$ L mol^{-1} s^{-1} and 4.5×10^7 L mol^{-1} s^{-1} for Cp_2TiCl_2 and HE, respectively, with $[Ir(ppy)_2(dtbbpy)]PF_6$). For the Barbier allylation reaction, allyl bromide could also quench the PC, although at a slower rate than Cp_2TiCl_2 ($k_q = 3.3 \times 10^9$ L mol^{-1} s^{-1} and 5.8×10^8 L mol^{-1} s^{-1} for Cp_2TiCl_2 and allyl bromide, respectively, with **4CzIPN**).[278] Again, in the allylation with 1,3-butadiene, $BrCF_2CO_2Et$ could also act as a quencher but at a much slower rate ($k_q = 3.65 \times 10^9$ L mol^{-1} s^{-1} and 3.05×10^7 L mol^{-1} s^{-1} for Cp_2TiCl_2 and $BrCF_2CO_2Et$, respectively, with $[Ir(dF(CF_3)ppy)_2(dtbbpy)]PF_6$.

Quantum yields of 0.016 and 0.08 were obtained for the Barbier allylation reaction and the allylation reaction with 1,3-butadiene, respectively, which suggest that a radical-chain mechanism is unlikely in both reactions.

Photocatalysts including **4CzIPN**, $[Ir(ppy)_2(dtbbpy)]PF_6$ and $[Ir(dF(CF_3)ppy)_2(dtbbpy)]PF_6$ all achieved the same high yields in the spirocyclisation of epoxides (94%, 95% and 94%, respectively) and in the allylation with 1,3-butadiene (85%, 86% and 89%, respectively) while $[Ru(bpy)_3](PF_6)_2$ proved much less successful (24% and 0% yield, in the two reactions, respectively).[277,279] Similarly, in the Barbier allylation, **4CzIPN** and $[Ir(dF(CF_3)ppy)_2(dtbbpy)]PF_6$ behaved comparably (92% and 86%, respectively), while $[Ru(bpy)_3](PF_6)_2$ was unsuccessful (0% yield). Reduction of the Cp_2TiCl species is fairly facile ($E_{red} = -0.22$ V) so in terms of thermodynamics, should be feasible for all photocatalysts ($E_{ox}^* = -1.04$ V, -0.96 V, -0.89 V and -0.81 V and for **4CzIPN**, $[Ir(ppy)_2(dtbbpy)]PF_6$, $[Ir(dF(CF_3)ppy)_2(dtbbpy)]PF_6$ and $[Ru(bpy)_3](PF_6)_2$ respectively). Hence, maybe the difference in yield is more related to regeneration of the photocatalyst ($E_{ox} = 1.52$ V, 1.21 V, 1.69 V and 1.29 V for **4CzIPN**, $[Ir(ppy)_2(dtbbpy)]PF_6$, $[Ir(dF(CF_3)ppy)_2(dtbbpy)]PF_6$ and $[Ru(bpy)_3](PF_6)_2$), respectively). Alternatively, since the possibility of a reductive quenching mechanism has already been suggested, this could be a reason for low yields for some photocatalysts.

Photoredox/iron catalysis

Two examples exist depicting the use of 4CzIPN in combination with an iron co-catalyst: the acylarylation of unactivated alkenes towards the synthesis of 3-(α-acyl) indolines (Fig. 112a);[280] and the reduction of CO_2 (Fig. 112b).[281] In the former, $FeCl_2$ was used as the iron catalyst, which was proposed to reductively quench the excited PC (Fig. 113). The photocatalytic cycle is closed by SET from the reduced PC to di-*tert*-butyl peroxide (DTBP), forming a *tert*-butanolate anion and a *tert*-butoxyl radical. The latter abstracts a hydrogen from the aldehyde reagent,

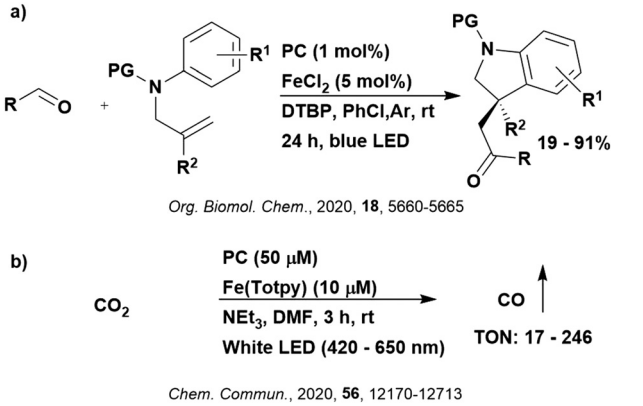

Fig. 112 Reaction scheme for the dual photoredox/Fe catalysis for the acylarylation of unactivated alkenes. PG = protecting group.

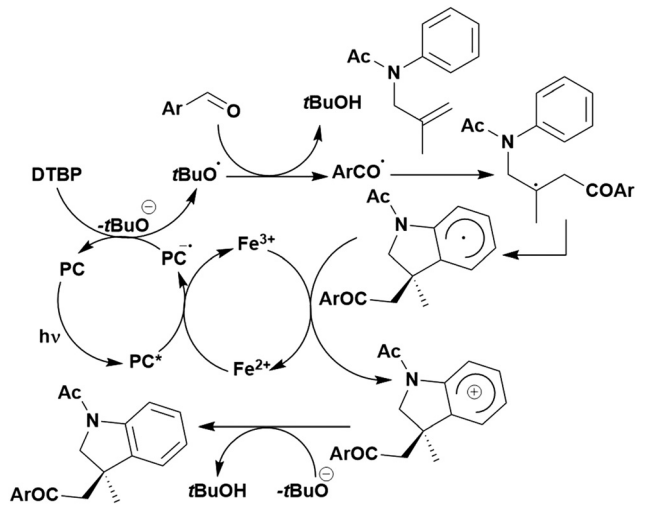

Fig. 113 Viable mechanism for the dual photoredox/Fe catalysis for the acylarylation of unactivated alkenes.

producing an acyl radical that can add to the alkene. From this adduct, rapid intramolecular radical trapping by the *N*-aryl moiety occurs, forming the dearomatized aryl radical, which is then oxidised by the Fe(III) species, closing the iron catalytic cycle. Finally, a deprotonation step occurs to yield the 3-(α-acyl) indoline. Addition of TEMPO prevented the formation of the final product and instead, and adduct with the acyl radical formed, demonstrating its presence as an active species in the reaction. A primary kinetic isotope effect value of 1.3 implies that C–H bond cleavage of the *N*-aryl moiety is unlikely to be involved in the rate determining step. A quantum yield of 0.24 was obtained; however, the authors suggested a radical chain process may exist.

Of the six PCs screened, only **4CzIPN** and *fac*-$Ir(ppy)_3$ provided product (62% and 52%, respectively), with the likes of eosin Y and $[Mes\text{-}Acr]ClO_4$ giving no/trace product. These results may be linked to the ground state reduction potential of the PC ($E_{red} = -1.21$ V, -2.19 V, -1.06 V and -0.57 V for **4CzIPN**, *fac*-$Ir(ppy)_3$, eosin Y and $[Mes\text{-}Acr]ClO_4$, respectively). Additionally, the stronger photooxidising capacity of **4CzIPN** in comparison to

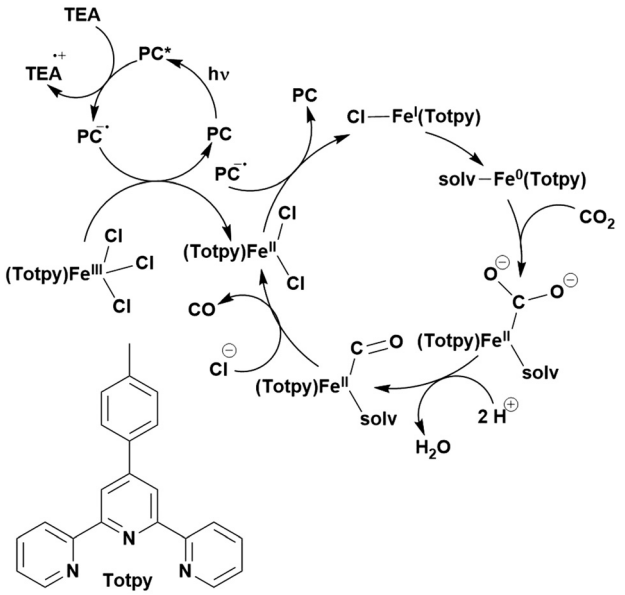

Fig. 114 Putative mechanism for CO_2 reduction using dual photoredox/Fe catalysis.

fac-Ir(ppy)$_3$ may contribute to the difference in yields obtained for these two (E_{red}* = 1.35 V and 0.31 V, respectively).

A terpyridine–Fe(III) complex was used as the metal catalyst for the reduction of CO_2 (Fig. 112b).[281] Reductive quenching of the excited PC occurs by the sacrificial electron donor NEt_3, as confirmed by Stern–Volmer quenching experiments. The reduced PC can then reduce the Fe(III) catalyst to Fe(II), with a second reduction step, proposed to occur from the reduced PC, invoked to generate a Fe(I) species (Fig. 114). The Fe(I) complex undergoes disproportionation to yield both an Fe(II) complex and the active Fe(0) species. Coordination of CO_2 to this Fe(0) species is followed by protonation, the cleavage of a C–O bond and the release of water. The final CO is liberated by replacement with a chloride ion or solvent to close the iron catalytic cycle. The evolution of two absorption bands at 620 nm and 798 nm upon irradiation implied the formation of the Fe(I) species. **4CzIPN** proved to be much more successful in this reaction than the other PCs investigated, providing a turnover number (TON) of 244 while the next best PC, $[Ru(bpy)_3]^{2+}$, could manage only 17. The higher TON obtained by **4CzIPN** compared to $[Ru(bpy)_3]^{2+}$ (E_{red}* = 1.35 V and 0.77 V, respectively) may be related to its greater driving force for the photooxidation of NEt_3 (E_{ox} = 0.77 V *vs.* SCE).

Photoredox/chromium catalysis

The penultimate example of metallaphotocatalysis involves the use of chromium chloride as the metal co-catalyst in the dialkylation of 1,3-dienes (Fig. 115).[282] Reductive quenching of the excited photocatalyst by a Hantzsch ester is proposed to occur, forming an alkyl radical and pyridinium (py) cation pyH^+ (Fig. 116). The alkyl radical can then add to the diene, with the resultant radical being trapped by the Cr(II) catalyst. A chromium alkoxide is then proposed to form *via* a six-membered Zimmerman–Traxler transition state upon addition of the aldehyde.[283,284]

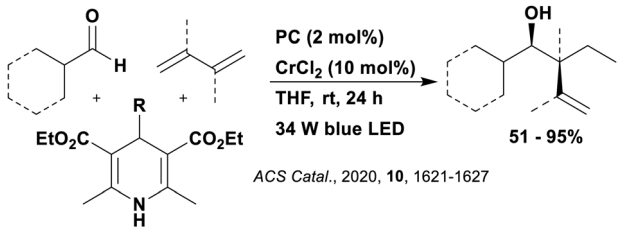

Fig. 115 Reaction scheme for the dialkylation of 1,3-dienes using metallaphotocatalysis with chromium chloride.

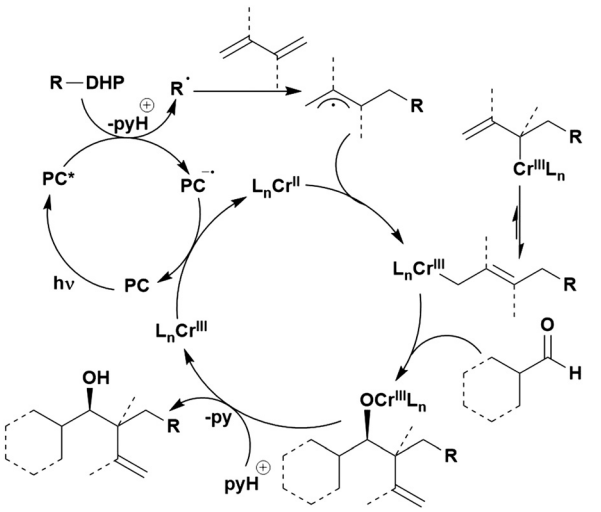

Fig. 116 Putative mechanism for the dialkylation of 1,3-dienes using metallaphotocatalysis with chromium chloride.

Release of the product is realised upon hydrolysis by the pyridinium cation, whereby closure of both catalytic cycles occurs through SET from the reduced photocatalyst to the Cr(III) complex. Support of this putative mechanism is obtained from Stern–Volmer quenching experiments, which reveal that only the Hantzsch ester can quench the excited PC. Addition of TEMPO inhibits the reaction, with an alkyl TEMPO adduct being isolated, indicating the formation of an alkyl radical in the process. The quantum yield of the reaction was determined to be 0.09 suggesting this is not a radical chain process. Only four photocatalysts were considered, with **4CzIPN** greatly outperforming its competitors (76% isolated yield comparison to 35%, 25% and 5% GC-FID yields obtained with $[Ir(dF(CF_3)ppy)_2(dtbbpy)]PF_6$, $[Ir(ppy)_2(dtbbpy)]PF_6$ and $[Ru(bpy)_3](PF_6)_2$, respectively, under the same conditions). These yields correlate with the photooxidising ability of the PC (E_{red}* = 1.35 V, 1.21 V, 0.66 V and 0.77 V for **4CzIPN**, $[Ir(dF(CF_3)ppy)_2(dtbbpy)]PF_6$, $[Ir(ppy)_2(dtbbpy)]PF_6$ and $[Ru(bpy)_3](PF_6)_2$, respectively). This is reasonable since the oxidation potential of the Hantzsch ester is E_{ox} = 1.10 V.[285]

Photoredox/copper catalysis

The final example of metallaphotocatalysis utilises a copper complex co-catalyst, for example in the decarboxylative radical sulfonylation reaction to form C(sp^3)-S bonds (Fig. 117a)[286] or the decarboxylative hydroalkylation of alkynes (Fig. 117b).[287]

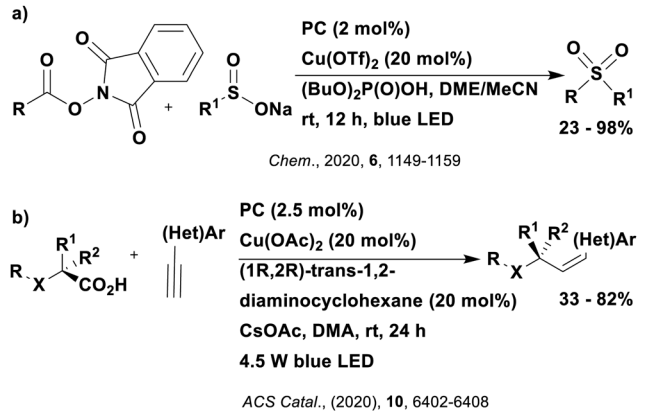

Fig. 117 Reaction scheme for photoredox/Cu dual catalysis where (a) is the decarboxylative radical sulfonylation reaction and (b) is the decarboxylative hydroalkylation of alkynes.

In the former reaction, the excited PC is proposed to reduce the *N*-hydroxyphthalimide, which readily forms an alkyl radical (Fig. 118). Simultaneously, the sulfinate anion is coordinated to the Cu(II) catalyst to produce the Cu(II)-SO_2R intermediate, which is intercepted by the alkyl radical to yield the sulfone product and a Cu(I) species. Oxidation of the Cu(I) complex by the oxidised PC closes both catalytic cycles. Evidence for this mechanism is provided in the form of Stern–Volmer quenching experiments, which showed *N*-hydroxyphthtalimide to be the most efficient quencher of the excited PC. Radical trapping experiments, with 1,1-diphenylethylene for example, provided proof of the presence of alkyl radicals while reaction of Cu(II) *p*-toluenesulfinate with an ethyl radical precursor yielded an ethylsulfone as expected, suggesting the Cu(II) species does act to assist RSO_2 group transfer. When optimising reaction conditions with primary alkyl acids, $[Cu(NCMe)_4]BF_4$ was first used as the copper source, which provided 59% yield with **4CzIPN** as the PC. All other PCs considered were transition metal complexes and under these conditions these managed between 8–39% yield, with $[Ir(dF(CF_3)ppy)_2(dtbbpy)]PF_6$ providing the highest yield. The greater yield provided by **4CzIPN** seems linked to its photoreducing ability (E_{ox}^* = −1.04 V and −0.89 V for **4CzIPN** and $[Ir(dF(CF_3)ppy)_2(dtbbpy)]PF_6$, respectively).

The proposed mechanism for the dual photoredox/Cu catalysed decarboxylative hydroalkylation of alkynes (Fig. 117b) is shown in Fig. 119. In this case, photocatalytic cycles involving both electron and energy transfer are proposed. Firstly, the excited PC is proposed to be reductively quenched by both α-amino and α-oxy carboxylates, as confirmed by Stern–Volmer quenching experiments. The Cu(II) catalyst generated *in situ* can also reductively quench the excited PC, but with a slower quenching rate, thus it is undetermined whether the active Cu(I) species is generated from SET (either from the PC* or from $PC^{\bullet -}$) or from a disproportionation reaction. Once the active Cu(I) species is formed, in the presence of base the alkyne can coordinate to the metal. The resultant adduct is photoexcited, which is thought to accelerate attack from the alkyl radical, itself generated from the α-amino carboxylate. The reduced photocatalyst reduces this intermediate to generate a vinyl anion. Closure of the copper catalytic cycle ensues by protonation and proto-demetalation. The authors then propose *E*/*Z* isomerisation of the alkene, mediated by energy transfer from the excited PC.

When trying to understand the mechanism, $Cu(OAc)_2$ was exchanged with Cu(I) phenylacetylide, and the reaction still

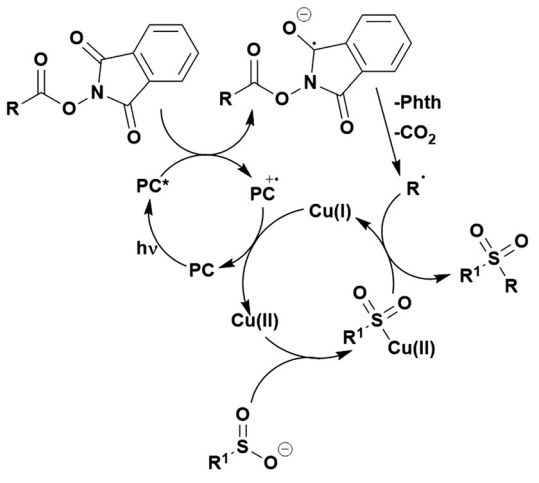

Fig. 118 Putative mechanism for the photoredox/Cu catalysed decarboxylative radical sulfonylation reaction.

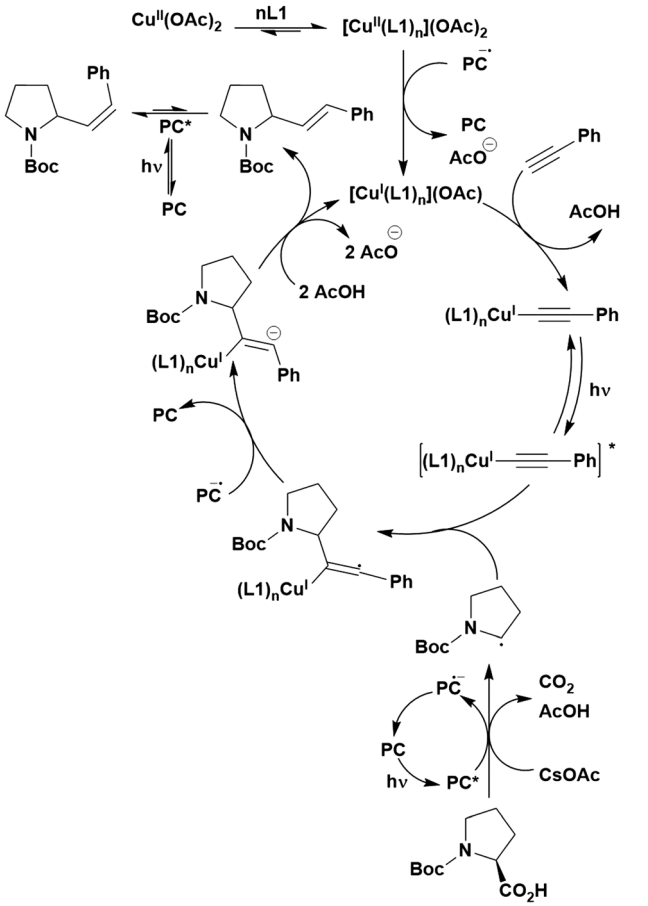

Fig. 119 Suggested mechanism for the decarboxylative hydroalkylation of alkynes using dual photoredox/Cu catalysis where L1 is (1R,2R)-trans-1,2-diaminocyclohexane.

proceeded with similar yield and *Z*-selectivity, suggesting this Cu(I) species is an active intermediate in the reaction. The addition of TEMPO quenches the reaction and instead an adduct is formed between tempo and the alkyl radical generated from the α-amino carboxylate, confirming the presence of the latter. A simple photocatalytic *E*/*Z* isomerization reaction of the alkene was undertaken using the PC, which yielded the same *Z*:*E* ratio, implying the PC is responsible for the isomerization. High throughput experimentation was used to identify the best conditions, with **4CzIPN** being selected as the PC. Comparison of the performance with other PCs is difficult as their relative success is given only in terms of conversion of reactants, whereas the success of **4CzIPN** is provided in terms of yield and selectivity of the final product.

Photoredox and HAT catalysis

There is now a wide body of literature that combines photoredox catalysis and a hydrogen atom transfer (HAT) catalyst. **4CzIPN** has been demonstrated to be compatible with this dual catalysis mode with a number of HAT catalysts, which are typically thiols or amines (Fig. 120). In the examples reported of this type of dual catalysis, the PC always participates in a reductive quenching cycle, where the excited PC is generally reductively quenched by the substrate or a sacrificial electron donor. Following this step, the substrate abstracts a H atom from the thiol HAT catalyst, generating a thiyl radical, which is reduced to a thiyl anion by the reduced PC (Fig. 121a). Subsequent protonation regenerates the HAT catalyst to close both catalytic cycles. Alternatively, if the HAT catalyst is an amine, then SET from the amine to the excited photocatalyst occurs instead (Fig. 121b).

Examples of this dual catalysis with **4CzIPN** as the PC include the hydrosilylation[288] and difunctionalisation[289] of alkenes (Fig. 122a and b, respectively) and silylation of quinoxalinones and heteroarenes (Fig. 122c).[290] In the former, the HAT catalyst chosen is dependent on the nature of alkene substituent, with quinuclidine-3-yl acetate being used for alkenes with electron-withdrawing groups and tri*iso*propylsilanethiol for alkenes with electron-donating groups. A follow up study by Wu *et al.* instead focused on the difunctionalisation of alkenes using quinuclidine-3-yl acetate as the HAT catalyst. In both cases, **4CzIPN** was shown to be the best photocatalyst (87% yield in the hydrosilylation of electron-deficient alkenes, and 75% in the difunctionalisation of alkenes), with only $[Ir(dF(CF_3)ppy)_2(dtbbpy)]PF_6$ providing somewhat comparable yields (80% yield in the hydrosilylation

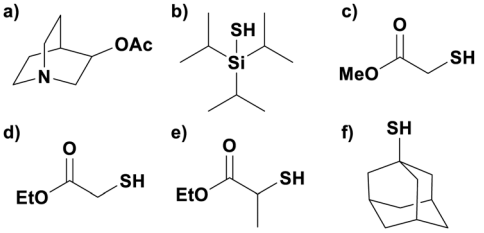

Fig. 120 Common hydrogen atom transfer catalysts; (a) quinuclidin-3-yl acetate, (b) triisopropylsilanethiol, (c) methyl thioglycolate, (d) ethyl thioglycolate, (e) ethyl 2-sulfanylpropanoate and (f) adamantane thiol.

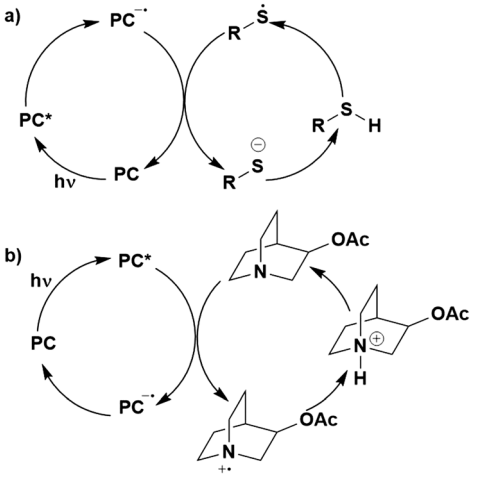

Fig. 121 Two generic mechanistic options for the combination of photocatalysis with a HAT catalyst where the HAT catalyst is (a) a thiol and (b) an amine.

of electron deficient alkenes, and 19% in the difunctionalisation of alkenes). This may be related to the photooxidising ability of the photocatalyst (E_{red}* = 1.35 V and 1.21 V for **4CzIPN** and $[Ir(dF(CF_3)ppy)_2(dtbbpy)]PF_6$, respectively), particularly since the oxidation of quinuclidine-3-yl acetate is quite challenging (E_{ox} = 1.22 V).[291]

Both electron and energy transfer of the PC are proposed as steps in the mechanism of the silylation of quinoxalinones and electron-deficient heteroarenes (Fig. 122c and 123).[290] Interaction of the PC and the HAT catalyst, quinuclidine, occurs as

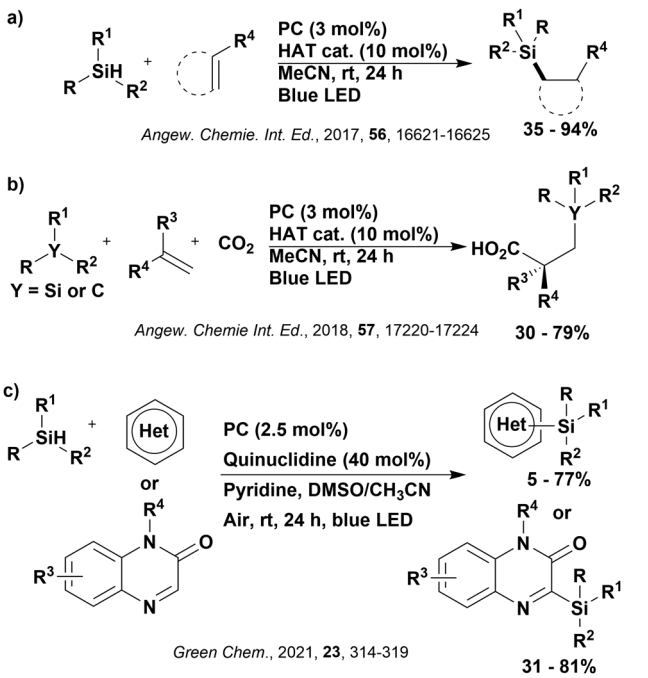

Fig. 122 Reaction schemes for the synergistic photoredox and HAT catalysis for (a) hydrosilylation and (b) difunctionalisation of alkenes and (c) silylation of quinoxalinones and heteroarenes.

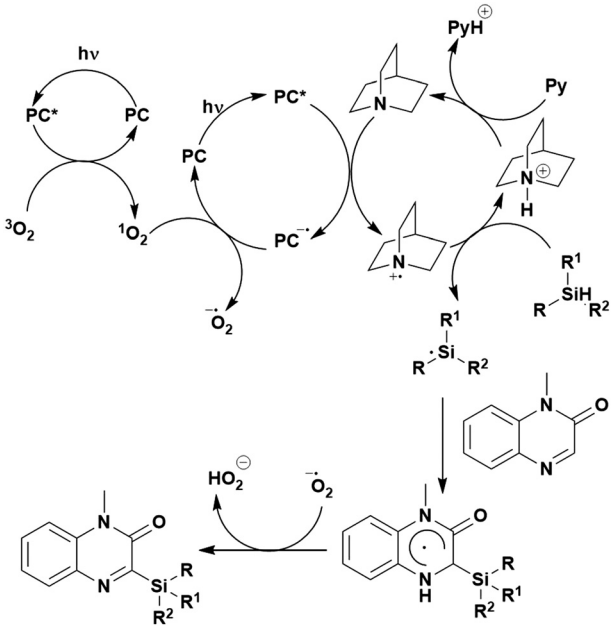

Fig. 123 Putative mechanism for the silylation of quinoxalinones.

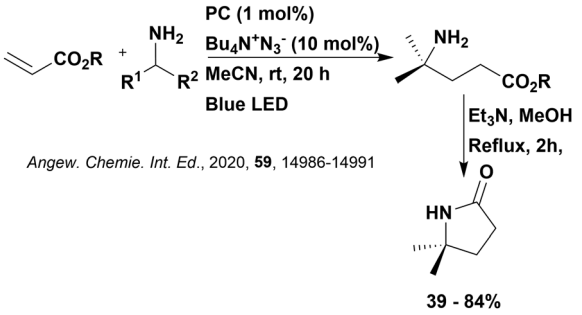

Fig. 124 Reaction scheme for the α-C–H alkylation of primary amines.

in the general mechanism shown in Fig. 121b, whereby the HAT catalyst reductively quenches the excited PC. Simultaneously, the excited PC undergoes PEnT to oxygen, generating singlet oxygen, which in turn is reduced by the reduced PC, to yield a superoxyl radical. The silyl radical, generated through HAT with the quinuclidinium radical cation, adds to the quinoxalinone, with the resultant compound undergoing direct HAT to the superoxyl radical, giving the final product. When TEMPO was added to the mixture, the reaction was inhibited and instead an adduct with the silyl radical was formed, confirming the presence of silyl radicals in this reaction. Moreover, upon addition of the singlet oxygen quencher, 1,4-diazabicyclo[2.2.2]octane (DABCO), the reaction was arrested, suggesting $^1O_2$ does indeed play a crucial role in the reaction. A primary kinetic isotope effect value of $k_H/k_D = 1.27$ implied cleavage of the Si–H bond was unlikely to be involved in the rate determining step. Finally, Stern–Volmer quenching studies showed that quinuclidine does indeed quench the luminescence of the PC. Only 3 PCs were investigated in this reaction, **4CzIPN**, $[Ir(dF(CF_3)ppy)_2(dtbbpy)]PF_6$ and $[Ir(ppy)_2(dtbbpy)]PF_6$ giving yields of 47%, 31% and 0%, respectively. These results correlate with the photooxidising ability of the PC (E_{red}* = 1.35 V, 1.21 V and 0.66 V, respectively). For the remainder of the study, **4CzIPN** was selected as the PC of choice.

Alternatively, alkenes can be used as the coupling partner in the α-tertiary amine synthesis of primary amines, using $[Bu_4N]N_3$ as the HAT catalyst (Fig. 124).[292] The excited PC is proposed to oxidise the azide anion, forming an azidyl radical Fig. 125). This radical then abstracts a proton from the α-C–H position of the primary amine, forming an α-amino radical, which undergoes rapid addition to the Michael acceptor. This *in situ*-generated α-carboxy-stabilised radical is then reduced by the reduced PC, closing the photocatalytic cycle, with subsequent protonation required to form the final product. This final protonation step is thought to occur from HN_3. The low quantum yield of 0.04 is consistent with this reaction not involving a radical chain process. In mechanistic investigations, Stern–Volmer quenching experiments indicated that both the azide anion and cyclohexylamine quenched the emission of the PC; however, the former is a much more efficient quencher (K_{SV} = 2.605 × 10^3 M^{-1} and 12.5 M^{-1} for the azide anion and cyclohexylamine, respectively), supporting the proposed mechanism shown in Fig. 125. Only three PCs were considered in this reaction: **4CzIPN**, $[Ir(dF(CF_3)ppy)_2(dtbbpy)]PF_6$ and $[Ir(ppy)_2(dtbbpy)]PF_6$, with all performing similarly well (85%, 83% and 79%, respectively). This difference in yield does correlate with photooxidising ability of the PC (E_{red}* = 1.35 V, 1.21 V and 0.66 V, for **4CzIPN**, $[Ir(dF(CF_3)ppy)_2(dtbbpy)]PF_6$ and $[Ir(ppy)_2(dtbbpy)]PF_6$, respectively), which is needed to oxidise the azide anion (E_{ox} = 0.87 V). However, since the yields obtained are very similar, despite the rather significant differences in E_{red}*, it is more likely that the photooxidising capacity of the PC is not the yield-determining factor in this reaction. Changes to the HAT catalyst have a much more substantial impact on the yield. Using **4CzIPN** as the PC, well-established HAT catalysts such as tri(isopropyl)silanethiolate and quinuclidine provided lower yields in comparison to $[Bu_4N]N_3$ (70%, 42% and 85%, respectively).

Dialkylation of the primary amine is much less efficient, with $[Ir(dF(CF_3)ppy)_2(dtbbpy)]PF_6$ performing comparably to **4CzIPN** (7% and 2%). Cresswell *et al.* suggests the Ir PC exhibits

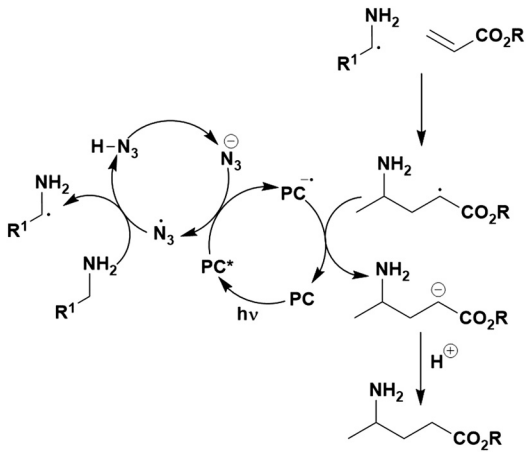

Fig. 125 Proposed mechanism for the α-C–H alkylation of primary amines.

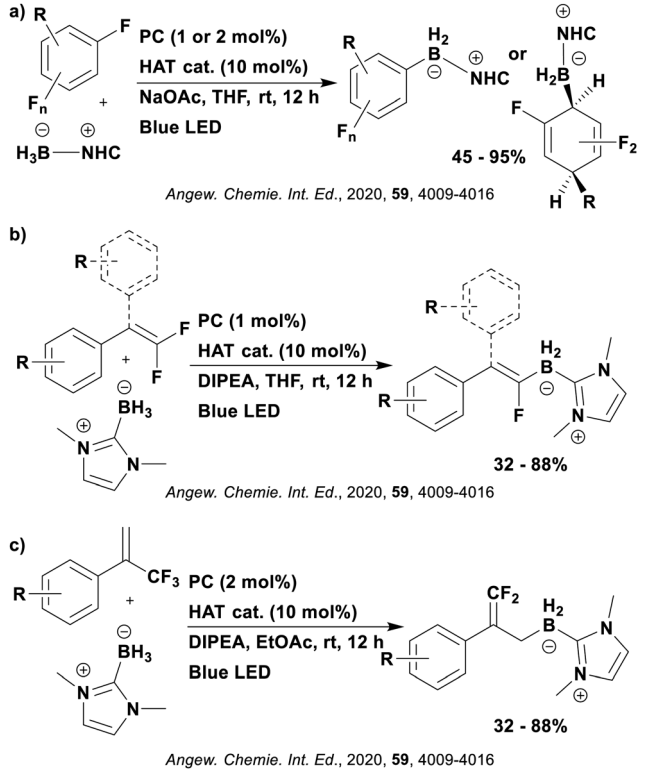

Fig. 126 Reaction schemes for the defluoroborylation of (a) polyfluoroarenes, (b) *gem*-difluoroalkenes and (c) trifluoromethylalkenes.

enhanced stability to photobleaching, although there is no corroborating evidence provided to support this contention.

An additional example of functionalisation of alkenes, but with less mechanistic clarity, can be seen in the defluoroborylation of polyfluoroarenes, *gem*-difluoroalkenes and trifluoromethylalkenes (Fig. 126a–c, respectively).[293] A radical-based pathway was confirmed by the use of TEMPO, and Stern–Volmer quenching experiments provided evidence that the thiol HAT catalyst was the species quenching the excited state of the PC, not the fluorinated reagents. Boryl radical intermediates are thought to be present in the mechanism, based on similar work from Taniguchi *et al.*[294] while a study from Weaver *et al.*[295] suggests the possibility of SET to the fluoroarene, generating the fluoroaryl radical anion, may occur. A quantum yield of 0.43 suggests this is not a radical chain process and the kinetic isotope effect observed indicates the HAT of the NHC borane may not contribute to the rate-determining step. Taking all of this into consideration, multiple reaction mechanisms are proposed, although all incorporate reductive quenching of the excited photocatalyst by the HAT catalyst, with the reduced PC being used to reduce one of the fluorinated intermediates. Optimisation involving the polyfluoroarenes indicated both **4CzIPN** and $[Ir(dF(CF_3)ppy)_2(dtbbpy)]PF_6$ as excellent PCs for this reaction. The iridium PC provided the greatest yield of 93% when used in concert with ethyl thioglycolate as the HAT catalyst, while **4CzIPN** managed 76% yield under these conditions. Instead, **4CzIPN** worked better when used with ethyl 2-sulfanylpropanoate as the HAT catalyst (90% yield) but use of this HAT catalyst with the iridium PC was not considered. For the *gem*-difluoroalkenes, $[Ir(dF(CF_3)ppy)_2(5,5'\text{-}dFbpy)]PF_6$ was found as the optimal photocatalyst (80% yield in comparison to 50% yield for **4CzIPN**). This is likely to be due to the ground state reduction potential (E_{red} = −1.16 V *vs.* SCE for $[Ir(dF(CF_3)ppy)_2(5,5'\text{-}dFbpy)]PF_6$).[296] Finally, for trifluoromethylalkenes, only **4CzIPN** was employed as the photocatalyst, yielding 86% of product during the solvent optimisation studies.

This form of dual catalysis can also be utilised in the redox neutral fragmentation of 1,2-diol derivatives, a reaction that can be applied to the fragmentation of lignin model compounds (Fig. 127).[297] The excited PC is proposed to be reductively quenched by the HAT catalyst, producing a thiyl radical. This thiyl radical then abstracts the α H-atom of the 1,2-diol derivative to generate a ketyl radical, regenerating the HAT catalyst (Fig. 128). Oxidation of this ketyl radical by oxygen produces a ketone, which is reduced to the radical anion by the reduced PC, completing the photocatalytic cycle. Subsequent C–O bond cleavage and protonation generates the final fragmentation products.

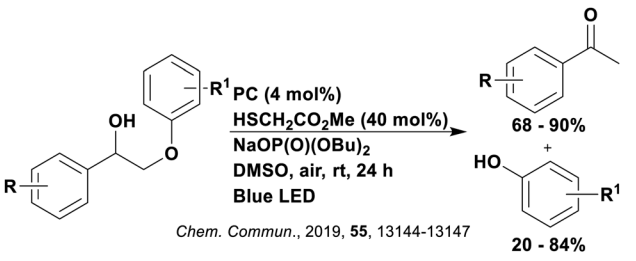

Fig. 127 Reaction scheme for the fragmentation of 1,2-diol derivatives.

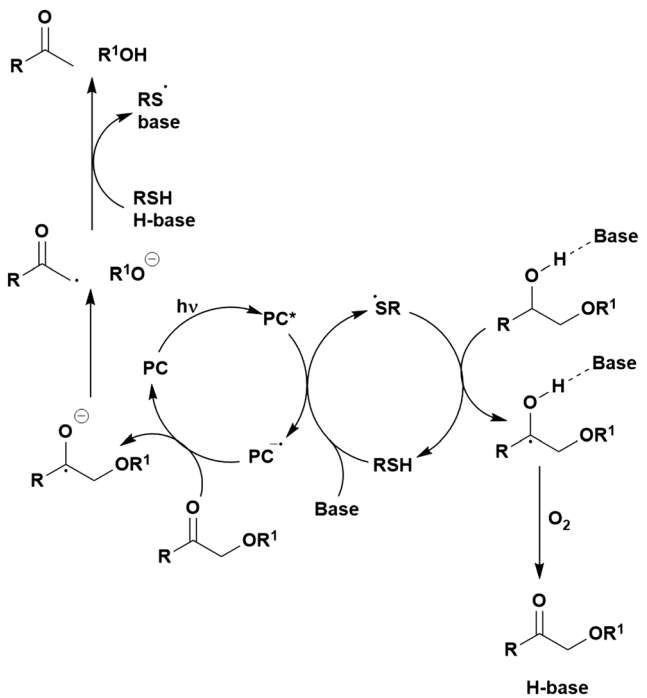

Fig. 128 Plausible mechanism for the dual catalytic fragmentation of 1,2-diol derivatives.[297]

This mechanism was supported by Stern–Volmer quenching experiments that showed efficient quenching of the PC upon addition of HAT catalyst and base. Iridium PC $[Ir(ppy)_2(dtbbpy)]PF_6$ was identified as the best photocatalyst with 1 mol% loading, forming 91% of the ketone and 81% of the alcohol. Using 5 mol% of photocatalyst, eosin Y and perylene yielded no product while **4CzIPN** managed 26% of both fragmentation products. Further optimisation of the conditions using **4CzIPN** resulted in yields of 80% and 57% for the ketone and alcohol, respectively. König *et al.* decided to use **4CzIPN** throughout the remainder of the study with these optimised conditions as it exhibited similar reaction efficiency but with less sensitivity to the reaction conditions (for example, doing the reaction under air rather than N_2 increases the yield for **4CzIPN** but decreases the yield dramatically for the iridium photocatalyst). In general, the difference in yield between the photocatalysts is likely linked with their ground state reduction potential (E_{red} = −1.51 V, −1.21 V and −1.06 V for $[Ir(ppy)_2(dtbbpy)]PF_6$, **4CzIPN** and eosin Y respectively), which must be sufficiently negative in order to reduce the in situ-formed ketone (E_{red} = −1.72 V for 2-phenoxy-1phenylethan-1-one).

Additionally, this synergistic catalysis can be used to make more subtle changes, such as the incorporation of deuterium or tritium into a substrate. This can be observed in terms of halogen atom transfer (XAT) of alkyl or aryl halides (Fig. 129a)[186] as well as hydrogen isotope exchange (HIE) at α-amino C(sp^3)–H bonds (Fig. 129b),[298] at the C1 position of aldehydes (Fig. 129c)[299] or at α-amino C(sp^3)–H bonds of amino acids and peptides (Fig. 129d).[300] In the former reaction, amino radicals are used a XAT reagents in order to functionalise aryl and alkyl halides, as previously

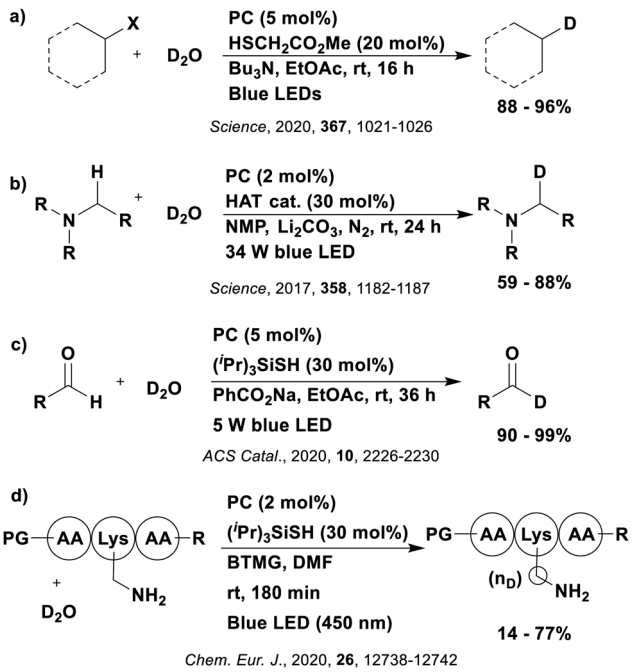

Fig. 129 Reaction schemes for the deuteration of (a) alkyl or aryl halides, (b) α-amino C(sp^3)–H bonds, (c) aldehydes and (d) amino acids and peptides. BTMG = 2-*tert*-butyl-1,1,3,3-tetramethylguanidine.

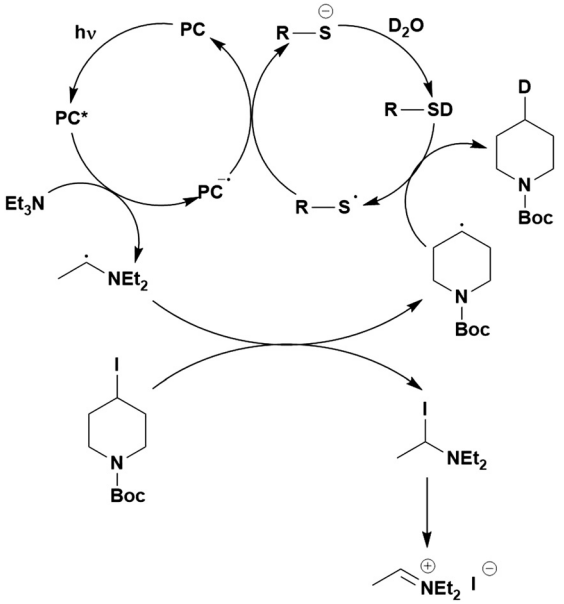

Fig. 130 Proposed mechanism for the dehalogenation of an alkyl iodide.

mentioned.[186] In the proposed mechanism, the excited PC is used to oxidise TEA, forming the α-aminoalkyl radical. This radical then undergo XAT with 4-iodo-*N*-boc-piperidine and the resultant alkyl radical on the piperidine substrate can abstract a deuterium from the HAT catalyst, methyl thioglycolate (Fig. 130). The thiyl radical produced is reduced by the reduced PC before being deuterated from D_2O closing both catalytic cycles. A wide variety of photocatalysts were considered for the standard dehalogenation of 4-iodo-*N*-boc-piperidine, with **4CzIPN** proving the best (98% yield), followed by $[Ir(dF(CF_3)ppy)_2(dtbbpy)]PF_6$ (83%), *fac*-$Ir(ppy)_3$ (78%) and $[Ir(ppy)_2(dtbbpy)]PF_6$ (74%). This difference in yield seems to be reflective of the photooxidising capacity of the photocatalyst (E_{red}* = 1.35 V, 1.21 V, 0.31 V and 0.66 V for **4CzIPN**, $[Ir(dF(CF_3)ppy)_2(dtbbpy)]PF_6$, *fac*-$Ir(ppy)_3$ and $[Ir(ppy)_2(dtbbpy)]PF_6$, respectively), which must be capable of oxidising TEA (E_{ox} = 0.77 V). Stern–Volmer quenching experiments confirm the amine XAT substrate is responsible for quenching of the PC, with negligible quenching observed with 4-iodo-*N*-boc-piperidine. The quantum yield of 0.065 for this reaction is suggestive that this is not a radical chain process.

For HIE at α-amino C(sp^3)–H bonds (Fig. 129b and d),[298,300] a very similar mechanism was proposed whereby the α-amino radical produced by reductive quenching of the excited PC abstracts a deuterium or tritium atom from the HAT catalyst, which in this case is either methyl thioglycolate or tri*iso*-propylsilanethiol. In the deuteration of simple amines (Fig. 129b), the best photocatalyst identified was substrate-dependent, with **4CzIPN**, $[Ir(ppy)_2(dtbbpy)]PF_6$ or $[Ir(F(Me)ppy)_2(dtbbpy)]PF_6$ being the photocatalysts that provided the highest product yields. For example, for substrates containing an aliphatic carboxylic acid group, less photooxidising photocatalysts were necessary in order to prevent photoredox-induced decarboxylation; hence, the iridium photocatalysts were more useful in this case (E_{red}* = 0.66 V, 0.94 V and 1.35 V for $[Ir(ppy)_2(dtbbpy)]PF_6$, $[Ir(F(Me)ppy)_2(dtbbpy)]PF_6$

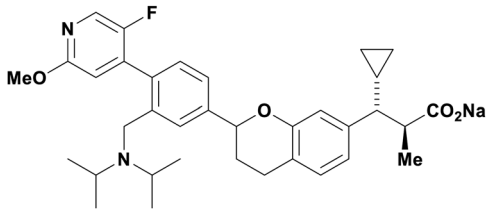

Fig. 131 Example of substrate that can be oxidised by **4CzIPN** in the deuteration reaction with a HAT catalyst.

and **4CzIPN**, respectively). An example of such a substrate can be seen in Fig. 131. When undergoing HIE with amino acids and peptides (Fig. 129d), both **4CzIPN** and $[Ir(dF(Me)ppy)_2(dtbbpy)]PF_6$ provided the same deuterium incorporation (1.6 D molecule^{-1}), while other PCs performed much worse (*fac*-$Ir(ppy)_3$ and $[Ir(dF(CF_3)ppy)_2(dtbbpy)]PF_6$ afforded 0.4 and 0.1 D molecule^{-1}, respectively).

In the deuteration of the C1 position of aldehydes (Fig. 129c),[299] the proposed mechanism is again similar to that shown in Fig. 130, except the excited PC is reductively quenched by sodium benzoate to give a benzoyloxy radical. The crucial acyl radical is formed by HAT to the benzoyloxy radical. A second HAT step between the deuterated HAT catalyst and the acyl radical affords the deuterated aldehyde. Only organic PCs were considered for this reaction, with **4CzIPN** generating the highest percentage of D incorporation (40%) while PCs like eosin Y managing $<5\%$. Further optimisation with **4CzIPN** resulted in 93% D incorporation. The superior photooxidising ability of **4CzIPN** may be linked to its higher success in this reaction (E_{red}^* = 1.35 V and 0.83 V for **4CzIPN** and eosin Y, respectively).

Finally, a report by Wendlandt *et al.* demonstrated the combination of photoredox catalysis with two distinct HAT catalytic cycles in the synthesis of rare sugar isomers through site-selective epimerisation (Fig. 132).[125] The excited PC is reductively quenched by quinuclidine, generating the quinuclidine radical cation, which abstracts a proton from the sugar (Fig. 133). The protonated quinuclidine is then deprotonated by an exogenous base while the sugar radical abstracts a proton from adamantane thiol to form the isomerised product. The subsequently formed thiyl radical is reduced by the reduced photocatalyst, closing the photocatalytic cycle. Stern–Volmer quenching experiments support this mechanism, revealing that the PC is quenched by quinuclidine but not by the thiol. Using 2 mol% of **4CzIPN** resulted in 92% yield of product while the only other photocatalyst considered, $[Ir(dF(CF_3)ppy)_2(dtbbpy)]PF_6$, managed 88% yield at 1 mol% loading.

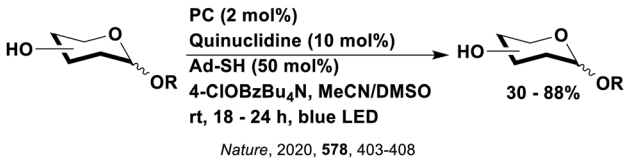

Fig. 132 Reaction scheme for the synthesis of rare sugar isomers through site selective epimerisation.

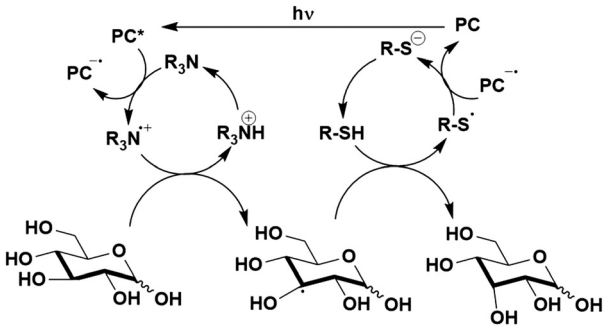

Fig. 133 Viable mechanism for the site selective epimerisation of sugars.

Photocatalysis/NHC catalysis

N-Heterocyclic carbene (NHC) catalysis can be used in conjunction with **4CzIPN** in photoredox catalysis as a method of synthesising amides from aldehydes and imines (Fig. 134a)[301] and making ketones from carboxylic acids (Fig. 134b).[302] The proposed mechanism for the former first involves condensation of the aldehyde with the NHC to yield a Breslow intermediate, which reductively quenches the excited PC (Fig. 135). Concurrently, the reduced PC reduces the imine to form a *N*-centre radical that couples with the Breslow intermediate radical. The NHC catalyst is then released to give the final amide product. The presence of radicals in this mechanism was confirmed by the addition of TEMPO (effectively inhibiting the reaction) as well as EPR spectroscopy, which detected a nitrogen centred radical. The aldehyde, the base or the NHC catalyst, individually, showed no significant quenching of the excited PC; however, a combination of the three reagents together produced a strong quenching of the luminescence.

For this reaction, three Ru(II) and eleven Ir(III) complexes (10 cationic and one neutral) were evaluated as PCs, alongside six organic dyes. **4CzIPN** outperformed the other PCs, yielding 43% of product. Yields obtained from the other PCs varied from 1–13%, except for $[Ir(ppy)_2(dtbbpy)]PF_6$, which managed 20%. The reduction of the imine is the challenging step

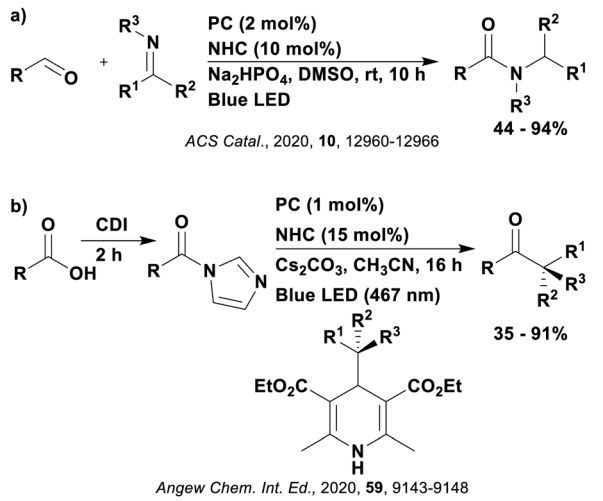

Fig. 134 Reaction scheme for the dual photoredox/NHC catalysis to form (a) amides and (b) ketones. CDI = carbonyldiimidazole.

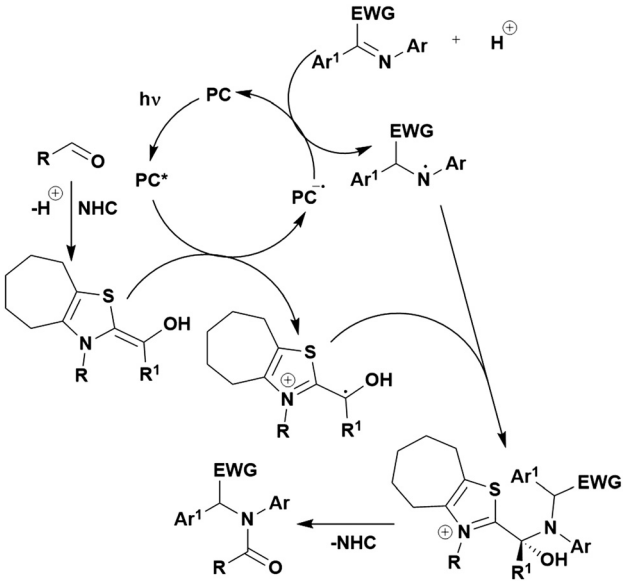

Fig. 135 Putative mechanism for the dual photoredox/NHC catalysis to form amides.

(E_{red} = −1.16 V *vs.* SCE for methyl 2-((4-fluorophenyl)imino)-2-(phenyl)acetate in the presence of NaH_2PO_4), which may explain why some PCs struggled (*e.g.*, eosin Y has E_{red} = −1.06 V and obtained 2% yield), especially since low conversions of the imine were typically obtained (58% conversion for **4CzIPN** and between 8–42% for other PCs).

In the dual catalytic synthesis of ketones from carboxylic acids (Fig. 134b),[302] the excited PC is reductively quenched by the DHP radical precursor, which after fragmentation, releases the alkyl radical. Meanwhile, the acyl triazolium species, generated by the addition of the NHC catalyst to the intermediate imidazole, is reduced by the reduced PC, affording the azolium radical. Loss of the NHC and radical coupling of the azolium and alkyl radicals, generates the final product. Addition of TEMPO inhibits the reaction, instead forming an adduct with the alkyl radical generated from the DHP precursor. Four PCs were considered, $[Ir(dF(CF_3)ppy)_2(dtbbpy)]PF_6$, **4CzIPN**, *fac*-$Ir(ppy)_3$ and $[Mes\text{-}Acr]BF_4$, providing yields of 63%, 42%, 11% and 0%, respectively. These results generally correlate with the ground state reduction potential of the PC (E_{red} = −1.37 V, −1.21 V and −0.57 V for $[Ir(dF(CF_3)ppy)_2(dtbbpy)]PF_6$, **4CzIPN** and $[Mes\text{-}Acr]BF_4$, respectively), as the reduced PC is needed to reduce the acyl triazolium species (phenyl acyl azolium has E_{red} = −1.29 V *vs.* SCE). For *fac*-$Ir(ppy)_3$, however, since E_{red} = −2.19 V, the poor yield is likely instead due to its poor photooxidising ability (E_{red}* = 0.31 V), which struggles to oxidise the DHP (benzyl Hantzsch ester has E_{ox} = 1.00 V *vs.* SCE).[303] The PC $[Ir(dF(CF_3)ppy)_2(dtbbpy)]PF_6$ was chosen for the remainder of the study on account of it providing the highest yields.

Photocatalysis/bromine catalysis

The final example of dual catalysis involving **4CzIPN** is the [3+2] cycloaddition reaction, facilitated by bromine radical catalysis (Fig. 136).[304] The proposed mechanism involves energy transfer

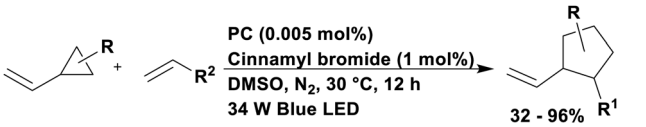

ACS Catal., 2020, **10**, 2609-2614

Fig. 136 Reaction scheme for the [3+2] cycloaddition of substituted vinyl and ethynylcyclopropanes with alkenes.

from the excited PC to the cinnamyl bromide pre-catalyst, generating the crucial bromyl radical (Fig. 137). Addition of this radical to the vinyl bond of the substituted cyclopropane generates a transient radical species that undergoes fast ring opening. The homoallyl radical intermediate then adds to the alkene reagent, followed by ring closure and elimination of the bromyl radical, closing the catalytic cycle. Stern–Volmer quenching experiments revealed that cinnamyl bromide acted as a quencher of the excited PC. Since cinnamyl bromide has a high oxidation potential of E_{ox} = 2.01 V, SET between the precatalyst and the photocatalyst is thermodynamically unfavourable (for **4CzIPN**, E_{red}* = 1.35 V and E_{ox} = 1.52 V), which eliminated this mechanism from consideration, leaving PEnT as the alternative plausible mechanism. A correlation between the triplet energy E_T of the PC and the yield of product was found, namely the higher the E_T, the greater yield. For example, $[Ir(dF(CF_3)ppy)_2(dtbbpy)]PF_6$ gave the highest yield (95%, E_T = 2.65 eV, 256 kJ mol^{-1}), closely followed by **4CzIPN** (93%, E_T = 2.52 eV, 243 kJ mol^{-1}), whereas $[Ir(ppy)_2(dtbbpy)]PF_6$ was inadequate (11%, E_T = 2.12 eV, 205 kJ mol^{-1}). Since this is an energy transfer mechanism, emphasis on the spectral overlap of the emission of the PC and absorption of cinnamyl bromide must be highlighted. The aforementioned PCs emit at 470 nm, 535 nm and 581 nm, for $[Ir(dF(CF_3)ppy)_2(dtbbpy)]PF_6$, **4CzIPN** and $[Ir(ppy)_2(dtbbpy)]PF_6$, respectively, in MeCN. From this, the more red-shifted the emission of the PC, the lower the yield of product indicating a poorer spectral overlap with the absorption of the precatalyst. **4CzIPN** was selected as the photocatalyst of choice for the study, although no further mechanistic studies were undertaken to determine which energy transfer mechanism

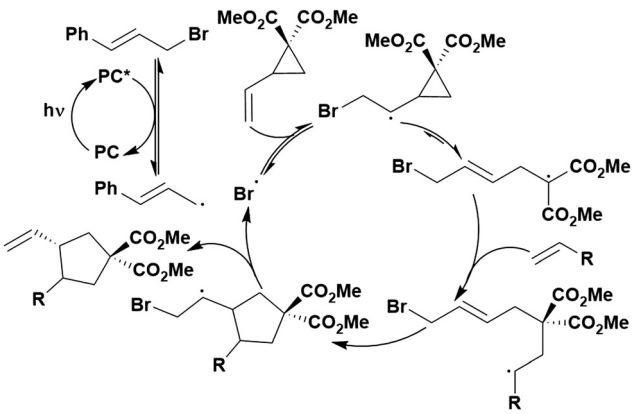

Fig. 137 Suggested mechanism for the dual catalytic [3+2] cycloaddition of vinyl cyclopropanes with alkenes.

is in operation. A quantum yield of 0.183 suggests this is not a radical chain process.

4. Other CDCB-based TADF organic photocatalysts

As a photocatalyst, **4CzIPN** has been shown to be effective in a wide range of transformations.[305] Though it is the most widely used TADF-based photocatalyst in recent years, it is not the only TADF molecule that has been used, with **4DPAIPN** in particular quickly becoming a popular choice.[306] In this section, we compare and contrast organic TADF photocatalysts, confining at first to compounds within the carbazolyl dicyanobenzene (CDCB) family of compounds. While in most cases the TADF nature of the photocatalyst is not explicitly explored, the results obtained can nonetheless be used to gain insight into to the link between the photophysical parameters of the photocatalyst and the observed photocatalytic ability.

Modification of the structure of the carbazole donor and dicyanobenzene acceptor moieties of **4CzIPN** results in donor–acceptor compounds with modulated redox potentials and photophysical properties. A comprehensive listing of the properties of these compounds is provided in Table 2. Since the spatially separated HOMO is localised on the donor moieties and the LUMO is localised on the acceptor core, changes to these components can be done almost independently to alter the oxidative and reductive capabilities of the photocatalyst in both the ground and excited state.

For example, consider **4CzIPN** and **4MeOCzIPN**. Both contain the same isophthalonitrile acceptor component, hence should

Table 2 Redox potentials and selected photophysical properties of benzonitrile and CDCB-based TADF compounds that have been considered as photocatalysts[a]

PC	λ_{abs}/nm	λ_{PL}/nm	$E_{0,0}$/eV (kJ mol^{-1})	ΔE_{ST}/eV	E_{ox}/V	E_{red}/V	E_{ox}*/V	E_{red}*/V	τ_{pf}/ns	τ_{df}/μs	Ref.
3,5-2CzBN		396[e]	3.34[e,m] (322)	0.40[e]						3.9[e]	307
2,3,6-3CzBN				0.31					9.6	102.7	308 and 309
2,4,6-3CzBN		431[e]	3.10[e,m] (299)	0.29					10.1	220.3	307–309
3,4,5-3CzBN	340	565	2.19[n] (211)		2.07	−1.58	−0.51	1.00			310
4CzBN	333[b]	442[e]	2.9[b] (280)	0.25	1.61	−1.63	−1.29	1.27	5.4	36.9	309, 311 and 312
4CzBN-Br	340[b]		2.8[b] (270)	0.22[b]	1.62	−1.50	−1.18	1.30		7.8[b]	311
5CzBN		512	2.83 (273)	0.07	1.41	−1.52	−1.42	1.31	16.2	7.8	114, 308 and 309
5CzBN-OMe		462	2.81 (271)		1.02[b]	−1.66[b]	−1.79[b]	1.15[b]			114
2CzPN	365	530	2.77[l] (267)	0.09[e]	1.47	−1.45	−1.3	1.32	12.9	15.4	60, 120, 121 and 308
2CzIPN	362	501	2.87[l] (277)	0.05[d]	1.46	−1.51	−1.41	1.36			120 and 313
2CzTPN	430[b]	511[b]	2.64[b,l] (255)	0.08[j]	1.4[b]	−1.3[b]	−1.24[b]	1.34[b]	34[j]	11.3[j]	120 and 314
4CzPN	435	535	2.56[l] (247)	0.25[e,i]	1.5	−1.16	−1.06	1.4	6.7	0.5	120, 121 and 315
4CzPN-Ph					1.24[c,d]	−1.29[c,d]					316
4CzPN-^{t}Bu					1.20[c,d]	−1.23[c,d]					316
4CzIPN	435	535	2.67[l] (258)	0.08[e]	1.52	−1.21	−1.04	1.35	18.7	1.39	60, 114, 120 and 121
4CzIPN-Me	456	603		0.307[h]		−1.23		1.31			317 and 318
4CzIPN-Ph	390	611		0.214[h]	1.41	−1.15			4	0.79	316 and 317
4CzIPN-^{t}Bu	380	588	2.53 (244)	0.308[h]	1.22	−1.32	−1.31	1.21	10	1.4	316, 317, 319 and 320
4CzIPN-OMe		482	2.61[f] (252)		1.11[f]	−1.34[f]	−1.5[f]	1.27[f]			114
4CzIPN-F			2.60[b] (251)		1.45[b]	−1.08[b]	−1.15[b]	1.52[b]			321
4CzIPN-Cl			2.68 (259)		2.05	−0.97	−0.63	1.71			321
4CzIPN-Br			2.58[b] (249)		1.76[b]	−1.06[b]	−0.82[b]	1.52[b]			321
4CzTPN[b]	463	556	2.43[l] (234)	0.38	1.44	−1.02	−0.99	1.41	6.5	1.46	120 and 121
4CzTPN-Me		561[e]							9.2[e]	1.5[e]	60
4CzTPN-Ph		577[e]			0.25[c,d]	−1.29[c,d]			9.0[e]	1.1[e]	60 and 316
4CzTPN-tBu				0.01[e,i]	0.21[c,d]	−1.24[c,d]					315 and 316
4CzTPN-Br	349[b]	546[e]	2.72[b] (262)						0.3[e]	4.8[b]	311 and 322
3CzClIPN		545	2.72 (262)		1.79	−1.16	−0.93	1.56	6.9		114
4CzBnBN		477[k]			1.48[g]	−1.72[g]	−1.45	1.21			323
4CzPEBN			2.88[g] (278)			−1.69[g]		1.19[g]			324
4DPAPN	448[g]	559[g]	2.46[g] (237)			−1.53[g]		0.93[g]			325
4DPAIPN	425	523	2.62[l] (253)		1.34	−1.52	−1.28	1.1			120
4DPAIPN-Cl			2.53 (244)		1.23	−1.44	−1.30	1.09			320
4DPAIPN-Br			2.53 (244)		1.12	−1.55	−1.41	0.98			320
3DPAClIPN		537	2.65 (256)		1.31	−1.41	−1.34	1.24	11.5		114
3DPAFIPN		525	2.68 (259)		1.3	−1.59	−1.38	1.09	4.2		114
3DPA2FBN		491	2.84 (274)		1.24[b]	−1.92[b]	−1.6[b]	0.92[b]	4.2		114

[a] All potentials are given in volts *versus* SCE. E_{ox}* = E_{ox} − $E_{0,0}$ and E_{red}* = E_{red} + $E_{0,0}$. 1 eV = = (1.602 × 10^{-22} k J) × N_A where N_A = Avogradro's constant. λ_{abs} refers to the absorption maximum of the CT band. λ_{PL} refers to the photoluminescence maximum. Data reported in MeCN at room temperature unless otherwise noted. $E_{0,0}$ determined from the intersection point of the normalised absorption and emission spectra unless otherwise noted. [b] Determined in dichloromethane. [c] Originally referenced *versus* Ag/AgNO$_3$, converted to be referenced *versus* SCE using E (*vs.* SCE) = E(*vs.* Ag/AgNO$_3$) + 0.30 V.[326] [d] Determined in tetrahydrofuran. [e] Determined in toluene. [f] Determined in CH$_3$CN/CH$_2$Cl$_2$ (5 : 1). [g] Determined in dimethylformamide. [h] Estimated by time-dependent (TD)DFT at the M06-2X/6-31+G(d) level. [i] Measured at 77 K. [j] Determined in 3 wt%-CzTPN:PzCz film measured at room temperature under N$_2$ (PzCz = hexakis(9H-carbazol-9-yl) cyclotriphosphazene). [k] Determined in DMA. [l] $E_{0,0}$ estimated using the medium wavelengths between the lowest fluorescence excitation peak (excitation λ_{max}) and the fluorescence peak (emission λ_{max}).[120] [m] $E_{0,0}$ obtained from the absorption spectrum.[307] [n] $E_{0,0}$ estimated from $E_{0,0}$ = hc/λ_{em}.[310]

have a similar LUMO energy level and reduction potential (E_{red} = −1.21 V and −1.34 V for **4CzIPN** and **4CzIPN-OMe**, respectively, in MeCN and MeCN:DCM(5 : 1)). The difference between these two emitters arises in the donor groups; **4CzIPN** has 4 carbazole (Cz) donor groups while **4CzIPN-OMe** has 4 methoxy substituted carbazole (MeOCz) donor groups. The addition of the methoxy groups results in **MeOCz** being a stronger donor than **Cz**. Therefore, the HOMO energy level of **4CzIPN-OMe** should be destabilised in comparison to **4CzIPN**. This is indeed the case, as is reflected by the ground state oxidation potential (E_{ox} = 1.52 V and 1.11 V for **4CzIPN** and **4CzIPN-OMe**, respectively, in MeCN and MeCN:DCM(5 : 1)). The smaller E_{ox} value of **4CzIPN-OMe** indicates it is a stronger ground state reductant than **4CzIPN**.

When instead understanding the influence of structure on the ground state oxidising capability, consider **3DPAFIPN** and **3DPA2FBN**. In this case, both have three similarly disposed DPA donor groups about the central benzene ring and so the HOMO energy level and consequently the oxidation potential should be similar (E_{ox} = 1.30 V and 1.24 V, for **3DPAFIPN** and **3DPA2FBN**, respectively, in MeCN and DCM). The main difference in these structures arises in the nature of the acceptor, where **3DPAFIPN** has two cyano groups and one fluoro substituent on the phenyl ring while **3DPA2FBN** has one cyano group and two fluoro substituents. Since cyano groups are more strongly electron-withdrawing than halogens, there is consequently a more stabilised LUMO in **3DPAFIPN**. As a result, **3DPAFIPN** is a stronger ground state oxidant, as reflected by the less negative ground state reduction potential (E_{red} = −1.59 V and −1.92 V for **3DPAFIPN** and **3DPA2FBN**, respectively, in MeCN and DCM).

As demonstrated, modification of the donor and acceptor groups clearly impacts upon the ground state redox potentials, which of course are linked to the excited state redox potentials, through $E_{ox}^* = E_{ox} - E_{0,0}$ and $E_{red}^* = E_{red} + E_{0,0}$. From these equations, it becomes clear that the changes in the optical gap must also be taken into consideration when discussing the impact on the excited state redox potentials. Destabilisation of the HOMO, as caused by the presence of a weaker donor, results in a larger $E_{0,0}$. Again consider **4CzIPN** and **4CzIPN-OMe**. When acting as a photooxidant, the hole left in the HOMO of the PC after excitation of an electron to the LUMO, can readily accept an electron from a donor. Since both **4CzIPN** and **4CzIPN-OMe** have the same acceptor unit, E_{red} should be similar. However, the weaker carbazole donor means **4CzIPN** has a larger optical gap ($E_{0,0}$ = 2.67 eV (258 kJ mol^{-1}) and 2.61 eV (252 kJ mol^{-1}) for **4CzIPN** and **4CzIPN-OMe**, respectively, in MeCN and MeCN:DCM(5 : 1)). When considering E_{red}^*, this means a more positive value for **4CzIPN** in comparison to **4CzIPN-OMe** (E_{red}^* = 1.35 V and 1.27 V for **4CzIPN** and **4CzIPN-OMe**, respectively, in MeCN and MeCN : DCM(5 : 1)) owing to the larger optical gap in the former. This translates to **4CzIPN** being a stronger photooxidant.

The same analysis can be used when considering the TADF compounds as photoreductants. In this case, the PC's electron that has been promoted to the LUMO can be donated to an acceptor substrate. Again, consider **3DPAFIPN** and **3DPA2FBN**. The more stabilized LUMO in **3DPAFIPN** coupled with comparable HOMO levels results in a decreased optical gap for this compound ($E_{0,0}$ = 2.68 eV (259 kJ mol^{-1}) and 2.84 eV (274 kJ mol^{-1}) for **3DPAFIPN** and **3DPA2FBN**, respectively, in MeCN). The larger optical gap observed for **3DPA2FBN** will result in a more negative E_{ox}^* value (E_{ox}^* = −1.38 V and −1.60 V for **3DPAFIPN** and **3DPA2FBN**, respectively, in MeCN and DCM), meaning **3DPA2FBN** in a stronger photoreductant than **3DPAFIPN**.

These examples highlight that modifications can be made in terms of both the nature and number of donor and acceptor moieties in order to modulate the electrochemical properties of the PCs. A range of these donor–acceptor molecules, including many that have sufficiently small ΔE_{ST} to be considered TADF, from the CDCB family (Fig. 138 and 139) have been reported to act as photocatalysts.

5. CDCB based molecules acting as independent photocatalysts

Other TADF molecules within the CDCB family of compounds have also been reported as photocatalysts. This section highlights their use and contrasts their performance with **4CzIPN**.

Photoinduced decarboxylation of carboxylic acids in the formation of C–C and C–X bonds

Both the γ,γ-difluoroallylation of cycloketone oxime ethers (Fig. 140a) and the fragmentation–alkynylation of oxime ethers (Fig. 140b) proceed through a photoinduced oxidative decarboxylation mechanism as shown in Fig. 141, whereby the excited PC can be used to decarboxylate the cycloketone oxime ethers in a reductive quenching cycle.[327] In the former reaction, the nucleophilic alkyl nitrile radical eventually is coupled to an electron-poor trifluoromethyl-substituted alkene and the resultant product undergoes single electron reduction by the reduced PC. Both **4CzIPN** and **4DPAIPN** were investigated as photocatalysts for this reaction, with **4CzIPN** providing the higher product yields (64% and 34%, respectively, at 5 mol% of catalyst loading); however, both fell short of the high yields obtained by [Ir(dF(CF$_3$)ppy)$_2$(dtbbpy)]PF$_6$ (76% yield). Oxidation of the oxime ether requires a strong photooxidant (E_{ox} = 1.48 V for an analogous compound),[321] which likely explains why **4DPAIN** provides inferior yields (E_{red}^* = 1.21 V, 1.35 V and 1.1 V for [Ir(dF(CF$_3$)ppy)$_2$(dtbbpy)]PF$_6$, **4CzIPN** and **4DPAIPN**, respectively). The other SET implicates the PC as a ground state reductant, for which the iridium photocatalyst has a superior redox potential (E_{red} = −1.37 V, and −1.21 V for [Ir(dF(CF$_3$)ppy)$_2$(dtbbpy)]PF$_6$ and **4CzIPN**), which may help to explain the differing yields obtained. Although **4DPAIPN** is an even greater ground state reductant (E_{red} = −1.52 V), its poor photooxidising ability acts as a barrier to its success in this reaction.

For the reaction involving the alkynylation of oxime ethers (Fig. 140b), a similar mechanism is in operation.[321] Again, the oxime ether is oxidatively decarboxylated by the excited photocatalyst, before the resultant alkyl nitrile radical is trapped by the ethynyl benziodoxolone (EBX) reagent (Fig. 141). Upon release of the product, the subsequent iodine radical is reduced by the reduced photocatalyst, closing the photocatalytic cycle.

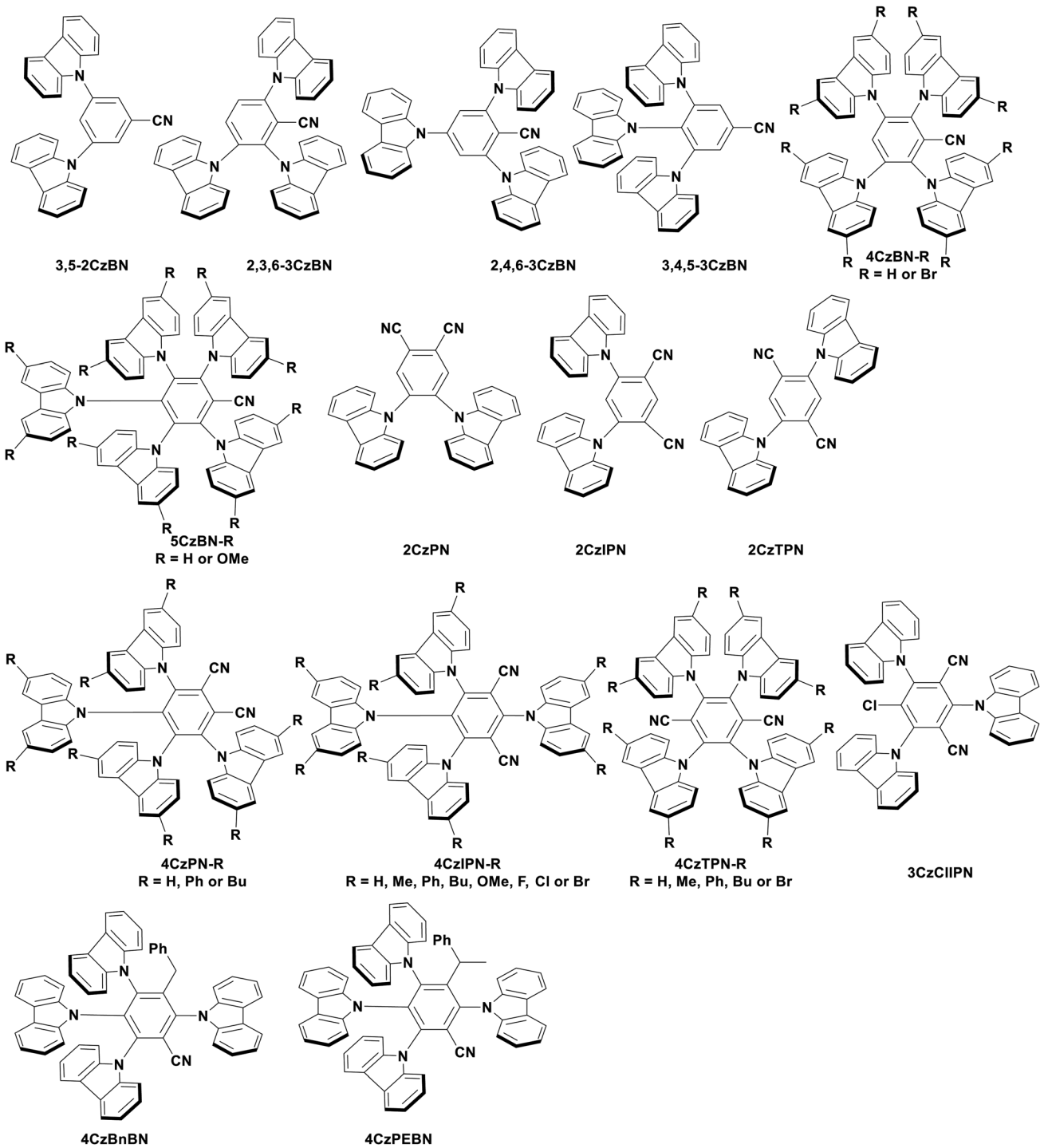

Fig. 138 Structures of TADF compounds with benzonitrile and CDCB-based structure used as photocatalysts.

The TADF compounds surveyed were **4CzIPN**, **4CzIPN-F**, **4CzIPN-Cl** and **4CzIPN-Br**, which gave yields of 50%, 75%, 80% and 75%, respectively; all managed >95% conversion of oxime ether except for **4CzIPN**, which showed only 60% conversion. The superiority of the halogenated compounds, in particular the chlorine-substituted compound, in comparison to **4CzIPN** is reflected in their much greater photooxidising capacity (E_{red}^* = 1.35 V, 1.52 V, 1.71 V, 1.52 V for **4CzIPN**, **4CzIPN-F**, **4CzIPN-Cl** and **4CzIPN-Br**, respectively), especially since 2-((cyclobutylideneamino)oxy)-2-methylpropanoate, the oxime ether carboxylate in Fig. 141, has an oxidation potential of E_{ox} = 1.48 V. Notably, $[Ir(dF(CF_3)ppy)_2(dtbbpy)]PF_6$ was used as a reference PC and managed >95% conversion and 55% yield at 1 mol% PC loading, compared to the 5 mol% utilised for the TADF compounds. In further optimisation studies, it was found that decreasing the catalyst loading from 5 mol% to 3 mol% for the TADF compounds could be achieved without having an

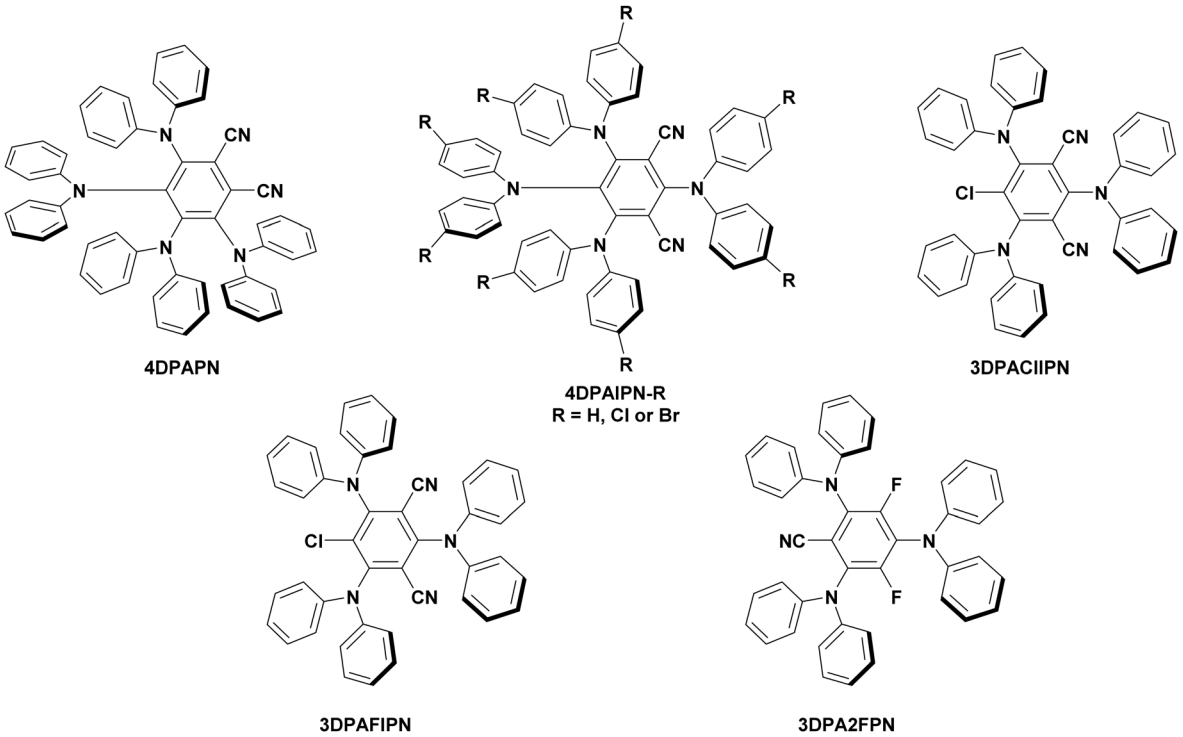

Fig. 139 Structure of CDCB based TADF compounds which involve diphenylamine (DPA) as donor groups which have been considered as photocatalysts.

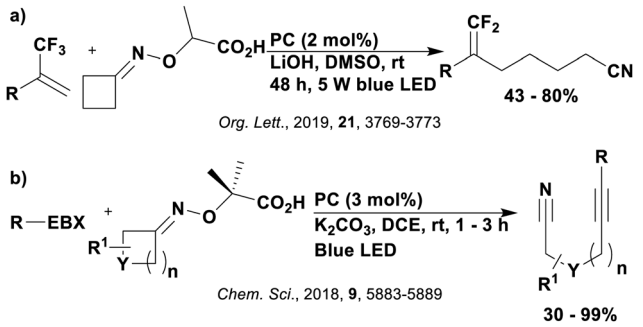

Fig. 140 Reaction scheme for (a) the neutral γ,γ-difluoroallylation of cycloketone oxime ethers with trifluoromethyl alkenes and (b) fragmentation–alkynylation of oxime ethers where EBX = ethynyl benziodoxolone.

impact on the yield, therefore 3 mol% of PC was used in the substrate scope. The low yield of product obtained using the iridium photocatalyst is due to significant formation of the side product 2-oxo-2-phenylethyl 2-iodobenzoate. Waser *et al.* postulate this is formed through a decomposition of Ph-EBX when water or oxygen is present and may be catalysed by photocatalysis, although the mechanism is not yet known. An additional side product shown in Fig. 141 is also proven to exist by ^{1}H NMR for the TADF compounds, which explains why their almost complete conversions are not reflected in the yields, however, high yields of the anticipated product are still obtained therefore, this side product is not thoroughly discussed.

Ethynyl benziodoxolone (EBX) reagents have also been used in conjunction with photocatalysis in the decarboxylative alkynylation of dipeptides (Fig. 142a) and peptide tetramers (Fig. 142b).[320] Although no mechanistic investigations were undertaken or catalytic cycles shown, the mechanism proposed by Waser *et al.* is referenced to be likely to be in operation,[328] which is reflective of the suggested mechanism shown in Fig. 141. A number of TADF compounds were considered as PCs in alkynylation of Cbz-Gly-Pro using Ph-EBX: **4CzIPN**, **4CzIPN-Cl**, **4CzIPN-^{t}Bu**, **4CzIPN-OMe**, **4DPAIPN**, **4DPAIPN-Cl** and **4DPAIPN-Br**, which gave yields of 99%, 89%, 44%, <5%, 43%, 65% and 50%, respectively. The iridium PC $[Ir(dF(CF_3)ppy)_2(dtbbpy)]PF_6$ was also considered, which provided 99% yield. The yields generally reflect the photoxidising capacity of the PC (E_{red}* = 1.35 V, 1.58 V, 1.21 V, 1.23 V, 0.90 V, 1.09 V, 0.98 V and 1.21 V for the TADF PCs and Ir PC, respectively). However, there are some exceptions to this, for example **4CzIPN-OMe** (E_{red}* = 1.23 V, <5%) performs poorly despite being more strongly photooxidising than the Ir PC. This is suggested to be linked to fast BET from the excited CT state of the PC, as proposed by Zeitler *et al.*[114] **4CzIPN-^{t}Bu** also performed worse than expected (E_{red}* = 1.21 V, 44%), with Waser *et al.* conjecturing that issues of stability of the PC may be responsible for the lower yield. For the subsequent substrate scope, **4CzIPN** was selected as the PC of choice.

An additional example involves functionalisation of an alkene, whereby decarboxylation of Cbz-proline by single electron oxidation from the excited photocatalyst produces an electron-rich radical that then can be added to the electron-poor diethyl maleate (Fig. 143).[114] The reduced photocatalyst is then used to reduce the resultant C-centred radical (Fig. 144). A variety of TADF compounds including **3CzClIPN**, **4CzIPN**, **5CzBN**, **3DPAClIPN**, **3DPAFIBN**,

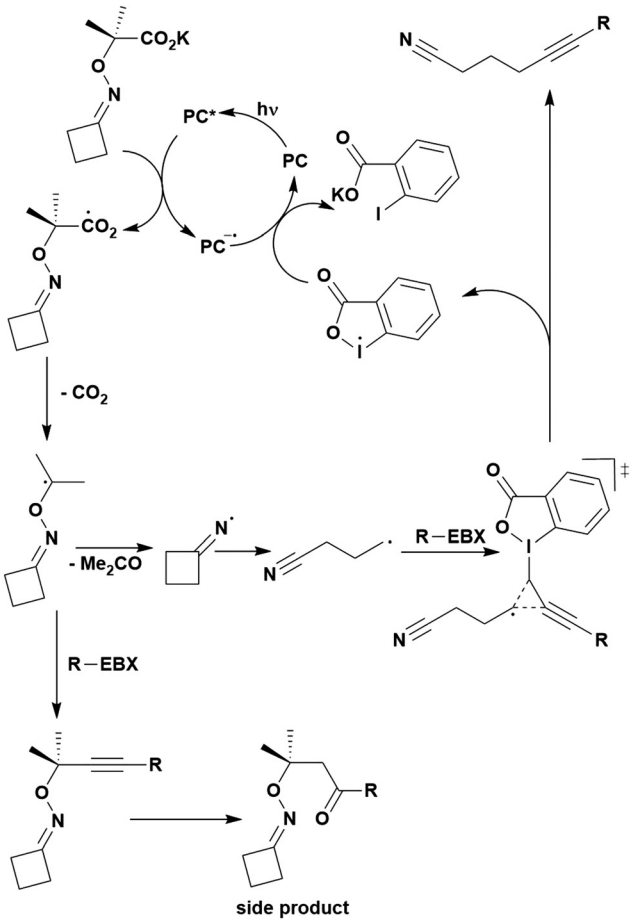

Fig. 141 Proposed mechanism for the alkynylation of oxime ethers.

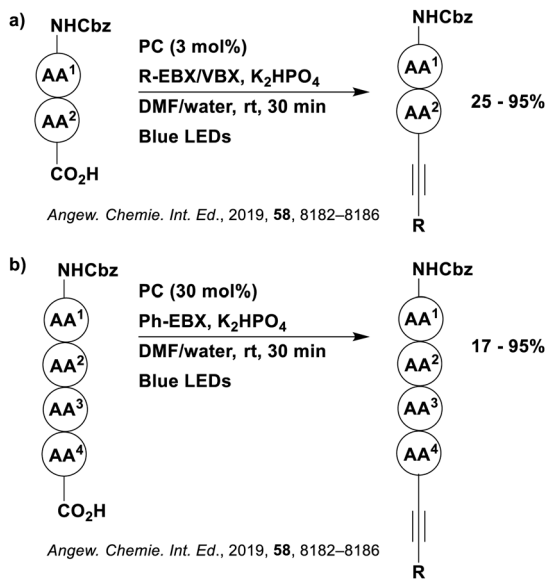

Fig. 142 Reaction scheme for the decarboxylative alkylnylation of (a) dipeptides and (b) peptide tetramers.

3DPA2FBN, **4CzIPN-OMe** and **5CzBN-OMe** were tested as photocatalysts in this model reaction. All photocatalysts produced the

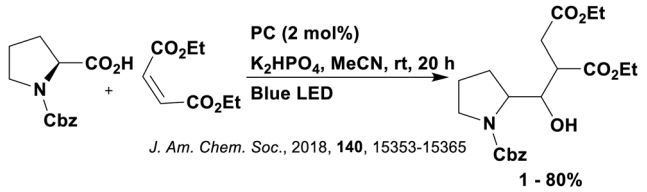

Fig. 143 Reaction scheme for the photocatalytic decarboxylative conjugate addition of Cbz-proline to diethyl maleate.

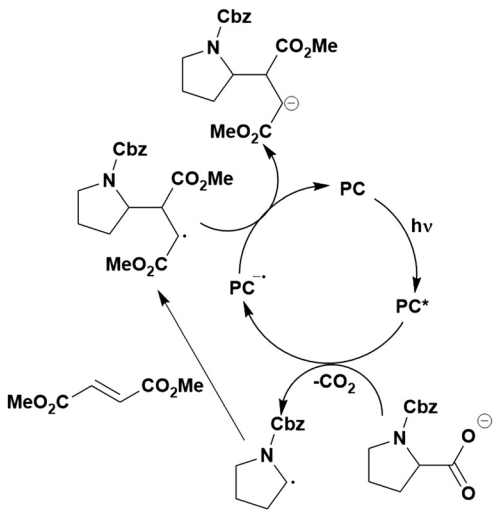

Fig. 144 Photoinduced decarboxylative conjugate addition of Cbz-protected proline to diethyl maleate.

final product but with varying yield, depending highly on their respective ground and excited state redox potentials. For example, **4CzIPN** and **3CzClIPN**, possessing the highest E_{red}* values of the series (E_{red}* = 1.35 V and 1.56 V, respectively), and hence the best photooxidants, produced the highest yields (80% and 77%, respectively). The yields were also higher, but comparable, than those previously reported using Mes-4MeOAcr-Ph (73%, E_{red}* = 1.65 V), the best known photocatalyst for this reaction.[23] The slight difference in yield between these photocatalysts can be correlated to the ground state reduction potentials (E_{red} = −1.21 V, −1.16 V and −0.82 V for **4CzIPN**, **3CzClIPN** and Mes-4MeOAc-Ph, respectively). Product yields varied from 1–37% for the other TADF photocatalysts and aligned with their reduced oxidising power in the excited state. Both methoxy-substituted photocatalysts, **4CzIPN-OMe** and **5CzBN-OMe** produced 3% and 1% yield, respectively, of the product despite having appropriate redox potentials. This is hypothesized by the authors to be as a result of fast, intramolecular BET from their excited charge transfer state, which is corroborated by their weak radiative emission intensity in comparison to the other compounds in the CDCB family. Zeitler *et al.* hypothesized that the stronger methoxy donor substituent triggers a competitive nonradiative relaxation process. It should be noted that these methoxy-substituted CDCB compounds have been shown as successful PCs in other reactions; for example, **5CzBN-OMe** was shown to be highly efficient in the photocatalytic formation of amides

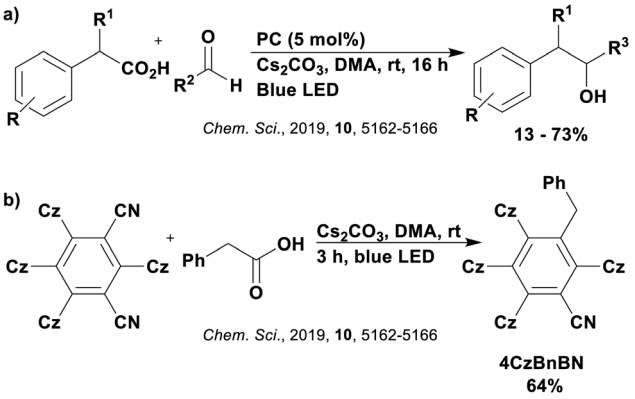

Fig. 145 Reaction scheme for the (a) benzylation of aliphatic aldehydes to secondary alcohols and (b) formation 4CzBnBN.

(see Section 6: HAT catalysis).[329] It is thus not evident what is the origin of their poor performance in the functionalisation of diethyl maleate.

The photoinduced decarboxylation of benzylic carboxylic acids can be used towards the synthesis of secondary alcohols (Fig. 145a).[323] As with the previous examples, the excited photocatalyst is used to oxidatively decarboxylate the carboxylic acid, generating a carbon-centred radical species, which is then reduced by the reduced photocatalyst to form the carbanion, closing the photocatalytic cycle (Fig. 146). The carbanion can then attack the electrophilic carbonyl carbon in the aliphatic aldehyde, producing the secondary alcohol product. Stern–Volmer quenching experiments confirmed that the excited PC is quenched by the carboxylate rather than the aldehyde. Three photocatalysts, **4CzIPN**, **4CzPN** and **3DPAFIPN**, were considered, producing respective yields of 75%, 55% and 6% in the reaction of phenylacetic acid and *n*-pentanal. Other photocatalysts investigated, including $[Ir(dF(CF)_3ppy)_2(dtbbpy)]PF_6$ provided very poor yields of 6% or less. Firstly, the excited PC must oxidise phenylacetate (PA) with NBu_4PA having an oxidation potential of E_{ox} = 1.27 V.[173] The photooxidising capacity of the PCs is as follows: E_{red}* = 1.21 V, 1.35 V, 1.40 V and 1.09 V for $[Ir(dF(CF)_3ppy)_2(dtbbpy)]PF_6$, **4CzIPN**, **4CzPN** and **3DPAFIPN**, respectively. Hence from this, it is clear to why both the iridium PC and **3DPAFIPN** perform poorly in this reaction, while **4CzIPN** and **4CzPN** are more than capable. Since only **4CzIPN** and **4CzPN** are photooxiding enough to complete the first step, only these two PCs will be discussed when considering the second SET, which is reduction of the benzylic radical (E_{red} = −1.43 V).[330,331] Both **4CzIPN** and **4CzPN** have similar ground state reducing ability (E_{red} = −1.21 V and −1.16 V, respectively), so their great difference in yield is unexpected. To understand this variation in product yields, mechanistic investigations were undertaken. Photodecomposition of **4CzIPN** was observed during the reaction, isolated as **4CzBnBN** (Fig. 145b). Reaction of phenylacetic acid and *n*-pentanal using **4CzBnBN** yields 39% of the desired product, leading König *et al.* to suggest it is the main active PC for carbanion generation, especially since it is very reducing in the ground state (E_{red} = −1.72 V). Photocatalytic carbanion generation has been discussed in detail in a recent review.[332] From this, the authors propose the mechanism shown in Fig. 146, whereby they invoke **4CzBnBN** as the PC. Since **4CzIPN** photo decomposes to form this strong ground state reductant **4CzBnBN**, this is likely why **4CzIPN** outperforms **4CzPN**.

Moreover, an oxidative quenching mechanism may be in operation, which is exemplified by the decarboxylation of *N*-(acyloxy)phthalimides (Fig. 147a)[333] or *N*-hydroxyphthalimide esters (Fig. 147b).[334] The former was used as the starting reagent for the radical–radical coupling to access alkylated *N*-heterocycles (Fig. 148). Previously, $[Ir(dF(CF_3)ppy)_2(dtbbpy)]PF_6$ had been identified as a superior photocatalyst, producing the alkylated isoquinoline in 90% yield.[335] Both **4CzIPN** and **2CzPN** were evaluated as potential replacement PCs, producing slightly lower product yields of 84% and 80%, respectively.[333] However, the CDCBs were present in a 1 mol% loading whilst the iridium

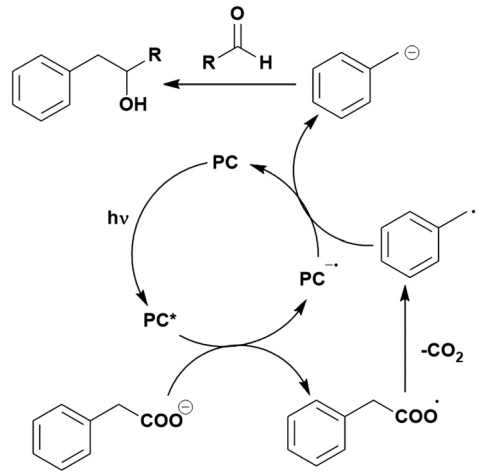

Fig. 146 Plausible mechanism for the benzylation of aliphatic aldehydes to secondary alcohols.

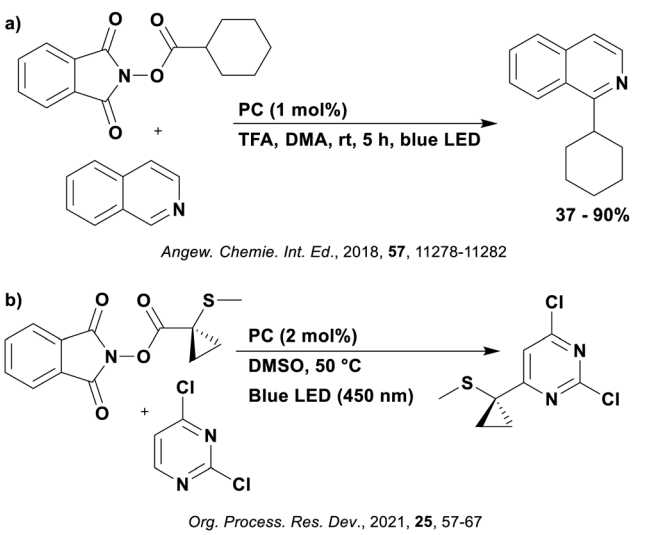

Fig. 147 Reaction scheme for the (a) decarboxylative alkylation of heteroarenes using *N*-(acyloxy)phthalimides and (b) an additive free photoredox Minisci reaction.

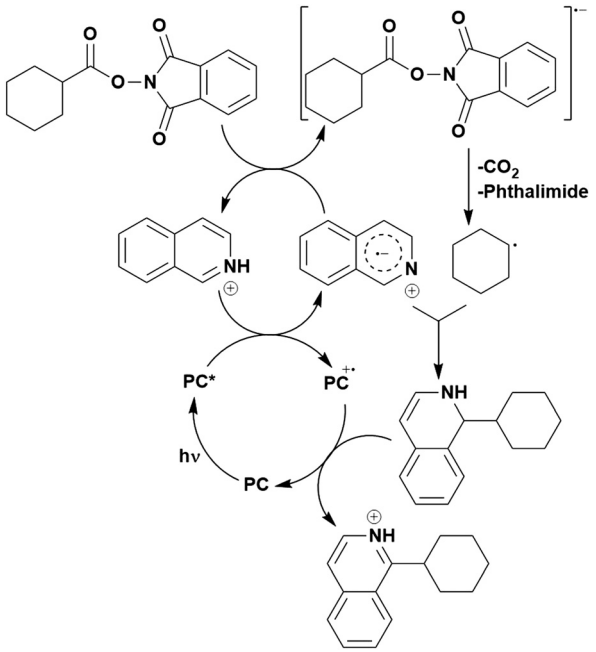

Fig. 148 Plausible photocatalytic cycle for the decarboxylative alkylation of *N*-heteroarenes with *N*-(acyloxy)phthalimides.

photocatalyst was employed at 2 mol% loading, which may explain the slightly different yields obtained.

The latter reaction (Fig. 147b) is an example of an additive-free Minisci reaction.[334] The excited PC is oxidative quenched by the *N*-hydroxyphthalimide ester to release a carbon-centred radical, which adds to the 2,4-dichloropyrimidine. The resulting adduct is oxidised by the oxidised PC to yield the final product. Organic TADF compounds **3CzClIPN**, **5CzBN** and **3DPA2FBN** were investigated as PCs, providing respective product yields of 7%, 29% and 43% under the same additive-free reaction conditions. **4CzIPN** also was considered and provided 26% yield, although this included the additive DIPEA. These yields generally align with the photoreducing ability of the PC (E_{ox}* = −0.93 V, −1.42 V and −1.60 V for **3CzClIPN**, **5CzBN** and **3DPA2FBN**, respectively), which must be capable of the reducing the *N*-hydroxyphthalimide ester (E_{red} = −1.22 V *vs.* SCE). The authors proposed that the addition of DIPEA results in a change to a reductive quenching mechanism, hence a discussion of the E_{ox}* value of **4CzIPN** is not relevant.

Formation of a sulfoxide by-product was observed for the **4CzIPN**-DIPEA system, which occurs through oxidation of the final sulfide product (E_{ox} = 1.90 V *vs.* SCE). The authors suggested that since the radical cation of **3DPA2FBN** is less oxidising than that of **4CzIPN** (E_{ox} = 1.24 V and 1.52 V, respectively), this by-product cannot be formed by **3DPA2FBN**, although thermodynamically, neither should be capable of initiating this SET.

Quantum yield determination of the **4CzIPN**-DIPEA system and the **3DPA2FBN** system gave values of 0.21 and 0.61, respectively. A radical chain process may be in operation in both cases, whereby the authors suggest that the final oxidation step to form the product can occur through either SET to the PC or to another molecule of the redox-active ester. No further investigations into the possible radical chain nature of this mechanism were conducted.

Stern–Volmer quenching experiments were conducted for **4CzIPN**, **3DPA2FBN** and **5CzBN**; however, the authors noted that since the systems were not degassed, the measurements applied only to prompt fluorescence quenching. It should be noted that the presence of O_2 does not guarantee full quenching of triplet excitons nor should it be assumed that O_2 behaves benignly to singlet excitons. The Stern–Volmer quenching constant K_{SV} with the hydroxyphthalimide ester was determined to be 2.32, 9.52 and 12.64, for **4CzIPN**, **3DPA2FBN** and **5CzBN**, respectively, indicating that the kinetics of electron transfer do vary considerably between PCs. When correcting these K_{SV} values with the lifetimes of the PC provided in Table 2, the quenching rate constant can be determined as 1.2×10^8 M^{-1} s^{-1}, 2.3×10^9 M^{-1} s^{-1} and 7.9×10^8 M^{-1} s^{-1} for **4CzIPN**, **3DPA2FBN** and **5CzBN**, respectively. The values align with the reported isolated yields implying both thermodynamic and kinetic factors play a role in influencing the product yield.

A similar example, although with less mechanistic clarity, involves the investigation of the impact of solvent and additives on the regioselectivity of the Minisci-type addition of amino acid-derived redox-active esters to quinolines (Fig. 149).[336] More polar solvents, such as DMA or DMSO, favour the C4 addition product while less polar solvents, such as toluene or dioxane, result in the C2 addition product. No discussion of the mechanism is presented, although similar reactions proceed through an oxidative quenching cycle.[337,338] Organic TADF compounds **4CzIPN**, **5CzBN** and **3DPAFIPN** were investigated in the PC screen alongside $[Ir(dF(CF_3)ppy)_2(dtbbpy)]PF_6$ providing yields of 48%, 30%, 45% and 39%, respectively, of the C2 addition product; all PCs achieved 8–10% of the C4 addition product as the PC screen was conducted in toluene, which favours formation of the C2 addition product. No further PC screen

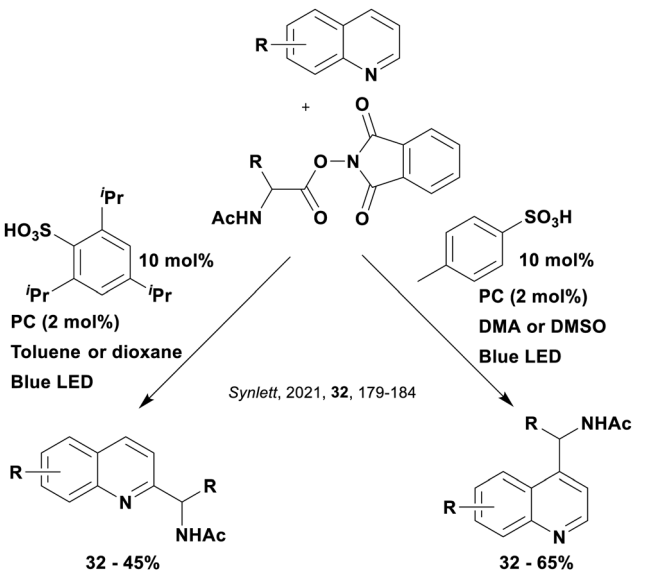

Fig. 149 Reaction scheme for the investigation into the regioselectivity of a Minisci type addition reaction when altering solvent and additives.

was conducted in the more polar DMA or DMSO solvents. **4CzIPN** was selected as the PC when synthesising the C4 addition product, providing yields of 32–65% and **3DPAFIPN** was chosen for making the C2 addition product, forming product in 32–45% yield, although there is no justification provided for this choice given they both provided similar yields of product in the PC screen. There is no obvious correlation between the redox potentials required for an oxidative quenching cycle and the yields obtained (for example, E_{ox} = 1.52 V, 1.41 V, 1.30 V, 1.69 V and E_{ox}* = −1.04 V, −1.42 V, −1.38 V, −0.89 V for **4CzIPN**, **5CzBN**, **3DPAFIPN** and $[Ir(dF(CF_3)ppy)_2(dtbbpy)]PF_6$, respectively).

Alternative radical precursors in the formation of C–C and C–X bonds

Utilisation of alternative radical precursors in the formation of C–C and C–X bonds is also possible using TADF compounds as photocatalysts, for example, in the arylation of arylidene malonates using cyanoarenes (Fig. 150a)[339] or the addition of malonates to alkenes (Fig. 150b).[340] For the former, the proposed mechanism involves two photocatalytic cycles (Fig. 151), with the excited PC being quenched in both cases by a sacrificial electron donor, TEA, as confirmed by Stern–Volmer quenching experiments. The radical cation generated on TEA exists in equilibrium with the α-amino radical, which itself can be deprotonated by neutral TEA. Both TEA or protonated TEA can engage in the PCET mechanism with the arylidene malonate. The reduced photocatalyst is then used to reduce both the arylidene malonate and the protonated cyanoarene, with these resultant radicals coupling together, and following elimination of HCN, generating the final arylated product. From the proposed mechanism, two photons are required (one for each catalytic cycle), to generate one molecule of product hence a quantum yield <0.5 would act in support of this closed photocatalytic mechanism proposed; the experimentally determined quantum yield of 0.28 provides some corroboration. An inverse secondary kinetic isotope effect is also observed for the formation of the arylidene malonate radical as expected due to the change in hybridisation from sp^2 to sp^3 upon reduction, again acting as corroboration of the proposed mechanism.

High throughput experimentation (HTE) was used to quickly identify optimal conditions, with **4DPAIPN** being the only TADF

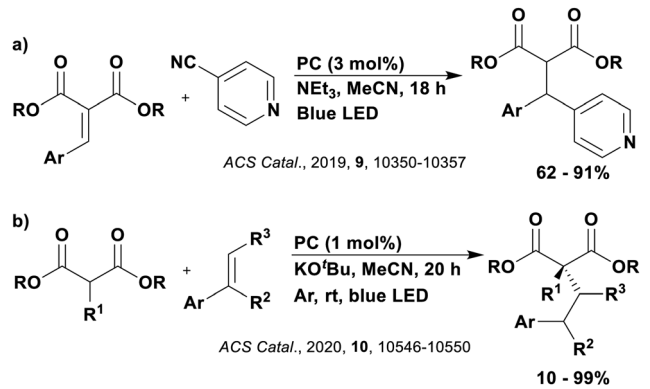

Fig. 150 Reaction schemes for the (a) arylation of arylidene malonates and (b) reaction of malonates with alkenes.

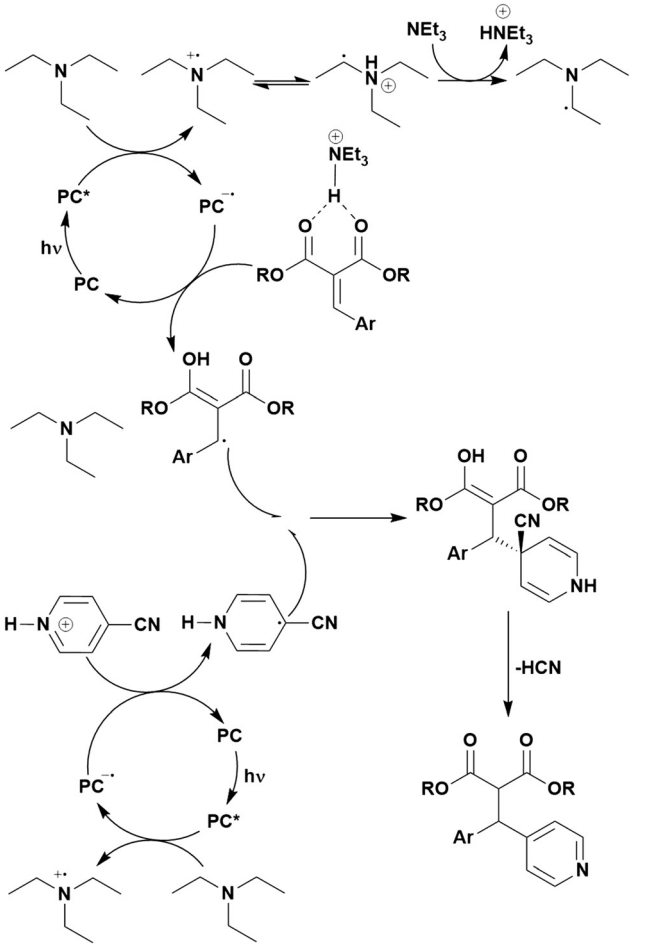

Fig. 151 Proposed mechanism for the arylation of arylidene malonates.

compound considered. A high yield of 85% was obtained with **4DPAIPN** and TEA as the sacrificial electron donor in MeCN, with the next highest yield of 70% being obtained with $[Ir(ppy)_2(dtbbpy)]PF_6$ under the same conditions. Other photocatalysts under these conditions provided little (33% with $[Ir(dF(CF_3)ppy)_2(dtbbpy)]PF_6$) to no yield (0% with *fac*-$Ir(ppy)_3$ and $[Ru(bpy)_3](PF_6)_2$. These results can be rationalized by considering the ground state reducing capacity of the PCs, which correlates with the final product yield (E_{red} = −1.52 V, −1.51 V, −1.37 V −1.33 V for **4DPAIPN** and $[Ir(ppy)_2(dtbbpy)]PF_6$, $[Ir(dF(CF_3)ppy)_2(dtbbpy)]PF_6$ and $[Ru(bpy)_3](PF_6)_2$). Although *fac*-$Ir(ppy)_3$ does have an appropriate ground state reduction potential (E_{red} = −2.19 V), it has very weak excited state oxidising capacity (E_{ox}* = 0.31 V), which may explain why it generates no product, especially since TEA has an oxidation potential of E_{ox} = 0.83 V.[160]

Upon identification of the optimal conditions in terms of photocatalyst, additives and solvent, additional conditions were investigated, for example the impact of the light irradiation power on the reaction yield. The irradiation intensity is based on the intensity control allowed on a Kessil PR160 456 nm light, with low intensity (irradiation: 25) giving an average yield of 79%, medium intensity (irradiation 75, standard conditions)

providing an average yield of 87% and high intensity (irradiation: 100) resulting in 88% average yield. As expected, a higher yield is observed when increasing the intensity from low to medium; however, the yield seems to plateau upon further increase.

In the reaction of malonates with alkenes (Fig. 150b), the proposed mechanism is simpler in that only one photocatalytic cycle is suggested.[340] The excited PC is reductively quenched by the malonate enolate tautomer, with the resultant radical adding to the alkene to form a benzyl radical. The reduced PC is then invoked to reduce this benzyl radical, which after protonation, yields the final product. Radical trapping experiments with TEMPO provided evidence for the radical nature of the proposed mechanism. Only organic PCs were considered in this reaction and in the initial PC screen, **4CzIPN** was the only CDCB-based structure. **4CzIPN** vastly outcompeted the other PCs, yielding 87% of product while the next best PC, eosin y, could achieve only 5%. The enolates of malonates typically have low oxidation potentials (*e.g.*, the enolate of diethyl malonate has E_{ox} = 0.59 V *vs.* SCE), thus it is likely that the step involving regeneration of the PC is the more thermodynamically challenging step, and the one best correlated to the reaction yield (E_{red} = −1.21 V and −1.06 V for **4CzIPN** and eosin Y, respectively). This hypotehesis is supported by the lower yields obtained when the benzyl radical contained electron-donating groups rather than electron-withdrawing groups, as the electron-donating groups cause the benzyl radical to be more difficult to reduce. For example, when using *p*-$MeOC_6H_4$ as the arene, the benzyl radical has a reduction potential of E_{red} = −1.82 V, and a yield of 0% was obtained with **4CzIPN**. By contrast, the benzyl radical of *p*-NCC_6H_4 has a reduction potential of E_{red} = −0.77 V and consequently a yield of 56% was obtained. For the arenes bearing electron-donating groups, **3DPA2FBN** was instead employed as the PC, and higher yields could be obtained (*e.g.*, 28% yield of product when using *p*-$MeOC_6H_4$) on account of its greater reducing capacity in the ground state (E_{red} = −1.92 V).

Cyanoarenes have also been used in conjunction with oximes and iminium chlorides for primary amine synthesis (Fig. 152a and b, respectively),[341] as well as in reaction with primary or secondary amines to form heteroarylamines (Fig. 152c).[342] High throughput experimentation was used to determine the optimal conditions when using oximes as the coupling partner, with **4CzIPN** and **4DPAIPN** being the TADF PCs under investigation. The best photocatalyst was identified as $[Ir(dF(Me)ppy)_2(dtbbpy)]PF_6$ giving a 71% yield with DIPA, while **4CzIPN** and **4DPAIPN** managed only 2% and 4%, respectively. For oxime reactants, the mechanism is proposed to involve both photocatalytic electron and energy transfer, with triplet–triplet sensitisation of the oxime being suggested. Photocatalysts with a triplet energy higher than that of the oxime ($E_T \approx$ 2.34 eV, 226 kJ mol^{-1} for *o*-benzoyl oxime under investigation) are capable of undergoing the triplet sensitisation process, for example $[Ir(dF(Me)ppy)_2(dtbbpy)]PF_6$ has a triplet energy of E_T = 2.42 eV (233 kJ mol^{-1}). However, this doesn't provide an explanation for the lack of success with **4CzIPN**, which has a triplet energy E_T = 2.52 eV (243 kJ mol^{-1}).[304]

The proposed mechanism for the coupling of cyanoarenes with amines (Fig. 152c) is somewhat similar to that shown in Fig. 151 in that the PC is reductively quenched by the amine reagent and the reduced PC is used to reduce the cyanoarene.[342] These two radicals then couple together, releasing HCN, to form the final product. A range of spectroscopic techniques were used to support these mechanistic studies, including flash vacuum photolysis and transient absorption spectroscopy. **3DPAFIPN** provided the highest yield in the PC screen and thus was subject to this spectroscopic analysis. Upon excitation of the PC, a characteristic absorption at 590 nm was observed and assigned to the triplet excited state of the photocatalyst ($^3PC^*$). After addition of the amine reagent, this band decreased in favour of two new absorption bands at 308 nm and 466 nm, which correspond to the amine radical cation and $PC^{\bullet -}$, suggesting the triplet state is responsible for the SET. Addition of the cyanoarene consequently resulted in quenching of the 466 nm band. The decrease in the lifetimes of $^3PC^*$ when in the presence of the amine (from 10.0 μs to 4.1 μs in MeCN) and of $PC^{\bullet -}$ when in the presence of the cyanoarene (from 109.1 μs to 12.6 μs in MeCN), were used to determine the rate of electron transfer as 5.1 × 10^8 M^{-1} s^{-1} for SET between the amine and PC*, and 7.0 × 10^7 M^{-1} s^{-1} for the SET between $PC^{\bullet -}$ and the cyanoarene.

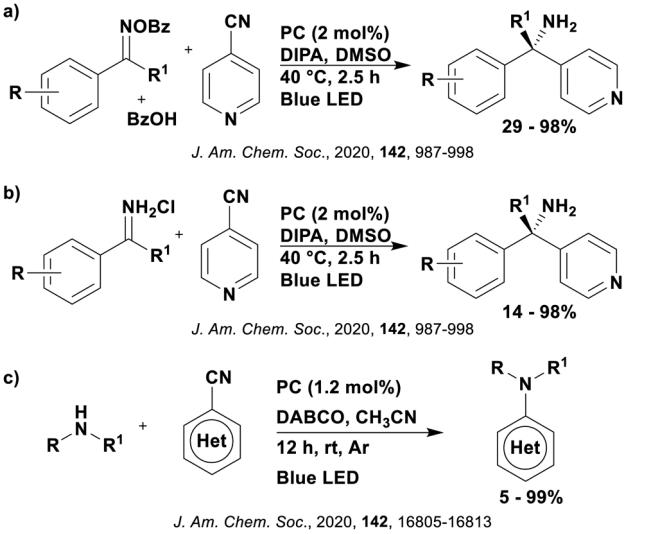

Fig. 152 Reaction scheme for the reaction of cyanoarenes with (a) oximes, (b) iminium chlorides and (c) amines.

3DPAFIPN, **4DPAIPN** and **4CzIPN** were tested as the PCs, providing yields of 99%, 99% and 0%, respectively. Transient absorption spectroscopy indicated that **4CzIPN** could be reductively quenched by the amine reagent, as indicated by the new absorption band at 465 nm; however, upon addition of the cyanoarene, no change in this absorption band was observed, implying that $\mathbf{4CzIPN}^{\bullet -}$ could not reduce the cyanoarene, despite having suitable redox potentials (E_{red} = −1.21 V for **4CzIPN** and −0.87 V for *p*-cyanopyridine) in the presence of the amine radical cation.

fac-$Ir(ppy)_3$ was also investigated as a PC in this reaction and provided a yield of 88%, although this PC was shown to proceed through an oxidative quenching pathway.

Adv. Synth. Catal., 2020, **362**, 242-247

Fig. 153 Reaction scheme for the generation of polycarbocyclic and polyheterocyclic cyclopropanes. RP = radical precursor.

Alkyl radicals generated from silicate or trifluoroborate radical precursors can add to olefins that are embedded within bicyclic scaffolds. Radical polar crossover can ensue to generate polycarbocyclic and polyheterocyclic cyclopropanes (Fig. 153).[343] The mechanism is thought to proceed as shown in Fig. 43, although no mechanistic studies were undertaken. Organic PCs **4CzIPN** and **4CzIPN-Cl** were considered in this reaction alongside iridium and ruthenium complexes. The ratio of product to internal standard (IS) as determined by HPLC was 1.31 and 1.40 for **4CzIPN** and **4CzIPN-Cl**, respectively, which was lower than that obtained for $[Ru(bpy)](PF_6)_2$ (1.63) and $[Ir(dF(CF_3)ppy)_2(dtbbpy)]PF_6$ (1.52). However, the ratio of reactant to the IS was also found to be lower for the organic PCs (0.27, 0.77, 1.11 and 1.14 for **4CzIPN**, **4CzIPN-Cl**, $[Ru(bpy)](PF_6)_2$ and $[Ir(dF(CF_3)ppy)_2(dtbbpy)]PF_6$, respectively), suggesting a higher conversion was possible for the organic PCs. Since the photooxidising ability of the organic PCs is higher (E_{red}^* = 1.35 V, 1.71 V, 0.77 V and 1.21 V for **4CzIPN**, **4CzIPN-Cl**, $[Ru(bpy)](PF_6)_2$ and $[Ir(dF(CF_3)ppy)_2(dtbbpy)]PF_6$, respectively), perhaps this may be why they achieve higher conversion of the reagents, although this does not explain why they achieve a lower product ratio.

Radical precursors involving DHPs have typically been used to form alkyl radicals; however, they can also be used to form carbamoyl radicals that can be added to olefins (Fig. 154).[344] Reductive quenching of the PC by the 4-carboxamido-Hantzsch esters releases the nucleophilic carbamoyl radical after aromatization-driven fragmentation. This radical adds to the electron-deficient olefin, the product of which is reduced by the reduced PC. Protonation of the resultant carbanion yields the final product. This proposed mechanism was supported by Stern–Volmer quenching studies, which showed that the luminescence quenching by the 4-carboxamido-Hantzsch ester was much faster than by the olefin (k_q = 9.22 × 10^{10} M^{-1} s^{-1} and 2.96 × 10^9 M^{-1} s^{-1}, respectively). Addition of TEMPO inhibited the reaction, instead forming an adduct with the carbamoyl radical. Only three PCs were investigated in the PC screen: **3DPAFIPN** (80%), **3DPA2FBN** (78%) and $[Mes\text{-}Acr]ClO_4$ (65%) with **3DPAFIPN** being selected for the remainder of the study. The origin behind the TADF compounds ability to outcompete $[Mes\text{-}Acr]ClO_4$ may be linked to the relative ground state reduction potentials of the PC (E_{red} = −1.59 V, −1.92 V and −0.57 V for **3DPAFIPN**, **3DPA2FBN** and $[Mes\text{-}Acr]ClO_4$, respectively).

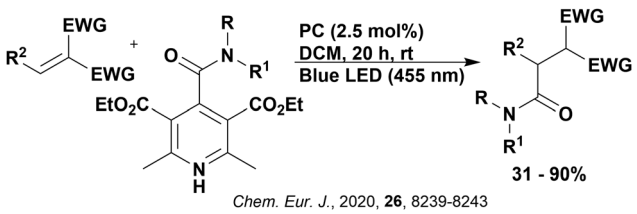

Chem. Eur. J., 2020, **26**, 8239-8243

Fig. 154 Reaction scheme for the addition of carbamoyl radicals to olefins.

Additionally, sodium trifluoromethylsulfinate may be used as radical precursor, which was used in the difunctionalisation of vinyl ureas (Fig. 155).[345] The excited photocatalyst is proposed to oxidise the trifluoromethylsulfinate anion, yielding the electrophilic trifluoromethyl radical (Fig. 156). This radical adds to the double bond on the urea, forming a tertiary radical which is reduced by the reduced PC. The carbanion formed then undergoes intramolecular nucleophilic aromatic substitution to produce the final difunctionalised product. Radical inhibition experiments with TEMPO confirm this is a radical process and radical trapping with 1,1-diphenylethylene demonstrated the presence of the trifluoromethyl radical. Stern–Volmer quenching experiments confirmed that the excited PC is quenched more efficiently by the trifluromethylsulfinate salt rather than the urea, while a quantum yield of 0.18 suggests that the reaction is not a radical chain mechanism. Both **4CzIPN** and **3DPAFIPN** were considered as TADF photocatalysts, with the former greatly outperforming the latter (89% yield and trace yield, respectively). Only $[Ir(dF(CF_3)ppy)_2(dtbbpy)]PF_6$ provided some competition for **4CzIPN**, obtaining 70% yield. This difference in yield is reflective of the photooxidising ability of the photocatalyst (E_{red}^* = 1.35 V, 1.21 V and 1.09 V for **4CzIPN**, $[Ir(dF(CF_3)ppy)_2(dtbbpy)]PF_6$ and **3DPAFIPN**, respectively), which needs to be sufficiently high to oxidise CF_3SO_2Na (E_{ox} = 1.05 V).

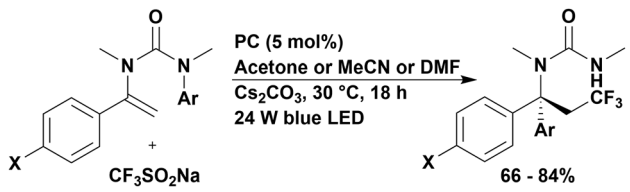

Angew. Chemie. Int. Ed., (2020), **59**, 11600-11606

Fig. 155 Reaction scheme for the difunctionalisation of vinyl ureas.

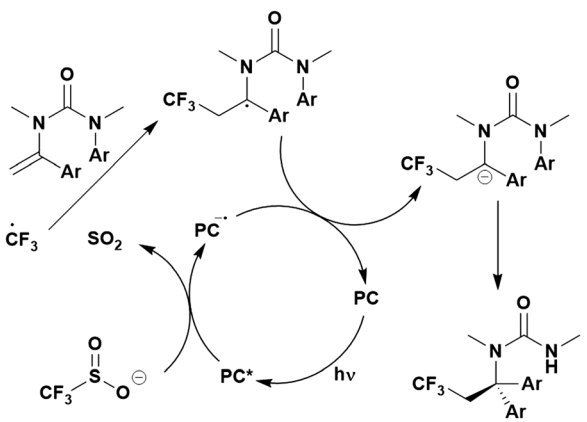

Fig. 156 Suggested mechanism for the difunctionalisation of vinyl ureas.

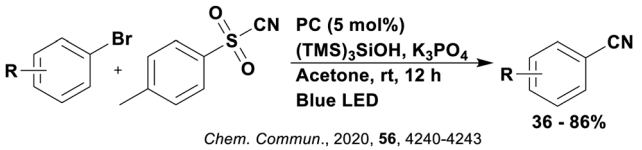

Chem. Commun., 2020, **56**, 4240-4243

Fig. 157 Reaction scheme for the photocatalytic cyanation of arenes.

Furthermore, cyanation of aryl or heteroaryl bromides is possible using photocatalysis (Fig. 157).[346] The excited PC is proposed to oxidise tris(trimethylsilyl) silanol (supersilanol), which forms a silicon-centred radical that can abstract a bromine from an aryl bromide (Fig. 158). The resultant weakly nucleophilic aryl radical adds to tosyl cyanide (TsCN) and, through a Barton nitrile transfer, yields the final product,[347,348] as well as the tosyl radical, which is reduced by the reduced photocatalyst. The mechanism was corroborated by addition of TEMPO, which suppressed formation of the expected product, instead yielding an aryl-TEMPO adduct, confirming the formation on an aryl radical. Only organic TADF compounds were considered as photocatalysts, providing yields of 71%, 55% and 0% for **4CzIPN**, **4CzTPN** and **4DPAIPN**, respectively. This difference in yield is correlated with the differing photooxidising ability of the PCs. Oxidation of supersilanol is quite challenging (E_{ox} = 1.54 V *vs.* SCE in MeCN)[349] and only strongly photooxidising PCs can complete the required SET (E_{red}* = 1.35 V, 1.41 V and 1.1 V for **4CzIPN**, **4CzTPN** and **4DPAIPN**, respectively), which explains the absence of yield for **4DPAIPN**. The lower yield obtained by **4CzTPN** may be related to the ground state reduction potential (E_{red} = −1.21 V and −1.02 V for **4CzIPN** and **4CzTPN**, respectively), which must be sufficiently negative to reduce the tosyl radical (E_{red} = −0.50 V *vs.* SCE in MeCN);[264,350] hence, this process is more thermodynamically favourable for **4CzIPN**.

Organic halides can be used as radical precursors for the formation of C–P bonds to produce asymmetrical phosphines and phosphonium salts (Fig. 159). The mechanism involves reductive quenching of the PC by sacrificial electron donors

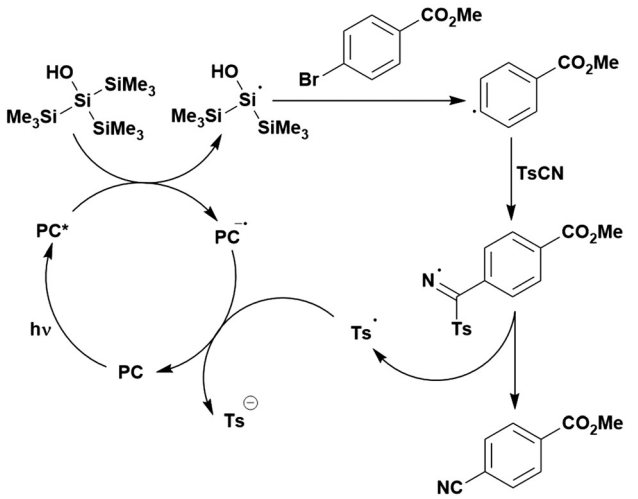

Fig. 158 Proposed mechanism for the photoredox mediated cyanation of aryl bromides *via* silyl radical mediated bromine abstraction.

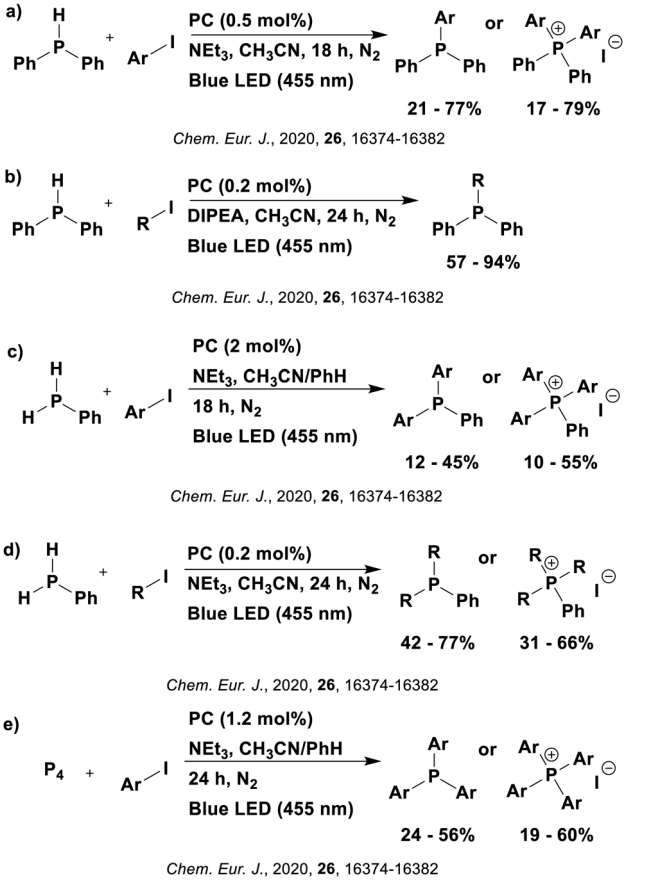

Fig. 159 Reaction scheme for the synthesis of phosphines and phosphonium salts using photocatalysis.

like NEt_3 or DIPEA, followed by reduction of an aryl or alkyl iodide to close the photocatalytic cycle. The resultant radical abstracts a hydrogen atom from the phosphine to yield phosphorus-centred radicals, which homocouples to form a diphosphine compound. Additional aryl or alkyl radicals, formed from the excess of organohalide, attack the P–P bond to yield the tertiary phosphine product. Upon addition of TEMPO, product formation is inhibited, providing evidence that this is a radical process. Further confirmation of the presence of organic radicals was provided by EPR spectroscopy. Monitoring of the reaction using $^{31}P\{^1H\}$ NMR spectroscopy indicated the consumption of the original phosphine and the formation of the self-coupled diphosphine species. Finally, Stern–Volmer experiments indicated that DIPEA (or NEt_3) was responsible for the quenching of the excited PC.

A photocatalyst screen was conducted for the functionalisation of P_4 with aryl iodides to yield the respective phosphonium salt (Fig. 159e). **3DPAFIPN** was identified as the optimal PC as it outperformed the other organic TADF PCs in the study, yielding 60% of product while **4CzIPN**, **5CzBN**, **4DPAPN**, **4DPAIPN** and **3DPA2FBN** all yielded between 11–22%; **3DPAClIPN**, **5CzBN-OMe** and **4CzPN** did not lead to product formation. The PCs **4CzIPN**, **3DPAClIPN**, **5CzBN**, **5CzBN-OMe** and **3DPA2FBN** instead yielded between 8–21% of the tertiary arylated phosphine. No comment is provided by the authors as to the variance in product formation or yield.

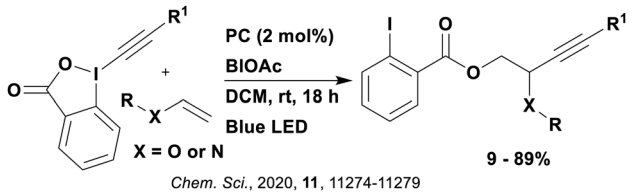

Fig. 160 Reaction scheme for the 1,2-oxyalkynylation of ene-carbamates and enol ethers.

Additionally, with the aid of benziodoxolones (EBXs), the 1,2-oxyalkynylation of ene-carbamates and enol ethers is possible to synthesise 1,2-amino alcohols and diols (Fig. 160).[351] A reductive quenching cycle is proposed to be in operation (Fig. 161), in which SET from the ene-carbamate to the excited PC occurs, supported by Stern–Volmer quenching experiments. The resultant radical is trapped by the carboxylate radical from EBX, with the product adding to a second molecule of EBX to yield the final functionalised product, alongside the iodanyl radical. This iodanyl radical oxidises the reduced PC to close the photocatalytic cycle and form the previously mentioned carboxylate radical. The authors additionally propose that 1-acetoxy-1,2-benziodoxol-3-(1*H*)-one (BIOAc) acts to oxidatively quench the excited PC, releasing more of the iodanyl radical species.

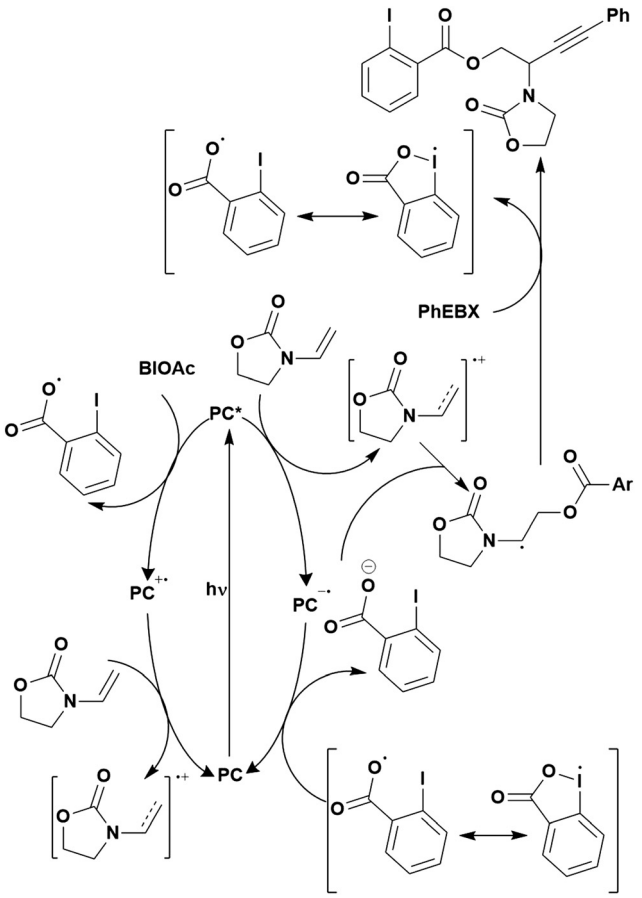

Fig. 161 Viable mechanism for the 1,2-oxyalkynylation of ene-carbamates.

The oxidised PC can then also be used to oxidise the ene-carbamate. This hypothesis was supported by the observation that in the absence of BIOAc, the yield decreases (65% after 5 days, compared to 89% after 18 h in the presence of BIOAc).

4CzIPN, **4CzIPN-Cl** and [Mes-Acr]ClO_4 were considered as PCs and in the absence of additives, yielded 30%, 42% and 5%, respectively. Thus, additional reaction optimisation was initiated with **4CzIPN-Cl** and a yield of 80% was obtained in the presence of BIOAc. This outcome was then compared with the use of organometallic PCs, with $[Ru(bpz)_3](PF_6)_2$ (21%) and $[Ir(dF(CF_3)ppy)_2(dtbbpy)]PF_6$ (24%) affording significantly lower product yield in the presence of BIOAc. Since the ene-carbamate, *N*-vinyloxazolidinone, has an oxidation potential of E_{ox} = 1.30 V *vs.* SCE, it is unsurprising that some PCs may struggle with this transformation (E_{red}* = 1.35 V and 1.21 V for **4CzIPN** and $[Ir(dF(CF_3)ppy)_2(dtbbpy)]PF_6$, respectively, in comparison with E_{red}* = 1.71 V for **4CzIPN-Cl**). Although this SET should be facile for both [Mes-Acr]ClO_4 and $[Ru(bpz)_3](PF_6)_2$ (E_{red}* = 2.06 V and 1.45 V, respectively), their lower yields may be linked to their more anodically shifted ground state reduction potentials (E_{red} = −0.57 V and −0.80 V, respectively) in comparison to **4CzIPN-Cl** (E_{red} = −0.97 V).

Finally, C–H bonds can be constructed using this form of photocatalysis, as in the hydrodefluorination of trifluoromethylarenes (Fig. 162).[352] The proposed mechanism, shown in Fig. 163, suggests the thiolate anion generated by deprotonation of 4-hydroxythiophenol (4-HTP) under basic conditions, is capable of reductively quenching the excited PC. The reduced PC then reduces the trifluoromethylarene to form a radical anion, which undergoes mesolytic cleavage of fluoride. The resultant C-centred difluorobenzylic radical is trapped by 4-HTP to form the desired product. Stern–Volmer quenching experiments indicated that a 1:1 combination of TMP:4-HTP was responsible for emission quenching of the PC. Addition of TEMPO resulted in the formation of an adduct between the C-centred difluorobenzylic radical and TEMPO, providing evidence for the formation of the radical species. The presence of this radical was also confirmed by the product identified upon addition of styrene to the reaction mixture. Moreover, utilisation of d_2-4-HTP resulted in incorporation of deuterium into the product, suggesting 4-HTP as the hydrogen atom donor. High throughput screening of the PC was conducted, with 28 PC considered. Of these, 13 were from the TADF CDCB family: **2CzPN**, **2CzIPN**, **2CzTPN**, **4CzPN**, **4CzIPN**, **4CzIPN-OMe**, **4CzTPN**, **5CzBN**, **5CzBN-OMe**, **3CzClIPN**, **4DPAIPN**, **3DPAClIPN** and **3DPAFIPN**. Specific individual yields for each PC were not provided, but from the graphical results of the PC screen,

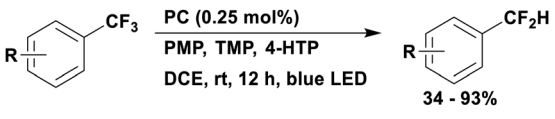

Fig. 162 Reaction scheme for the hydrodefluorination of trifluromethylarenes where PMP = 1,2,2,6,6- pentamethylpiperidine, TMP = 2,2,6,6-tetramethylpiperidine and 4-HTP = 4-hydroxythiophenol.

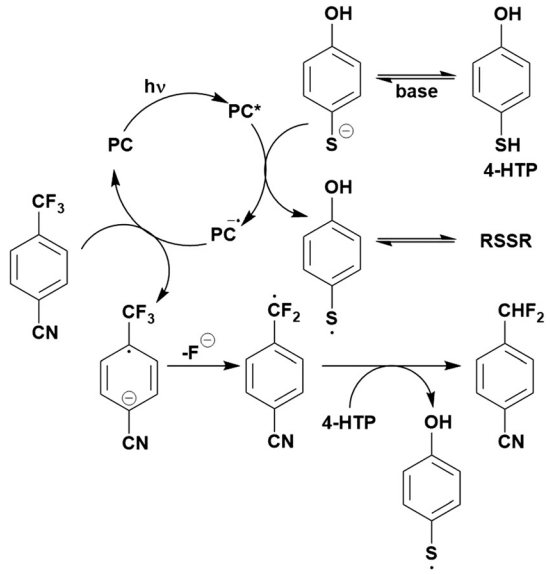

Fig. 163 Plausible mechanism for the hydrodefluorination of trifluoromethylarenes.

4DPAIPN was clearly identified as the best PC, with *fac*-Ir(ppy)$_3$ being the next best. The only other TADF PCs to provide any significant product yield were **5CzBN-OMe**, **3DPAClIPN** and **3DPAFIPN**. For further optimisation studies, the respective yields of **4DPAIPN** and *fac*-Ir(ppy)$_3$ were provided as 62% and 53%, respectively, which is likely linked with the photooxidising ability of the PC (E_{red}* = 1.10 V and 0.31 V for **4DPAIPN** and *fac*-Ir(ppy)$_3$, respectively). The failure of the other PCs to promote the reaction is probably linked to their ground state reduction potentials, which must be significantly reducing to reduce the trifluoromethylarene, where, for example, 4-(trifluoromethyl)benzonitrile has E_{red} = −1.79 V.

Bromination

The photocatalytic bromination of anisole has also been investigated using a TADF photocatalyst (Fig. 164), whereby the crucial oxidation step (E_{ox} (MeOAr/MeOAr$^{\bullet+}$) = 1.79 V) is particularly challenging,[114] hence requiring a strongly oxidising photocatalyst. Impressively, **3CzClIPN** was demonstrated to perform comparably to Fukuzumi's catalyst Mes-Acr-Me$^+$ (89% and 87%, respectively).[114] There are two potential mechanisms (Fig. 165) for this transformation, although the oxidative quenching mechanism is hypothesized to be in operation as a result of the redox potentials of **3CzClIPN**. The excited state reduction potential of **3CzClIPN** (E_{red}* = 1.56 V *vs.* SCE) is slightly too low to initiate the required SET while the ground state oxidation potential (E_{ox} = 1.79 V *vs.* SCE) is sufficient.

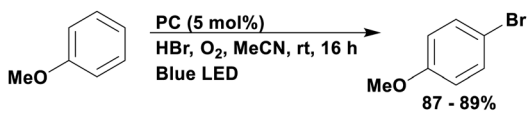

J. Am. Chem. Soc., 2018, **140**, 15353-15365

Fig. 164 Reaction scheme for the bromination of anisole.

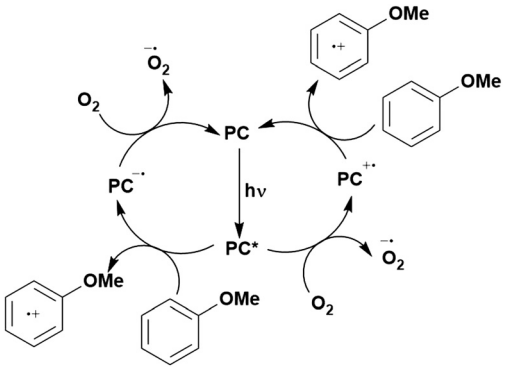

Fig. 165 Oxidative and reductive quenching cycles possible for the photocatalytic bromination of anisole.

Cyanation

Conversion of benzyl alcohols and methylated arenes to benzonitriles using sodium azide (Fig. 166)[353] is also possible using photoredox catalysis. A reductive quenching mechanism is invoked in which the azide is proposed to undergo SET to the excited PC, forming an azidyl radical (Fig. 167). Closure of the photocatalytic cycle proceeds by oxidation of the reduced PC by O_2. Meanwhile, the azidyl radical abstracts a hydrogen atom from the Lewis acid-coordinated benzyl alcohol, generating an α-alkoxy radical, which in the presence of oxygen, forms an aldehyde. This benzaldehyde reacts in a Schmidt reaction with hydrazoic acid, followed by loss of water and N_2 to yield the final benzonitrile. The reactions proceed in similar way with

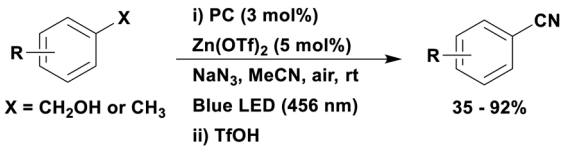

Chem. Eur. J., 2020, **26**, 14070-14074

Fig. 166 Reaction scheme for the photocatalytic cyanation of benzyl alcohols/methyl arenes.

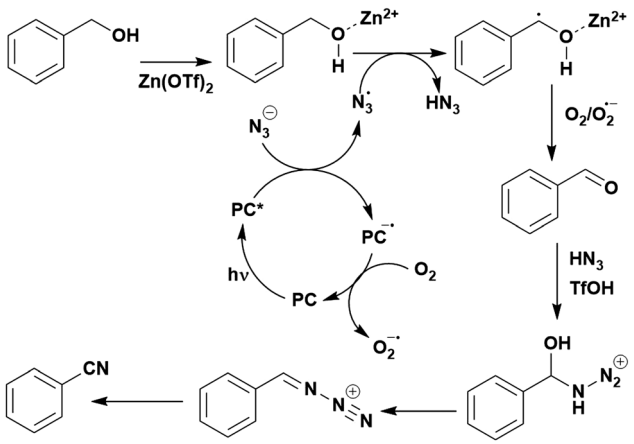

Fig. 167 Proposed mechanism for the photocatalytic cyanation of benzyl alcohols/methyl arenes.

toluene derivatives where the azidyl radical abstracts a proton from the weak benzylic C–H bond to form a benzyl radical. The benzyl radical is intercepted by O_2 to yield a benzyl peroxo radical, which is converted to the benzaldehyde. The conversion to nitrile proceeds as before. EPR spectroscopy reveals the presence of the azidyl radical, while confirmation of the radical photocatalytic mechanism was corroborated by the use of radical scavengers and radical trapping agents. Organic TADF compounds **4CzIPN**, **4CzIPN-Br** and **4DPAIPN** were each tested, providing yields of 89%, 92% and 0%. These differences in yield seem to correlate with the photooxidising ability of the PC (E_{red}* = 1.35 V, 1.52 V and 1.1 V for **4CzIPN**, **4CzIPN-Br**, and **4DPAIPN**, respectively), as the PC must be capable of oxidising the azide anion (E_{ox} = 1.08 V *vs.* SCE). **4CzIPN** was, however, used as the PC for the remainder of the study.

Reduction

The reductive capacity of the photocatalysts **3CzClIPN**, **4CzIPN**, **5CzBN**, **3DPAClIPN**, **3DPAFIBN**, **3DPA2FBN**, **4CzIPN-OMe** and **5CzBN-OMe**, was considered in the reductive C–O bond cleavage of lignin derivatives (Fig. 168).[114] Both steps, reduction to *p*-methoxy acetophenone (*cf.*, *e.g.*, E_{red} = −1.74 V *vs.* SCE for 2-oxo-2-phenylethyl acetate) and reductive dimerization of acetophenone derivatives to their corresponding pinacols (*cf.*, *e.g.*, acetophenone, E_{red} = −2.64 V *vs.* SCE),[354] require a strongly reducing photocatalyst in the ground state (Fig. 169). The yields observed using the aforementioned TADF molecules track with their corresponding redox potentials. For instance, **3DPA2FBN** with the most negative ground state reduction potential (E_{red} = −1.92 V *vs.* SCE) delivered the highest yield of 77% after 18 hours, outperforming $[Ir(ppy)_2(dtbbpy)]PF_6$ as the typical organometallic catalyst for this reaction (56% yield after 12 hours), although this is unsurprising since the iridium photocatalyst is less reducing (E_{red} = −1.51 V). **3CzClIPN**, with the least negative reduction potential in the series (E_{red} = −1.16 V *vs.* SCE), produced no pinacol. Similarly, the methoxy-substituted photocatalysts did not have enough reducing power to deliver the final pinacol product but were capable of mediating the first reduction step, producing the *p*-methoxy acetophenone.

Additionally, reduction of aryl halides has been shown to be feasible using CDCB-based organic compounds as PCs (Fig. 170), with the reduced aryl halide capable of engaging in a coupling

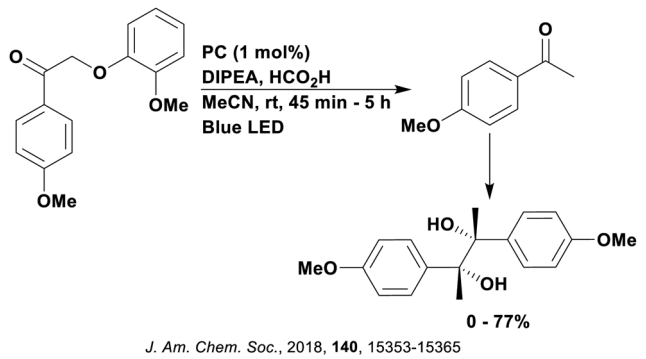

J. Am. Chem. Soc., 2018, **140**, 15353-15365

Fig. 168 Reaction scheme for the reduction of lignin model derivative.

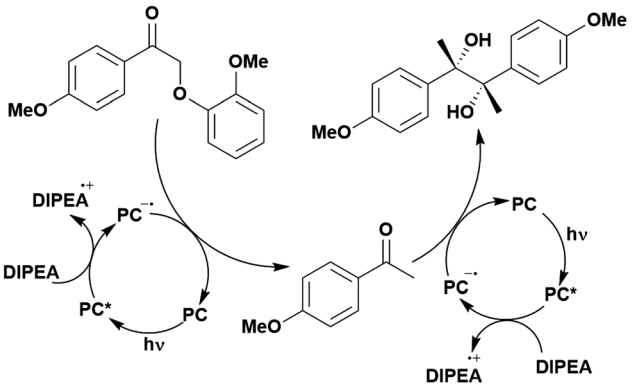

Fig. 169 Proposed mechanism for the double photocatalytic reduction of lignin derivatives to pinacols *via* a *p*-methoxy acetophenone intermediate.

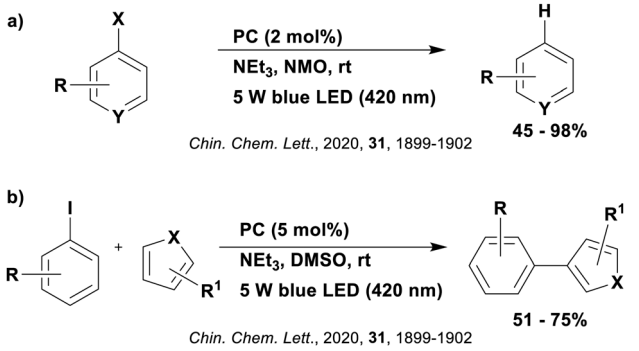

Fig. 170 Reaction schemes for the reduction of aryl halides.

reaction with an additional aryl group in $C(sp^2)$–$C(sp^2)$ type coupling (Fig. 170b).[310] The proposed mechanism involves reductive quenching of the excited PC by NEt_3, with the reduced PC being used to reduce the aryl halide. After loss of the halide, the aryl radical can either abstract a proton from $NEt_3^{\bullet+}$ to yield the formally reduction product or add to an unsaturated bond such as to a heterocycle to form the $C(sp^2)$–$C(sp^2)$ coupled product. Stern–Volmer quenching studies confirmed that NEt_3 can effectively quench the luminescence of the PC while product inhibition was observed upon addition of TEMPO.

Six CDCB compounds were investigated as PCs: **4CzPN**, **4CzIPN**, **5CzBN**, **4DPAPN**, **3,4,5-3CzBN** and **2CzPN**, providing yields of 51%, 54%, 70%, 35%, trace and trace, respectively. For comparison, $[Ru(bpy)_3](PF_6)_2$ was also tested and this produced only trace amounts of product. Reduction of aryl halides is thermodynamically challenging and so the ground state reducing ability of the PCs is likely to govern this process (E_{red} = −1.16 V, −1.21 V, −1.52 V, −1.53 V, −1.58 V, −1.45 V, −1.33 V, for **4CzPN**, **4CzIPN**, **5CzBN**, **4DPAPN**, **3,4,5-3CzBN**, **2CzPN** and $[Ru(bpy)_3](PF_6)_2$ respectively). The authors suggested that the superior performance of **5CzBN** is attributed to its strong reduction ability; however, other PCs with equally strong E_{red} values struggled in this reaction, while **4CzPN**, with the least reducing E_{red} value, performed adequately. This suggests that another factor is responsible for the relative success of the PCs in this reaction.

Detriflation

The reductive capabilities of **3DPA2FBN** have been exploited in the photocatalytic detriflation of nonactivated aryl triflates (Fig. 171).[114] This type of reaction had only previously been reported for aryl triflates with electron-withdrawing substituents on the aryl group (*e.g. p*-CN-benzene derivatives).[355] The defunctionalisation of naphthyl triflate (E_{red} = −2.01 V *vs.* SCE)[356] was considered, with both **3DPA2FBN** and *fac*-Ir(ppy)$_3$ under investigation owing to their very negative ground state reduction potentials (E_{red} = −1.92 V and −2.19 V, respectively). Both photocatalysts proved successful in this reaction with comparable yields of 86% and 90%; the slightly higher yield obtained by the iridium photocatalyst correlates with its more negative reduction potential.

Polymerisation

Free radical and cationic polymerisations can be initiated using CDCB-based photocatalysts, which through reaction with an additive, either bis(4-*tert*-butylphenyl)iodonium hexafluorophosphate (Iod) or ethyl 4-(dimethylamino)benzoate (EDB) or both, produce the required species necessary to initiate the respective polymerisation reaction.[311] This can be achieved through both reductive and oxidative quenching mechanisms (Fig. 172). The molecules considered as photocatalysts were **4CzTPN**, **4CzTPN-Br**, **4CzBN** and **4CzBN-Br** and all were shown to work in both two and three component systems in the polymerisation reactions. The success of the polymerisation in this case is defined by the rate of polymerisation and functional conversion (FC) of the monomer to the polymer (*e.g.*, conversion of a diepoxide functionality in the monomer to the polymer without this epoxy functional group). In the polymerisation reactions, **4CzBN** was the most efficient, followed by **4CzBN-Br**, **4CzTPN-Br** and finally **4CzTPN**, for example, in the polymerisation of EPOX in a two-component system, FC = 54%, 46%, 34% and 27%, respectively under 455 nm excitation. All four TADF molecules outperformed the traditional photoinitiator bis(2,4,6-trimethylbenzoyl)phenylphosphine oxide (BAPO), which could not initiate the polymerisation in the aforementioned reaction conditions; no other photocatalysts were considered. The efficiency rate of the CDCBs seems to follow the electron transfer quantum yield in the photooxidation process generating $PC^{+\bullet}$ and $Ar^{\bullet}$ to initiate cationic and free radical polymerisations, respectively. These quantum yields were calculated by using Stern–Volmer quenching constants from the equation $\Phi_{et(S1)} = K_{SV}[Iod]/(1 + K_{SV}[Iod])$. These high electron transfer quantum yields also follow the energy of the S_1 state (S_1 = 2.90 eV (280 kJ mol^{-1}), 2.80 eV (270 kJ mol^{-1}), 2.72 eV (262 kJ mol^{-1}) and 2.50 eV (241 kJ mol^{-1}) for **4CzBN**, **4CzBN-Br**, **4CzTPN-Br** and **4CzTPN**, respectively), suggesting the singlet excited state is important in this process.

Cyclisation

Borylcyclopropanation reactions can be photocatalysed by CDCB-based TADF molecules (Fig. 173).[357] Diiodoborylmethane is used as the radical precursor, which after reduction by the exited photocatalyst and cleavage of a carbon–iodine bond, generates a borylmethyl radical (Fig. 174). This radical then adds to the double bond of α-MIDA-boryl styrene, forming a benzylic radical, which can then undergo cyclopropyl ring closure. Sodium thiosulfate was used a sacrificial reductant to regenerate the photocatalyst and close the catalytic cycle. Three TADF molecules were considered as the photocatalyst, **4CzIPN**, **4CzIPN-^{t}Bu** and **4CzIPN-Br**, providing respective yields of 67%, 58% and 26%.

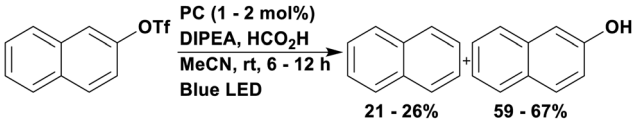

J. Am. Chem. Soc., 2018, **140**, 15353-15365

Fig. 171 Reaction scheme for the defunctionalisation of naphthyl triflate.

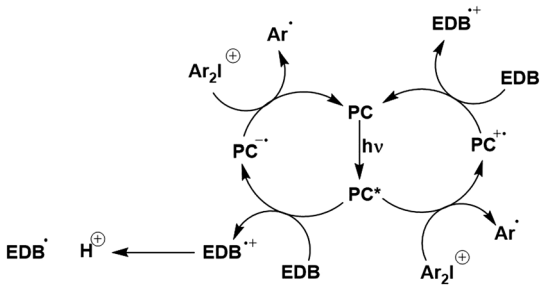

Fig. 172 Photocatalytic polymerisation initiations involving both oxidative and reductive quenching cycles where EDB is ethyl 4-(dimethylamino)-benzoate and Ar_2I^+ is bis(4-*tert*-butylphenyl)iodonium.

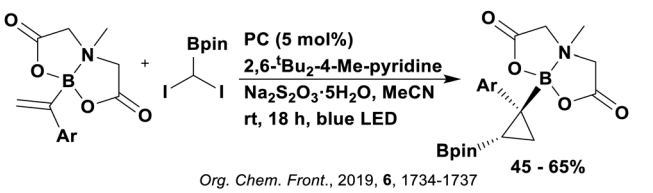

Org. Chem. Front., 2019, **6**, 1734-1737

Fig. 173 Reaction scheme for photocatalysed borylcyclopropanation.

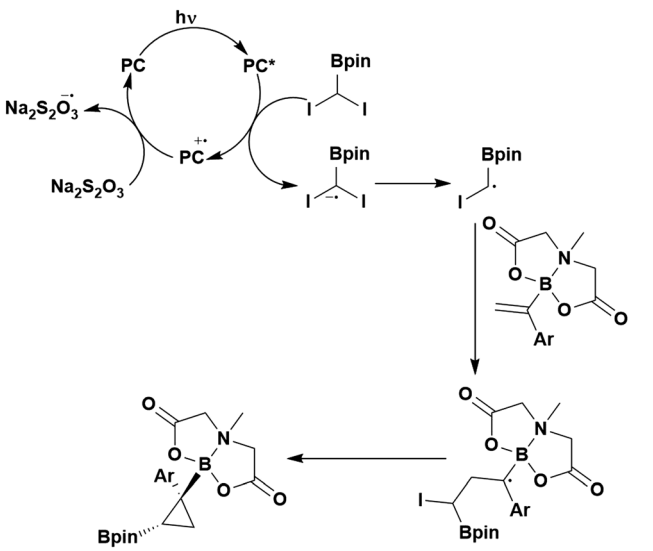

Fig. 174 Proposed mechanism for the photocatalytic borylcyclopropanation.

These yields are reflective of their photoreducing capability (E_{ox}* = −1.04 V, −1.31 V and −0.82 V for **4CzIPN**, **4CzIPN-^{t}Bu**, and **4CzIPN-Br**, respectively), especially given that diiodoborylmethane has a reduction potential of E_{red} = −1.01 V. However, this correlation fails to explain the yield obtained using **4CzIPN-^{t}Bu**, which obtained a lower yield than when using **4CzIPN** despite being a stronger photooxidant. The reason for the poorer performance of **4CzIPN-^{t}Bu** may be linked to its reduced oxidising capacity in the ground state (E_{ox} = 1.22 V and 1.52 V for **4CzIPN-^{t}Bu** and **4CzIPN**, respectively). Alternative photocatalysts were not considered by Ooi *et al.* in this study; however, a study by Charette *et al.* showed the borylcyclopropanation of styrene using diiodoborylmethane was possible in 78% yield using xanthone as a photocatalyst (E_{ox}* = −1.42 V)[358] although this result was obtained using a flow set-up.[359]

Photocatalysed cyclisation reactions have also been reported in the context of the hydroarylation of arenes (Fig. 175).[360] The proposed mechanism involves reductive quenching of the PC by DIPEA. The resultant reduced PC then reduces the aryl halide to form an aryl radical, which undergoes 5-*exo*-trig cyclisation to form a cyclohexadienyl radical. The reduced PC is invoked again to reduce this radical to the anion, which is then protonated to yield the final product. Stern–Volmer quenching experiments reveal DIPEA to be an efficient quencher of the excited PC, while executing the reaction in D_2O resulted in deuterium incorporation at the C(sp^3) on the dearomatized ring, providing further confirmation of the radical-polar crossover mechanism. For this reaction, **3DPAFIPN** proved to be the superior PC (86% product yield), in comparison to 4CzIPN (49%), 5CzBN (46%), 3DPA2FBN (66%), [Ir(ppy)$_2$(dtbbpy)]PF$_6$ (66%) and *fac*-Ir(ppy)$_3$ (31%).

Reduction of the cyclohexadienyl radical (E_{red} = −1.34 V) is possible for all PCs (E_{red} = −1.59 V, −1.52 V, −1.92 V, −1.51 V and −2.19 V for **3DPAFIPN**, **5CzBN**, **3DPA2FBN**, [Ir(ppy)$_2$(dtbbpy)]PF$_6$ and *fac*-Ir(ppy)$_3$, respectively) except for **4CzIPN** (E_{red} = −1.21 V), which explains why it performed poorly. The excited PC must also be capable of oxidation of DIPEA (E_{ox} = 0.81 V),[35] which is facile for **3DPAFIPN**, **5CzBN** and **3DPA2FBN** (E_{red}* = 1.09 V, 1.31 V and 0.92 V, respectively), but explains the reduced yields obtained with [Ir(ppy)$_2$(dtbbpy)]PF$_6$ and *fac*-Ir(ppy)$_3$ (E_{red}* = 0.66 V and 0.31 V, respectively). From these redox potentials, it is clear to understand how **3DPAFIPN** performed so effectively in comparison to the other PCs; however, this analysis does not explain why the use of **5CzBN** and **3DPAF2BN** gave such low yields, suggesting something other than the thermodynamics of the PC is responsible for the poor yields in these two reactions.

An additional cyclisation example is exemplified in the photosynthesis of phosphorylated heteroaromatics (Fig. 176).[318]

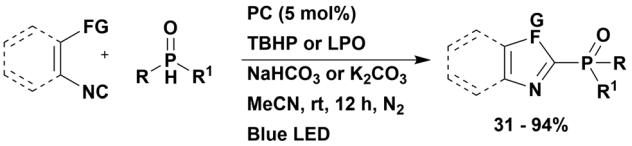

J. Am. Chem. Soc., 2021, **143**, 964-972

Fig. 176 Reaction scheme for the synthesis of phosphorylated heteroaromatics.

The proposed mechanism is reminiscent of that shown in Fig. 76. The excited photocatalyst is reductively quenched by the tautomer of diphenylphosphine oxide, hydroxydiphenylphosphine, in the presence of base, in a PCET step. The resultant phosphoryl radical undergoes radical addition to the isocyano group of the aryl reagent, with the adduct proceeding to undergo an intramolecular cyclisation, oxidation, and deprotonation to afford the final product. Simultaneously, the photocatalytic cycle is closed by SET to TBHP (*tert*-butyl hydroperoxide). Radical scavengers were employed to verify that this reaction includes radical processes, with an adduct being formed with the phosphoryl radical. Further confirmation of the presence of phosphoroyl radicals was provided by EPR spectroscopy. A quantum yield of 0.3 suggests that this reaction does not proceed *via* a radical chain process while a primary kinetic isotope effect k_H/k_D of 1.2 implied that cleavage of the C(sp^2)–H bond is unlikely to be the rate determining step.

A wide variety of CDCB-based organic compounds were considered in this reaction: **4CzIPN-Br** (0%), **4CzTPN** (0%), **4CzIPN-Cl** (19%), **4CzPN** (34%), **4DPAIPN** (40%), **4CzIPN-Ph** (44%), **4CzIPN-Me** (45%), **4CzIPN-OMe** (66%), **4CzIPN** (78%) and **4CzIPN-^{t}Bu** (80%), with **4CzIPN-^{t}Bu** being selected for the remainder of the study. The authors noted that for the substituted **4CzIPN** analogues, the yield increases in line with a decrease in the photooxidising ability (from E_{red}* = 1.73 V for **4CzIPN-Br** to 1.21 V for **4CzIPN-^{t}Bu**), although they provide no mechanistic reasoning for this. The low yield of the halo-substituted compounds was attributed to poor solubility of the PCs in acetonitrile.

Isomerisation

A large number of organic TADF molecules have been studied as photocatalysts for the photosensitised *E*/*Z* isomerisation of stilbene (Fig. 177).[325] These include **3,5-2CzBN**, **2,3,6-3CzBN**, **2,4,6-3CzBN**, **4CzBN**, **5CzBN**, **2CzTPN**, **2CzPN**, **2CzIPN**, **4CzTPN**, **4CzPN** and **4CzIPN**. This reaction proceeds through a Dexter energy transfer mechanism *via* a triplet biradical intermediate (Fig. 178), implicating the triplet state of the PC. As discussed in Section **1**, DET requires spectral overlap (eqn (10)), and typically the triplet energies of the PC and substrate are used as a

J. Am. Chem. Soc., 2020, **142**, 9163-9168

Fig. 175 Reaction scheme for the hydroarylation of arenes.

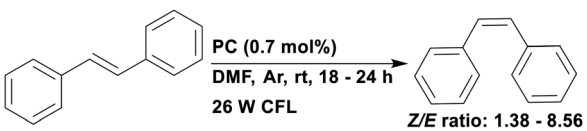

J. Am. Chem. Soc., 2018, **140**, 13719-13725

Fig. 177 Reaction scheme for the *E*/*Z* isomerisation of alkenes.

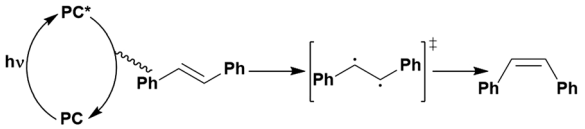

Fig. 178 Proposed mechanism for the *E*/*Z* isomerisation of alkenes.

surrogate to determine whether the reaction is thermodynamically feasible. In *E*/*Z* isomerization, the thermodynamics of the photochemoselective isomerization of the *E*-isomer to the *Z*-isomer require E_T (*E*-isomer) < E_T (PC) < E_T (*Z*-isomer).

The *E*/*Z* isomers of stilbene have triplet energies of 2.2 eV (212 kJ mol^{-1}) and 2.5 eV (241 kJ mol^{-1}), respectively).[361] Zhang *et al.* found the greatest *Z*/*E* ratio is generated by **4CzTPN** (*Z*/*E* = 8.56, 90% yield of *Z*-isomer, E_T = 2.34 eV (226 kJ mol^{-1})), followed by **4CzPN** (*Z*/*E* = 8.10, 89% yield of *Z*-isomer, E_T = 2.45 eV (236 kJ mol^{-1})) while the lowest is obtained by the compounds whose triplet energy is too high for example **2,4,6-3CzBN** (*Z*/*E* = 1.38, 58% yield of *Z*-isomer, E_T = 2.87 eV, 277 kJ mol^{-1}) and **2,3,6-3CzBN** (*Z*/*E* = 1.50, 60% yield of *Z*-isomer, E_T = 2.77 eV, 267 kJ mol^{-1}), whereby the E_T is sufficiently large that the PC can sensitise both *E* and *Z* isomers.[325] Reference PC [Ru(bpy)$_3$](PF$_6$)$_2$ (E_T = 2.03 eV, 196 kJ mol^{-1})[88] yields 87% of the *Z*-isomer (*Z*/*E* = 6.69).

When rationalising the obtained results, Zhang *et al.* invoke the ^{3}CT state of the TADF compounds as the dominant state from which this energy transfer can occur. This is supported by a transient absorption spectroscopy study of **2CzPN** and **4CzIPN** where both were shown to exhibit ^{3}LE and ^{3}CT states using femtosecond and nanosecond transient absorption spectroscopy. The kinetic traces of the nanosecond transient absorption spectra are then studied with increasing amounts of *E*-stilbene, causing both the ^{3}LE and ^{3}CT spectral regions to decrease, implying both are involved in the energy transfer process. Global fitting of this data indicates that for **2CzPN**, energy transfer from the ^{3}LE state is quicker than from the ^{3}CT while for **4CzIPN**, the opposite is observed. Since using **4CzIPN** as a PC results in a greater proportion of the *Z*-isomer (*Z*/*E* = 6.7 and 1.7 for **4CzIPN** and **2CzPN**, respectively), it seems more significant to have the energy transfer operating from the ^{3}CT state.

Cycloadditions

The final class of reactions to be discussed is cycloaddition reactions, starting with the [2+2] cycloaddition of enone substrates (Fig. 179).[362] This reaction is known to proceed *via* a Dexter energy transfer mechanism with *fac*-Ir(ppy)$_3$ as the photosensitizer.[363] Ten TADF compounds were considered as PCs in this reaction: **4CzIPN**, **4CzIPN-^{t}Bu**, **4CzIPN-Ph**, **4CzIPN-OMe**, **4CzPN**, **4CzPN-^{t}Bu**, **4CzPN-Ph**, **5CzBN**, **5CzBN-OMe** and **3DPAFIPN**, all of which giving yields ranging from 60–71%, except **4CzIPN-OMe**, which managed only 23%. These yields are comparable to that obtained with *fac*-Ir(ppy)$_3$ under the same conditions (64%); notably, there is a background reaction where the product forms in 21% in the absence of any PC. Since **4CzIPN-^{t}Bu** gave the highest yield of product, this compound was selected as the PC for the substrate scope. Mechanistically, since similar yields were reported with most of the TADF compounds despite their very different reduction potentials, this suggests that SET to chalcone (E_{red} = −1.48 V)[363] is not occurring as it would be expected that more strongly reducing PCs would yield more product whereas this is not the case. Addition of TEMPO inhibits the reaction, confirming the presence of the biradical intermediate. Luo *et al.* postulated that a FRET pathway does not occur due to the lack of spectral overlap between the absorption of the chalcone and the emission of the PC, suggesting instead that energy transfer must result from the triplet state through a DET mechanism. Stern–Volmer quenching experiments were conducted using both **4CzIPN-^{t}Bu** and **4CzIPN-OMe**, indicating that chalcone quenches the former much more efficiently than the latter (K_{SV} = 0.0624 and 0.0304, respectively). Luo *et al.* contented that the low triplet energy of **4CzIPN-OMe** (2.27 eV) is responsible for its poor performance.

The effect of the excitation wavelength upon the reaction was also considered using **4CzIPN** as the PC. Upon 24 h of irradiation, the same yields were obtained using 425 nm and 455 nm LEDs (68%), while 395 nm yielded only 52%. At a reduced reaction time of 15 h, the 425 nm LED was identified as the superior light choice (63% and 58% yields from 425 nm and 455 nm LEDs, respectively). The reduced yield obtained using 395 nm was suggested to be linked to the irreversible side reactions that may ensue under high energy irradiation,[364] although no evidence of this was provided.

A second cycloaddition reaction that has been shown to be effectively photocatalysed by TADF compounds is a dearomative cycloaddition reaction, which is possible with naphthols (Fig. 180) and indoles, and proceeds *via* an energy transfer mechanism.[365] TADF compounds **2CzPN**, **3DPA2FBN** and **3DPADIPN** were all considered as PCs in the dearomatisation of an indole substrate, providing a reactant to product ratio of 13 : 1, 1.5 : 1 and 3 : 1, respectively, under the same reaction conditions.

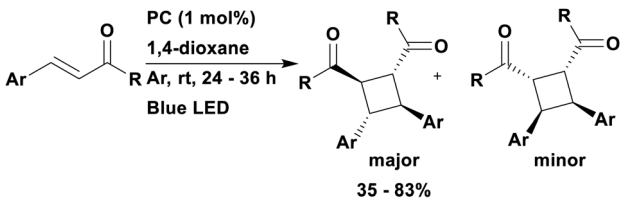

Org. Biomol. Chem., 2020, **18**, 3707–3716

Fig. 179 Reaction scheme for the [2+2] dimerization of substituted olefins.

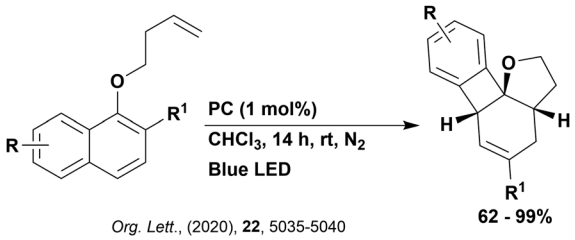

Org. Lett., (2020), **22**, 5035-5040

Fig. 180 Reaction scheme for the dearomative cycloaddition.

Despite producing the worst outcome of these three organic PCs, **2CzPN** was chosen as the PC for the remainder of the study. With naphthols, **2CzPN** was shown to outperform $[Ir(dF(CF_3)ppy)_2(dtbbpy)]PF_6$, the PC previously identified as the best for this reaction.[366] For example, with 1-(1-(but-3-en-1-yloxy)naphthalen-2-yl)ethan-1-one, **2CzPN** produced 94% yield of product while the Ir PC yielded 86%. However, it should be noted that slightly different reaction conditions were used by König *et al.* for **2CzPN** ($CHCl_3$, 0.1 M, 14 h) in comparison to those of Glorius *et al.* for the iridium PC (1,4-dioxane, 0.04 M, 18 h). Similar superiority of **2CzPN** is observed when using indoles. Recyclability of the PC was also investigated in this study, with 88% of **2CzPN** being recovered. This recycled PC was then used in the cycloaddition of the aforementioned naphthol, yielding 90% of product, similar to the 94% yield obtained when using the PC for the first time, thereby demonstrating that there is no loss of activity.

No mechanistic investigations were undertaken in this study, however, König *et al.* suggested that **2CzPN** mimics quite strongly the success of $[Ir(dF(CF_3)ppy)_2(dtbbpy)]PF_6$ on account of their similar E_T values [2.63 eV (254 kJ mol^{-1}) and 2.61 eV (252 kJ mol^{-1}), respectively]. The mechanism in operation was assumed to be the same as that proposed by each of Glorius, Bochet and Ohkuma, depending on the substrate in question.[366–369] Therefore, this reaction is described by analogy as a triplet sensitisation process, although there is no direct evidence that **2CzPN** operates from the T_1 state.

6. CDCB-based molecules used in dual catalysis

As previously documented, **4CzIPN** has been extensively used as a component in dual catalysis, hence it follows that photocatalysts of similar structure would also be compatible in this class of reactions.

Photocatalysis/nickel cross-coupling

In photoredox/Ni C(sp^3)–C(sp^2) cross-coupling reactions, both carboxylic acids and alkyltrifluoroborates have been used as the radical precursors, which upon single electron oxidation by the photocatalyst form alkyl radicals. These can then be cross-coupled with aryl halides (Fig. 181a and b). Zhang *et al.* investigated a wide number of CDCB-based photocatalysts, including **4CzIPN**, **2CzIPN**, **4CzPN**, **2CzPN**, **4CzTPN**, **2CzTPN** and **4DPAIPN**.[120] In the reaction with carboxylic acids as the radical precursors (Fig. 181a), all of the TADF compounds investigated should be able to participate in SET from the carboxylic acid to the excited photocatalyst (E_{red}* ranging from 1.10 V–1.40 V), owing to a low oxidation potential E_{ox} = 0.93 V of *N*-Boc-Pro. Almost all should also be able to reduce the Ni(II) complex ($E_{red} \approx -1.1$ V for the Ni(II) species and varies from −1.16 V to −1.50 V for the TADF compounds). Only **4CzTPN**, with E_{red} = −1.02 V, may not be able to complete the second SET. However, only **4CzIPN** and **4DPAIPN** gave yields of greater than 80%, with **2CzIPN** providing a yield of 56% and the other TADF photocatalysts, yielding between 5–20% of product. Zhang *et al.*

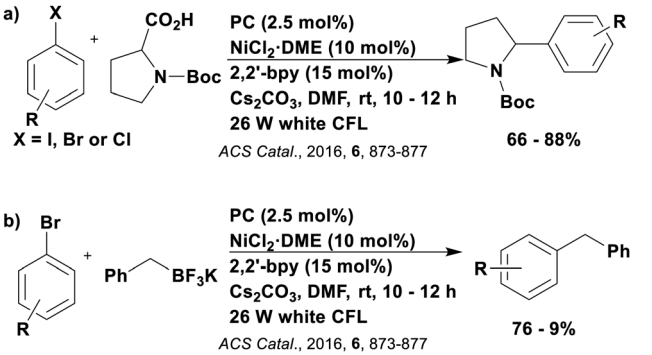

Fig. 181 Reaction schemes for the coupling of aryl halides with (a) carboxylic acids or (b) trifluoroborate salts in dual catalysis.

tentatively hypothesised that the low activities of most of these photocatalysts was attributed to their photoinstability in the required reaction conditions where the solvent was DMF. Evidence for the photodecomposition of the PC came from the observed large blue-shift (~100 nm) of the emission maximum in reaction mixtures containing the low-yielding CDCBs; HPLC analysis corroborated the contention that the PCs had degraded under these conditions whereas use of **4CzIPN**, **4DPAIPN** and **2CzIPN** led to reasonable recovery of photocatalyst. High yields were obtained using $[Ir(dF(CF_3)ppy)_2(dtbbpy)]^+$ and $[Ir(dF(CF_3)ppy)_2(bpy)]^+$ (83% and 82%, respectively), owing to their appropriate redox potentials (E_{red}* = 1.21 V and 1.32 V and E_{red} = −1.37 V and −1.37 V, respectively) while neither the Ru(II) nor other organic photocatalysts tested were able to photocatalyse the reaction. For the cross-coupling with alkyltrifluoroborates (Fig. 181b), yields ranging from 72–91% were achieved for **4CzIPN**, **4DPAIPN**, **2CzIPN** and **4CzPN**. High yields were also obtained for $[Ir(dF(CF_3)ppy)_2(dtbbpy)]^+$ and $[Ir(dF(CF_3)ppy)_2(bpy)]^+$ (89% and 83%, respectively). For both cross-coupling reactions, **4DPAIPN** was shown to provide the highest yields, which may be due to its large ground state reduction potential, making the reduction of the Ni(II) species more facile.

The formation of two C(sp^3)–C(sp^2) bonds is also possible using this form of dual catalysis, as is illustrated by the reaction of aryl halides with dichloromethane (Fig. 182).[370] The proposed mechanism essentially follows that shown for the generic mechanism shown in Fig. 84, but proceeds through this process twice to form the two C–C bonds. Four photocatalytic cycles and two nickel catalytic cycles are proposed, all of which involve reductive quenching of the PC by sacrificial electron donor TEA, supported by Stern–Volmer experiments. The reduced PC is invoked to reduce dichloromethane, forming the chloromethyl radical.

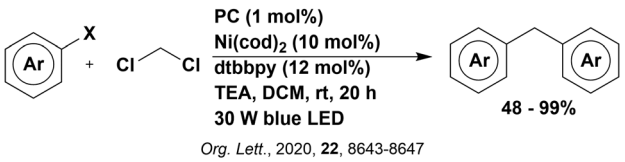

Fig. 182 Reaction scheme for the cross coupling of aryl halides with dichloromethane.

The resultant C(sp^3)–C(sp^2) coupling then occurs as in Fig. 84. Once the first coupling is complete, the reduced PC is proposed to reduce the benzyl chloride derivate, delivering a benzyl radical that then enters into the nickel catalytic cycle (again, as in Fig. 84), alongside another equivalent of the aryl halide, to yield the final product. Addition of TEMPO supressed the reaction, with an adduct being formed with the chloromethyl radical. The presence of the chloromethyl radical was corroborated by the products formed upon addition of 1,1-diphenylethylene to the reaction mixture as a radical trapping agent.

Both **4CzIPN** and **4CzTPN** proved successful in this reaction (63% and 35%, respectively), while $[Ir(dF(CF_3)ppy)_2(dtbbpy)]PF_6$ and $[Ru(bpy)_3]Cl_2$ provided no product. The transition metal PCs may have failed due to their lower photooxidising ability (E_{red}* = 1.35 V, 1.41 V, 0.77 V and 1.21 V for **4CzIPN**, **4CzTPN**, $[Ir(dF(CF_3)ppy)_2(dtbbpy)]PF_6$ and $[Ru(bpy)_3]Cl_2$, respectively), while the difference in yield for the TADF compounds correlates with their E_{red} values (E_{red} = −1.21 V and −1.02 V for **4CzIPN** and **4CzTPN**, respectively).

Additionally, C(sp^2)–C(sp) cross-coupling is possible using metallaphotocatalysis, as can be seen in the carboxylation of styrenes (Fig. 183a and b).[371] Reductive quenching of the PC by a Hantzsch ester is observed before a SET transmetallation pathway occurs for the carboxylation in which the photocatalyst is used to reduce a nickel(II) species. Carboxylation of the *in situ*-formed Ni(I) complex, followed by product dissociation and regeneration of the Ni(II) catalyst encompasses the proposed mechanism (Fig. 184). The nickel catalyst used was $NiBr_2$.glyme in combination with neocuproine or 1,4-bis(diphenylphosphino)butane (dppb), depending on the regioselectivity required for the cross-coupling with styrenes. The three TADF photocatalysts considered, **4CzIPN**, **4CzTPN** and **4CzPN**, provided yields of 66%, 3% and 0%, respectively, of the Markovnikov hydrocarboxylation product. Iridium photocatalyst $[Ir(dF(Me)ppy)_2(dtbbpy)]PF_6$ provided a similar yield to **4CzIPN** of 67%. The difference in yield is likely due to differing reduction capacity of the reduced photocatalyst (E_{red} = −1.21 V, −1.02 V, −1.16 V and −1.44 V for **4CzIPN**, **4CzTPN**, **4CzPN** and $[Ir(dF(Me)ppy)_2(dtbbpy)]PF_6$, respectively), suggesting a strong ground state reductant is necessary to achieve high yields.

Moreover, photoredox/Ni cross-coupling reactions can be used to form C(sp^2)–O bonds. This approach was applied towards the

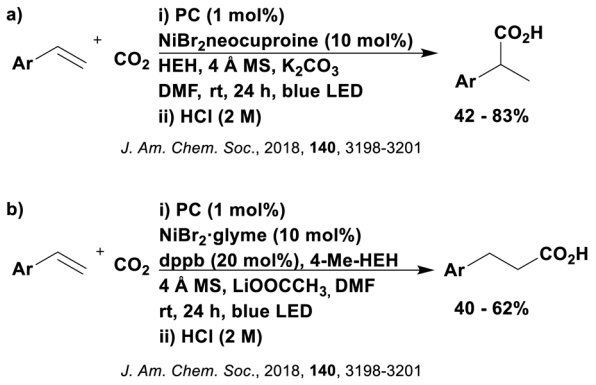

Fig. 183 Reaction schemes for the carboxylation of styrene.

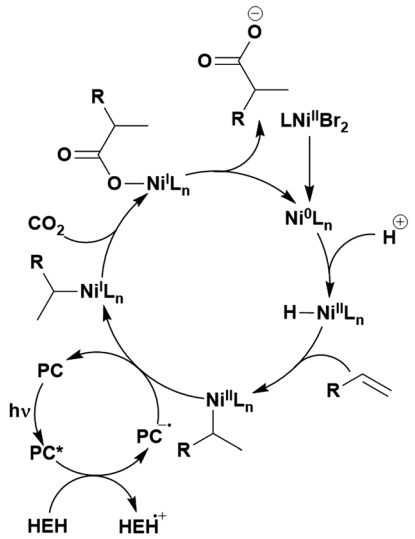

Fig. 184 Proposed mechanism for the carboxylation of styrene.

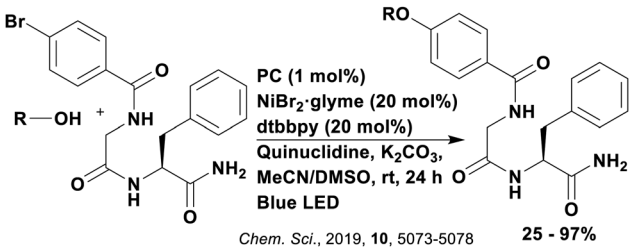

Fig. 185 Reaction scheme for photoredox Ni-catalysed peptide C(sp^2)–O cross coupling.

formation of C–O bonds within peptides post synthesis (Fig. 185) whereby the photocatalyst, in its excited state, is required to oxidise the nickel catalyst in order to facilitate reductive elimination, and the reduced photocatalyst is required to reduce the nickel catalyst (Fig. 186).[372] In the photocatalyst screen, TADF molecules **4CzIPN** and **4DPAIPN** were considered, of which **4DPAIPN** gave higher yields than all the other photocatalysts tested. A comparison between **4DPAIPN** and $[Ir(dF(CF_3)ppy)_2(dtbbpy)]PF_6$, which produced the second highest product yield (81% and 61%, respectively), reveals that the most significant difference in thermodynamic parameters arises in the ground state reduction potentials (E_{red} = −1.52 V for **4DPAIPN** *vs.* E_{red} = −1.37 V for $[Ir(dF(CF_3)\ ppy)_2(dtbbpy)]PF_6$), suggesting the stronger ground state reducing power of **4DPAIPN** contributes to the higher yields obtained when this photocatalyst is in use.

Typically, dual catalysis for cross-coupling occurs through a photoredox-based mechanism; however, the same bonding-forming reaction can proceed *via* an energy transfer mechanism, such as the cross-coupling of carboxylic acids with aryl halides (Fig. 187a).[325] Oxidative addition of an aryl halide to the Ni(0) catalyst followed by addition of the carboxylate radical, results in a Ni(II) complex. The excited photocatalyst can then transfer energy to this species (Fig. 188),[373] which then undergoes reductive elimination to close the catalytic cycle and eject the product.

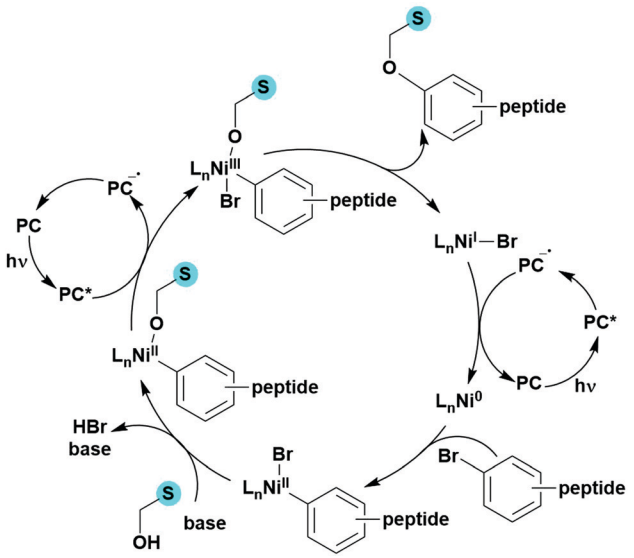

Fig. 186 Proposed mechanism for C(sp^2)–O cross coupling using photoredox/Ni dual catalysis where S = serine.

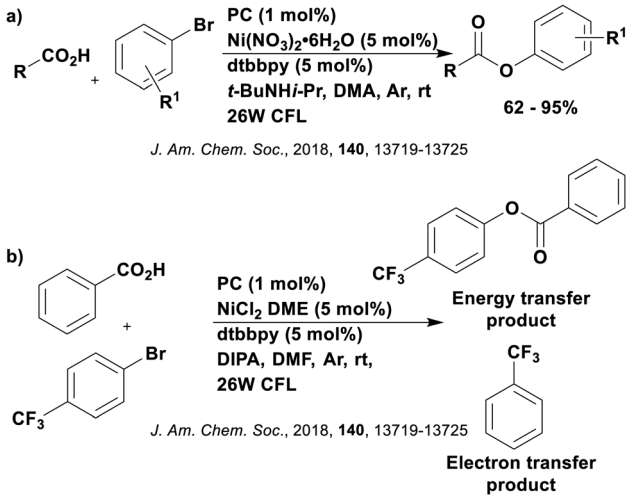

Fig. 187 Reaction scheme showing (a) the cross coupling of carboxylic acids with aryl halides and (b) the two potential products for this reaction.

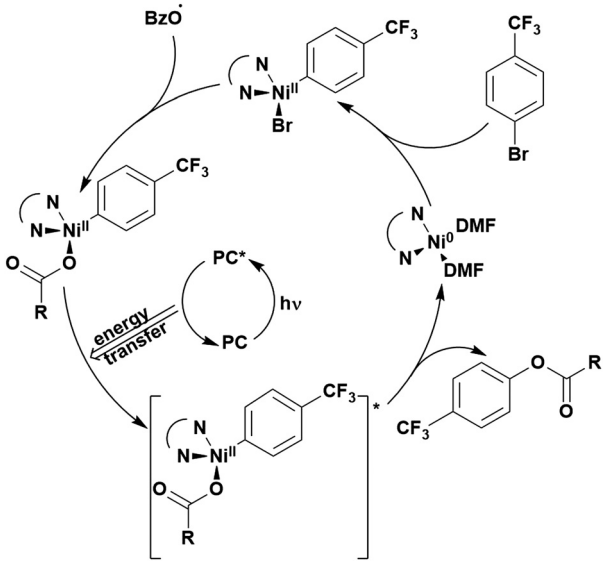

Fig. 188 Proposed photocatalytic energy transfer mechanism in the cross coupling of carboxylic acids with aryl halides.

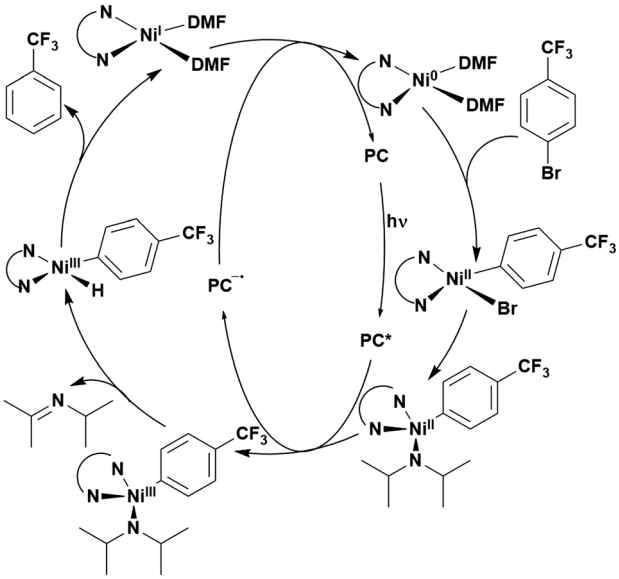

Fig. 189 Proposed mechanism for the electron transfer route in the coupling of aryl halides with carboxylic acids.

Organic photocatalysts were investigated, including **4CzIPN**, **4DPAIPN** and **4DPAPN**.[325] The authors showed that both energy and electron transfer mechanisms were occurring competitively, producing two different products (Fig. 187b). Photocatalysts with strong excited state oxidation potentials are capable of oxidising a Ni(II) complex, generating a Ni(III) complex that can then release an imine; the presence of this imine was confirmed by GC-MS. Reductive elimination of the arene produces a Ni(I) complex that is reduced by the reduced PC, closing the photocatalytic cycle. The resultant Ni(0) complex partakes in oxidative addition with the aryl halide to continue the nickel catalytic cycle (Fig. 189). In order to suppress the SET required to generate the photoredox product, a weaker photooxidant must be used so that it is no longer thermodynamically feasible to undergo electron transfer. For example, for the aforementioned photocatalysts, the yields of the PEnT product are shown to increase with decreasing photooxidising ability (trace, 17% and 51% yields for **4CzIPN**, **4DPAIPN** and **4DPAPN**, respectively, which have E_{red}^* = 1.35 V, 1.1 V and 0.93 V, respectively). **4DPAPN** proved the most efficient out of the organic compounds tested; however, it still produced inferior yields in comparison to *fac*-Ir(ppy)$_3$ (70%) under the same reaction conditions. This is likely to be as a result of the even smaller photooxidising capacity of *fac*-Ir(ppy)$_3$ which has E_{red}^* = 0.31 V.

Photoredox/Pd cross coupling

In addition to Ni, CDCB-based organic PCs have been shown to be effective in dual catalysis with Pd catalysts. An example is the

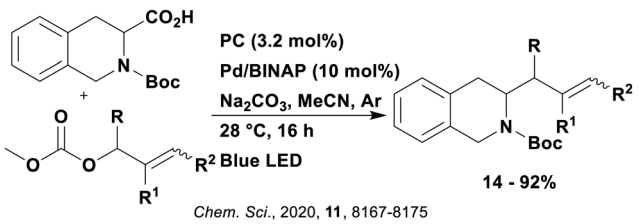

Chem. Sci., 2020, **11**, 8167-8175

Fig. 190 Reaction scheme for the decarboxylative C(sp^3)–C(sp^3) coupling of carboxylic acids and π-electrophiles.

decarboxylative C(sp^3)–C(sp^3) coupling of carboxylic acids with π-electrophiles (Fig. 190),[374] which uses $Pd(OAc)_2$, in the presence of BINAP (2,2′-bis(diphenylphosphino)-1,1′-binaphthalene), as the Pd catalyst. The proposed dominant catalytic pathway involves oxidative addition of the allyl carbonate to Pd(0) to generate a π-allyl-Pd carboxylate species, which reductively quenches the excited PC (Fig. 191). Decarboxylation followed by reductive elimination ensues, releasing the product. Both catalytic cycles are closed concurrently by SET transfer from the reduced PC to the Pd(I) species, regenerating the initial two catalysts.

In the presence of TEMPO, the reaction is inhibited, suggesting this is indeed a radical process while Stern–Volmer quenching experiments indicated the most efficient quenching of the excited PC occurred by the π-allyl-Pd carboxylate species. Four organic TADF compounds were tested as PCs in this reaction: **4CzIPN**, **4CzPN**, **2CzTPN** and **4DPAIPN**, providing yields of 82%, 48%, 5% and 0%, respectively. Additionally, $[Ir(dF(CF_3)ppy)_2(dtbbpy)]PF_6$ gave 84% yield of product; **4CzIPN** was used as the PC for the remainder of the study due to the lower cost of the organic PC.

The PC must be capable of reducing the Pd(I) species, which is estimated to have $E_{red} = -1.26$ V. This difficult reduction may explain why lower yields were obtained for **4CzPN** in comparison to **4CzIPN** ($E_{red} = -1.21$ V, -1.16 V, -1.30 V, -1.52 V and -1.37 V for **4CzIPN**, **4CzPN**, **2CzTPN**, **4DPAIPN** and $[Ir(dF(CF_3)ppy)_2(dtbbpy)]PF_6$, respectively). The photooxidising ability of the PCs are relatively similar, save for **4DPAIPN**, which may explain why this compound could not photocatalyze reaction ($E_{red}^* = 1.35$ V, 1.40 V, 1.34 V, 1.1 V and 1.21 V for **4CzIPN**, **4CzPN**, **2CzTPN**, **4DPAIPN** and $[Ir(dF(CF_3)ppy)_2(dtbbpy)]PF_6$, respectively). However, it seems as though something other than these thermodynamics considerations is responsible for the difference in yields as **2CzTPN** for example, performed very poorly despite having the appropriate redox potentials required for the mechanism proposed.

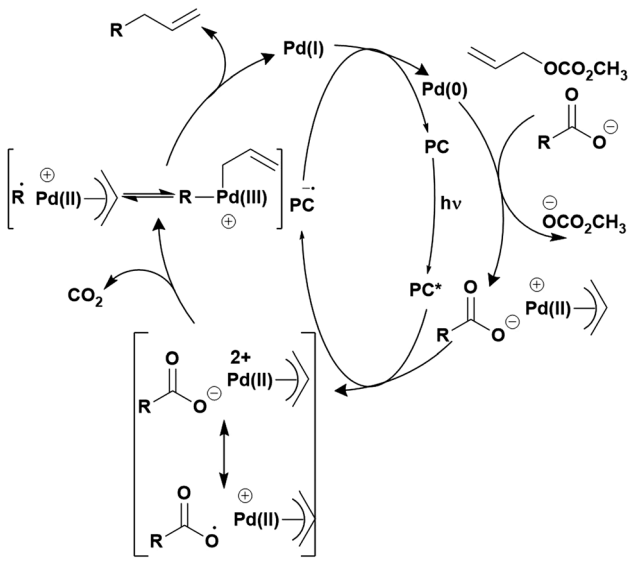

Fig. 191 Viable mechanism for the decarboxylative C(sp^3)–C(sp^3) cross coupling of carboxylic acids and π-electrophiles.

Photoredox/Ti cross coupling

Synergistic catalysis involving TADF PCs and a titanium catalyst, Cp_2TiCl_2, can be seen in the allylation of aromatic and aliphatic aldehydes (Fig. 192).[375] The proposed mechanism involves oxidative quenching of the excited PC by the titanium catalyst, before regeneration of the PC through oxidation of the Hantzsch ester (Fig. 193). Stern–Volmer quenching experiments indicated both the titanium catalyst and the Hantzsch ester can quench the excited **3DPAFIPN** emission, although the former does so at a faster rate ($k_q = 5.2 \times 10^8$ M^{-1} s^{-1} and 1.5×10^7 M^{-1} s^{-1}, respectively). A quantum yield of 0.013 is suggestive that this is not a radical chain process. Both **4CzIPN** and **3DPAFIPN** were studied as organic photocatalysts, providing respective yields of 45% and 99% at 5 mol% loading. Transition metal complex $[Ir(dF(CF_3)ppy)_2(dtbbpy)]PF_6$ also proved very successful, giving 96% yield at 1 mol% loading. The Hantzsch ester has an oxidation potential $E_{ox} = 1.0$ V, which makes oxidation facile for all three photocatalysts ($E_{ox} = 1.3$ V, 1.52 V and 1.69 V for **3DPAFIPN**, **4CzIPN** and $[Ir(dF(CF_3)ppy)_2(dtbbpy)]PF_6$, respectively). Therefore the difference in yield may be related more to the photoreducing

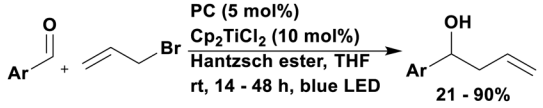

ACS Catal., 2020, **10**, 3857-3863

Fig. 192 Reaction scheme for the allylation of aromatic aldehydes.

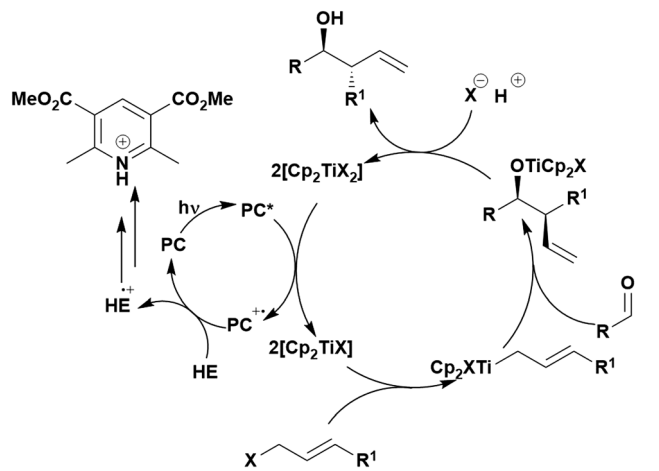

Fig. 193 Proposed mechanism for the dual catalytic allylation of aldehydes.

capacity of the photocatalyst (E_{ox}* = −1.38 V, −1.04 V and −0.89 V for **3DPAFIPN**, **4CzIPN** and [Ir(dF(CF$_3$)ppy)$_2$(dtbbpy)]PF$_6$, respectively), although this does not fully explain the poor yield obtained by **4CzIPN**. One possible explanation may be that for this PC there is a change in mechanism to favour a reductive quenching pathway as **4CzIPN** is the most photooxidising of the three (E_{red}* = 1.09 V, 1.35 V and 1.21 V for **3DPAFIPN**, **4CzIPN** and [Ir(dF(CF$_3$)ppy)$_2$(dtbbpy)]PF$_6$, respectively) and it was shown by Stern–Volmer quenching experiments that the Hantzsch ester does quench the photocatalyst emission.

Photoredox/Cu cross coupling

Metallaphotoredox catalysis involving copper complexes has been investigated with a variety of CDCB type photocatalysts in the context of the decarboxylative C(sp^3)–N coupling of anilines (Fig. 194a) and imines (Fig. 194b).[376] Reductive quenching of the excited PC by NEt$_3$ is proposed to occur (Fig. 195), with the reduced PC then being invoked to reduce the *N*-hydroxyphthalimide (NHPI) ester. Resultant decarboxylation and fragmentation produce an alkyl radical. Meanwhile, the aniline reagent coordinates to the Cu(I) catalyst, with the resultant complex undergoing HAT to the NEt$_3$ radical cation. The alkyl radical is then trapped by the Cu(II)-anilido complex followed by reductive elimination to close the copper catalytic cycle and release the final product. Fluorescence quenching experiments showed that the aniline, CuCl and NEt$_3$ could each quench the excited PC (K_{SV} = 375.47, 278.27 and 205.25, respectively), while the NHPI could not. A combination of CuCl: aniline and CuCl:NEt$_3$ were likewise considered as quenchers, but provided no significant luminescence quenching. The authors suggested that due to binding with aniline or NEt$_3$, there is no free CuCl to quench the PC. Since the coupling was only successful when using NEt$_3$ or DIPEA, rather than other bases, the authors contended that these amines act as more than a simple base and are serving to reductively quench the PC, despite having a lower Stern–Volmer quenching constant than the aniline. A low quantum yield of 0.054 was obtained, implying no radical chain process is in operation.

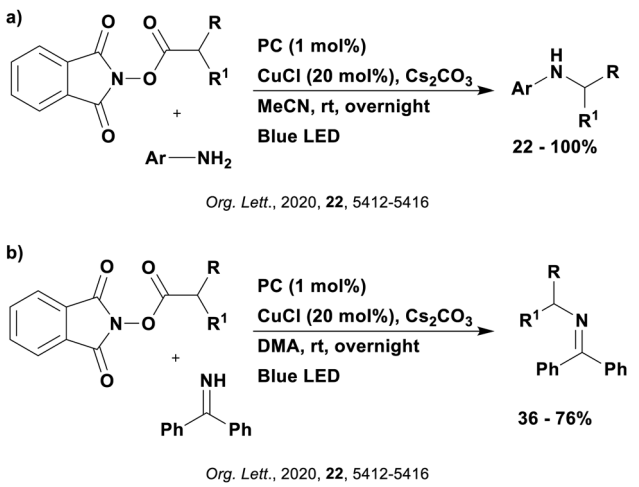

Fig. 194 Reaction schemes for the decarboxylative C(sp^3)–N coupling of (a) anilines and (b) imines.

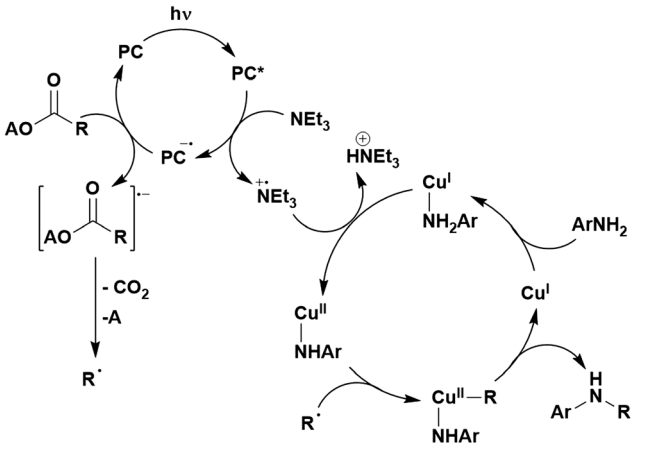

Fig. 195 Proposed mechanism for the decarboxylative C(sp^3)–N coupling of anilines where A represents phthalimide and R is an alkyl group.

In the photocatalyst screen, **4CzIPN** (100%) **4DPAIPN-Br** (85%), **4DPAIPN-Cl** (75%) **4DPAIPN** (72%), **4CzIPN-^{t}Bu** (59%) and **4CzIPN-Cl** (10%) were all considered. It should be noted that the mechanism proposed differs from that suggested for an analogous coupling with [Ru(bpy)$_3$](PF$_6$)$_2$, which proceeds *via* an oxidative quenching.[377] The authors suggested the different mechanism proceeding with **4CzIPN** may be on account of it being a stronger photooxidant (E_{red}* = 1.35 V and 0.77 V for **4CzIPN** and [Ru(bpy)$_3$](PF$_6$)$_2$, respectively). Hence, with this is mind, it is possible some of the other organic TADF compounds, which are weaker photooxidants, may also operate *via* an oxidative quenching mechanism, which may explain the differences in yields (E_{red}* = 0.98 V, 1.09 V, 1.1 V, 1.21 V for **4DPAIPN-Br**, **4DPAIPN-Cl**, **4DPAIPN** and **4CzIPN-^{t}Bu**, respectively). Although **4CzIPN-Cl** is a strong photooxidant (E_{red}* = 1.71 V), it has a much weaker reducing capacity in ground state than **4CzIPN** (E_{red} = −0.71 V and −1.21 V for **4CzIPN-Cl** and **4CzIPN**, respectively), which may explain why it only afforded a 10% product yield.

Dual photocatalytic hydrogen production

Photocatalytic water reduction has received significant attention as a potential renewable hydrogen energy vector, accessed through benign and sustainable methods.[378] TADF-based photocatalysts have been considered as the photosensitiser component for this process, such as **4CzPN-R**, **4CzIPN-R** and **4CzTPN-R** where R = H, Ph or ^{t}Bu.[316] A sacrificial reductant, triethylamine (TEA), as well as *in situ* generated water reduction catalyst (WRC) PdCl$_2$(PPh$_3$)$_2$ are also required (Fig. 196). Stern–Volmer experiments suggested both

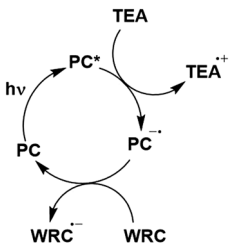

Fig. 196 Photocatalytic cycle for the water reduction reaction.

oxidative and reductive quenching mechanisms may be possible, since both $PdCl_2(PPh_3)_2$ and TEA can quench the emission of the PC; however, the large excess of TEA compared to the WRC implies that the reductive quenching cycle dominates. The success of the photocatalyst was assessed by the turnover number (TON), where TON = moles (H_2)/moles (PC) and the volume of H_2 produced. The photocatalytic activity increases following **4CzTPN-R** < **4CzPN-R** < **4CzIPN-R**, whereby the phthalonitrile cyano groups are positioned *para*, *ortho* and *meta*, respectively. For **4CzIPN-R** and **4CzPN-R**, the photocatalytic activity also increases following R = Ph < ^{t}Bu < H, while for **4CzTPN-R**, R = H < Ph < ^{t}Bu. The best TADF photocatalyst **4CzIPN-H** produced higher TON than the known photosensitiser $[Ru(bpy)_3]Cl_2$ (2023 and 144, respectively), although the reaction was considerably more sluggish, proceeding in 60 hours compared to 5 hours when using the ruthenium complex. The authors concluded that the delayed fluorescence component (τ_d = 1–2 μs for **4CzPN** and **4CzIPN** in THF) was not essential, since the reductive quenching necessary for the photocatalytic cycle, took place on a much faster timescale (0.2–0.3 ns) than the intersystem crossing/reverse intersystem crossing cycle.

Photocatalytic hydrogen production is also possible through dehydrogenation of amines (Fig. 197a). A **4CzPN** motif (Fig. 197b) has been incorporated into a supramolecular assembly consisting of four pendant Co^{III} cobaloxime moieties. This system serves to promote the catalytic acceptorless dehydrogenation (CAD) of secondary amine to imines.[379] The cobaloxime $Co(dmgH)_2PyCl$ is a well-known hydrogen evolution catalyst,[380] which has been used in conjunction with a range of photosensitisers. For example, with a platinum(II) terpyridyl acetylide chromophore[381] or a rhodamine based photosensitiser,[382] water reduction is possible, whilst aromatic C–H thiolation could occur when the Co co-catalyst was used in combination with $[Ru(bpy)_3]Cl_2$.[383] The proposed mechanism for the CAD procedure is shown in Fig. 198. Upon excitation of the photocatalyst, the Cobalt co-catalyst is reduced

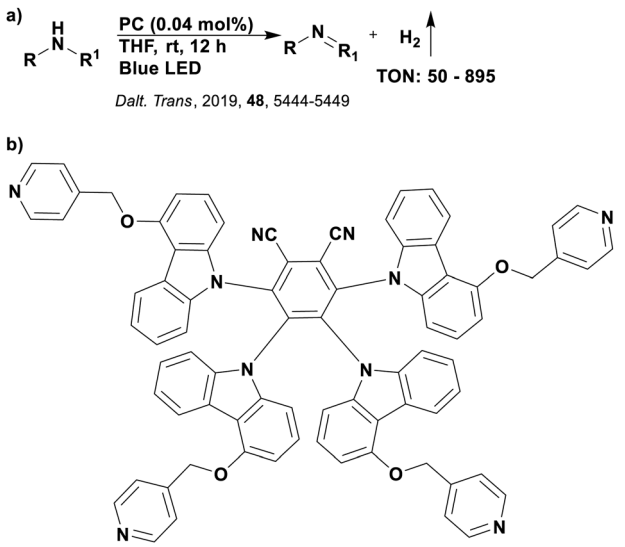

Fig. 197 (a) Reaction scheme for the photocatalytic dehydrogenation of secondary amines and (b) photoactive component (1) of the supramolecular catalyst.

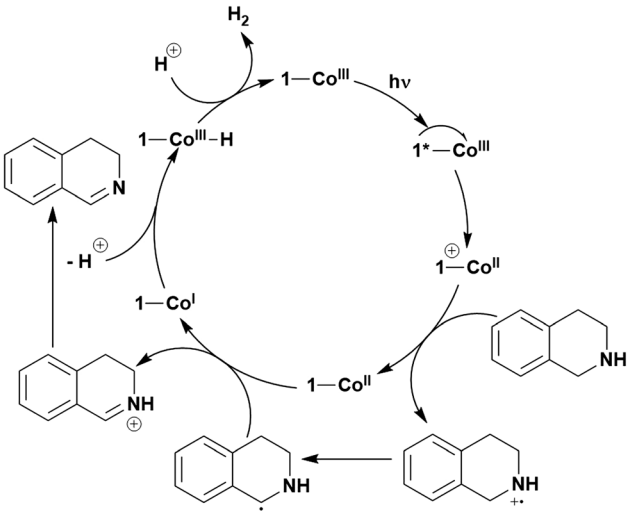

Fig. 198 Mechanism for the catalytic acceptorless dehydrogenation of secondary amines to imines using a supramolecular assembly.

following a SET from the excited **4CzPN** motif to Co^{III}. The oxidised photocatalyst then promotes oxidation of the secondary amine to the α-amino radical and concomitant regeneration of the **4CzPN** moiety. This carbon-based radical is then further oxidized by the cobalt(II) species to afford the iminium ion, which is deprotonated by the as-formed cobalt(I) to afford the final imine product. The success of this photocatalyst was shown through the TON rather than yield of the imine product. Using a photoactive **4CzPN**-based moiety and $Co(dmgH)_2PyCl$ as two separate entities only yielded a TON of 53 in comparison to 305 obtained for the combined supramolecular assembly, highlighting the advantages of covalently linking the two species together.

HAT catalysis

Finally, dual catalysis using a CDCB-based TADF molecule as the photocatalyst has been reported to work effectively alongside a HAT catalyst in the trifluoromethylthiolation of tertiary ethers (Fig. 199).[384] The excited photocatalyst undergoes reductive quenching from the thiolate anion, generating the thiyl radical. This electrophilic thiyl radical then undergoes HAT with the most hydridic α-C–H group to the ether, generating an alkoxyl radical. Cleavage of the C–O bond then results in the required alkyl radical. This part of the mechanism was confirmed by Stern–Volmer quenching experiments where emission of the PC was quenched by the presence of thiolate anions, and radical trapping experiments with TEMPO demonstrated the existence of the tertiary alkyl radical.

Two potential mechanistic pathways were proposed for the regeneration of the photocatalyst: pathway A (Fig. 200a) involves

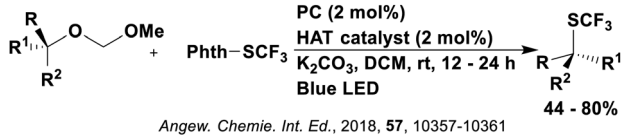

Fig. 199 Reaction scheme for the trifluoromethylthiolation of tertiary ethers.

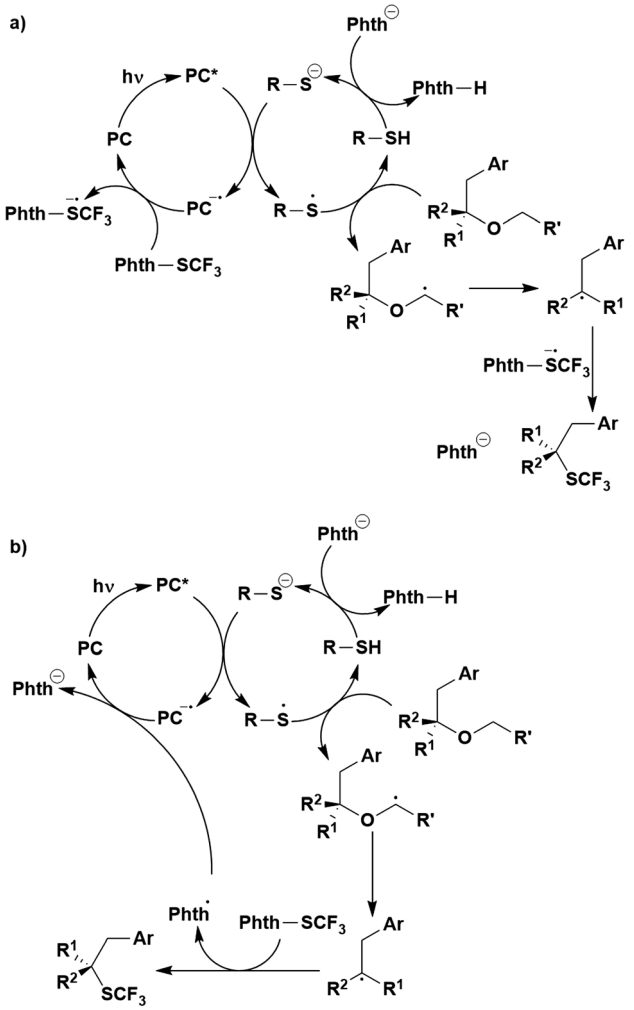

Fig. 200 Two proposed mechanisms for the carbotrifluoromethylthiolation of tertiary ethers using dual catalysis.

the reduced PC acting to reduce Phth-SCF_3 with the resultant radical coupling generating the product, with loss of the Phth anion; alternatively, pathway B (Fig. 200b) implicates the addition of the alkyl radical to Phth-SCF_3, followed by release of the Phth radical, which is reduced to the anion by the reduced PC, regenerating the PC. The quantum yield was calculated to be 0.024, ruling out a radical chain pathway. **4CzIPN** gave the highest product yield of 76% while **4CzPN** gave the second highest product yield of 63% with other organic photocatalysts, such as eosin Y, proving unsuccessful. Both **4CzIPN** and **4CzPN** have similar ground and excited state reduction potentials (E_{red} = −1.21 V and −1.16 V and E_{red}* = 1.35 V and 1.40 V, respectively), which explains why they have similar yields whereas eosin Y is much weaker photooxidant and ground state reductant (E_{red}* = 0.83 V and E_{red} = −1.06 V); hence may not be able to complete the required SET.

An additional example of dual photocatalysis with HAT catalysis can be seen in the carboxylation of benzylic C–H bonds (Fig. 201).[324] The proposed mechanism involves reductive quenching of the excited photocatalyst by the tri*iso*propylsilanethiol HAT

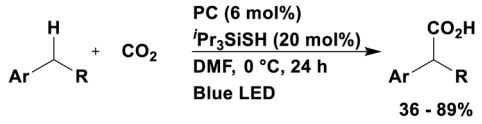

J. Am. Chem. Soc., 2019, **141**, 11393-11397

Fig. 201 Reaction scheme for the photocarboxylation of benzylic C–H bonds.

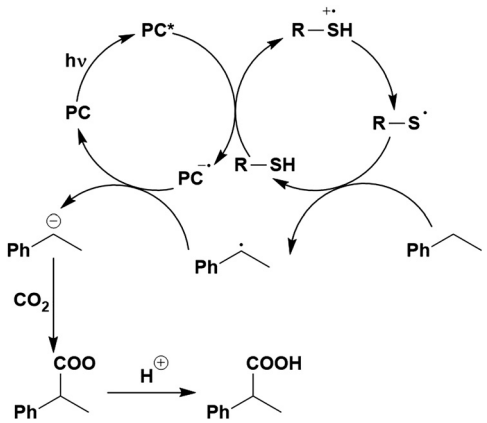

Fig. 202 Proposed mechanism for the photocarboxylation of benzylic C–H bonds.

catalyst (Fig. 202). This is unusual, as typically the thiol anion is suggested to reductively quench the photoexcited state of the PC. Regardless, the electrophilic thiyl radical that is generated after deprotonation of the oxidised HAT catalyst can abstract a H atom from the aryl substrate, closing the HAT catalytic cycle. The benzylic radical is then reduced by the reduced PC, closing the photocatalytic cycle. Carboxylation and protonation of the benzylic anion forms the required product. This proposed mechanism is supported by radical trapping experiments with TEMPO, confirming the presence of radical intermediates. The C–H bond cleavage step is postulated to be the rate-determining step from the observed kinetic isotope effect. In the photocatalyst screen, five TADF PCs investigated, **4CzIPN**, **5CzBN**, **3DPA2FBN**, **3DPAFIPN**, and **4CzBN**, afforded similar product yields (14%, 7%, 11%, 14% and 23%, respectively) whereas the three iridium photocatalysts considered, *fac*-Ir(ppy)$_3$, [Ir(ppy)$_2$(dtbbpy)]PF_6 and [Ir(dF(CF_3)ppy)$_2$(dtbbpy)]PF_6, all yielded no product under the same reaction conditions. **4CzIPN** was selected as the photocatalyst for this reaction, and further optimisation resulted in an increase in yield from 14% to 57%. König *et al.* rationalized the success of the TADF compounds compared to the iridium complexes by suggesting the organic compounds can generate an *in situ* photocatalyst, which cannot be formed with the transition metal PCs. When ethylbenzene was used as the starting material, the formation of 2,3,4,6-tetra(9-*H*-carbazol-9-yl)-5-(1-phenylethyl)-benzonitrile (**4CzPEBN**) was detected, which was believed to be the active photocatalyst in the reaction (Fig. 203). The phenylethyl radical has a very negative reduction potential (E_{red} = −1.60 V), hence in terms of thermodynamics, the ground state reduction potential of **4CzIPN** is not sufficiently reducing (since E_{red} = −1.21 V) whereas **4CzPEBN** can complete this

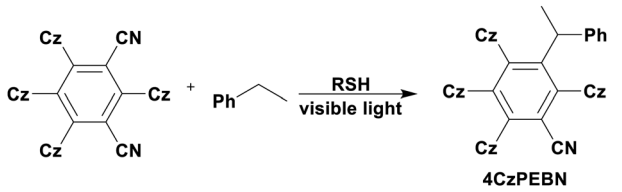

Fig. 203 Proposed generation of 4CzPEBN from 4CzIPN, where Cz = carbazole.

transformation (E_{red} = −1.69 V). This *in situ*-generated photocatalyst allows for challenging reductive transformations to occur, which are not possible with the iridium photocatalysts.

This mode of dual catalysis has been applied to the generation of benzylic carbanions, which were used to produce homobenzylic alcohols when reacted with electrophiles such as ketones and aldehydes (Fig. 204a and b).[385] The mechanism proposed is similar to the one in Fig. 202, except that in this case the HAT catalyst, $(^{i}Pr)_3SiSH$, is first deprotonated before undergoing SET to the excited PC (Fig. 205). The resultant thiyl radical abstracts a proton from ethylbenzene to form the benzylic radical, closing the HAT catalytic cycle. This benzylic radical is subsequently reduced to the benzylic carbanion by the reduced PC, completing the photocatalytic cycle. Reaction between the benzylic carbanion and a carbonyl results in the desired product. Mechanistic investigations were undertaken to confirm the presence of the carbanion as well as Stern–Volmer quenching experiments, which corroborated quenching of the excited PC by the thiolate. Optimisation of the reaction involving ketones was first conducted, with **4CzIPN**, **3DPA2FBN** and **3DPAFIPN** being the TADF compounds under investigation and indeed being the only successful photocatalysts, providing yields of 30%, 50% and 28%, respectively. Their success seems to be a reflection of their suitably reducing ground state reduction potentials (E_{red} = −1.21 V, −1.92 V and −1.59 V, for **4CzIPN**, **3DPA2FBN** and **3DPAFIPN**, respectively). Other PCs considered, including eosin Y, $[Ir(dF(CF_3)ppy)_2(dtbbpy)]PF_6$ and $[Ru(bpy)_3](PF_6)_2$, all yielded no product, despite having appropriate redox potentials. Perhaps this may be related to the formation of **4CzPEBN** as suggested by the earlier study of König *et al.*,[324] although there is no mention of this in the follow up study by the same group. When using aldehydes, **4CzIPN**, **3DPA2FBN**, **3DPAFIPN** and **4CzBN** provided yields of 20%, 10%, 32% and 20%, respectively. The reaction was shown to plateau after a few hours, and it was uncovered that the presence of alcohols poisons the reaction, with König *et al.* proposing deleterious protonation of the carbanion.

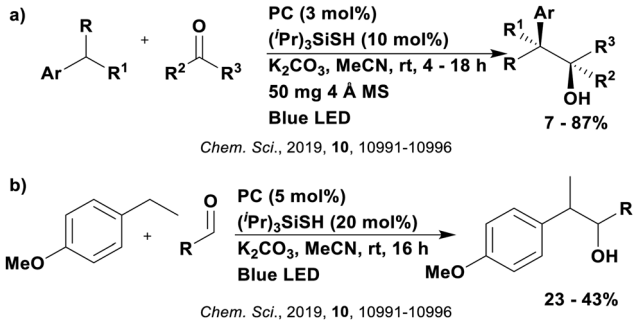

Fig. 204 Reaction scheme for the synthesis of secondary and tertiary homobenzylic alcohols from unfunctionalised starting materials and (a) ketones or (b) aldehydes.

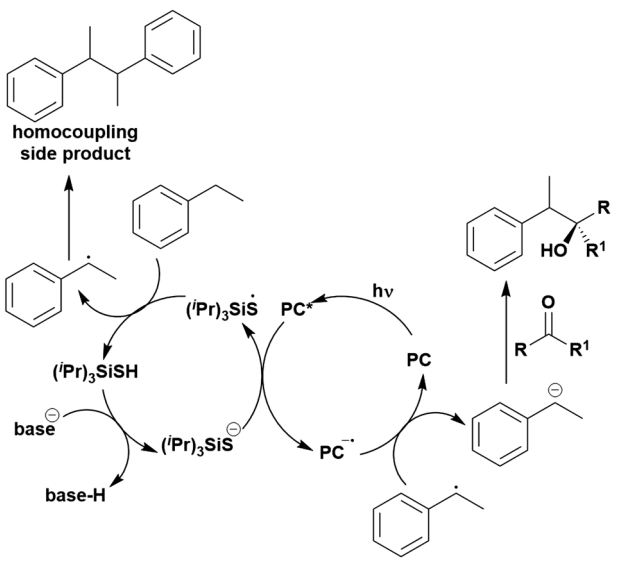

Fig. 205 Possible mechanism for the dual catalytic generation of benzylic carbanions.

Amide synthesis, through coupling of an alcohol and an amine (Fig. 206),[329] is additionally possible. The mechanism was proposed to involve two photocatalytic cycles and can be thought of as a two-step process. The first cycle (Fig. 207a) involves oxidative quenching of the excited PC by oxygen, followed by oxidation of the HAT catalyst, quinuclidine, to close the photocatalytic cycle. The quinuclidine radical cation can then abstract a H atom from the α-hydroxy position of the H-bonded alcohol, resulting in the α-hydroxy radical. Oxidation of this radical produces the aldehyde. The second photocatalytic cycle by comparison depends on the nature of the amine. For both primary and secondary amines, the excited PC is reductively quenched by the presence of sacrificial electron donor DIPEA, to generate the reduced PC. Although DIPEA is an amine, its role in this reaction is purely sacrificial. An additional amine is present, which is used as the coupling partner. When this is a secondary amine (Fig. 207b), regeneration of the PC occurs by oxidation from oxygen, to form a superoxide radical. The aldehyde previously formed then reacts with amine, producing a hemiaminal, which can be oxidised by the superoxide radical to form the amide. By contrast, the proposed mechanism for a primary amine suggests

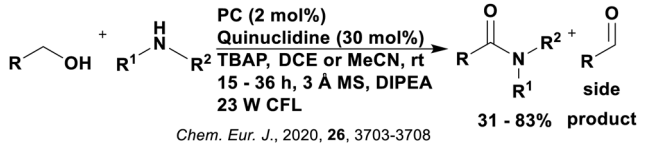

Fig. 206 Reaction scheme for the synthesis of amides from alcohols and amines.

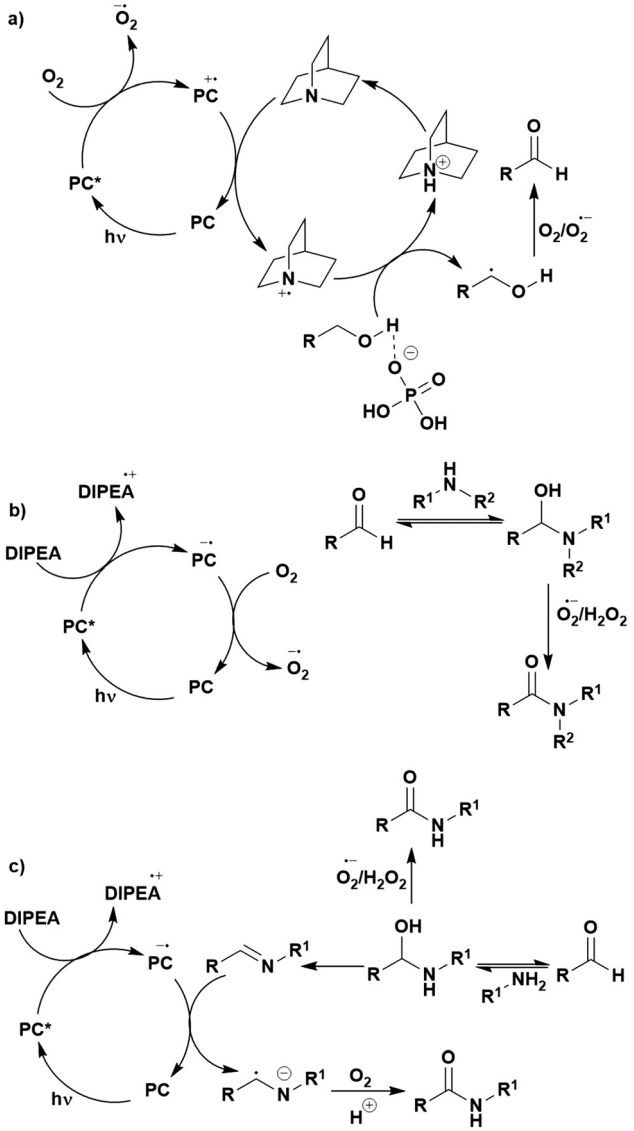

Fig. 207 Plausible mechanism for the dual catalytic synthesis of amides from alcohols and amines: (a) formation of the aldehyde, (b) reaction with secondary amine and (c) reaction with a primary amine.

that the reduced PC is used to reduce an *in situ*-formed imine, which following oxidation and protonation, yields the amide product (Fig. 207c). Radical trapping experiments confirmed the presence of the superoxide radical and Stern–Volmer quenching experiments indicated that DIPEA was acting as the quencher of the excited PC; however, no additional mechanistic evidence was provided, causing Singh *et al.* to propose five different mechanisms for the second photocatalytic cycle.

Initial optimisation of the reaction conditions focused on the reaction of a benzylic alcohol with piperidine. Reference photocatalysts $[Ru(bpy)_3](PF_6)_2$ and eosin Y produced no product while **4CzIPN** and **4CzIPN-Br** yielded 68% and 61% of amide, respectively, with additional aldehyde side product of 29% and 33%, respectively. The oxidation potential of quinuclidine is moderate (E_{ox} = 1.1 V), hence the photocatalyst must be sufficiently oxidising in the ground state, which the TADF PCs most certainly are (E_{ox} = 1.52 V and 1.76 V for **4CzIPN** and **4CzIPN-Br**, respectively) while eosin Y is not (E_{ox} = 0.78 V). Although $[Ru(bpy)_3](PF_6)_2$ is sufficiently oxidising in the ground state (E_{ox} = 1.29 V), the problem here is its photoreducing ability (E_{ox}* = −0.81 V), which isn't sufficient to reduce oxygen (E_{red} = −0.86 V).[269] When primary amines were investigated, **4CzIPN** yielded only 15% of the amide product, hence **5CzBN-OMe** was considered, which proved more efficient, affording a product yield of 67%. Singh *et al.* hypothesised that the change in performance is due to the *in situ* formation of an imine (E_{red} < −1.5 V),[386] which cannot be reduced by the reduced **4CzIPN** (E_{red} = −1.21 V) but can be reduced with **5CzBN-OMe** (E_{red} = −1.79 V). The success of **5CzBN-OMe** in this reaction seems to contradict the hypothesis of Zeitler *et al.* who suggested this TADF compound suffered from problems of BET, making it an inefficient PC.[114]

Finally, a base-free Corey Seebach reaction has been developed using this combination of dual catalysis (Fig. 208).[387] In the proposed mechanism, the excited PC is reductively quenched by the HAT catalyst $^{i}Pr_3SiSH$, which after deprotonation, yields the $^{i}Pr_3SiS$ radical. This radical can abstract a proton from the dithiane, with the resultant dithiyl radical being reduced by the reduced PC, closing the photocatalytic cycle. The carbanion nucleophile generated can attack non-activated ketones, with the final product formed after protonation. Support for this mechanism was provided in terms of Stern–Volmer quenching experiments which indicated the HAT catalyst was the cause of the luminescence quenching of the PC. The radical–radical homo-coupled side product, occurring from coupling of the dithiyl radical species, was detected by HRMS, with increasing yield of this species observed in the absence of the ketone electrophile. Deuterium labelling studies also acted in support of the mechanism; with deuterated *tert*-butanol as the electrophile, the deuterated dithiane product could be isolated.

In the PC screen, four TADF compounds and two iridium PCs were tested, with both iridium species (*fac*-Ir(ppy)$_3$ and $[Ir(dF(CF_3)ppy)_2(dtbbpy)]PF_6$) producing no product. Three of the TADF compounds did not fair much better; **4CzIPN**, **3DPAFIPN** and **4CzBN** all yielded between 2–7% while **3DPA2FBN** managed to afford 30% of product. The dithiyl radical is difficult to reduce (E_{red} = −1.87 V *vs.* SCE), which hence explains why the majority of PCs struggled with this reaction (E_{red} = −1.37 V, −1.21 V, −1.59 V and −1.63 V for $[Ir(dF(CF_3)ppy)_2(dtbbpy)]PF_6$, **4CzIPN**, **3DPAFIPN** and **4CzBN**, respectively) in comparison to **3DPAF2BN** (E_{red} = −1.92 V). Despite *fac*-Ir(ppy)$_3$ being suitably reducing in the ground state (E_{red} = −2.19 V), its poor photooxidising ability may have prevented the complex from turning over the reaction (E_{red}* = 0.31 V compared to 0.92 V for **3DPA2FBN**).

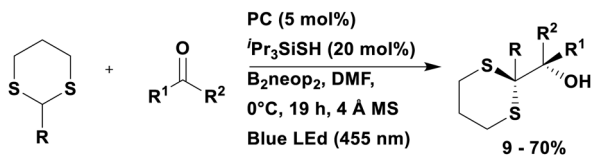

Chem. Eur. J., 2020, **26**, 12945-12950

Fig. 208 Reaction scheme for the base-free Corey-Seebach reaction.

7. Other organic TADF photocatalysts

While most of the examples in the literature have focused on **4CzIPN** as well as structurally related CDCB family of compounds as organic TADF photocatalysts, there are three reports thus far that exists for evaluating another class of TADF molecules as PCs, all in polymerisation reactions. In the first study, four organic compounds based on carbazole/sulfone-based structures (Fig. 209),[58] di(4-(4-(carbazole-9-yl)phenyl)sulfone) (**CzS1**), di(4-(4-(9-phenylcarbazol-3-yl)phenyl)sulfone) (**CzS2**), 9,9′-(sulfonylbis(4,1phenylene))-bis(9*H*-carbazole) (**2Cz-DPS**) and 9,9′-(sulfonylbis(4,1phenylene))-bis(3,6-di-*tert*-butyl-9*H*-carbazole) (**2TCz-DPS**), were tested as photocatalysts in the free radical polymerisation of methacrylates. FRP of methacrylates can proceed *via* both a reductive or oxidative quenching cycle, depending on whether a sacrificial reductant is present or oxidants such as iodonium salts are used.[229] Since iodonium salts are employed in combination with the TADF compounds, an oxidative quenching mechanism is proposed to be in operation. Of these four sulfones, only two have an experimentally determined ΔE_{ST} sufficiently small to be considered TADF molecules: **2Cz-DPS** and **2TCz-DPS**. While all four compounds were effective in the photopolymerisation reaction, **2TCz-DPS**, which displayed the longest emission lifetime (Table 3), was the most efficient in terms of both the rate of polymerisation and conversion. The ground state oxidation potentials of **CzS1** and **CzS2** are considerably less positive than **2Cz-DPS** and **2TC-DPS** (E_{ox} = 0.81 V, 0.82 V, 1.32 V and 1.26 V, respectively), which may explain their poorer performance as photocatalysts in this reaction. This study by Lalevée *et al.* focused predominately on copper complexes as PCs, with only a scant mention of these organic compounds as photocatalysts. It is difficult to ascertain how potentially useful these PCs are as there is no comparison to reference photocatalysts, making it challenging to put these results into context.

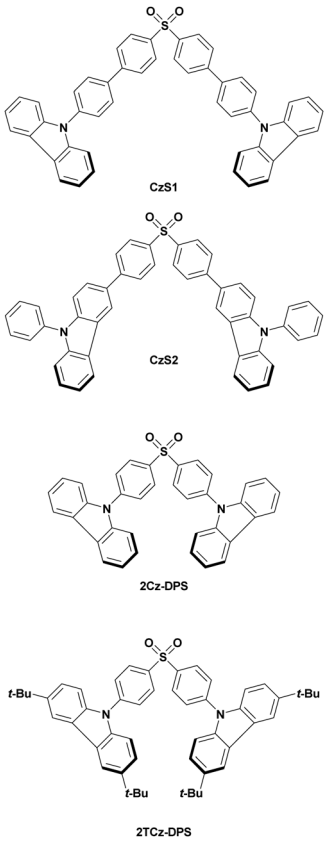

Fig. 209 Carbazole-sulfone based molecules tested as photocatalysts.

In the second example of other organic TADF photocatalysts considered as PCs, a computer-aided design strategy was implemented to identify donor–acceptor organic compounds that may have appropriate photophysical and electrochemical properties to act as a PC in the atom transfer radical polymerisation (ATRP) of methyl methacrylates, using diethyl 2-bromo-2-methylmalonate (DMB) as the initiator.[113] The reaction is similarly proposed to proceed *via* an oxidative quenching mechanism, so significant focus was placed upon computing E_{ox}* and E_{ox}. A large combination of donors and acceptors were considered with the structures tested as PCs in the polymerisation reaction shown in Fig. 210 and their respective measured properties reported in Table 4.

In the polymerisation of methyl methacrylates, **2DPA-BP**, **2DHPZ-DPS**, **DMDP-TRZ** and **4DPAIPN** and provided the highest product yield (82%, 78%, 77%, respectively in DMF and 75% in DMSO for **4DPAIPN**), which is an improvement over *fac*-Ir(ppy)$_3$ (50% in DMF). The poorest yields were obtained using **2PXZ-BP**, **PTZ-TRZ** and **2PTZ-BP** (3%, 4% and 7%, respectively). The reduced

Table 3 Redox potentials and selected photophysical properties of 4CzIPN and other organic photocatalysts based on the carbazole/sulfone structure[a]

PC	λ_{abs}/nm	λ_{PL}/nm	$E_{0,0}$/eV (kJ mol^{-1})	ΔE_{ST}/eV	E_{ox}/V	E_{red}/V	E_{ox}*/V	E_{red}*/V	τ_{pf}/ns	τ_{df}/μs	Ref.
4CzIPN	435	535	2.67[h] (258)	0.08[b]	1.52	−1.21	−1.04	1.35	18.7	1.39	60, 114, 120 and 121
CzS1	293[b]	399[b]	3.16 (305)	0.62[c]	0.81[d]		−2.35		2.55[b]	—	388
CzS2	300[b]	381[b]	3.16 (305)	0.65[c]	0.82[d]		−2.34		1.51[b]	—	388
2Cz-DPS	345[f]	407[e]	3.12[g] (301)	0.28[e]	1.32	−1.96	−1.80	1.16			113 and 389–391
2TCz-DPS	342[f]	404[b]	3.08[g] (297)	0.32[b]	1.26	−2.06	−1.82	1.02	5.3[b]	270[b]	113, 389, 391 and 392

[a] All potentials are given in volts *versus* SCE. E_{ox}* = E_{ox} − $E_{0,0}$ and E_{red}* = E_{red} + $E_{0,0}$. 1 eV = (1.602 × 10^{-22} kJ) × N_A where N_A = Avogradro's constant. λ_{abs} refers to the absorption maximum of the CT band. λ_{PL} refers to the photoluminescence maximum. Data reported in MeCN at room temperature unless otherwise noted. $E_{0,0}$ determined from the intersection point of the normalised absorption and emission spectra unless otherwise noted. [b] Determined in toluene. [c] Estimated from the difference between fluorescence and phosphorescence maxima at 77 K. [d] Determined in CH_2Cl_2. [e] Determined in chlorobenzene. [f] Determined using powder sample. [g] Determined from the onset of the gated PL spectra at 77 K (delay time: 2 μs and gating time: 200 μs). [h] $E_{0,0}$ estimated using the medium wavelengths between the lowest fluorescence excitation peak (excitation λ_{max}) and the fluorescence peak (emission λ_{max}).[120]

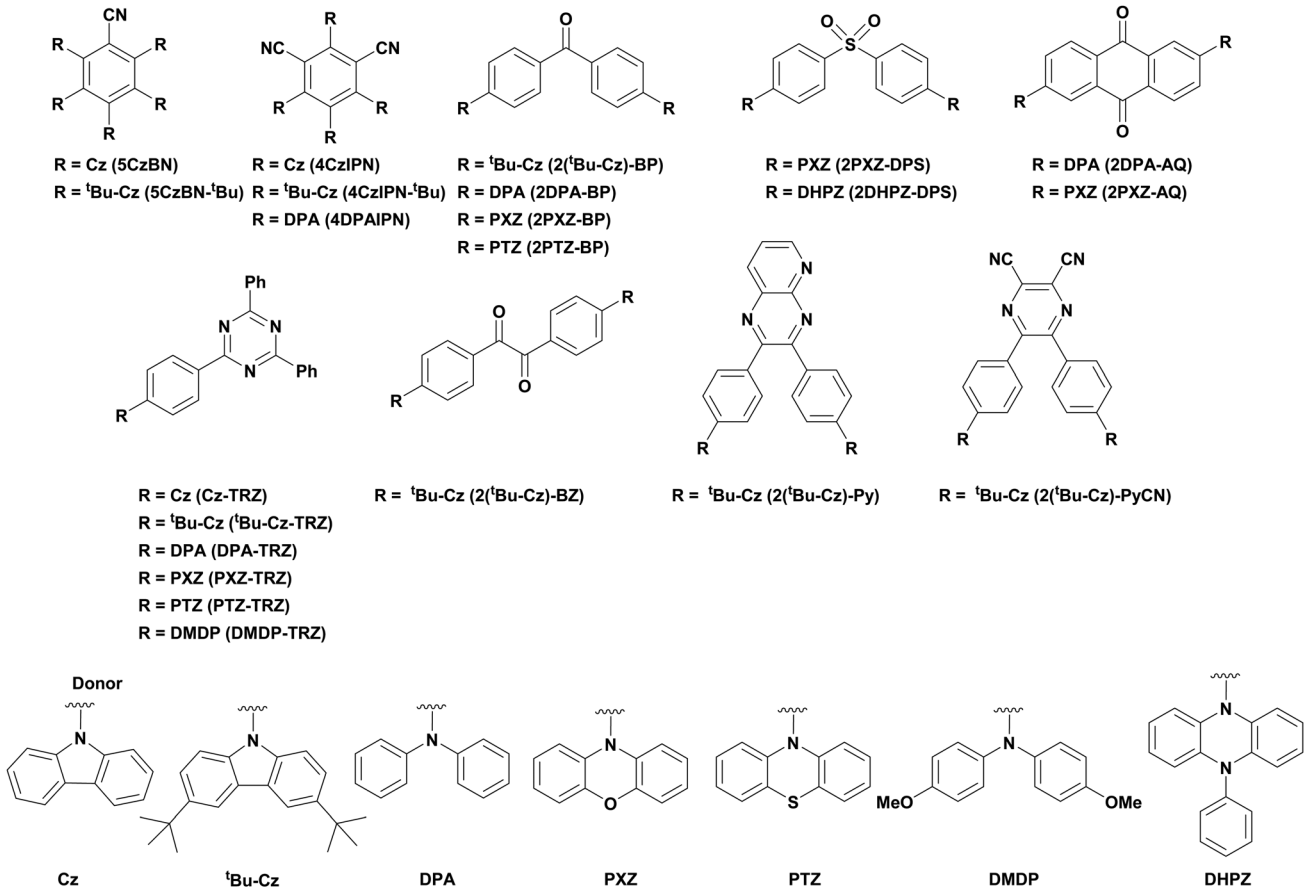

Fig. 210 Donor–acceptor compounds considered as photocatalysts for the polymerisation of methyl acrylates.

yields obtained by some of the organic PCs are hypothesised by Kwon *et al.* to be due to inefficient triplet generation, weak visible light absorption, redox potential mismatch or a combination of these factors. The criteria for a good PC in this reaction is suggested to be linked to efficient generation of long-lived triplet excited states, strong reducing power of T_1, high stability of radical cations and broad, strong visible light absorption. This was suggested due to the results obtained with **4DPAIPN** as a PC, which performed particularly well, especially at a loading of 0.5 ppm, giving a yield of 75% in DMSO and 60% in DMF, in comparison to *fac*-Ir(ppy)$_3$, which performed second best at these low loadings, giving 49% yield in DMF. The properties of these two PCs were then compared, where it was found that the molar absorptivity of the CT band of **4DPAIPN** is roughly one order of magnitude larger than that of *fac*-Ir(ppy)$_3$ (ε = 13 900 M^{-1} cm^{-1} and 2450 M^{-1} cm^{-1} at 458 nm for **4DPAIPN** and *fac*-Ir(ppy)$_3$, respectively). Moreover, the excited state lifetime is considerably longer for **4DPAIPN** (28 μs for τ_{df} for **4DPAIPN** and 1 μs for *fac*-Ir(ppy)$_3$). **4DPAIPN** was also shown to form a highly stable radical cation as demonstrated by the reversible oxidation waves observed by CV. Finally, the redox potentials indicate that while *fac*-Ir(ppy)$_3$ is the better photoreductant (E_{ox}* = −1.28 V and −1.73 V for **4DPAIPN** and *fac*-Ir(ppy)$_3$, respectively), both have sufficient photoreducing capacity to reduce MMA-Br (E_{red} ∼ −0.9 V). The higher performance of **4DPAIPN** may be due to it being a stronger ground state oxidant (E_{ox} = 1.34 V and 0.77 V for **4DPAIPN** and *fac*-Ir(ppy)$_3$, respectively).

The triplet state was suggested as being the state that participates in SET although no evidence is provided to support this assertion. Triplet exciton generation was confirmed with most of the molecules by the observed phosphorescence at 77 K using gated photoluminescence spectroscopy; the small calculated ΔE_{ST} values imply that these compounds are TADF. No further spectroscopic investigations were undertaken to prove the participation of the triplet state in this reaction mechanism.

A follow up study from the same group investigated the same subset of compounds in photoinduced electron/energy-transfer reversible addition–fragmentation chain-transfer (PET-RAFT) of methyl methacrylate.[402] Since both electron and energy transfer processes are feasible photocatalytic pathways for this reaction, both the redox potentials and the energy of the triplet state were considered when choosing which organic PCs to investigate. Based on these considerations, **5CzBN**, **4CzIPN**, **4DPAIPN**, **2DPA-BP**, **2DHPZ-DPS** and **DMDP-TRZ** were chosen for investigation, which provided monomer conversion of 35%, 22%, 70%, 10%, 21% and 43%, respectively. **4DPAIPN** was thus clearly identified as the best PC for this reaction, providing comparable monomer conversion to *fac*-Ir(ppy)$_3$ (72%). Again, the success of **4DPAIPN** was assigned to its strong visible light absorption, suitable redox potentials, stability of the radical

Table 4 Redox potentials and selected photophysical properties of organic photocatalysts based on the donor–acceptor structures shown in Fig. 163[a]

PC	λ_{abs}/nm	λ_{PL}/nm	$E_{0,0}$/eV (kJ mol^{-1})	ΔE_{ST}/eV	E_{ox}/V	E_{red}/V	E_{ox}*/V	E_{red}*/V	τ_{pf}/ns	τ_{df}/μs	Ref.
5CzBN	384[e]		2.86[e,f] (276)	0.07[e]	1.41	−1.50	−1.45	1.36			113
		512	2.83 (273)	0.07	1.41	−1.52	−1.42	1.31	16.2	7.8	114, 308 and 309
5CzBN-^{t}Bu	400[e]		2.78[e,f] (268)	0.06[e]	1.12	−1.61	−1.66	1.17			113
		480[c]		0.17[c]					15.0[c]	3.4[c]	312
4CzIPN	431[e]		2.75[e,f] (265)	−0.03[e]	1.52	−1.21	−1.23	1.54			113
	435	535	2.67 [g] (258)	0.08[c]	1.52	−1.21	−1.04	1.35	18.7	1.39	60, 114, 120 and 121
4CzIPN-^{t}Bu	451[e]		2.62[e,f] (253)	0.00[e]	1.30	−1.31	−1.32	1.31			113
	380	588	2.53 (244)	0.308[h]	1.22	−1.32	−1.31	1.21	10	1.4	316, 317, 319 and 320
4DPAIPN			2.42[e,f] (233)	0.17[e]	1.01	−1.66	−1.41	0.76			113
	425	523	2.62[g] (253)		1.34	−1.52	−1.28	1.1			120
2(^{t}Bu-Cz)-BP	364[e]		2.93[e,f] (283)	0.13[e]	1.05	−1.66	−1.88	1.27			113
2DPA-BP	375[e]		2.62[e,f] (253)	0.42[e]	1.02	−1.84	−1.60	0.78			113
2PXZ-BP	401[e]		2.52[e,f] (243)	0.19[e]	0.79	−1.61	−1.73	0.91			113
	413[c]	509[c]		0.3[i]					23[d]	12[d]	393
2PTZ-BP	343[e]		2.93[e,f] (283)	0.28[e]	0.74	−1.73	−2.19	1.2			113
2PXZ-DPS	383[e]		2.81[e,f] (271)	0.02[e]	0.84	−1.87	−1.97	0.94			113
		507[c]	2.73[c,r] (263)	0.08[c]					15[c]	2.5[c]	394
2DHPZ-DPS	431[e]		2.56[e,f] (247)	0.03[e]	0.26	−1.98	−2.30	0.58			113
		577[c]	2.40[c,r] (232)						5.6[c]	0.28[c]	394
2DPA-AQ	445[e]		n.d.	n.d.	1.20[b]	−0.83[b]	n.d.	n.d.			113
	449[c]	601[c]	2.42[c] (233)	0.27[c]					5.3[c]	377[c]	395
2PXZ-AQ	529[e]		n.d.	n.d.	0.79	−0.74	n.d.	n.d.			113
Cz-TRZ	359[e]		2.88[e,f] (278)	0.39[e]	1.30	−1.63	−1.58	1.25			113
	363[c]	446[c]		0.32[j]	1.43[b]	−1.78[b]			4.8[k]		396
^{t}Bu-Cz-TRZ	373[e]		2.85[e,f] (275)	0.25[e]	1.20	−1.65	−1.65	1.20			113
	380[c]	439[c]		0.30[c]					7.8[k]	40.6[k]	397
DPA-TRZ	388[e]		2.59[e,f] (250)	0.37[e]	1.00	−1.73	−1.59	0.86			113
	389[b]	451[b]		0.59[c,i]							398
PXZ-TRZ	411[e]		2.43[e,f] (234)	0.22[e]	0.73	−1.63	−1.70	0.80			113
	420[c]	545[c]		0.07[l]					19[c]	0.676[c]	399
PTZ-TRZ	363[e]		2.82[e,f] (272)	0.48[e]	0.73	−1.62	−2.09	1.20			113
		409, 562[c,m]		1.14, 0.18[m,n]							400
DMDP-TRZ	390[e]		2.52[e,f] (243)	0.14[e]	0.77	−1.76	−1.75	0.76			113
2(^{t}Bu-Cz)-BZ	387[e]		2.58[e,f] (249)	0.35[e]	1.36	−1.07	−1.32	1.51			113
	389[c]	553[c]	2.58[c,o] (249)	0.13[p]					12.6[p]	24.9[p,q]	401
2(^{t}Bu-Cz)-Py	396[e]		2.35[e,f] (227)	0.49[e]	1.20	−1.37	−1.15	0.98			113
2(^{t}Bu-Cz)-PyCN	386[e]		2.49[e,f] (240)	0.26[e]	1.21	−1.06	−1.28	1.43			113
	429[c]	532[c]	2.30[c,o] (222)	0.43[p]					25.2[p]	210.5[p,q]	401

[a] All potentials are given in volts *versus* SCE. $E_{ox}^* = E_{ox} - E_{0,0}$ and $E_{red}^* = E_{red} + E_{0,0}$. 1 eV = $(1.602 \times 10^{-22}$ kJ$) \times N_A$ where N_A = Avogradro's constant. λ_{abs} refers to the absorption maximum of the CT band. λ_{PL} refers to the photoluminescence maximum. Data reported in MeCN at room temperature unless otherwise noted. $E_{0,0}$ determined from the intersection point of the normalised absorption and emission spectra unless otherwise noted. [b] Measured in DCM. [c] Measured in toluene. [d] Measured in 6 wt%-doped film in a host matrix, where the host is 1,3-bis(carbazole-9-yl)benzene (mCP), measured at 300 K under vacuum. [e] Measured in DMF. [f] $E_{0,0}$ (T_1) was evaluated from the onset of gated PL spectrum at 77 K (delay time: 2 μs and gating time: 200 μs.[113] [g] $E_{0,0}$ estimated using the medium wavelengths between the lowest fluorescence excitation peak (excitation λ_{max}) and the fluorescence peak (emission λ_{max}).[120] [h] Estimated by time-dependent (TD)DFT at the M06-2X/6-31+G(d) level. [i] Estimated using onset wavelengths of the emission spectra using doped mCP films (6 wt%-doped), with E_s measured at 300 K and E_T at 5 K. [j] Determined from the onset of prompt and delayed spectra of 10 wt% doped films in bis[2-(diphenylphosphino)phenyl] ether oxide (DPEPO), measured at 77 K. [k] Measured in doped DPEPO films (10 wt%). [l] Estimated by TD-DFT at the the PBE0/6-31G level. [m] Obtained for the quasi-axial and quasi-equatorial conformers, respectively. [n] Estimated used TD-DFT at the CAMB3LYP/cc-pVDZ level. [o] Estimated from the absorption edge.[401] [p] Measured using doped 4,4′-bis(*N*-carbazolyl)-1,1′-biphenyl (CPB) films (7 wt%). [q] Average lifetime calculated by $\tau_{av} = \Sigma A_i\tau_i^2/\Sigma A_i\tau_i$ where A_i is the pre-exponential for lifetime τ_i. [r] Estimated from the emission onset.[394]

cation formed and long-lived excited state lifetimes. However, since the mechanism in operation was not clarified, it becomes difficult to assign which of these factors is most important.

These studies from Kwon *et al.* have identified a wide range of donor–acceptor compounds that may have potential as photocatalysts. While **4DPAIPN** was identified in both cases as one of the most promising PCs, these investigations illustrate the value of a wider search into TADF compounds as photocatalysts.

8. Conclusions

Undoubtedly, photocatalysis has already proven to be a powerful tool for a wide range of organic transformations. These reactions proceed under much milder reaction conditions in comparison to alternative synthetic techniques. To further enhance the scope and diversity of reactions that can be photocatalyzed, new photocatalysts must be discovered. Organic photocatalysts provide an alluring class of catalysts as they are relatively inexpensive to synthesize, have toxicity profiles that are superior to heavy transition metal photocatalysts and can easily be structurally diversified. This review has documented why one organic photocatalyst, **4CzIPN**, has become so popular. **4CzIPN** has often been used on account of it being a "greener", less toxic and cheaper photocatalyst, which can broadly undergo the same organic transformations as cationic iridium photocatalysts, without compromising on yields.

The intrinsic photophysical properties of **4CzIPN**, associated with the property of TADF, mean that this compound exhibits comparable excited state lifetimes to heavy metal photocatalysts. Factors such as similar ground and excited state redox properties, as well as enhanced molar absorptivity in the 400–450 nm region in comparison to $[Ir(dF(CF_3)ppy)_2(dtbbpy)]^+$, contribute to **4CzIPN** being a formidable photocatalyst. However, what is less clear is whether having accessible singlet and triplet excited states is intrinsically beneficial to enhancing reactivity in either PET or PEnT based reactions. On the other hand, the small ΔE_{ST} in TADF compounds implies that significantly less energy is lost during ISC to the triplet state than what is typically found in transition metal PCs, leading to a wider accessible excited state redox window given the higher energy optical gaps that are typically available to TADF compounds. A more in depth photophysical study would be required to adequately address this key point. What is, however, clear is that the donor–acceptor nature of these compounds allows for facile modification of the structure and a corresponding broad range of accessible ground and excited state redox potentials. These qualities alone explain the exponentially increasing popularity of this class of PCs.

From a mechanistic point of view, noteworthy is that TADF compounds, unlike heavy metal phosphorescent PCs, can participate in both Förster and Dexter energy transfer processes, which may be advantageous in PEnT reactions. However, the efficiency with which TADF compounds can participate in these mechanisms requires further investigation. When considering a photoredox catalysis mechanism, SET can potentially occur from the both the S_1 and T_1 states. Accessing SET from the S_1 is advantageous in that this state is a more potent oxidant and reductant than the corresponding triplet state, conferring to TADF compounds yet another advantage to transition metal complexes, which participate in SET purely from their T_1 state.

Despite the great potential of TADF PCs, their development is only in its infancy, lagging far behind the volume of TADF compounds designed for OLEDs. A more concerted and robust investigation of other TADF compounds seems certainly warranted.

Conflicts of interest

There are no conflicts to declare.

Acknowledgements

We thank Syngenta and the EPSRC Centre for Doctoral Training in Critical Resource Catalysis (CRITICAT) for financial support [PhD studentship to ''M.A.B.''; Grant code: EP/L016419/1]. We wish to thank Prof. Dr. Andreas Steffen for helpful discussions. We thank Francis Millward, Callum Prentice, Lea Hämmerling and Bryony Hockin for proof reading of this document.

Notes and references

1 D. A. Nicewicz and D. W. C. Macmillan, *Science*, 2008, **322**, 77–80.
2 M. A. Ischay, M. E. Anzovino, J. Du and T. P. Yoon, *J. Am. Chem. Soc.*, 2008, **130**, 12886–12887.
3 J. M. R. Narayanam, J. W. Tucker and C. R. J. Stephenson, *J. Am. Chem. Soc.*, 2009, **131**, 8756–8757.
4 D. M. Arias-Rotondo and J. K. McCusker, *Chem. Soc. Rev.*, 2016, **45**, 5803–5820.
5 K. C. Harper, E. G. Moschetta, S. V. Bordawekar and S. J. Wittenberger, *ACS Cent. Sci.*, 2019, **5**, 109–115.
6 N. A. Romero and D. A. Nicewicz, *Chem. Rev.*, 2016, 10075–10166.
7 R. A. Marcus, *J. Phys. Chem.*, 1989, **93**, 3078–3086.
8 R. A. Marcus, *Discuss. Faraday Soc.*, 1960, **29**, 21–31.
9 D. Rehm and A. Weller, *Ber. Bunsenges.*, 1969, **73**, 834–839.
10 R. A. Marcus, *J. Chem. Phys.*, 1956, **24**, 966–978.
11 K. Teegardin, J. I. Day, J. Chan and J. Weaver, *Org. Process Res. Dev.*, 2016, **20**, 1156–1163.
12 A. Juris and V. Balzani, *Helv. Chim. Acta*, 1981, **64**, 2175–2182.
13 J. Breu, P. Sto, S. Schrader, A. Starukhin, W. J. Finkenzeller, H. Yersin, P. Chemie, D. Regensburg, R. V. August, V. Re, M. Recei and V. No, *Chem. Mater.*, 2005, 1745–1752.
14 G. St-Pierre, S. Ladouceur, D. Fortin and E. Zysman-Colman, *Dalton Trans.*, 2011, **40**, 11726–11731.
15 Metals Daily, https://www.metalsdaily.com/live-prices/pgms/, (accessed 3 June 2020).
16 A. Lebeau, in *Hamilton and Hardy's Industrial Toxicology*, ed. R. D. Harbidon, M. M. Bourgeois and G. T. Johnson, Wiley-Blackwell, New Jersey, 6th edn, 2015, pp. 187–192.
17 J. R. Ludwig and C. S. Schindler, *Chem*, 2017, **2**, 313–316.
18 P. Nuss and M. J. Eckelman, *PLoS One*, 2014, **9**, e101298.
19 N. Robertson, B. M. Hockin, C. Li and E. Zysman-Colman, *Catal. Sci. Technol.*, 2019, **9**, 889–915.
20 C. B. Larsen and O. S. Wenger, *Chem. – Eur. J.*, 2018, **24**, 2039–2058.
21 H. Huang, X. Li, C. Yu, Y. Zhang, P. S. Mariano and W. Wang, *Angew. Chem., Int. Ed.*, 2017, **56**, 1500–1505.
22 D. Ravelli, M. Fagnoni and A. Albini, *Chem. Soc. Rev.*, 2013, **42**, 97–113.
23 H. G. Roth, S. F. Oliver, L. Campeau, D. Nicewicz and D. A. Dirocco, *J. Org. Chem.*, 2016, **81**, 7244–7249.
24 D. A. Nicewicz and T. M. Nguyen, *ACS Catal.*, 2014, **4**, 355–360.
25 V. Srivastava and P. P. Singh, *RSC Adv.*, 2017, **7**, 31377–31392.
26 Z. Li, H. Song, R. Guo, M. Zuo, C. Hou, S. Sun, X. He, Z. Sun and W. Chu, *Green Chem.*, 2019, **21**, 3602–3605.
27 M. N. Hopkinson, B. Sahoo and F. Glorius, *Adv. Synth. Catal.*, 2014, **356**, 2794–2800.
28 S. Sharma and A. Sharma, *Org. Biomol. Chem.*, 2019, **17**, 4384–4405.
29 Z. Y. Yu, J. N. Zhao, F. Yang, X. F. Tang, Y. F. Wu, C. F. Ma, B. Song, L. Yun and Q. W. Meng, *RSC Adv.*, 2020, **10**, 4825–4831.
30 M. A. Miranda and H. García, *Chem. Rev.*, 1994, **94**, 1063–1089.
31 M. Fagnoni, D. Dondi, D. Ravelli and A. Albini, *Chem. Rev.*, 2007, **107**, 2725–2756.
32 D. Ravelli and M. Fagnoni, *ChemCatChem*, 2012, **4**, 169–171.

33 M. L. Marin, L. Santos-Juanes, A. Arques, A. M. Amat and M. A. Miranda, *Chem. Rev.*, 2012, **112**, 1710–1750.
34 S. Fukuzumi and K. Ohkubo, *Chem. Sci.*, 2013, **4**, 561–574.
35 J. Luo, X. Zhang, J. Lu and J. Zhang, *ACS Catal.*, 2017, **7**, 5062–5070.
36 N. J. Turro, V. Ramamurthy and J. C. Scaiano, *Principles of Molecular Photochemistry – An Introduction*, University Science Books, Sausalito, 2009.
37 M. Kasha, *Discuss. Faraday Soc.*, 1950, **9**, 14–19.
38 O. A. El Seoud, W. J. Baader and E. L. Bastos, *Practical Chemical Kinetics in Solution*, John Wiley & Sons, Amsterdam, *First Edit.*, 2016.
39 P. A. M. Dirac, *Proc. R. Soc. A*, 1928, **117**, 610–624.
40 D. G. Fedorov, S. Koseki, M. W. Schmidt and M. S. Gordon, *Int. Rev. Phys. Chem.*, 2003, **22**, 551–592.
41 M. A. El-Sayed, *J. Chem. Phys.*, 1963, **38**, 2834–2838.
42 T. J. Penfold, E. Gindensperger, C. Daniel and C. M. Marian, *Chem. Rev.*, 2018, **118**, 6975–7025.
43 T. J. Penfold, F. B. Dias and A. P. Monkman, *Chem. Commun.*, 2018, **54**, 3926–3935.
44 P. A. M. Dirac, *Proc. R. Soc. London, Ser. A*, 1927, **114**, 243–265.
45 E. Fermi, *Z. Phys.*, 1934, **88**, 161–177.
46 J. Tanaka, *Bull. Chem. Soc. Jpn.*, 1965, **38**, 86–102.
47 I. S. K. Kerkines, I. D. Petsalakis, G. Theodorakopoulos and W. Klopper, *J. Chem. Phys.*, 2009, **131**, 224315.
48 F. Gaida, A. G. Griesbeck and M. Vollmer, in *Science of Synthesis: Photocatalysis in Organic Synthesis*, ed. B. Konig, Thieme Verlagsgruppe, New York, 2019.
49 J. S. Wilson, N. Chawdhury, M. R. A. Al-Mandhary, M. Younus, M. S. Khan, P. R. Raithby, A. Köhler and R. H. Friend, *J. Am. Chem. Soc.*, 2001, **123**, 9412–9417.
50 J. Widengren, Ü. Mets and R. Rigler, *J. Phys. Chem.*, 1995, **99**, 13368–13379.
51 N. I. Nijegorodov and W. S. Downey, *J. Phys. Chem.*, 1994, **98**, 5639–5643.
52 N. R. Verhart, P. Navarro, S. Faez and M. Orrit, *Phys. Chem. Chem. Phys.*, 2016, **18**, 17655–17659.
53 K. Kalyanasundaram, *Coord. Chem. Rev.*, 1982, **46**, 159–244.
54 V. Balzani and S. Campagna, *Top. Curr. Chem.*, 2007, **280**, 143–203.
55 E. Yu-Tzu, Li, T. Y. Jiang, Y. Chi and P. T. Chou, *Phys. Chem. Chem. Phys.*, 2014, **16**, 26184–26192.
56 D. S. M. Ravinson and M. E. Thompson, *Mater. Horizons*, 2020, **7**, 1210–1217.
57 A. Juris and V. Balzani, *Coord. Chem. Rev.*, 1998, **84**, 85–277.
58 M. Bouzrati-zerelli, N. Guillaume, F. Goubard, D. Gigmes, J. P. Fouassier and J. Laleve, *New J. Chem.*, 2018, **42**, 8261–8270.
59 Y. Zhang, T. S. Lee, J. M. Favale, D. C. Leary, J. L. Petersen, G. D. Scholes, F. N. Castellano and C. Milsmann, *Nat. Chem.*, 2020, **12**, 345–352.
60 H. Uoyama, K. Goushi, K. Shizu, H. Nomura and C. Adachi, *Nature*, 2012, **492**, 234–238.
61 F. B. Dias, T. J. Penfold and A. P. Monkman, *Methods Appl. Fluoresc.*, 2017, **5**, 012001.
62 M. Y. Wong and E. Zysman-Colman, *Adv. Mater.*, 2017, **29**, 1605444.
63 Y. Tao, K. Yuan, T. Chen, P. Xu, H. Li, R. Chen, C. Zheng, L. Zhang and W. Huang, *Adv. Mater.*, 2014, **26**, 7931–7958.
64 Y. Im, M. Kim, Y. J. Cho, J.-A. Seo, K. S. Yook and J. Y. Lee, *Chem. Mater.*, 2017, **29**, 1946–1963.
65 J. W. Verhoeven, *Pure Appl. Chem.*, 1996, **68**, 2223–2286.
66 F. Strieth-kalthoff, M. J. James, M. Teders, L. Pitzer and F. Glorius, *Chem. Soc. Rev.*, 2018, **47**, 7190–7202.
67 T. Förster, *Discuss. Faraday Soc.*, 1959, **27**, 7–17.
68 H. Sahoo, *J. Photochem. Photobiol., C*, 2011, **12**, 20–30.
69 J. R. Lakowicz, *Principles of Fluorescence Spectroscopy*, Springer, New York, 3rd edn, 2006.
70 A. D. McNaught and A. Wilkinson, *IUPAC Compendium of Chemical Terminology*, Blackwell Scientific Publications, Oxford, 2nd edn, 1997.
71 D. L. Dexter, *J. Chem. Phys.*, 1953, **21**, 836–850.
72 S. Bai, P. Zhang, P. Antoniou, S. S. Skourtis and D. N. Beratan, *Faraday Discuss.*, 2019, **216**, 301–318.
73 C. R. J. Stephenson, T. P. Yoon and D. W. C. MacMillan, *Visible Light Photocatalysis in Organic Chemistry*, Wiley-VCH, Germany, 2018.
74 E. P. Wigner, *Nachr. Akad. Wiss. Goettingen, Math.-Phys. Kl.*, 1927, 375–381.
75 H. Maudera and K. Petersb, *Chem. Ber.*, 1991, **124**, 407–410.
76 A. Sinicropi, F. Barbosa, R. Basosi, B. Giese and M. Olivucci, *Angew. Chem., Int. Ed.*, 2005, **44**, 2390–2393.
77 B. Giese, P. Wettstein, C. Stähelin, F. Barbosa, M. Neuburger, M. Zehnder and P. Wessig, *Angew. Chem., Int. Ed.*, 1999, **38**, 2586–2587.
78 L. J. Johnston and J. C. Scaiano, *Chem. Rev.*, 1989, **89**, 521–547.
79 W. Adam, H. Platsch and J. Wirz, *J. Am. Chem. Soc.*, 1989, **111**, 6896–6898.
80 B. Giese, F. Barbosa, C. Stähelin, S. Sauer, P. Wettstein and C. Wyss, *Pure Appl. Chem.*, 2000, **72**, 1623–1629.
81 W. H. Kramer and A. G. Griesbeck, *J. Chem. Educ.*, 2008, **85**, 701–709.
82 V. Alezra and T. Kawabata, *Synthesis*, 2016, 2997–3016.
83 T. Šumanovac Ramljak, M. Sohora, I. Antol, D. Kontrec, N. Basarić and K. Mlinarić-Majerski, *Tetrahedron Lett.*, 2014, **55**, 4078–4081.
84 A. G. Griesbeck, W. Kramer and J. Lex, *Angew. Chem., Int. Ed.*, 2001, **40**, 577–579.
85 F. Strieth-Kalthoff and F. Glorius, *Chem*, 2020, **6**, 1888–1903.
86 N. J. Turro, *Pure Appl. Chem.*, 1977, **49**, 405–429.
87 H. Nakanotani, T. Higuchi, T. Furukawa, K. Masui, K. Morimoto, M. Numata, H. Tanaka, Y. Sagara, T. Yasuda and C. Adachi, *Nat. Commun.*, 2014, **5**, 4016.
88 C. K. Prier, D. A. Rankic and D. W. C. MacMillan, *Chem. Rev.*, 2013, **113**, 5322–5363.
89 D. Rehm and A. Weller, *Isr. J. Chem.*, 1970, **8**, 259–271.
90 S. Farid, J. P. Dinnocenzo, P. B. Merkel, R. H. Young, D. Shukla and G. Guirado, *J. Am. Chem. Soc.*, 2011, **133**, 11580–11587.
91 S. E. Braslavsky, *Pure Appl. Chem.*, 2007, **79**, 293–465.

92 R. A. Marcus and N. Sutin, *Biochem. Biophys. Acta*, 1985, **811**, 265–322.
93 G. L. Closs and J. R. Miller, *Science*, 1988, **240**, 440–447.
94 J. R. Miller, *J. Am. Chem. Soc.*, 1984, **106**, 3047–3049.
95 T. Asahi and N. Mataga, *J. Phys. Chem.*, 1989, **93**, 6575–6578.
96 I. R. Gould, D. Ege, J. E. Moser and S. Farid, *J. Am. Chem. Soc.*, 1990, **112**, 4290–4301.
97 I. R. Gould and S. Farid, *Acc. Chem. Res.*, 1996, **29**, 522–528.
98 G. McLendon, *Acc. Chem. Res.*, 1988, **21**, 160–167.
99 J. R. Winkler and H. B. Gray, *Chem. Rev.*, 1992, **92**, 369–379.
100 G. Mclendon and R. Hake, *Chem. Rev.*, 1992, **92**, 481–490.
101 H. Rau, R. Frank and G. Greiner, *J. Phys. Chem.*, 1986, **90**, 2476–2481.
102 K. Kikuchi, Y. Takahashi, T. Katagiri, T. Niwa, M. Hoshi and T. Miyashi, *Chem. Phys. Lett.*, 1991, **180**, 403–408.
103 S. Fukuzumi, K. Ohkubo, T. Suenobu, K. Kato, M. Fujitsuka and O. Ito, *J. Am. Chem. Soc.*, 2001, **123**, 8459–8467.
104 U. Megerle, M. Wenninger, R. J. Kutta, R. Lechner, B. König, B. Dick and E. Riedle, *Phys. Chem. Chem. Phys.*, 2011, **13**, 8869–8880.
105 U. Steiner, G. Winter and H. E. A. Kramer, *J. Phys. Chem.*, 1977, **81**, 1104–1110.
106 L. Bergmann, *New Emitters for OLEDs: The Coordination- and Photo-Chemistry of Mononuclear Neutral Copper(I) Complexes*, Logos Verlag, Berlin, 2016.
107 K. Ohkubo and S. Fukuzumi, *Org. Lett.*, 2000, **2**, 3647–3650.
108 M. Fujita, A. Ishida, S. Takamuku and S. Fukuzumi, *J. Am. Chem. Soc.*, 1996, **118**, 8566–8574.
109 J. W. Verhoeven, *J. Photochem. Photobiol., C*, 2006, **7**, 40–60.
110 J. Hore and R. W. Broadhurst, *Prog. Nucl. Magn. Reson. Spectrosc.*, 1993, **25**, 345–402.
111 B. D. Ravetz, N. E. S. Tay, C. L. Joe, M. Sezen-Edmonds, M. A. Schmidt, Y. Tan, J. M. Janey, M. Eastgate and T. Rovis, *ACS Cent. Sci.*, 2020, **6**, 2053–2059.
112 J. Haimerl, I. Ghosh, B. König, J. Vogelsang and J. M. Lupton, *Chem. Sci.*, 2019, **10**, 681–687.
113 V. K. Singh, C. Yu, S. Badgujar, Y. Kim, Y. Kwon, D. Kim, J. Lee, T. Akhter, G. Thangavel, L. S. Park, J. Lee, P. C. Nandajan, R. Wannemacher, B. Milián-Medina, L. Lüer, K. S. Kim, J. Gierschner and M. S. Kwon, *Nat. Catal.*, 2018, **1**, 794–804.
114 E. Speckmeier, T. G. Fischer and K. Zeitler, *J. Am. Chem. Soc.*, 2018, **140**, 15353–15365.
115 M. Streiter, T. Fischer, C. Wiebeler, S. Reichert, J. Langenickel, K. Zeitler and C. Deibel, Impact of chlorine on the internal transition rates and excited states of the thermally delayed activated fluorescence molecule 3CzClIPN, http://arxiv.org/abs/2001.11317, (accessed 20 May 2020).
116 D. M. Hedstrand, W. H. Kruizinga and R. M. Kellogg, *Tetrahedron Lett.*, 1978, **19**, 1255–1258.
117 C. A. Parker and C. G. Hatchard, *Trans. Faraday Soc.*, 1961, **57**, 1894–1904.
118 A. Penzkofer, A. Beidoun and M. Daiber, *J. Lumin.*, 1992, **51**, 297–314.
119 R. Ishimatsu, S. Matsunami, K. Shizu, C. Adachi, K. Nakano and T. Imato, *J. Phys. Chem. A*, 2013, **117**, 5607–5612.
120 J. Luo and J. Zhang, *ACS Catal.*, 2016, **6**, 873–877.
121 R. Ishimatsu, S. Matsunami, T. Kasahara, J. Mizuno, T. Edura, C. Adachi, K. Nakano and T. Imato, *Angew. Chem., Int. Ed.*, 2014, **53**, 6993–6996.
122 T. Koike and M. Akita, *Inorg. Chem. Front.*, 2014, **1**, 562–576.
123 M. S. Lowry, J. I. Goldsmith, J. D. Slinker, R. Rohl, R. A. Pascal, G. G. Malliaras and S. Bernhard, *Chem. Mater.*, 2005, **17**, 5712–5719.
124 A. Singh, K. Teegardin, M. Kelly, K. S. Prasad, S. Krishnan and J. D. Weaver, *J. Organomet. Chem.*, 2015, **776**, 51–59.
125 Y. Wang, H. M. Carder and A. E. Wendlandt, *Nature*, 2020, **578**, 403–408.
126 L. Flamigni, A. Barbieri, C. Sabatini, B. Ventura and F. Barigelletti, in *Photochemistry and Photophysics of Coordination Compounds II*, ed. V. Balzani and S. Campagna, Springer Berlin Heidelberg, Berlin, Heidelberg, 2007, pp. 143–203.
127 J. D. Slinker, A. A. Gorodetsky, M. S. Lowry, J. Wang, S. Parker, R. Rohl, S. Bernhard and G. G. Malliaras, *J. Am. Chem. Soc.*, 2004, 2763–2767.
128 S. Ladouceur, D. Fortin and E. Zysman-Colman, *Inorg. Chem.*, 2011, **50**, 11514–11526.
129 A. C. Benniston, A. Harriman, P. Li, J. P. Rostron, H. J. Van Ramesdonk, M. M. Groeneveld, H. Zhang and J. W. Verhoeven, *J. Am. Chem. Soc.*, 2005, 16054–16064.
130 D. P. Hari and B. Ko, *Chem. Commun.*, 2014, **50**, 6688–6699.
131 X. Zhang, I. Zhang and L. Liu, *Photochem. Photobiol.*, 2010, **86**, 492–498.
132 T. Shen, Z. G. Zhao, Q. Yu and H. J. Xu, *J. Photochem. Photobiol., A*, 1989, **47**, 203–212.
133 E. M. Arbeloa, C. M. Previtali and S. G. Bertolotti, *ChemPhysChem*, 2018, **19**, 934–942.
134 A. Seret, E. Gandin and A. Van De Vorst, *Chem. Phys. Lett.*, 1987, **135**, 427–431.
135 L. Ludvíková, P. Friš, D. Heger, P. Šebej, J. Wirz and P. Klán, *Phys. Chem. Chem. Phys.*, 2016, **18**, 16266–16273.
136 A. Penzkofer, M. Simmel and D. Riedl, *J. Lumin.*, 2012, **132**, 1055–1062.
137 L. E. Cramer and K. G. Spears, *J. Am. Chem. Soc.*, 1978, **100**, 221–227.
138 L. Buzzetti, G. E. M. Crisenza and P. Melchiorre, *Angew. Chem., Int. Ed.*, 2019, **58**, 3730–3747.
139 M. A. Cismesia and T. P. Yoon, *Chem. Sci.*, 2015, **6**, 5426–5434.
140 E. G. Moschetta, T. Knauber, F. Susanne, F. Lévesque and L. J. Edwards, *Nat. Commun.*, 2020, **11**, 804–807.
141 R. C. McAtee, E. J. McClain and C. R. J. Stephenson, *Trends Chem.*, 2019, **1**, 111–125.
142 J. R. Ochola and M. O. Wolf, *Org. Biomol. Chem.*, 2016, **14**, 9088–9092.
143 S. P. Pitre, C. D. McTiernan and J. C. Scaiano, *Acc. Chem. Res.*, 2016, **49**, 1320–1330.
144 Z. Zhang, W. Xiao, J. Xuan, J. Xuan, Z. Zhang and W. Xiao, *Angew. Chem., Int. Ed.*, 2015, 15632–15641.
145 L. M. Reid, T. Li, Y. Cao and C. P. Berlinguette, *Sustainable Energy Fuels*, 2018, **2**, 1905–1927.

146 W. Wang, H. Huang, C. Yu, Y. Zhang, Y. Zhang and P. S. Mariano, *J. Am. Chem. Soc.*, 2017, **139**, 9799–9802.
147 J. Davies, L. Angelini, M. A. Alkhalifah, L. M. Sanz, N. S. Sheikh and D. Leonori, *Synthesis*, 2018, 821–830.
148 A. Noble, R. S. Mega, D. Pflästerer, E. L. Myers and V. K. Aggarwal, *Angew. Chem., Int. Ed.*, 2018, **57**, 2155–2159.
149 H. Jiang and A. Studer, *Chem. – Eur. J.*, 2019, **25**, 516–520.
150 O. Zhang and J. W. Schubert, *J. Org. Chem.*, 2020, **85**, 6225–6232.
151 N. X. Xu, B. X. Li, C. Wang and M. Uchiyama, *Angew. Chem., Int. Ed.*, 2020, **59**, 10639–10644.
152 S. P. Morcillo, E. M. Dauncey, J. H. Kim, J. J. Douglas, N. S. Sheikh and D. Leonori, *Angew. Chem., Int. Ed.*, 2018, **57**, 12945–12949.
153 X. L. Lyu, S. S. Huang, H. J. Song, Y. X. Liu and Q. M. Wang, *RSC Adv.*, 2019, **9**, 36213–36216.
154 C. Shu, R. S. Mega, B. J. Andreassen, A. Noble and V. K. Aggarwal, *Angew. Chem., Int. Ed.*, 2018, **57**, 15430–15434.
155 T. C. Sherwood, H. Xiao, R. G. Bhaskar, E. M. Simmons, S. Zaretsky, M. P. Rauch, R. R. Knowles and T. G. M. Dhar, *J. Org. Chem.*, 2019, **84**, 8360–8379.
156 R. Gueret, L. Pelinski, T. Bousquet, M. Sauthier, V. Ferey and A. Bigot, *Org. Lett.*, 2020, **22**, 5157–5162.
157 N. Bortolamei, A. A. Isse and A. Gennaro, *Electrochim. Acta*, 2010, **55**, 8312–8318.
158 D. D. M. Wayner, B. A. Sim and D. Griller, *J. Am. Chem. Soc.*, 1989, 755–757.
159 J. Guo, Q. Wu, Y. Xie, J. Weng and G. Lu, *J. Org. Chem.*, 2018, **83**, 12559–12567.
160 H. G. Roth, N. A. Romero and D. A. Nicewicz, *Synlett*, 2016, 714–723.
161 N. R. Patel, C. B. Kelly, A. P. Siegenfeld and G. A. Molander, *ACS Catal.*, 2017, **7**, 1766–1770.
162 C. Zheng, Y. Wang, Y. Xu, Z. Chen, G. Chen and S. H. Liang, *Org. Lett.*, 2018, **20**, 4824–4827.
163 Z. Sun, B. Tang, K. K. C. Liu and H. Y. Zhu, *Chem. Commun.*, 2020, **56**, 1294–1297.
164 H. Cramail, Y. Landais and E. Grau, *Chem. Commun.*, 2018, **54**, 9337–9340.
165 A. H. Jatoi, G. G. Pawar and Y. Landais, *Chem. Commun.*, 2019, **55**, 466–469.
166 T. C. Sherwood, N. Li, A. N. Yazdani and T. G. M. Dhar, *J. Org. Chem.*, 2018, **83**, 3000–3012.
167 E. W. Webb, J. B. Park, E. L. Cole, D. J. Donnelly, S. J. Bonacorsi, W. R. Ewing and A. G. Doyle, *J. Am. Chem. Soc.*, 2020, **142**, 9493–9500.
168 S. He, X. Chen, F. Zeng, P. Lu, Y. Peng, L. Qu and B. Yu, *Chin. Chem. Lett.*, 2020, **31**, 1863–1867.
169 A. N. Herron, D. Liu, G. Xia and J. Q. Yu, *J. Am. Chem. Soc.*, 2020, **142**, 2766–2770.
170 X. L. Huang, Y. Z. Cheng, X. Zhang and S. L. You, *Org. Lett.*, 2020, **22**, 9699–9705.
171 Y. Z. Cheng, X. L. Huang, W. H. Zhuang, Q. R. Zhao, X. Zhang, T. S. Mei and S. L. You, *Angew. Chem., Int. Ed.*, 2020, **59**, 18062–18067.
172 Q.-F. Bao, M. Li, Y. Xia, Y.-Z. Wang, Z.-Z. Zhou and Y.-M. Liang, *Org. Lett.*, 2021, **23**(3), 1107–1112.
173 L. Capaldo, L. Buzzetti, D. Merli, M. Fagnoni and D. Ravelli, *J. Org. Chem.*, 2016, **81**, 7102–7109.
174 J. K. Matsui, D. N. Primer and G. A. Molander, *Chem. Sci.*, 2017, **8**, 3512–3522.
175 S. B. Lang, R. J. Wiles, C. B. Kelly and G. A. Molander, *Angew. Chem., Int. Ed.*, 2017, **56**, 15073–15077.
176 A. Cartier, E. Levernier, V. Corcé, T. Fukuyama, A. Dhimane, C. Ollivier, I. Ryu and L. Fensterbank, *Angew. Chem., Int. Ed.*, 2019, **58**, 1789–1793.
177 Z. Wang, S. Zheng and Z. Lu, *Chem. Sci.*, 2019, **10**, 4389–4393.
178 S. T. J. Cullen and G. K. Friestad, *Org. Lett.*, 2019, **21**, 8290–8294.
179 A. Cartier, E. Levernier, A. L. Dhimane, T. Fukuyama, C. Ollivier, I. Ryu and L. Fensterbank, *Adv. Synth. Catal.*, 2020, **362**, 2254–2259.
180 G. Ikarashi, T. Morofuji and N. Kano, *Chem. Commun.*, 2020, **56**, 10006–10009.
181 X. Wang, M. Yang, W. Xie and J. Wu, *Chem. Commun.*, 2019, **55**, 6010–6013.
182 T. Chinzei, K. Miyazawa, Y. Yasu, T. Koike and M. Akita, *RSC Adv.*, 2015, **2**, 21297–21300.
183 J. C. Tellis, J. K. Matsui, B. A. Vara and G. A. Molander, *ACS Catal.*, 2016, **6**, 8004–8008.
184 M. Jou, D. N. Primer and G. A. Molander, *J. Am. Chem. Soc.*, 2016, **138**, 475–478.
185 B. Zhang, Y. Yi, Z. Q. Wu, C. Chen and C. Xi, *Green Chem.*, 2020, **22**, 5961–5965.
186 T. Constantin, M. Zanini, A. Regni, N. S. Sheikh, F. Juliá and D. Leonori, *Science*, 2020, **367**, 1021–1026.
187 D. Kaiser, A. Noble, V. Fasano and V. K. Aggarwal, *J. Am. Chem. Soc.*, 2019, **141**, 14104–14109.
188 J. Wu, Z. Wang, X. Y. Chen, Y. Wu, D. Wang, Q. Peng and P. Wang, *Sci. China: Chem.*, 2020, **63**, 336–340.
189 S. Cai, Y. Tian, J. Zhang, Z. Liu, M. Lu, W. Weng and M. Huang, *Adv. Synth. Catal.*, 2018, **360**, 4084–4088.
190 M. Lu, Z. Liu, J. Zhang, Y. Tian, H. Qin, M. Huang, S. Hu and S. Cai, *Org. Biomol. Chem.*, 2018, **16**, 6564–6568.
191 N. Meng, Y. Lv, Q. Liu, R. Liu, X. Zhao and W. Wei, *Chin. Chem. Lett.*, 2021, **32**, 258–262.
192 Q. F. Bao, Y. Xia, M. Li, Y. Z. Wang and Y. M. Liang, *Org. Lett.*, 2020, **22**, 7757–7761.
193 H. Wang, J. Zhang, J. Shi, F. Li, S. Zhang and K. Xu, *Org. Lett.*, 2019, **21**, 5116–5120.
194 J. Li, L. Li, M. Zhou and H. Wang, *Org. Chem. Front.*, 2018, **5**, 1003–1007.
195 V. I. Supranovich, G. N. Chernov, V. V. Levin and A. D. Dilman, *Eur. J. Org. Chem.*, 2020, 393–396.
196 M. Zheng, J. Hou, L. Zhan, Y. Huang, L. Chen, L. Hua, Y. Li, W. Tang and B. Li, *ACS Catal.*, 2021, **11**, 542–553.
197 Z. Wang, X. Ji, J. Zhao and H. Huang, *Green Chem.*, 2019, **21**, 5512–5516.
198 X. Ji, Q. Liu, Z. Wang, P. Wang, G.-J. Deng and H. Huang, *Green Chem.*, 2020, **22**, 8233–8237.
199 Z. Wang, Q. Liu, X. Ji, G. J. Deng and H. Huang, *ACS Catal.*, 2020, **10**, 154–159.

200 R. Bevernaegie, S. A. M. Wehlin, E. J. Piechota, M. Abraham, C. Philouze, G. J. Meyer, B. Elias and L. Troian-Gautier, *J. Am. Chem. Soc.*, 2020, **142**, 2732–2737.
201 J. J. Perkins, J. W. Schubert, E. C. Streckfuss, J. Balsells and A. ElMarrouni, *Eur. J. Org. Chem.*, 2020, 1515–1522.
202 M. Lu, H. Qin, Z. Lin, M. Huang, W. Weng and S. Cai, *Org. Lett.*, 2018, **20**, 7611–7615.
203 M. Lu, T. Zhang, D. Tan, C. Chen, Y. Zhang, M. Huang and S. Cai, *Adv. Synth. Catal.*, 2019, **361**, 4237–4242.
204 Z. Lin, M. Lu, B. Liu, J. Gao, M. Huang, Z. Gan and S. Cai, *New J. Chem.*, 2020, **44**, 16031–16035.
205 J. A. Milligan, J. P. Phelan, V. C. Polites, C. B. Kelly and G. A. Molander, *Org. Lett.*, 2018, **20**, 6840–6844.
206 J. P. Phelan, S. B. Lang, J. S. Compton, C. B. Kelly, R. Dykstra, O. Gutierrez and G. A. Molander, *J. Am. Chem. Soc.*, 2018, **140**, 8037–8047.
207 C. Shu, A. Noble and V. K. Aggarwal, *Angew. Chem., Int. Ed.*, 2019, **58**, 3870–3874.
208 N. B. Bissonnette, J. M. Ellis, L. G. Hamann and F. Romanov-Michailidis, *Chem. Sci.*, 2019, **10**, 9591–9596.
209 Z. Song, C. Zhang and S. Ye, *Org. Biomol. Chem.*, 2019, **17**, 181–185.
210 H. Tian, H. Yang, C. Tian, G. An and G. Li, *Org. Lett.*, 2020, **22**, 7709–7715.
211 J. Li, X.-E. Yang, S.-L. Wang, L.-L. Zhang, X.-Z. Zhou, S.-Y. Wang and S.-J. Ji, *Org. Lett.*, 2020, **22**, 4908–4913.
212 T. Ju, Q. Fu, J. H. Ye, Z. Zhang, L. L. Liao, S. S. Yan, X. Y. Tian, S. P. Luo, J. Li and D. G. Yu, *Angew. Chem., Int. Ed.*, 2018, **57**, 13897–13901.
213 R. Alam and G. A. Molander, *Org. Lett.*, 2018, **20**, 2680–2684.
214 M. Graglia, N. Kanna and D. Esposito, *ChemBioEng Rev.*, 2015, **2**, 377–392.
215 A. J. Ragauskas, G. T. Beckham, M. J. Biddy, R. Chandra, F. Chen, M. F. Davis, B. H. Davison, R. A. Dixon, P. Gilna, M. Keller, P. Langan, A. K. Naskar, J. N. Saddler, T. J. Tschaplinski, G. A. Tuskan and C. E. Wyman, *Science*, 2014, **344**, 1246843.
216 W. Boerjan, J. Ralph and M. Baucher, *Annu. Rev. Plant Biol.*, 2003, **54**, 519–546.
217 J. Luo, X. Zhang and J. Zhang, *ACS Catal.*, 2015, **5**, 2250–2254.
218 K. Walsh, H. F. Sneddon and C. J. Moody, *Org. Lett.*, 2014, **16**, 5224–5227.
219 L. J. Mitchell and C. J. Moody, *J. Org. Chem.*, 2014, **79**, 11091–11100.
220 V. Photocatalysts, D. Liu, M. Jiao, Z. Feng, X. Wang, G. Xu and P. Xu, *Org. Lett.*, 2018, **20**, 5700–5704.
221 L. Wu and Q. Liu, *Org. Lett.*, 2019, **4**, 885–889.
222 X. C. Liu, X. L. Chen, Y. Liu, K. Sun, Y. Y. Peng, L. B. Qu and B. Yu, *ChemSusChem*, 2020, **13**, 298–303.
223 X. Y. Yuan, F. L. Zeng, H. L. Zhu, Y. Liu, Q. Y. Lv, X. L. Chen, L. Peng and B. Yu, *Org. Chem. Front.*, 2020, **7**, 1884–1889.
224 J. Y. Gu, W. Zhang, S. R. Jackson, Y. H. He and Z. Guan, *Chem. Commun.*, 2020, **56**, 13441–13444.
225 W. J. Zhou, Z. H. Wang, L. L. Liao, Y. X. Jiang, K. G. Cao, T. Ju, Y. Li, G. M. Cao and D. G. Yu, *Nat. Commun.*, 2020, **11**, 3263.
226 W. J. Yoo and S. Kobayashi, *Green Chem.*, 2013, **15**, 1844–1848.
227 F.-L. Zeng, X.-L. Chen, K. Sun, H.-L. Zhu, X.-Y. Yuan, Y. Liu, L.-B. Qu, Y.-F. Zhao and B. Yu, *Org. Chem. Front.*, 2021, **8**, 760–766.
228 Z. Huang, Y. Gu, X. Liu, L. Zhang and Z. Cheng, *Macromol. Rapid Commun.*, 2017, **38**, 1600461.
229 G. M. Miyake and J. C. Theriot, *Macromolecules*, 2014, **47**, 8255–8261.
230 Z. Huang, L. Zhang, Z. Cheng and X. Zhu, *Polymers*, 2017, **9**, 4–11.
231 S. J. S. Düsel and B. König, *Eur. J. Org. Chem.*, 2020, 1491–1495.
232 J. Twilton, C. C. Le, P. Zhang, M. H. Shaw, R. W. Evans and D. W. C. Macmillan, *Nat. Rev. Chem.*, 2017, **1**, 0052.
233 O. S. Wenger, *Chem. – Eur. J.*, 2021, **27**, 2270–2278.
234 A. Dumoulin, J. K. Matsui, Á. Gutiérrez-Bonet and G. A. Molander, *Angew. Chem., Int. Ed.*, 2018, **57**, 6614–6618.
235 S. Parisien-collette and S. K. Collins, *ChemPhotoChem*, 2018, **2**, 855–859.
236 P. N. D. Cross-coupling, R. Alam and G. A. Molander, *J. Org. Chem.*, 2017, **82**, 13728–13734.
237 E. E. Stache, T. Rovis and A. G. Doyle, *Angew. Chem., Int. Ed.*, 2017, **56**, 3679–3683.
238 J. K. Matsui and G. A. Molander, *Org. Lett.*, 2017, **19**, 436–439.
239 S. O. Badir, A. Dumoulin, J. K. Matsui and G. A. Molander, *Angew. Chem., Int. Ed.*, 2018, **57**, 6610–6613.
240 H. Hsieh, C. W. Coley, L. M. Baumgartner, K. F. Jensen and R. I. Robinson, *Org. Process Res. Dev.*, 2018, **22**, 542–550.
241 Y. Ma, S. Liu, Y. Xi, H. Li, K. Yang, Z. Cheng, W. Wang and Y. Zhang, *Chem. Commun.*, 2019, **55**, 14657–14660.
242 R. S. Mega, V. K. Duong, A. Noble and V. K. Aggarwal, *Angew. Chem., Int. Ed.*, 2020, **59**, 4375–4379.
243 C. Ollivier, L. Fensterbank, C. Le and C. Ollivier, *Chem. Commun.*, 2016, **52**, 9877–9880.
244 J. Yi, S. O. Badir, L. M. Kammer and G. A. Molander, *Org. Lett.*, 2019, **21**, 3346–3351.
245 T. J. Steiman, J. Liu, A. Mengiste and A. G. Doyle, *J. Am. Chem. Soc.*, 2020, **142**, 7598–7605.
246 L. Huang, T. Ji and M. Rueping, *J. Am. Chem. Soc.*, 2020, **142**, 3532–3539.
247 J. C. Tellis, D. N. Primer and G. A. Molander, *Science*, 2014, **345**, 433–436.
248 H. Guan, Q. Zhang, P. J. Walsh and J. Mao, *Angew. Chem., Int. Ed.*, 2020, **59**, 5172–5177.
249 S. Z. Sun, Y. Duan, R. S. Mega, R. J. Somerville and R. Martin, *Angew. Chem., Int. Ed.*, 2020, **59**, 4370–4374.
250 M. Garbacz and S. Stecko, *Adv. Synth. Catal.*, 2020, **362**, 3213–3222.
251 E. M. Dauncey, S. U. Dighe, J. J. Douglas and D. Leonori, *Chem. Sci.*, 2019, **10**, 7728–7733.
252 J. Davies, N. S. Sheikh and D. Leonori, *Angew. Chem., Int. Ed.*, 2017, **56**, 13361–13365.
253 M. Durandetti, M. Devaud and K. Perichon, *New J. Chem.*, 1996, **20**, 659–667.
254 C. Lévêque, V. Corcé, L. Chenneberg, C. Ollivier and L. Fensterbank, *Eur. J. Org. Chem.*, 2017, 2118–2121.

255 M. S. Santos, A. G. Corrêa, M. W. Paixão and B. König, *Adv. Synth. Catal.*, 2020, **362**, 2367–2372.
256 Z. J. Wang, S. Zheng, E. Romero, J. K. Matsui and G. A. Molander, *Org. Lett.*, 2019, **21**, 6543–6547.
257 A. G. Diallo, D. Roy, S. Gaillard, M. Lautens and J. L. Renaud, *Org. Lett.*, 2020, **22**, 2442–2447.
258 F. Cong, X.-Y. Lv, C. S. Day and R. Martin, *J. Am. Chem. Soc.*, 2020, **142**, 20594–20603.
259 Q. Y. Meng, S. Wang and B. König, *Angew. Chem., Int. Ed.*, 2017, **56**, 13426–13430.
260 X. Q. Zhu, H. R. Li, Q. Li, T. Ai, J. Y. Lu, Y. Yang and J. P. Cheng, *Chem. – Eur. J.*, 2003, **9**, 871–880.
261 A. Klein, A. Kaiser, B. Sarkar, M. Wanner and J. Fiedler, *Eur. J. Inorg. Chem.*, 2007, 965–976.
262 J. Santandrea, C. Minozzi, C. Cruché and S. K. Collins, *Angew. Chem., Int. Ed.*, 2017, **56**, 12255–12259.
263 L. Huang, C. Zhu, L. Yi, H. Yue, R. Kancherla and M. Rueping, *Angew. Chem., Int. Ed.*, 2020, **59**, 457–464.
264 B. Persson, *Acta Chem. Scand., Ser. B*, 1977, **31**, 88–89.
265 B. Zhao, R. Shang, W.-M. Cheng and Y. Fu, *Org. Chem. Front.*, 2018, **5**, 1782–1786.
266 S. S. Shah, M. Shee, A. K. Singh, A. Paul and N. D. P. Singh, *J. Org. Chem.*, 2020, **85**, 3426–3439.
267 S. Sheri, A. Paul, M. Bera, Y. Venkatesh and N. D. P. Singh, *Org. Lett.*, 2018, **20**, 5533–5536.
268 Y. B. Dudkina, D. Y. Mikhaylov, T. V. Gryaznova, A. I. Tufatullin, O. N. Kataeva, D. A. Vicic and Y. H. Budnikova, *Organometallics*, 2013, **32**, 4785–4792.
269 C. Su, R. Tandiana, B. Tian, A. Sengupta, W. Tang, J. Su and K. P. Loh, *ACS Catal.*, 2016, **6**, 3594–3599.
270 C. Zheng, W. Cheng, H. Li, R. Na and R. Shang, *Org. Lett.*, 2018, **20**, 2559–2563.
271 J.-C. Grenier-Petel and S. K. Collins, *ACS Catal.*, 2019, **9**, 3213–3218.
272 Q. Meng, T. E. Schirmer, K. Katou and B. Kçnig, *Angew. Chem., Int. Ed.*, 2019, **58**, 5723–5728.
273 K. Takizawa, T. Sekino, S. Sato, T. Yoshino, M. Kojima and S. Matsunaga, *Angew. Chem., Int. Ed.*, 2019, **58**, 9199–9203.
274 M. Kojima and S. Matsunaga, *Synthesis*, 2020, 1934–1946.
275 H. Zhang, Q. Xiao, X. K. Qi, X. W. Gao, Q. X. Tong and J. J. Zhong, *Chem. Commun.*, 2020, **56**, 12530–12533.
276 K. E. Ruhl and T. Rovis, *J. Am. Chem. Soc.*, 2016, **138**, 15527–15530.
277 S. Lin, Y. Chen, F. Li, C. Shi and L. Shi, *Chem. Sci.*, 2020, **11**, 839–844.
278 F. S. Li, Y. Q. Chen, S. J. Lin, C. Z. Shi, X. Y. Li, Y. C. Sun, Z. W. Guo and L. Shi, *Org. Chem. Front.*, 2020, **7**, 3434–3438.
279 F. Li, S. Lin, Y. Chen, C. Shi, H. Yan, C. Li, C. Wu, L. Lin, C. Duan and L. Shi, *Angew. Chem., Int. Ed.*, 2021, **60**, 1561–1566.
280 Y. Li, F. Ying, T. Fu, R. Yang, Y. Dong, L. Lin, Y. Han, D. Liang and X. Long, *Org. Biomol. Chem.*, 2020, **18**, 5660–5665.
281 Y. Wang, X. W. Gao, J. Li and D. Chao, *Chem. Commun.*, 2020, **56**, 12170–12173.
282 J. L. Schwarz, H. M. Huang, T. O. Paulisch and F. Glorius, *ACS Catal.*, 2020, **10**, 1621–1627.
283 C. T. Buse and C. H. Heathcock, *Tetrahedron Lett.*, 1978, **19**, 1685–1688.
284 T. Hiyama, K. Kimura and H. Nozaki, *Tetrahedron Lett.*, 1981, **22**, 1037–1040.
285 J. P. Cheng, Y. Lu, X. Q. Zhu, Y. Sun, F. Bi and J. He, *J. Org. Chem.*, 2000, **65**, 3853–3857.
286 J. He, G. Chen, B. Zhang, Y. Li, J. R. Chen, W. J. Xiao, F. Liu and C. Li, *Chem*, 2020, **6**, 1149–1159.
287 M. M. Mastandrea, S. Cañellas, X. Caldentey and M. A. Pericàs, *ACS Catal.*, 2020, **10**, 6402–6408.
288 R. Zhou, Y. Y. Goh, H. Liu, H. Tao, L. Li and J. Wu, *Angew. Chem., Int. Ed.*, 2017, **56**, 16621–16625.
289 J. Hou, A. Ee, H. Cao, H.-W. Ong, J.-H. Xu and J. Wu, *Angew. Chem., Int. Ed.*, 2018, **57**, 17220–17224.
290 C. Dai, Y. Zhan, P. Liu and P. Sun, *Green Chem.*, 2021, **23**, 314–319.
291 M. H. Shaw, V. W. Shurtleff, J. A. Terrett, J. D. Cuthbertson and D. W. C. MacMillan, *Science*, 2016, **352**, 1304–1308.
292 A. Ryder, W. Cunningham, G. Ballantyne, T. Mules, A. Kinsella, J. Turner-Dore, C. Alder, L. Edwards, B. McKay, M. Grayson and A. J. Cresswell, *Angew. Chem., Int. Ed.*, 2020, **59**, 14986–14991.
293 W. Xu, H. Jiang, J. Leng, H. W. Ong and J. Wu, *Angew. Chem., Int. Ed.*, 2020, **59**, 4009–4016.
294 M. Shimoi, T. Watanabe, K. Maeda, D. P. Curran and T. Taniguchi, *Angew. Chem., Int. Ed.*, 2018, **57**, 9485–9490.
295 S. M. Senaweera, A. Singh and J. D. Weaver, *J. Am. Chem. Soc.*, 2014, **136**, 3002–3005.
296 G. J. Choi, Q. Zhu, D. C. Miller, C. J. Gu and R. R. Knowles, *Nature*, 2016, **539**, 268–271.
297 K. Chen, J. Schwarz, T. A. Karl, A. Chatterjee and B. König, *Chem. Commun.*, 2019, **55**, 13144–13147.
298 Y. Y. Loh, K. Nagao, A. J. Hoover, D. Hesk, N. R. Rivera, S. L. Colletti, I. W. Davies and D. W. C. Macmillan, *Science*, 2017, **358**, 1182–1187.
299 Y. Zhang, P. Ji, Y. Dong, Y. Wei and W. Wang, *ACS Catal.*, 2020, **10**, 2226–2230.
300 F. Legros, P. Fernandez-Rodriguez, A. Mishra, R. Weck, A. Bauer, M. Sandvoss, S. Ruf, M. Méndez, H. Mora-Radó, N. Rackelmann, C. Pöverlein and V. Derdau, *Chem. – Eur. J.*, 2020, **26**, 12738–12742.
301 M.-S. Liu and W. Shu, *ACS Catal.*, 2020, **10**, 12960–12966.
302 A. V. Davies, K. P. Fitzpatrick, R. C. Betori and K. A. Scheidt, *Angew. Chem., Int. Ed.*, 2020, **59**, 9143–9148.
303 L. Buzzetti, A. Prieto, S. R. Roy and P. Melchiorre, *Angew. Chem., Int. Ed.*, 2017, **56**, 15039–15043.
304 D. F. Chen, C. H. Chrisman and G. M. Miyake, *ACS Catal.*, 2020, **10**, 2609–2614.
305 T. Shang, L. Lu, Z. Cao, Y. Liu, W. He and B. Yu, *Chem. Commun.*, 2019, **55**, 5408–5419.
306 P. P. Singh and V. Srivastava, *Org. Biomol. Chem.*, 2021, **19**, 313–321.
307 D. Zhang, M. Cai, Z. Bin, Y. Zhang and D. Zhang, *Chem. Sci.*, 2016, **7**, 3355–3363.
308 T. Hosokai, H. Matsuzaki, H. Nakanotani, K. Tokumaru, T. Tsutsui, A. Furube, K. Nasu, H. Nomura, M. Yahiro and C. Adachi, *Sci. Adv.*, 2017, **3**, e1603282.

309 T. Hosokai, *J. Photonics Energy*, 2018, **8**, 032102.
310 W. Ou, R. Zou, M. Han, L. Yu and C. Su, *Chin. Chem. Lett.*, 2020, **31**, 1899–1902.
311 A. Al Mousawi, D. M. Lara, G. Noirbent, F. Dumur, J. Toufaily, T. Hamieh, T. Bui, F. Goubard, B. Gra, D. Gigmes, J. P. Fouassier and J. Laleve, *Macromolecules*, 2017, **50**, 4913–4926.
312 D. Zhang, M. Cai, Y. Zhang, D. Zhang and L. Duan, *Mater. Horiz.*, 2016, **3**, 145–151.
313 Y. J. Cho, S. K. Jeon, B. D. Chin, E. Yu and J. Y. Lee, *Angew. Chem., Int. Ed.*, 2015, **54**, 5201–5204.
314 T. Nishimoto, T. Yasuda, S. Y. Lee, R. Kondo and C. Adachi, *Mater. Horiz.*, 2014, **1**, 264–269.
315 C. Wang, C. Deng, D. Wang and Q. Zhang, *J. Phys. Chem. C*, 2018, **122**, 7816–7823.
316 Z. Yu, W. Lou, H. Junge, A. Päpcke, H. Chen, L. Xia, B. Xu, M. Wang, X. Wang, Q. Wu, B. Lou, S. Lochbrunner, M. Beller, S. Luo, S. Key and G. C. Technology, *Catal. Commun.*, 2019, **119**, 11–15.
317 R. Ishimatsu, T. Edura, C. Adachi, K. Nakano and T. Imato, *Chem. – Eur. J.*, 2016, **22**, 4889–4898.
318 Y. Liu, X. Chen, X. Li, S. Zhu, S. Li, Y. Song, L. Qu and B. Yu, *J. Am. Chem. Soc.*, 2021, **143**(2), 964–972.
319 Y. J. Cho, K. S. Yook and J. Y. Lee, *Adv. Mater.*, 2014, **26**, 6642–6646.
320 M. Garreau, F. Le Vaillant and J. Waser, *Angew. Chem., Int. Ed.*, 2019, **58**, 8182–8186.
321 F. Le Vaillant, M. Garreau, S. Nicolai, G. Gryn'Ova, C. Corminboeuf and J. Waser, *Chem. Sci.*, 2018, **9**, 5883–5889.
322 A. Kretzschmar, C. Patze, S. T. Schwaebel and U. H. F. Bunz, *J. Org. Chem.*, 2015, **80**, 9126–9131.
323 K. Donabauer, M. Maity, A. L. Berger, G. S. Huff, S. Crespi and B. König, *Chem. Sci.*, 2019, **10**, 5162–5166.
324 Q. Meng, T. E. Schirmer, A. L. Berger, K. Donabauer and B. Konig, *J. Am. Chem. Soc.*, 2019, **141**, 11393–11397.
325 J. Lu, B. Pattengale, Q. Liu, S. Yang, W. Shi, S. Li, J. Huang and J. Zhang, *J. Am. Chem. Soc.*, 2018, **140**, 13719–13725.
326 R. A. Scott and C. M. Lukehart, *Applications of physical methods to inorganic and bioinorganic chemistry*, John Wiley & Sons, 2007, vol. 2.
327 Y. He, D. Anand, Z. Sun and L. Zhou, *Org. Lett.*, 2019, **21**, 3769–3773.
328 F. Le Vaillant, M. D. Wodrich and J. Waser, *Chem. Sci.*, 2017, **8**, 1790–1800.
329 S. S. Shah, M. Shee, Y. Venkatesh, A. K. Singh, S. Samanta and N. D. P. Singh, *Chem. – Eur. J.*, 2020, **26**, 3703–3708.
330 B. A. Sim, D. Griller and D. D. M. Wayner, *J. Am. Chem. Soc.*, 1989, **111**, 754–755.
331 D. D. M. Wayner, D. J. McPhee and D. Griller, *J. Am. Chem. Soc.*, 1988, **110**, 132–137.
332 K. Donabauer and B. Konig, *Acc. Chem. Res.*, 2021, **54**, 242–252.
333 K. P. L. Kuijpers, C. Bottecchia, D. Cambié, K. Drummen, N. J. König and T. Noël, *Angew. Chem., Int. Ed.*, 2018, **57**, 11278–11282.
334 M. A. Graham, G. Noonan, J. H. Cherryman, J. J. Douglas, M. Gonzalez, L. V. Jackson, K. Leslie, Z. Q. Liu, D. McKinney, R. H. Munday, C. D. Parsons, D. T. E. Whittaker, E. X. Zhang and J. W. Zhang, *Org. Process Res. Dev.*, 2021, **25**, 57–67.
335 W. Cheng, R. Shang, M. Fu and Y. Fu, *Chem. – Eur. J.*, 2017, **23**, 2537–2541.
336 B. W. Hadrys and R. J. Phipps, *Synlett*, 2021, 179–184.
337 W. M. Cheng, R. Shang and Y. Fu, *ACS Catal.*, 2017, **7**, 907–911.
338 R. S. J. Proctor, H. J. Davis and R. J. Phipps, *Science*, 2018, **360**, 419–422.
339 R. C. Betori and K. A. Scheidt, *ACS Catal.*, 2019, **9**, 10350–10357.
340 S. Bas, Y. Yamashita and S. Kobayashi, *ACS Catal.*, 2020, **10**, 10546–10550.
341 M. C. Nicastri, D. Lehnherr, Y. H. Lam, D. A. Dirocco and T. Rovis, *J. Am. Chem. Soc.*, 2020, **142**, 987–998.
342 C. Zhou, T. Lei, X.-Z. Wei, C. Ye, Z. Liu, B. Chen, C.-H. Tung and L.-Z. Wu, *J. Am. Chem. Soc.*, 2020, **142**, 16805–16813.
343 J. A. Milligan, K. L. Burns, A. V. Le, V. C. Polites, Z. J. Wang, G. A. Molander and C. B. Kelly, *Adv. Synth. Catal.*, 2020, **362**, 242–247.
344 L. Cardinale, M. O. Konev and A. Jacobi von Wangelin, *Chem. – Eur. J.*, 2020, **26**, 8239–8243.
345 R. Abrams and J. Clayden, *Angew. Chem., Int. Ed.*, 2020, **59**, 11600–11606.
346 M. Shee, S. S. Shah and N. D. P. Singh, *Chem. Commun.*, 2020, **56**, 4240–4243.
347 D. H. R. Barton, J. C. Jaszberenyi and E. A. Theodorakis, *Tetrahedron Lett.*, 1991, **32**, 3321–3324.
348 D. H. R. Barton, J. C. Jaszberenyi and E. A. Theodorakis, *Tetrahedron*, 1992, **48**, 2613–2626.
349 C. Le, T. Q. Chen, T. Liang, P. Zhang and D. W. C. MacMillan, *Science*, 2018, **360**, 1010–1014.
350 V. Pirenne, G. Kurtay, S. Voci, L. Bouffier, N. Sojic, F. Robert, D. M. Bassani and Y. Landais, *Org. Lett.*, 2018, **20**, 4521–4525.
351 S. G. E. Amos, S. Nicolai and J. Waser, *Chem. Sci.*, 2020, **11**, 11274–11279.
352 J. B. I. Sap, N. J. W. Straathof, T. Knauber, C. F. Meyer, M. Médebielle, L. Buglioni, C. Genicot, A. A. Trabanco, T. Noël, C. W. Am Ende and V. Gouverneur, *J. Am. Chem. Soc.*, 2020, **142**, 9181–9187.
353 M. Shee, S. S. Shah and N. D. P. Singh, *Chem. – Eur. J.*, 2020, **26**, 14070–14074.
354 M. Nakajima, E. Fava, S. Loescher, Z. Jiang and M. Rueping, *Angew. Chem., Int. Ed.*, 2015, **54**, 8828–8832.
355 I. Ghosh, R. S. Shaikh and B. Kçnig, *Angew. Chem., Int. Ed.*, 2017, **56**, 8544–8549.
356 A. Jutand and S. Ne, *Eur. J. Org. Chem.*, 1998, 1811–1821.
357 T. Ohtani, Y. Tsuchiya, D. Uraguchi and T. Ooi, *Org. Chem. Front.*, 2019, **6**, 1734–1737.
358 H. J. Timpe, K. P. Kronfeld, U. Lammel, J. P. Fouassier and D. J. Lougnot, *J. Photochem. Photobiol., A*, 1990, **52**, 111–122.
359 M. Sayes, G. Benoit and A. B. Charette, *Angew. Chem., Int. Ed.*, 2018, **57**, 13514–13518.
360 A. R. Flynn, K. A. McDaniel, M. E. Hughes, D. B. Vogt and N. T. Jui, *J. Am. Chem. Soc.*, 2020, **142**, 9163–9168.

361 W. G. Herkstroeter and D. S. McClure, *J. Am. Chem. Soc.*, 1968, **90**, 4522–4527.
362 Q. A. Wu, F. Chen, C. C. Ren, X. F. Liu, H. Chen, L. X. Xu, X. C. Yu and S. P. Luo, *Org. Biomol. Chem.*, 2020, **18**, 3707–3716.
363 T. Lei, C. Zhou, M. Y. Huang, L. M. Zhao, B. Yang, C. Ye, H. Xiao, Q. Y. Meng, V. Ramamurthy, C. H. Tung and L. Z. Wu, *Angew. Chem., Int. Ed.*, 2017, **56**, 15407–15410.
364 D. M. Schultz and T. P. Yoon, *Science*, 2014, **343**, 1239176.
365 A. B. Rolka and B. Koenig, *Org. Lett.*, 2020, **22**(13), 5035–5040.
366 M. J. James, J. L. Schwarz, F. Strieth-Kalthoff, B. Wibbeling and F. Glorius, *J. Am. Chem. Soc.*, 2018, **140**, 8624–8628.
367 U. Streit, F. Birbaum, A. Quattropani and C. G. Bochet, *J. Org. Chem.*, 2013, **78**, 6890–6910.
368 N. Arai and T. Ohkuma, *Tetrahedron Lett.*, 2019, **60**, 151252.
369 F. Birbaum, A. Neels and C. G. Bochet, *Org. Lett.*, 2008, **10**, 3175–3178.
370 W. Xu, P. Zheng and T. Xu, *Org. Lett.*, 2020, **22**, 8643–8647.
371 Q. Meng and S. Wang, *J. Am. Chem. Soc.*, 2018, **140**, 3198–3201.
372 T. K. Sawyer and N. Sciammetta, *Chem. Sci.*, 2019, **10**, 5073–5078.
373 E. R. Welin, C. Le, D. M. Arias-rotondo, J. K. Mccusker and D. W. C. Macmillan, *Science*, 2017, **385**, 380–385.
374 K. C. Cartwright and J. A. Tunge, *Chem. Sci.*, 2020, **11**, 8167–8175.
375 A. Gualandi, F. Calogero, M. Mazzarini, S. Guazzi, A. Fermi, G. Bergamini and P. G. Cozzi, *ACS Catal.*, 2020, **10**, 3857–3863.
376 G. Barzanò, R. Mao, M. Garreau, J. Waser and X. Hu, *Org. Lett.*, 2020, **22**, 5412–5416.
377 R. Mao, A. Frey, J. Balon and X. Hu, *Nat. Catal.*, 2018, **1**, 120–126.
378 S. X. Zou and Y. Zhang, *Chem. Soc. Rev.*, 2015, **44**, 5148–5180.
379 D. Chao and M. Zhao, *Dalton Trans.*, 2019, **48**, 5444–5449.
380 S. Roy, A. Bhunia, N. Schuth, M. Haumann and S. Ott, *Sustainable Energy Fuels*, 2018, **2**, 1148–1152.
381 P. Du, K. Knowles and R. Eisenberg, *J. Am. Chem. Soc.*, 2008, **130**, 12576–12577.
382 T. M. McCormick, B. D. Calitree, A. Orchard, N. D. Kraut, F. V. Bright, M. R. Detty and R. Eisenberg, *J. Am. Chem. Soc.*, 2010, **132**, 15480–15483.
383 G. Zhang, C. Liu, H. Yi, Q. Meng, C. Bian, H. Chen, J. X. Jian, L. Z. Wu and A. Lei, *J. Am. Chem. Soc.*, 2015, **137**, 9273–9280.
384 W. Xu, J. Ma, X. Yuan, J. Dai, J. Xie and C. Zhu, *Angew. Chem., Int. Ed.*, 2018, **57**, 10357–10361.
385 A. L. Berger, K. Donabauer and B. König, *Chem. Sci.*, 2019, **10**, 10991–10996.
386 J. L. Jeffrey, F. R. Petronijević and D. W. C. Macmillan, *J. Am. Chem. Soc.*, 2015, **137**, 8404–8407.
387 K. Donabauer, K. Murugesan, U. Rozman, S. Crespi and B. König, *Chem. – Eur. J.*, 2020, **26**, 12945–12950.
388 J. Ye, Z. Chen, M. Fung, C. Zheng, X. Ou, X. Zhang, Y. Yuan and C. Lee, *Chem. Mater.*, 2013, **25**, 2630–2637.
389 J. Fan, L. Lin and C. Wang, *Chem. Phys. Lett.*, 2016, **652**, 16–21.
390 M. Aydemir, S. Xu, C. Chen, M. R. Bryce, Z. Chi and A. P. Monkman, *J. Phys. Chem. C*, 2017, **121**, 17764–17772.
391 S. Xu, T. Liu, Y. Mu, Y. Wang, Z. Chi, C. Lo, S. Liu, Y. Zhang, A. Lien and J. Xu, *Angew. Chem., Int. Ed.*, 2015, **54**, 874–878.
392 Q. Zhang, J. Li, K. Shizu, S. Huang, S. Hirata, H. Miyazaki and C. Adachi, *J. Am. Chem. Soc.*, 2012, **134**, 14706–14709.
393 S. Y. Lee, T. Yasuda, Y. S. Yang, Q. Zhang and C. Adachi, *Angew. Chem., Int. Ed.*, 2014, **53**, 6402–6406.
394 Q. Zhang, B. Li, S. Huang, H. Nomura, H. Tanaka and C. Adachi, *Nat. Photonics*, 2014, **8**, 326–332.
395 Q. Zhang, H. Kuwabara, W. J. Potscavage, S. Huang, Y. Hatae, T. Shibata and C. Adachi, *J. Am. Chem. Soc.*, 2014, **136**, 18070–18081.
396 N. Sharma, E. Spuling, C. M. Mattern, W. Li, O. Fuhr, Y. Tsuchiya, C. Adachi, S. Bräse, I. D. W. Samuel and E. Zysman-Colman, *Chem. Sci.*, 2019, **10**, 6689–6696.
397 X. Li, J. Li, D. Liu, D. Li and R. Dong, *New J. Chem.*, 2020, 9743–9753.
398 Y. Zhang, Y. Zheng, B. Wang, H. Ran, X. Wang, J. Y. Hu and Q. Wang, *J. Mater. Chem. C*, 2020, **8**, 4461–4468.
399 H. Tanaka, K. Shizu, H. Miyazaki and C. Adachi, *Chem. Commun.*, 2012, **48**, 11392–11394.
400 H. Tanaka, K. Shizu, H. Nakanotani and C. Adachi, *J. Phys. Chem. C*, 2014, **118**, 15985–15994.
401 X. Cai, X. Li, G. Xie, Z. He, K. Gao, K. Liu, D. Chen, Y. Cao and S. J. Su, *Chem. Sci.*, 2016, **7**, 4264–4275.
402 Y. Song, Y. Kim, Y. Noh, V. K. Singh, S. K. Behera, A. Abudulimu, K. Chung, R. Wannemacher, J. Gierschner, L. Lüer and M. S. Kwon, *Macromolecules*, 2019, **52**, 5538–5545.

